Charles University in Prague	Université Louis Pasteur - Strasbourg I
Faculty of Mathematics and Physics	IPCMS/GONLO Strasbourg
Czech Republic	France

Thése

présentée pour obtenir le grade de

Docteur de l'Université Louis Pasteur (Université Strasbourg I)

Discipline: Optique Quantique et Optoéléctronique

par

RNDr. Kateřina Dohnalová

Study of optical amplification in silicon based nanostructures

Soutenue publiquement le 18 Septembre 2007 à Prague

Membres du jury:

Directeur de thése:	Bernd Hönerlage	Prof.	Physique
Codirecteur de thése:	Ivan Pelant	Prof.	Physique
Rapporteur Interne:	Jean-Jacques Grob	DR,CNRS,HDR	Physique
Rapporteur Externe:	Jiří Čtyroký	Prof.	Physique
Rapporteur Externe:	Jean Oberlé	Prof.	Physique
Examinateur:	Štefan Višňovský	Prof.	Physique
Examinateur:	Jiří Oswald	Ing.,CSc.	Physique
Examinateur:	Pierre Gilliot	CR,CNRS,HDR	Physique
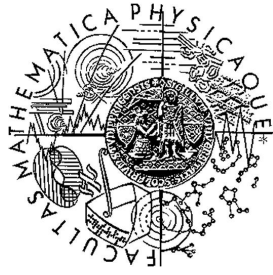
Charles University in Prague

Faculty of Mathematics and Physics

Czech Republic

Université Louis Pasteur - Strasbourg I

IPCMS/GONLO Strasbourg

France

Doctoral Thesis

"thése en cotutelle"

Study of optical amplification in silicon based nanostructures

by

RNDr. Kateřina Dohnalová

Prague & Strasbourg, September 2007

Study of optical amplification in silicon based nanostructures

Supervisors:

Prof. RNDr. Ivan Pelant, DrSc.
Institute of Physics, Academy of Sciences of the Czech Republic, Prague, Czech Republic

Prof. Dr. Bernd Hönerlage
Institute de Physique et Chimie des Matériaux de Strasbourg, Université Louis Pasteur, Strasbourg, France

Advisors:

Prof. RNDr. Petr Malý, DrSc.
Faculty of Mathematics and Physics, Charles University, Prague, Czech Republic

Doc. RNDr. Jan Valenta, Ph.D.
Faculty of Mathematics and Physics, Charles University, Prague, Czech Republic

RNDr. Kateřina Herynková, Ph.D.
Institute of Physics, Academy of Sciences of the Czech Republic, Prague, Czech Republic

Referees:

Prof. Dr. Jean Oberlé
Départements de Physique, Université Bordeaux 1, Talence, France

Prof. Ing. Jiří Čtyroký DrSc.
Institute of Photonics and Electronics, Academy of Sciences of the Czech Republic, Prague, Czech Republic

Dr. Jean-Jacques Grob
Institut d'Électronique du Solide et des Systemes, Strasbourg, France

Abstract

The aim of this work was to prepare light-emitting structure on the basis of silicon nanocrystals (Si-ncs) embedded in a silicon dioxide (SiO_2) based matrix of a sufficiently good optical quality and stable emission properties, which exhibits positive optical gain and can be used as an active material in a laser cavity. The technique of sample preparation is based on a combination of the modified electrochemical etching of silicon wafers and the SiO_2 based sol-gel processing. This method enables us to achieve relatively small oxidized Si-ncs ($\sim$2-3 nm), embedded at virtually arbitrary volume fraction in a SiO_2 based matrix, which is believed to be advantageous for easier stimulated emission (StE) onset observation. The optical gain coefficient was measured using the standard "Variable Stripe Length" (VSL) method, the application of which, however, is limited for low gain. Therefore we implemented a supplemental "Shifting Excitation Spot" (SES) method, enabling us to determine the optical gain coefficient even of such a small magnitude that will not be recognized by the VSL method itself. We observed a positive net gain coefficient originating from the StE in different Si-ncs/SiO_2 samples under different excitation and detection conditions. To prepare a laser system, a positive net gain observation is essential as well as a positive optical feedback. Using an external cavity as a resonator requires a high optical quality sample. This is, however, hardly achievable under the high Si-ncs volume fraction requirements for the StE onset. Because of that we decided to build an optically induced "Distributed Feedback Laser" (DFL) system, where the cavity is distributed over the whole sample volume and the cavity grating constant ($\sim$166 nm) is lower than expected mean homogeneity length in our sample ($\sim$0.5-1.0 μm). Therefore, a positive but low effect on the emission of Si-ncs is expected. Moreover, such type of DFL cavity is easily tuneable. The functionality of the DFL setup was tested using reference organic dye solutions in methanol, where a tuneable lasing action was successfully achieved. Similar tuneable cavity modes were also observed in different Si-ncs/SiO_2 samples, however, of broader widths and less intense, compared to the organic dyes, which is mainly given by their lower optical quality. To understand and describe the mode selection in such a material, we developed a simple theoretical model, enabling us to determine the selected mode shape with respect to the sample homogeneity length and the character of the inhomogeneities. We proved the active feedback of the DFL cavity on the emission of our Si-ncs/SiO_2 samples and proposed some further steps for future sample improvement.

Résumé

Le but principal de ce travaille fut de préparer un matériau photo-luminescent à base de nano-cristaux de Silicium dans une matrice de silice (SiO_2) de qualité optique suffisante pour permettre l'observation d'un gain optique. Des nano-cristaux de silicium peu oxydés de tailles comprises entre 2 et 3 nm ont été obtenus par abrasion électrochimique de wafer de silicium. Les nano-cristaux avec une concentration variable permettant l'observation de leur émission stimulée sont dilués dans une matrice de silice obtenue par procédé sol-gel. Un dispositif optique dit "de zone à longueur variable" ("Variable Stripe Length" VSL) a été utilisé pour la mesure du gain optique des nano-cristaux. Cependant cette méthode seule reste peu fiable pour les matériaux à faible gain optiques tels que les nano-cristaux de silicium. Pour cette raison nous avons combiné la méthode VSL avec celle du "spot d'excitation déplacé " ("Shifting Excitation Spot" SES). Ceci nous permet d'observer des gains faibles qui n'auraient pas pu être atteint avec la méthode VSL seule. Nos résultats montrent clairement l'apparition d'un gain sous différentes conditions d'excitations. Pour préparer un laser il est nécessaire d'avoir un matériau, montrant du gain optique, mais il faut aussi appliquer une contra réaction optique suffisante. L'utilisation d'une cavité optique externe nécessite des échantillons de grande qualité optique. Ceci n'est pas compatible avec un gain élevé qui demande une concentration très forte en nano-cristaux de silicium. Pour cela nous avons construit un laser à "cavité à contra réaction distribuée" ("Distributed Feedback Laser" DFL). Dans ce type de cavité, la contra réaction est distribuée sur l'ensemble de l'échantillon. Le pas du réseau (166 nm) est inférieure aux variations moyennes de densité ($\sim$0.5-1.0 μm) et peut être facilement modifié. Nous espérons ainsi obtenir un gain faible mais suffisant pour être observable. La cavité DFL est tout d'abord calibrée à l'aide de différents colorants dilués dans une solution de méthanol où nous avons observés des modes laser biens définis. Des modes d'émissions laser similaires (des pics plus larges et moins intenses que dans le cas des colorants) ont été obtenus dans nos échantillons Si-ncs/SiO_2. Ceci est principalement dû à la moindre qualitóptique de nos échantillons. Pour comprendre les précédentes observations, nous avons développé un modèle théorique simple nous permettant de retrouver et d'expliquer les modes expérimentaux en jouant sur la variation de densité et les caractéristiques des Si-ncs. L'effet de la contra réaction de la cavité DFL sur nos échantillons est clairement identifié par ce modèle. Ceci nous permet d'entrevoir de nouvelles perspectives pour la caractérisation optique et l'amélioration de nos échantillons.

Abstrakt

Tato disertační práce je věnována studiu vzorků na bázi křemíkových nanokrystalů (Si-ncs) v SiO$_2$ matrici. Cílem je využití těchto vzorků jako aktivního prostředí v laserovém rezonátoru, a proto byly připravovány s důrazem na optickou kvalitu, stabilní optické vlastnosti a kladný optický zisk. Vzorky jsou připravovány metodou kombinující elektrochemické leptání krystalického křemíku a přípravu SiO$_2$ matrice metodou sol-gel. Tato metoda umožňuje připravit vzorky obsahující libovolné množství malých Si-ncs (2-3 nm), což je považováno za výhodné pro snažší pozorování stimulované emise. Optický zisk jsme studovali metodou "Variable Stripe Length" (VSL), jejíž přesnost je ovšem v případě nižších hodnot optického zisku značně omezená. Z tohoto důvodu jsme navrhli metodu VSL rozšířit o tzv. "Shifting Excitation Spot" (SES) metodu, která nám umožňuje měřit i nižší hodnoty optického zisku. Kombinací těchto dvou metod jsme pozorovali kladný optický zisk v různých typech našich vzorků za různých experimentálních podmínek. Pro přípravu laseru je ovšem vedle kladného optického zisku nutná také přítomnost kladné zpětné vazby. Použití externího rezonátoru vyžaduje velmi vysokou optickou kvalitu aktivního materiálu, těžko dosažitelnou v případě našich vzorků, kde je pořeba pro dosažení optického zisku splnit současně také podmínku vysoké hustoty Si-ncs v SiO$_2$ matrici. Proto jsme se rozhodli použít jiný typ rezonátoru - laserem indukovanou mřížku ("Distributed Feedback Laser" (DFL)). Mřížková konstanta rozložené zpětné vazby je kratší (166 nm) než je charakteristická vzdálenost na níž je aktivní prostředí dostatečně opticky homogenní (0,5-1,0 μm), díky čemuž můžeme očekávat kladný, i když menší vliv zpětné vazby. Tento typ zpětné vazby je navíc snadno laditelný. Funkčnost DFL zpětné vazby jsme testovali na organických barvivech, u nichž jsme úspěšně pozorovali laserové mody. Podobné laditelné mody, ovšem značně rozšířené s nižší intenzitou (v porovnání s mody v organických barvivech), jsme pozorovali také ve spektrech našich vzorků. Pro popis modové selekce ve vzorcích s nižší optickou kvalitou jsme vytvořili jednoduchý teoretický model, umožňující charakterizovat homogenitu vzorků. Prokázali jsme aktivní vliv rozložené zpětné vazby DFL na emisní spektra našich vzorků a navrhli jsme další kroky k vylepšení jejich optické kvality.

Acknowledgements

Prague & Strasbourg, September 2007   RNDr. Kateřina Dohnalová

List of abbreviations and symbols:

Technology

CMOS	Complementary Metal Oxide Semiconductor
EtOH	ethanol
H_2O_2	hydrogen peroxide
HF	Hydro-fluoric acid
ITRS	International Technology Roadmap for semiconductors
LED	Light Emitting Diode
MeOH	methanol
PECVD	Plasma Enhanced Chemical Vapor Deposition
por-Si	porous silicon
Si-ncs	silicon nanocrystals
SiO_2	silicon dioxide
TMOS	tetrametoxysilane

Properties

e-h	electron hole pair
FCA	Free Carrier Absorption
FWHM	Full Width in the Half of the Maxima
LO, LA phonons	Longitudinal Optical and Acoustic phonons
QD	Quantum dot
StE	Stimulated Emission
STE	Self-Trapped Exciton
TO, TA phonons	Transverse Optical and Acoustic phonons

Measurement

μ-PL	micro Photoluminescence
DFL	Distributed Feedback Laser
FTIR	Fourier Transformation Infrared Spectroscopy
HRTEM	High Resolution Transmission Electron Microscopy
NA	Numerical Aperture
PL	Photoluminescence
PMT	Photomultiplier
P&P	Pump and Probe method
RTO	Rapid Thermal Oxidation
SES	Shifting Excitation Spot method
VSL	Variable Stripe Length method

Institutes

AVČR	Akademie Věd České Republiky
ASCR(=AVČR)	Academy of Sciences of the Czech Republic
FZÚ	Fyzikální Ústav
IoP(=FZÚ)	Institute of Physics
IPCMS	Institute de Physique et Chimie des Matériaux de Strasbourg
GONLO	Group d'Optique Nonlinéaire

Contents

Chapter 1

INTRODUCTION - SILICON PHOTONICS AND SILICON-BASED LASER

"Silicon Photonics is a critical part of tera-Scale computing as we need the ability to move massive amounts of data on and off these very high performance chips"

Justin Rattner, Intel Chief Technology Officer [1]

1.1 Interconnection bottleneck

The recent silicon-based CMOS (Complementary Metal Oxide Semiconductor) technology "shrinks" continuously according to the Moor's law towards nanoscale devices to perform a higher speed of information transmission and processing at lower costs. Astronomical number of transistors and densely packed kilometers of electrical wires critically limit the performance of the existing silicon microelectronics [2] [3] [4] [5]. The most critical problems are due to (i) the increasing gap between the gate delay and the interconnection delay [3]; (ii) high probability of information losses and latency due to the crosstalks between dense multilevel interconnections (problems with isolation of interconnections); (iii) limited information capacity of electrical interconnections, given by the RC constant; (iv) high density of interconnections and (v) a critical heat dissipation (recently ~ 100 W/cm^2). Si microelectronics technical details - its recent state and expected evolution till 2020 - are freely available in the "International Technology Roadmap for semiconductors" at ITRS web site [6]. To overcome these so-called "interconnection bottleneck" problems, many approaches have been recently developed [7]. First of all - the existing CMOS technology can be

improved by using low-resistivity metals for electrical interconnections (Cu instead of Al) and low-κ dielectrics (material with a small dielectric constant relative to SiO_2) as porous dielectrics or air voids as isolators. Such solution, however, just pushes the "interconnection bottleneck" problems farther in time. Other more radical solutions can be using a more efficient liquid nitrogen cooling system in "Cryo-CMOS" [8] or complete rearrangement and reconstruction of the chip architecture as into the 3D-architecture, molecular microelectronics or silicon-based microphotonics, which we will discuss here in more details.

1.2   Silicon microphotonics

Existing optoelectronics is comparable with the electronics in the 50-ties as for the material diversity and the device scale [9] [10]. Fiber-optics communication has been recently well established due to the high, virtually unlimited, information capacity of $\sim 10^{12}$ bit/s, which is about six orders higher than the maximal information capacity of the electrical interconnections, limited by the RC-constant. Moreover, many different information channels can be transmitted by the speed of light without any heating dissipation and information losses or cross-talks through a single optical waveguide via multiplexing. However, replacing of the recent silicon microelectronics by the existing optoelectronics would be a very expensive and unpractical solution due to the different exotic and toxic materials used for the optical devices fabrication and their relatively large scale, compared with the recent microelectronics. For illustration, the CMOS technology recently uses only the silicon based materials for transistors (Si, SiO_2, Si_3N_4) and metals (Al, Cu) for electrical interconnections. Recent optoelectronics, on the other hand, uses mostly III-V materials as InGaAsP and InGaAs for lasers, amplifiers and detectors, $LiNbO_3$ for modulators and silicon based materials (Si, Si_3N_4, SiO_2, SiO_xN_y) for passive devices. The recent CMOS logical devices are of the $\sim$nm scale, while the optical devices are at least of three orders larger ($\sim\mu$m) due to the larger "effective size" of a photon, compared with an electron or hole.

The research on optical circuits (integrated micro-photonics) started in the 70-ties. The aim here is to process and guide the information encoded into light on integrated optical chips containing the active devices as light emitters (laser diode), modulators, amplifiers and detectors and the passive devices as waveguides, (de)multiplexors, etc. and latterly, the existing electronic intelligence (possibly the optical one in the future) (Fig. 1.1). The first EPIC (Electronic and Photonic Integrated Circuit) - H-fractal structure for synchronous optical clocking - was built in 2003 by Intel and MIT (Massachusetts Institute of Technology) using CMOS compatible technology [11].
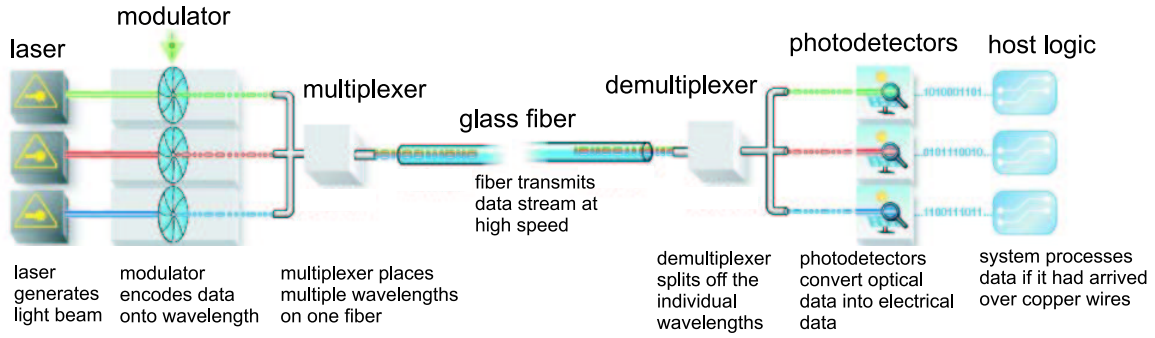
Figure 1.1: *Silicon photonics building blocks, as presented by Intel Co. [12]. Silicon based laser is the last missing key device for the all-silicon on-chip integrated optical circuit.*

Silicon is believed to be the optimum material for the optical components fabrication due to mainly economical and practical reasons. Production of high quality silicon materials and CMOS proceeding technology are the most developed and cheapest, compared with any other semiconductor material technology as those of the III-V or II-VI materials. Moreover, the silicon technologies are less toxic and the sources of the silicon minerals are still huge, since silicon is the most common element (after oxygen element 46.6%) in the Earth's Crust (27.7%) [13]. However, even though silicon physical properties are excellent for microelectronics, they are inappropriate for optoelectronics, because the bulk silicon cannot emit laser-light due to its indirect energy band structure and the electro-optical effects (as Pockels effect) are absent. It is thus logical that the main problems in silicon based photonics arise mainly with the silicon based modulator and laser diode development. The passive devices as waveguides and (de)multiplexors does not represent a critical problem. On the contrary, a high refractive index contrast between crystalline silicon and its native oxide SiO_2 advantageously enables a high optical confinement necessary for the further photonics devices scale shrinking.

Concerning the silicon based modulator: to match the recent performance requirements, the modulation of light for the silicon microphotonics has to reach at least the GHz frequency band, which appears to be a difficult task, since the fast and efficient electro-optical effects are absent. Despite all the difficulties, however, the first silicon based CMOS compatible $\sim$GHz modulator working on the free-carrier dispersion effect was presented in 2004 by Intel company [14]. The free-carrier dispersion effect, used for the light modulation, is based on the free carriers injection which results both in a modified absorption and a change in refractive index. It is still relatively slow, compared to the fast all-optical Kerr effect, as it is associated with the physical movement of the charge within the device, however, it can be driven electrically. Other possibilities which can be used for the light modulation as thermal effects and

mechanical switching are too slow to match the up-to-date frequency requirements.

In the following we will concentrate on the silicon based laser diode development.

1.2.1   Si-based laser diode

The indirect band gap structure of bulk silicon leads to a very low probability of the radiative recombination. The nature of the band gap structure, however, can be modified when playing with the symmetry of the material. In silicon based nanostructures, the translation symmetry is broken and several new features appear due to the quantum confinement effects, as efficient light emission in visible spectral range. It is thus not very surprising, that the first efficient light emission was observed from a silicon based nanostructure material - porous Si (por-Si) - in 1990 by Canham [15]. This observation has started a silicon-boom in optoelectronics and gave a strong motivation for the investigation of a silicon-based laser. The first positive optical gain in silicon nanocrystals (Si-ncs) embedded in SiO_2 based matrices was reported in 2000 by Pavesi et al. [16] and a first efficient silicon based LED with efficiency close to GaAs was presented in 2002 by STMicroelectronics [17]. A kind of laser-like emission was observed in December 2005 from nano-patterned crystalline silicon [18], however, has not yet been fully understood and argued. The laser light can be generally achieved via two different processes: (i) dissipative processes as the light amplification by stimulated emission (StE) and (ii) non-dissipative processes as e.g. the stimulated Raman process. Optically pumped Si-Raman "laser" was presented in February 2005 by Intel and UCLA (University of California, Los Angeles) [19], however, since the stimulated Raman process is purely the light wavelength conversion, it cannot be excited electrically. To the best of our knowledge, however, the silicon-based electrically driven laser diode, where the lasing will be achieved via the the light amplification by StE, has not been successfully built yet and represents the last missing key device for the all-silicon-based integrated micro-photonics development. Recently, the technology found a new possibility - a hybrid solution, based on integration of an electrically driven InP-based laser diode into the silicon microphotonics, demonstrated by Intel and the UCSB (University of California Santa Barbara) in September 2006 [20]. This approach may represent a practical solution for the realization of the microphotonics integrated chip, however, the basic question whether silicon can lase or not has to be still answered.

The fabrication material and the physical concept of the remaining devices will be determined by the Si laser operation spectral range. Concerning the operation wavelength, the recent investigations can be divided into two main groups - the first one's most favorable emission spectral range lies within the recent fiber-optics telecommu-

nication "windows" - infrared 1.3 μm and 1.55 μm - which, however, can not be detected by the purely silicon detector. An alloy $Si_{1-x}Ge_x$ with higher amount of Ge has to be used instead, where the lattice mismatch between $Si_{1-x}Ge_x$ and crystalline silicon is very high $\sim$4.2% and causes critical technological problems. The second group investigation is focused on Si-ncs-based emitters with a wide emission spectrum across the visible region $\sim$(350-850) nm, which can be easily transmitted by SiO_2 waveguides and detected by a purely silicon detector. Moreover, a wide emission spectrum will be highly advantageous for the signal multiplexing. The main possible disadvantage here is that the wavelengths shorter than 1.1 μm can be reabsorbed by the bulk silicon in adjacent parts to the optoelectronic chip. Both possibilities - the infrared and the visible spectral region - are currently investigated in parallel.

To this end, many different silicon based materials for the silicon based laser fabrication have been recently studied, among them also Si-ncs embedded in the SiO_2 based matrices [16] [21] [22], [23] [24] [25] (for the review see e.g. [26]) which represent the main topic of this doctoral thesis.

1.3   Outline of the thesis

The motivation of this work, Si-based laser development, was discussed in the previous section. Our group at the Institute of Physics in Prague in close cooperation with Charles University in Prague, IPCMS in Strasbourg, Royal Institution in Stockholm, Vilnius University and Australian National University in Canberra has been already involved in the research of light emission and electroluminescence of silicon based materials for a long time [27] [28] [29]. We have already published interesting results on the optical gain measurements in Si-ncs/SiO_2 based materials [21], which is the main reason why we have continued with the further study in the frame of my PhD work. The aim of this work has been (i) to prepare a Si-ncs/SiO_2 based light emitting structure of a sufficiently high optical quality and stable (non-degrading in time) emission properties, which would exhibit a positive optical gain and could be used as an active material in a laser cavity; (ii) to build and optimize the Variable Stripe Length (VSL) & Shifting Excitation Spot (SES) method for the low optical gain measurements and to characterize the optical gain properties of prepared samples under a pulsed nanosecond UV optical excitation; (iii) to realize the first attempt of a laser action in our system of densely packed Si-ncs adding an optical feedback suitable for the Si-ncs/SiO_2 samples; (iv) describe theoretically the mode selection in such a material and propose the future steps.

The thesis is organized as follows - in the first two chapters 1 and 2 a short summary of the motivation and theoretical background of this work will be presented. The rest of the thesis is devoted to our original experimental results obtained with the samples of Si-ncs embedded in the SiO_2 based matrix. Chapter 3 describes the technique of sample preparation based on a modified electrochemical etching of silicon wafers combined with a sol-gel processing, inspired by the original work of one of our colleagues - see V. Švrček et al. [30]. In the following chapter 4 we present a characterization of basic structural properties of Si-ncs as the size distribution and the surface passivation character. The aim here is, following the theoretical discussion in the chapter 2, to achieve small Si-ncs with blue-shifted emission spectra embedded at high volume fractions in SiO_2 based matrix with stable emission properties. We decided to prepare our samples on our own, because the direct experimental feedback for the sample preparation technique improvement is necessary: Samples of a sufficiently good quality and properties only can be used in subsequent optical gain and optical feedback experiments. The basic optical properties as the light emission and absorption spectra together with the time resolved Photoluminescence (PL) emission spectra are presented in the following chapter 5. Optical gain measurement methods VSL & SES (Variable Stripe Length and Shifting Excitation Spot) and a critical review of the VSL method for the low-gain materials measurements are presented in the chapter 6, where also the most significant results measured in our Si-ncs/SiO_2 samples will be presented and discussed. In the chapter 7 we describe the experimental realization of a tunable Distributed Feedback Laser (DFL) cavity together with a simple theoretical model, which we have developed to better understand the spectral shape and position of the measured cavity modes. We will analyze and compare the experimental results obtained in our Si-ncs/SiO_2 samples with the model and show the principal obstacles, preventing us from the achievement of a net laser action. Finally, in the chapter 8 we will summarize the results, we attempt to critically assess prospects for lasing in an ensemble of Si-ncs embedded in SiO_2 based matrix and present our hints for the future improvement.

The results obtained throughout my PhD thesis are reported in impacted journals Refs. [31] [32] [33] [34] [35] [36] [37] [38] [39], non-impacted journals [40] [41] and many different international conference proceeding (see list of publications in section 9.3). The Ref. [36] has been selected for publishing in July 4, 2006 issue of Virtual Journal of Nanoscale Science & Technology (www.vjnano.org) and Ref. [37] was granted by a "Young Scientist Award" at the E-MRS (European Materials Research Society) Spring Meeting in Nice, France (June 2006). In the frame of this PhD thesis I have

been invited to talk about this exciting subject and our particular results at University of Stuttgart in Germany, at the Institute of Physics (Department of Theoretical Physics) in Strasbourg in France and at IPCMS Strasbourg in France (see list of publications in section 9.3).

Chapter 2

OPTICAL PROPERTIES OF OXIDIZED SI-NCS

Necessary conditions for lasing are (i) a positive net optical gain and (ii) a positive optical feedback. For the positive net optical gain, a stimulated emission (StE) onset and a low optical losses are essential. The problem connected with searching light emitting silicon-based material for a laser diode application is sometimes formulated in the phrase *"optical circuits have yet to find their silicon"* [9]. The problems with the light emission and StE onset in bulk crystalline silicon arises mainly from the indirect nature of the band-gap and fast nonradiative processes depleting the population inversion as an Auger recombination and a Free Carrier Absorption (FCA). Optical properties of Si-ncs, however, differ in many points from those of the bulk silicon. Si-ncs based material exhibits efficient tunable light emission in the visible spectral range and a positive net optical gain has been reported by several groups [16] [21] [22] [31] [32] [34]. In this chapter we will review the main differences in the basic optical properties between the bulk silicon and Si-ncs, important for the StE onset and the light amplification.

2.1 Stimulated emission in bulk crystalline silicon

In an indirect band-gap material like bulk silicon, radiative recombination is a simultaneous three particle process - a phonon assisted e-h pair recombination - of very low probability. Compared to the efficient nonradiative processes as the Auger recombination or the FCA with a decay time τ_{nr} of the order of nanoseconds, the decay of the radiative processes τ_r is very long of the order of milliseconds. The competition between radiative and nonradiative transitions can be described by an internal luminescence quantum efficiency $\eta_{int} = \frac{\tau_{nr}}{\tau_r + \tau_{nr}}$ which determines the number of all radiative transitions compared to the sum of all transitions. In a direct band gap

material as GaAs, η_{int}^{GaAs} equals to 0.5, i.e. each second recombination process leads to a photon emission, while in bulk Si it is each millionth process only (η_{int}^{Si}=10^{-6}). Thus, bulk silicon is an inefficient emitter, emitting weakly in the infrared spectral region $\lambda \sim$1.1 μm, as driven by the bulk silicon band-gap energy of E_g=1.1 eV. The internal quantum efficiency can be increased by lowering the number of nonradiative transitions as it has been demonstrated in an ultra-pure crystalline silicon LED made by Green et al. in [42] or by increasing the number of radiative transitions by a higher spatial localization of the carriers within the crystalline silicon p-n junction [43] [44].

The main limitation of the StE onset in bulk silicon stems, as stated above, from the FCA losses and the nonradiative Auger recombination, both depleting the population inversion at high pumping rates, necessary for the StE achievement. The Auger process in bulk silicon is a three-body process, the probability of which is dependent on the third power of the free carrier density $P_A \sim n_{FC}^3$. Its recombination decay time in bulk silicon is about $\tau_A \sim$10 ns (for n_{FC}=10^{19}cm^{-3}) only. According to the Drude model, the FCA coefficient depends linearly on the density of free carriers and quadratically on the wavelength of absorbed light as $\alpha_{FCA}(\lambda, n_{FC}) \sim$10$^{-18}n_{FC}\lambda^2$. It is approximately of the same magnitude in direct and indirect band-gap materials ($\alpha_{FCA} \approx$10 cm^{-1}). Besides depleting the population inversion, the FCA increases the overall optical losses given by the sum $\alpha_{tot}(\lambda) = \alpha_{FCA}(\lambda)+K(\lambda)+\alpha(\lambda)$, where $\alpha(\lambda)$ is the absorption coefficient (interband and/or impurity), defined by the Fermi's Golden rule and $K(\lambda)$ means the optical losses caused by the light scattering. Attenuation of light at a wavelength λ in the material with positive optical losses $\alpha_{tot}(\lambda) > 0$ can be defined as a relative change (decrease) of the light intensity $I(x, \lambda)$, passing an infinitesimal distance dx:

$$\alpha_{tot}(\lambda) = \frac{dI(x,\lambda)}{dx}\frac{1}{I(x,\lambda)} \tag{2.1}$$

By integration this differential equation over the optical path of length d we get the well known Beer-Lambert formula:

$$I(d, \lambda) = I(0, \lambda)e^{-\alpha_{tot}(\lambda)d} \tag{2.2}$$

In the equilibrium state, total optical losses are always positive $\alpha_{tot}(\lambda) > 0$ and the passing light will be attenuated. On the other hand, under the external pumping the population inversion can be established between the relevant energy states (three- or four-level system) and the absorption coefficient $\alpha(\lambda)$ can switch, due to the StE onset, to its negative values, defined as a positive optical gain $g(\lambda)$. Moreover, if the optical losses $\alpha_{FCA}(\lambda) + K(\lambda)$ are small enough to ensure the relation

$$(|\alpha_{FCA}(\lambda) + K(\lambda)| < |\alpha(\lambda)|) \wedge (\alpha(\lambda) < 0) \Rightarrow (\alpha_{tot}(\lambda) < 0), \tag{2.3}$$

then the total optical losses $\alpha_{tot}(\lambda)$ became negative and the light passing through the material will be amplified. The magnitude of the light amplification is characterized by the net optical gain coefficient $G(\lambda)$, defined as the negative value of the total optical losses $\alpha_{tot}(\lambda)$. In direct-gap materials, the maximal positive value of the $\alpha(\lambda)$ is equal to the maximal absolute value of $g(\lambda)$, i.e. $|\alpha_{max}(\lambda)| = |g_{max}(\lambda)|$. This we demonstrate in Fig. 2.1(a) (as taken from [45]), where the normalized absorption/gain coefficient in a direct-gap material with E_g=1.1 eV is plotted as a function of the quasi-Fermi energies separation $\Delta\mu$ (caused by an external pumping). The electronic population inversion is established, if $\Delta\mu$ is larger than the gap energy 1.1 eV (yellow field in Fig. 2.1(a)).
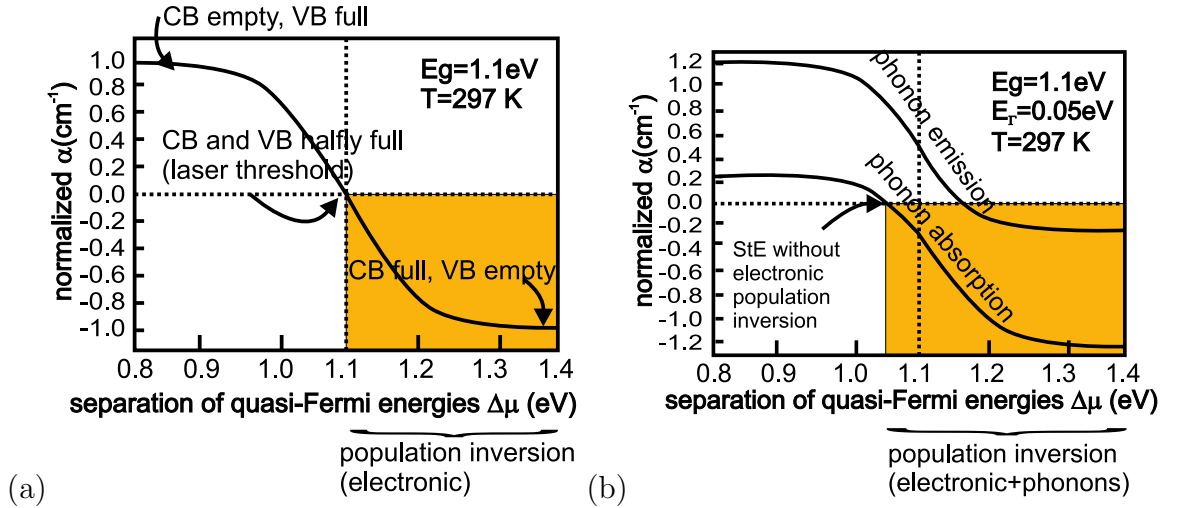
Figure 2.1: *Absorption/gain coefficient dependence on the population of the conduction band (CB) and the valence band (VB) in (a) a direct and (b) an indirect band-gap material of the gap energy of 1.1 eV. Yellow fields marks the region where the population inversion is established. Taken from [45].*

For example, in a direct band-gap material as the bulk GaAs of a sufficiently high optical quality, the light amplification condition Eq. 2.3 can be easily satisfied, since $\alpha_{max} \approx 1500$ cm^{-1} is much larger than the magnitude of FCA losses $\alpha_{FCA} \approx 10$ cm^{-1} (for $n = p = 10^{18}$cm^3). In indirect band-gap material like bulk silicon, on the other hand, the situation is different. The radiative recombination involves the third particle - phonon, which absorption and emission have to be involved into the absorption/gain coefficient calculation. This leads to the splitting of the single absorption/gain curve into the two curves separated from the original one by the phonon energy $\pm \sim$50 meV (see Fig. 2.1(b); as taken from [45]). In the processes involving the phonon emission we get $|g_{max}(\lambda)| \ll |\alpha_{max}(\lambda)|$, while in the processes with the phonon absorption we

have $|g_{max}(\lambda)| \gg |\alpha_{max}(\lambda)|$. Thus, at low temperatures ($<$100 K) when the phonon states are not populated and only phonon emission related transitions are possible, FCA losses will always exceed the possible optical gain, making the light amplification hardly achievable. A similar results has been already suggested by Dumke et al. in [46]. On the other hand, Trupke et al. have recently put forward an interesting idea [45]: at room temperature the phonon states become populated and FCA losses can become smaller than the positive optical gain coefficient. Moreover, a combination of an electronic and a phonon population inversion is necessary for the StE onset (yellow field in Fig. 2.1(b)), suggesting surprisingly a possibility of a positive optical gain before the purely electronic population inversion can be established. Although it may seem theoretically possible, to the best of our knowledge, up to now no bulk silicon based laser diode founded on this effect has been reported and the question whether it is possible or not remains opened. We rather change the subject and describe now the most important optical properties of Si-ncs embedded in an SiO$_2$ based matrix, which represents the subject of our primary interest here.

2.2   Optical properties of Si-ncs

Compared to bulk silicon, Si-ncs exhibit many different features due to the quantum confinement effects, caused by the spatial localization of carriers within the small crystalline Si-nc core. The optical properties strongly differ as a function of the spatial confinement of the exciton with respect to the free exciton Bohr radius in bulk silicon a_B=4.9 nm. In the *weak confinement regime*, when the Si-ncs diameter R_{Si-ncs} is larger than a_B, Si-ncs surface does not critically influence the electronic properties of the core and the emission is mainly due to the phonon-related band-to-band transitions. The electronic and optical properties in such case can be described with a sufficient accuracy by simple bulk approaches as e.g. the Effective Mass Approximation. However, since our Si-ncs average size, estimated using High Resolution Transmission Electron Microscopy (HRTEM) and Raman spectra in chapter 4, is only $R_{Si-ncs}\sim$2.7 nm, our nanocrystals belong mostly to the second category - a *strong confinement regime*, where $R_{Si-nc} < a_B$. Here the surface potential and the quantum confinement effects critically influence the electronic and optical properties of Si-ncs. Therefore, more advanced theoretical approaches as e.g. Density Functional Approach [47] [48] or Linear Combination of Atomic Orbitals method has to be used instead for the calculation of the electronic properties. These methods represent very complex and time consuming methods, however, for estimation of the basic features of the optical properties in such small crystallites, a simple model of the particle in a

3D Quantum Well (i.e. Quantum Dot - QD) is sufficient. Since it is not our primary goal here to discuss the theory in more details, we will in the following just briefly summarize the most important effects influencing the light emission and the optical gain in small oxidized Si-ncs.

2.2.1 Quantum confinement effects

2.2.1.1 Symmetry breaking

The bulk approximations cannot be used in a small Si-nc mainly due to the short scale periodicity of the crystalline lattice caused by the spatial confinement and the lattice distortion following mainly from the Si-ncs surface reconstruction. Since the translation symmetry and the $\vec{k}$ vector cannot be properly defined in such a system, the band structure as in the bulk silicon can be hardly achievable. According to the theoretical calculations of Yu et al. [49], the complete symmetry breaking appears for R_{Si-ncs} between 1.5 nm and 2.5 nm ($\sim$300-500 Si atoms), which is very close to the average diameter of our Si-ncs ($\sim$2.7 nm), estimated by HRTEM and Raman spectra in chapter 4.
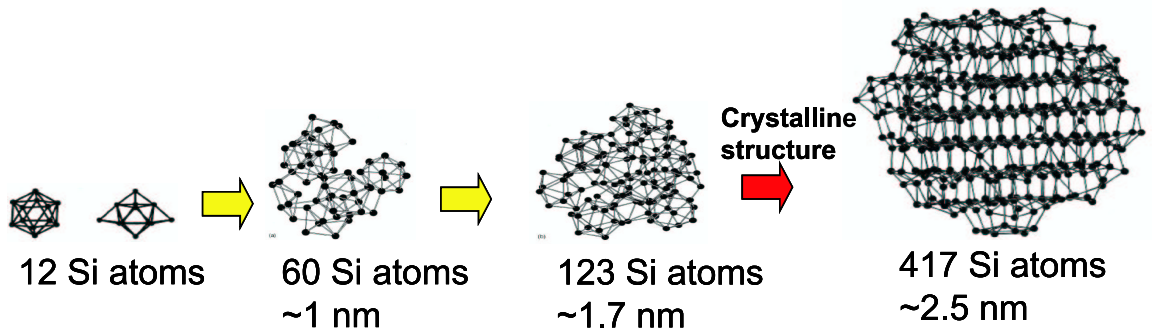
Figure 2.2: *Theoretical simulation of the crystalline silicon symmetry breaking in small Si-ncs according to Yu et al. [49]. Above the Si-ncs diameter of $\sim$2 nm, clearly crystalline Si-nc core appears, while below this size the core remains amorphous.*

2.2.1.2 Atomic-like energy states

The density of states in spatially confined systems strongly differs from that in bulk semiconductors. Fig. 2.3 shows the density of states as a function of the carriers energy for bulk (3D) material, Quantum Well (2D), Quantum Wire (1D) and Quantum Dot - QD - (0D). In particular, the density of states in QD is close to $\delta(E_i)$ function, leading to a narrower atomic-like emission line and a lower laser threshold. The energy states of an e-h pair in the QD of a rectangular or a round shape form a discrete set of atomic-like energy levels separated by ΔE_i (Fig. 2.3).
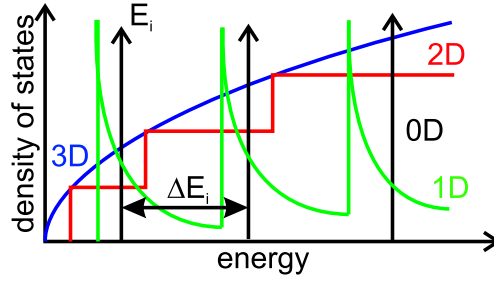
Figure 2.3: *Density of states in spatially confined systems - 3D (bulk), 2D (Quantum Well), 1D (Quantum Wire) and OD (Quantum Dot - QD). Si-ncs can be described as a QD system, where the density of states is close to $\delta(E_i)$ function. The energy states form then a discrete set of atomic-like energy levels, separated by some ΔE_i.*

Both the lowest energy of the e-h pair in Si-ncs, the confined gap energy $E_0 \equiv E_g^{conf}$ and the separation ΔE_i increase with the decreasing Si-ncs size R_{Si-ncs}. The confined gap energy E_g^{conf} dependence on R_{Si-ncs} can be described by a simple reciprocal quadratic law $E_g^{conf} = E_g + \frac{\hbar^2 \pi^2}{2mR_{Si-ncs}^2}$, where $\hbar$ is the Planck constant, m denotes the reduced mass of e-h pair and E_g means the bulk gap energy of ∼1.1 eV. According to [50] it can be numerically estimated using the equation ∼$1.16 + 11.8/R_{Si-ncs}^2$, simulated in Fig. 2.4(a). Tuneability of the E_g^{conf} by the crystallite size leads to a tunable wavelength of the confined e-h pair related emission as shown in Fig. 2.4(b) [50]. Thus, the emission and the absorption spectrum of an ensemble of Si-ncs with broader size distribution will be inhomogeneously broadened and remains broad even at low temperatures. A fine structure in the absorption and the emission spectra of an ensemble of Si-ncs, from which the origin of the radiative transitions can be determined, will be hardly achievable. Moreover, a disordered surface potential and phonon related transitions would lead to a further broadening of the spectra, as observed even from a single Si-nc spectroscopy [51].

Moreover, higher E_g^{conf} in spatially confined systems leads to a higher binding energy of the excitons and multi-excitonic systems, which become stable even at room temperature. The thermalization of the excited carriers via emission of optical phonons can be lowered or completely suppressed ("phonon bottleneck"), because ΔE_i >70 meV (LO). However, the "phonon bottleneck" effect has not yet been observed in Si-ncs systems, since the relaxation can still be realized via the emission of the acoustic phonons (TA, LA), whose energy spectrum is continuous.

2.2.1.3 Fermi Golden rule, oscillator strength and quasi-direct recombination

As mentioned above, the band-to-band absorption coefficient can be calculated from the Fermi Golden rule, which generally defines the number of radiative transi-
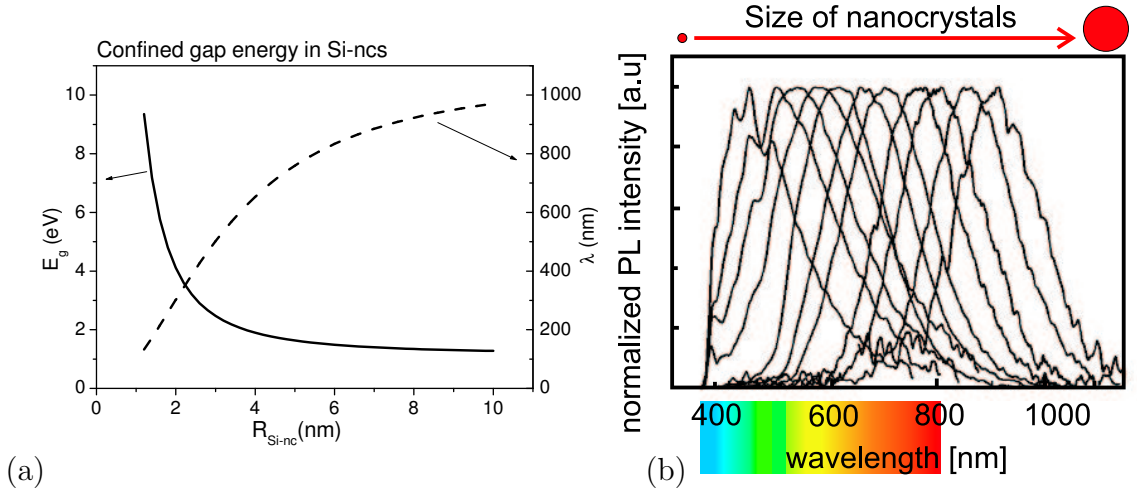
Figure 2.4: *(a) The confined band gap energy as a function of the Si-ncs size. (b) Tuneability of the emission wavelength by the Si-ncs average size in the non-oxidized Si-ncs ensemble according to Kim et al. [50].*

tions per second as

$$W_{ck} \approx \omega F_{cv}(\omega) J_{cv}(\omega) \tag{2.4}$$

$$F_{cv}(\omega) \sim |\langle \Psi_{c,\vec{k}} | \vec{e}\vec{p}_{cv}(\vec{k}) | \Psi_{v,\vec{k}} \rangle|^2$$

where ω is the frequency, $F_{cv}(\omega)$ is the oscillator strength, $\Psi_{c,\vec{k}}$, $\Psi_{v,\vec{k}}$ stand for the electron and hole wavefunctions, $\vec{e}\vec{p}_{cv}(\vec{k})$ means the electrical dipole moment projection onto the photon polarization direction and $J_{cv}(\omega)$ is the joint density of states. The band-to-band absorption/gain coefficient is given by a term $\alpha \propto F_{cv}(\omega) J_{cv}(\omega)$. The oscillator strength magnitude is very sensitive to the overlap of the electron and hole wavefunctions, which increases with the spatial localization of the carriers within the smaller crystalline Si-nc core (see Fig. 2.5). This directly results in a higher probability of the radiative recombination and a shorter radiative decay time τ_{rad} in smaller Si-ncs and thus to a higher internal quantum efficiency η_{int}.

What is even more important is that due to the Heisenberg relations of uncertainty, the e-h wavefunctions overlap in smaller Si-ncs will increase also in $\vec{k}$-space, leading to the quasi-direct transitions, i.e. transitions without phonon assistance. A simple sketch of the basic idea of the quasi-direct transition is plotted in Fig. 2.6(a). These quasi-direct transitions has to be involved in an oscillator strength calculation of smaller Si-ncs (bottom Fig. 2.6(a)), since their contribution, beside the phonon-related transitions, is believed to become significant in Si-ncs of $R_{Si-ncs} < 2$ nm (see Fig. 2.6(b)). The more detailed study of the phonon-related transitions and their competition with the quasi-direct transitions in small Si-ncs is discussed in [52] [53].
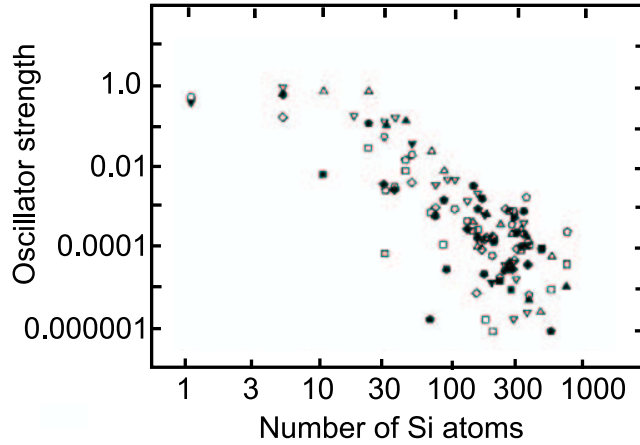
Figure 2.5: *Oscillator strength magnitude as a function of the crystallites size according to Yu et al. [49].*
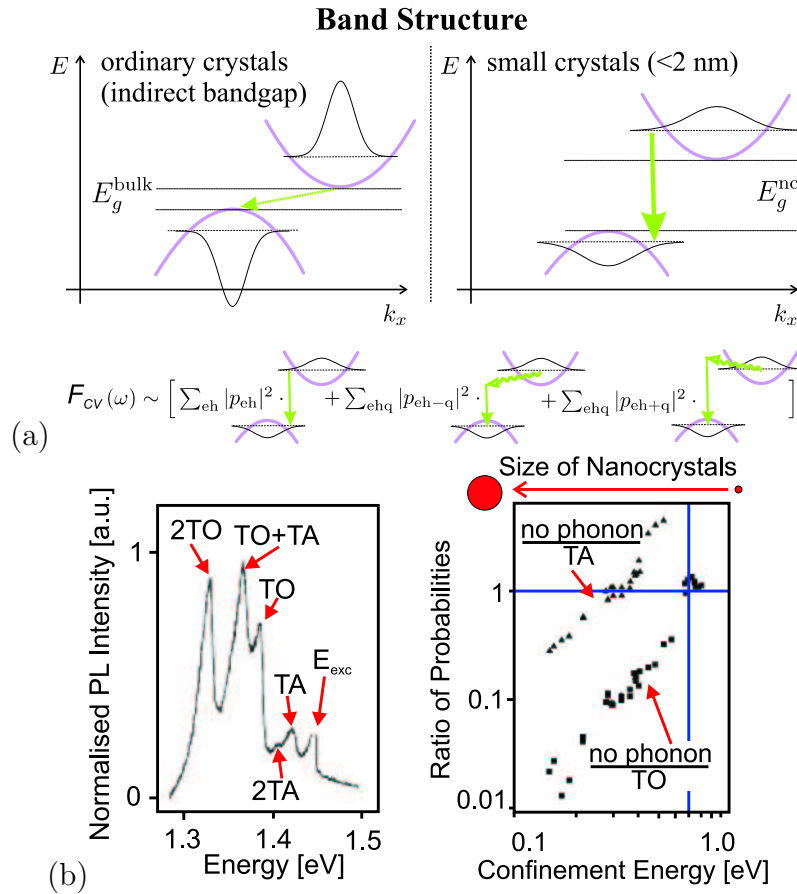
Figure 2.6: *(a) Quasi-direct transitions versus phonon-related transitions [52]. (b) Competition between the phonon-related (TO, TA) and quasi-direct transitions according to Kovalev et al. [53].*

2.2.2   Light emission in oxidized Si-ncs, surface/interface states

Basic difference in the light emission mechanism between non-oxidized Si-ncs (i.e. hydrogen passivated) and oxidized Si-ncs (i.e. oxygen surface passivated) has been

established experimentally by many authors [47] [54] [55] [56] [57] [58] [59]. The emission of the H-terminated Si-ncs is generally explained in terms of the recombination of "free" excitons, confined within the Si-nc crystalline core, the radiative recombination of which decays in nanosecond scale (may be even faster) and the photon energy is proportional to the confined gap energy (see Fig. 2.4(b), [47] [50]), i.e. it is tunable via the Si-ncs size. On the other hand, in oxidized Si-ncs, the main recombination mechanism corresponds, beside the confined "free" exciton recombination, to a trapped exciton at Si-ncs/SiO$_2$ surface/interface, usually known as the "Self-Trapped Exciton" (STE) [55] [58] [60] [61]. The trapping leads to a spatial separation of the carriers. According to [47], the trapped electron state is a p-state localized on the Si atom of the SiO bond and the trapped hole state is a p-state localized on the oxygen atom; see Fig. 2.7(a). Spatial carriers separation leads to an increase in the PL decay time due to the lower recombination probability and to a lower Auger recombination rate. Trapped confined e-h pair is then localized between the Si-nc core and a deformed SiO$_2$ surface shell. Due to that, below a certain size limit, the emission photon energy becomes insensitive to the Si-ncs size (Fig. 2.7(b-B)). It happens when the surface/interface related states (blue lines in Fig. 2.7(a)) appear located inside the opened gap (red lines in Fig. 2.7(a)). Disordered potential on the surface, extrinsic nature of the self-trapping process and the matrix distortion around the Si-ncs surface shell cause the size insensitivity and broadening of the emission spectrum. However, as suggested previously, the origin of the emission in oxidized Si-ncs is probably due to both the "free" confined exciton and the self-trapped exciton radiative recombination [16] [55] [62] [63]. Moreover, the trapped excitonic energy states form a four-level system (Fig. 2.8 [60] [61] [64]), believed to be advantageous for the easier StE onset observation. The schematic configuration coordinate diagram of the ground state (G), the normal (core) excitonic state (E) and the self-trapped excitonic state (STE) is sketched in Fig. 2.8 [60] [61].

Energy levels form a four level system, where the population inversion can be easily established even at lower excitation pumping rates (even for $\langle N \rangle = 1$, where $\langle N \rangle$ is number of excited e-h pair per nanocrystal). This is very important feature, since the population inversion can be established below the pump fluency necessary for the Auger mechanism onset in confined system, requiring $\langle N \rangle > 1$ (see discussion in section 2.2.3). Such a four-level system formation can be also explained, according to the very recent article of V. I. Klimov et al. [65], in terms of inhibition of absorption transition caused by the Stark effect (spatially separated e-h pair leads to a strong local electric field formation), breaking the exact balance between the absorption and stimulated emission and allowing the optical amplification due to a single exciton (i.e.
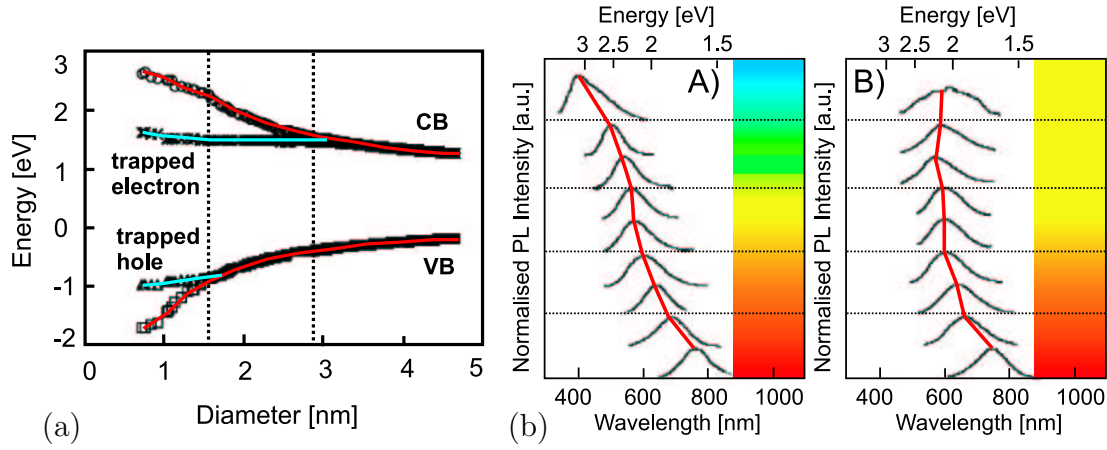
Figure 2.7: *As taken from [47]: (a) Electronic states in Si-ncs as a function of cluster size and surface passivation. The red lines represent the increasing gap energy. The blue lines are related to the trapped electron state (p-state localized on the Si atom of the SiO bond) and the trapped hole state (p-state localized on the oxygen atom). (b) Room temperature PL spectra from porous silicon samples with different porosities kept under argon atmosphere (A) and after exposure to air (B).*
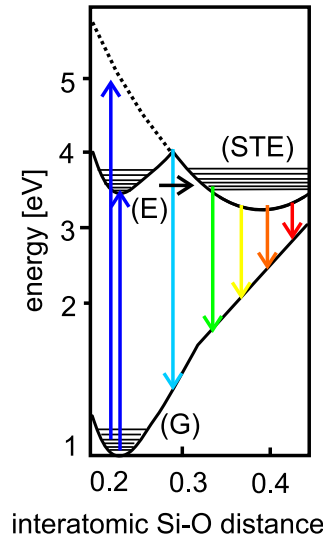
Figure 2.8: *Configuration coordinate diagram of the exciton ground state (G), the core excited state (E) and the self-trapped exciton (STE) as a function of the silicon and oxygen interatomic distance according to [60] [61].*

$\langle N \rangle = 1$).

In small Si-ncs, the surface/volume ratio is larger, leading to an enhancement of the surface related processes. A different surface passivation and the Si-ncs surrounding matrix composition will lead to different optical and electronic properties, because of different confinement potentials and the Si-ncs interdot energy barrier. The low surface potential barrier can lead to a "hopping" effect [66], i.e. diffusion of the excitons between the different Si-ncs, which will directly influence the radiative and the nonradiative recombination decay time distribution (see the stretched expo-

nential decay model in section 5.2). The high quality surface passivation is essential for lowering the efficient nonradiative surface trapping on e.g. dangling bonds [67] and can be improved by many different methods. Within our preparation technique, beside the natural Si-ncs oxidation, we contribute to the passivation of the Si-ncs surface also by introducing phosphorus atoms dissolved in the SiO_2 sol-gel P509, used for the matrix preparation (see section 3.2).

2.2.3 Nonradiative processes

Both the relaxation in the translation momentum conservation and the enhanced Coulomb interactions due to the stronger e-h wavefunction overlap in smaller Si-ncs not only enhance the radiative recombination rate, but can also lead to an opposite effect: increased Auger rates compared to the bulk silicon. On the other hand, the atomic-like structure of energy levels in confined systems will hinder Auger processes because of the reduced availability of final states satisfying the energy conservation. As a result, Auger recombination can only occur efficiently with the participation of a phonon (as a four-particle process) or with the involvement of a final state from the continuum of states outside the QD (Auger ionization). The most simple approximation of the Auger rate in QDs comes from the standard bulk-like approach, by introducing an effective carrier concentration per single QD, $n_{FC} = \frac{N}{V}$, where N is the number of excited e-h pairs (i.e. confined exciton) per dot and V is the volume of the single dot. According to this model, the Auger process decay time in small crystallites has been suggested to decrease with their size as $\tau_A \sim R^3$ (Klimov et al. in [68]). The Auger rate in small Si-ncs has been estimated by Delerue et al. to be $\tau_A \sim 1$ ns [69]. However, two main differences in the confined systems have to be considered - (i) the Auger recombination decay τ_A is not a continuous function of the effective density of free carriers as in the bulk material, but is represented by a set of discrete Auger rate values, characteristic for 2, 3, ... e-h pairs recombination; (ii) under a moderate excitation fluency, when less than 2 e-h pairs per dot (i.e. $\langle N \rangle < 2$) are excited, the Auger mechanism cannot occur by any means [70]. This is an important point, since the population inversion in a four-level system represented by oxidized Si-ncs [64] can be established even for $\langle N \rangle < 2$, when the nonradiative Auger process is inhibited. Moreover, the spatial separation of the excited carriers in the oxidized Si-ncs systems, emitting via the self-trapped exciton recombination, can significantly lower the probability of the Auger mechanism even at higher excitation fluency $\langle N \rangle \geq 2$ [71].

Let us now discuss the FCA losses in confined systems. The FCA cross section σ_{FCA} decreases according to the Drude model with the decreasing wavelength of the

absorbed photon as $\sigma_{FCA} \sim \lambda^2$. Therefore, the blue-shifted emission from the smaller Si-ncs will be less absorbed by the free carriers (Fig. 2.9), leading to a lower total optical losses $\alpha_{tot}(\lambda)$ and a higher probability of the StE onset. Thus, a system of smaller Si-ncs with a blue-shifted emission is preferred for the purpose of this thesis and became for us one of the most important requirements imposed on the prepared samples. Moreover, the FCA losses can be lowered using shorter excitation pulses as suggested by e.g. Mikhailovsky et al. in [72]. From a rough comparison of the FCA and emission cross-sections σ_{FCA} and σ_{em} in Fig. 2.9 we expect the FCA losses contribution being significantly lowered in samples with emission wavelength below $\sim$650 nm. As we will show in chapter 5, this condition is fully satisfied in our samples, the emission spectra of which being peaked around 580-650 nm.
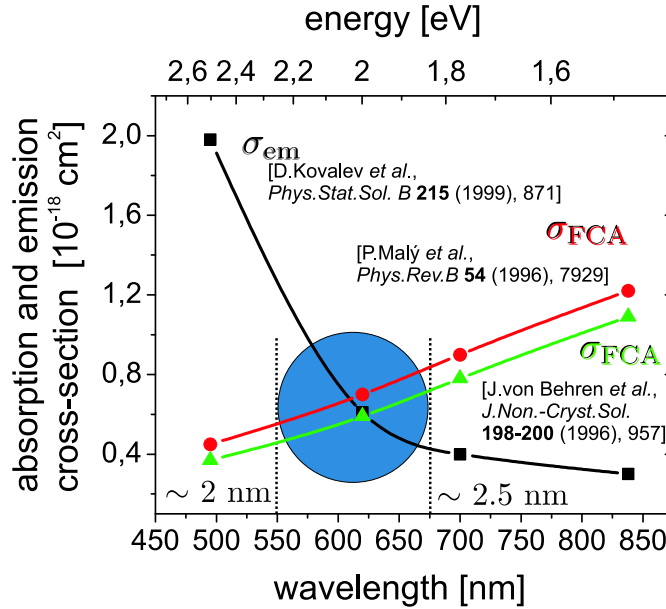
Figure 2.9: *FCA (σ_{FCA}) and emission (σ_{em}) cross-sections taken from the literature. FCA losses are significantly lowered in smaller Si-ncs, whose emission is more efficient and shifted to shorter wavelengths.*

2.2.4   Stimulated emission in oxidized Si-ncs

The necessary condition for the StE onset, as expressed by Eq. 2.3, can be rewritten in terms of the dynamics of these processes as follows

$$\tau_{FCA}, \tau_A, \tau_{surf} > \tau_{StE} \Rightarrow \text{stimulated emission} \tag{2.5}$$

i.e. the StE build-up time τ_{StE} has to be shorter than the decay time of all possible nonradiative processes as τ_A (Auger recombination), τ_{FCA} (FCA losses) and the surface trapping rate into the deep trap states as dangling bonds τ_{surf}. τ_{StE}

is given by the Si-ncs/SiO$_2$ volume fraction ξ, gain cross section $\sigma(\lambda)$, number of emitted photons n_{ph} and Si-ncs diameter R_{Si-nc} as $\tau_{StE} = \frac{4}{3}\pi(\frac{R_{Si-nc}}{2})^3\frac{1}{c\sigma n_{ph}\xi}$, where c is the light velocity [64]. Therefore, the StE dynamics can be tuned by the excitation intensity, Si-nc size and the volume fraction.

The Auger decay time τ_A, as we discussed above, can be tuned by the excitation intensity and Si-nc size as $\tau_A \sim \frac{R^3_{Si-nc}}{n_{FC}}$, i.e. in fact by the same dependence on R_{Si-nc} as τ_{StE}. The onset of StE is therefore strongly affected by a delicate balance between τ_{StE} and τ_A.

This, at first sight, makes the achievement of StE difficult if not impossible. It is basically true, nevertheless, there exist several conditions in favor of the StE occurrence in sufficiently small Si-ncs:

- Auger mechanism in confined systems is quantized (see discussion above in section 2.2.3) and can be completely eliminated using moderate pumping fluency (when less than 2 e-h pairs per single Si-ncs are generated).

- Quite recently we observed another important feature, influencing the Auger rate in our oxidized Si-ncs. The ultrafast emission decay in the subpicosecond range has been observed, interpreted in terms of ultrafast exciton trapping on the surface/interface states (self-trapped exciton formation; see Ref. [35] and discussion in section 5.2.4). Therefore, in our samples we expect another type of Auger mechanism, caused by the interaction of the self-trapped excitons, the rate of which can be expected to be lower than the one caused by the "free" confined excitons interaction, due to the spatial separation of the carriers [71].

- The decrease of τ_A with shrinking R_{Si-ncs} ought to be slower compared with corresponding decrease of τ_{StE} owing to shorter exciton lifetime in smaller Si-ncs.

As we discussed above in section 2.2.3, the FCA decay time τ_{FCA} can be tuned by the excitation intensity and Si-nc size, because $\tau_{FCA} \sim \frac{1}{n_{FC}}$, $\alpha_{FCA} \sim \lambda^2$, $\tau_{FCA} \sim \frac{1}{\sigma_{FCA}} \sim \frac{1}{\lambda^2} \sim \frac{1}{R^4_{Si-nc}}$. According to our estimations (see Fig. 2.9 and discussion in section 2.2.3), the FCA losses are significantly lowered in samples with blue-shifted emission as observed in our Si-ncs/SiO$_2$ samples (see chapter 5).

The surface trapping rate τ_{surf} into the deep trap states as dangling bonds is generally too slow, compared with the other nonradiative processes and can be thus neglected.

The above discussion leads to some theoretical requirements imposed on an ideal sample: (i) a high volume fraction of Si-ncs in the SiO_2 matrix, (ii) small Si-ncs average diameter and (iii) blue-shifted emission.

2.2.5 Laser on Si-ncs/SiO$_2$

To enclose and conclude the review section, we will discuss the possibility of lasing of the Si-ncs based system. As mentioned above, the necessary conditions for lasing are (i) a positive net optical gain and (ii) a positive optical feedback. The positive net gain has been recently demonstrated in different Si-ncs embedded in different SiO_2 based matrices as e.g. prepared by ion implantation [16], Plasma Enhanced Chemical Vapor Deposition (PECVD) [64], embedding por-Si grains in a sol-gel SiO_2 matrix [32] by our group, etc. Despite these successful and independent positive net gain observations, no Si-ncs based laser diode has been reported yet and our publications Refs. [36] and [37] appear to be the first report on such attempt to realize a laser cavity on Si-ncs/SiO$_2$ based samples.

It follows from the above discussion that research on such laser structure requires a system of small Si-ncs with blue-shifted emission, embedded at a high volume fraction into a matrix with a good optical homogeneity and negligible scattering losses $K \rightarrow 0$. The recently prepared Si-ncs/SiO$_2$ based materials, where the positive net gain coefficient has been already reported [16] [64], preserve the high optical quality only at the cost of lower Si-ncs volume fraction. On the other hand, samples with the high Si-ncs content usually suffer from the scattering losses K on the Si-ncs aggregates that form naturally in such systems. Lower optical quality of such samples appears to be the main problem for laser structure realization, since they cannot be placed into a standardly used type of resonator with external mirrors. To this end we proposed to use a different type of a distributed cavity as in Distributed Feedback Laser (DFL), as we will describe in the following experimental parts of the thesis.

Chapter 3

PREPARATION OF SI-NCS/SiO$_2$ SAMPLES

According to the previous discussion, a Si-ncs/SiO$_2$ sample with a high volume fraction of small Si-nc with narrow size distribution and blue shifted emission is supposed to be a favorable candidate for the StE observation. Preparation of such an ideal system maintaining the high optical quality remains a technological problem. Preparation methods as ion implantation, Plasma Enhanced Chemical Vapor Deposition or high temperature annealing of sub-stoichiometric SiO$_x$ ($x <2$) phase lead usually either to high volume fraction samples with relatively large Si-ncs or to low volume fraction samples with smaller Si-ncs. Our preparation method is based on the electrochemical etching of crystalline Si substrate modified with respect to the original Canham work [15] and combined with the sol-gel technology. This preparation technique has been inspired by the original work of one of our colleagues - see V. Švrček et al. [30] and has been slightly modified to prepare samples, suitable for the future optical gain investigation and optical feedback application. This method leads to relatively small oxidized Si-ncs ($\sim$2.7 nm; see Fig. 4.1), embedded at a high volume fraction (10-20 vol.%; see Fig. 3.4) in an SiO$_2$ based matrix, passivating the Si-ncs surface. The size of Si-ncs can be tuned within some range by etching parameters. The volume fraction in the sol-gel based SiO$_2$ matrix is virtually arbitrary, limited only by the material cohesion. Such a preparation method is relatively fast and cheap with a good reproducibility. Hand in hand with these important advantages, however, problems arise with an aggregation of the Si-ncs into larger clumps in the SiO$_2$ sol-gel matrix, lowering the optical quality of the samples. This method, however, still offers a large variety of possible modifications and their investigation will enable us in the future - as we believe - to improve the samples optical quality to a large extent. The details of the preparation technique and description of the three main

different types of our Si-ncs/SiO$_2$ samples, prepared with emphasis on matching the theoretical requirements for optical gain and as high as possible optical quality will be discussed hereafter.

3.1   Electrochemical etching

Samples were fabricated starting from a porous silicon (por-Si) layer [15] [73], prepared by a modified electrochemical etching of a p-type crystalline silicon wafer. Such a method offers fast and cheap production of a relatively large amount of oxidized Si-ncs in a form of a powder. Etching reaction was realized at ambient conditions applying between the crystalline silicon wafer connected to the positive bottom anode (Al desk) and the acidic etching bath in a teflon chamber with a dipped negative Pt cathode. The scheme and the principle sketch are shown in Fig.3.1(a-c).
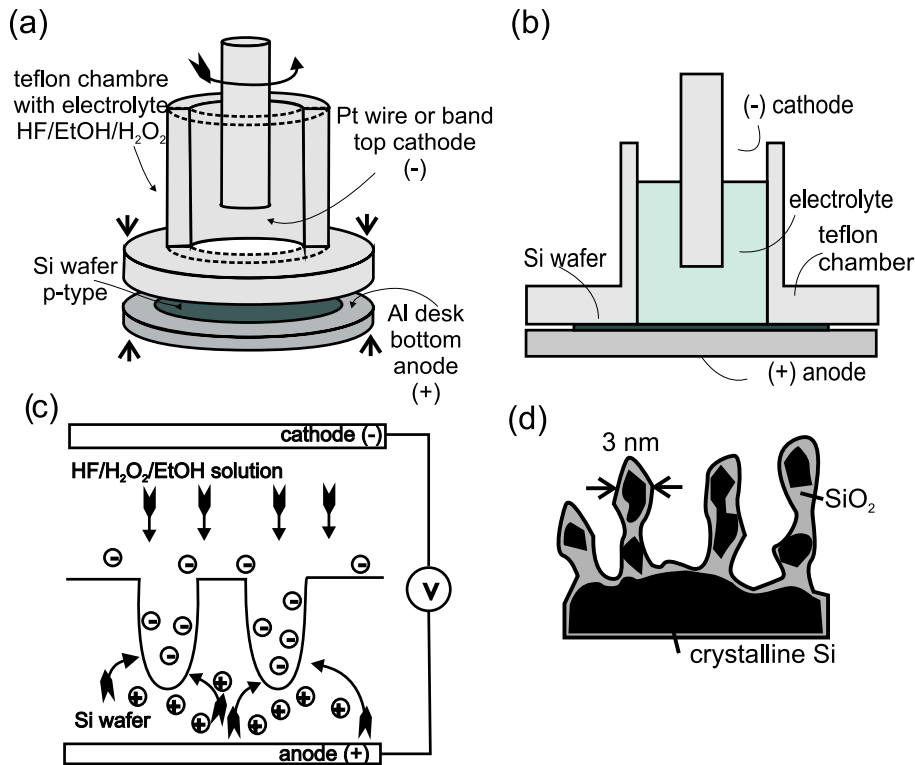
Figure 3.1: *(a)(b) Scheme of the electrochemical etching setup, (c) principle of the etching reaction and (d) a sketch of the resulting pore structure of porous silicon layer.*

The standard etching solution consists of a mixture of hydrophobic 50% HF (hydro-fluoric acid) with ethanol (EtOH). The primary reagent is HF; EtOH increases the wettability of the solution on the silicon surface. The dissolution reaction of the Si wafer by HF acid follows the scheme

$$
\begin{aligned}
\text{Si+2HF+xh}^+ &\rightarrow \text{SiF}_2\text{+2H}^+\text{+(2-x)e}^- \\
\text{SiF}_2\text{+2HF} &\rightarrow \text{SiF}_4\text{+H}_2 \\
\text{SiF}_4\text{+2HF} &\rightarrow \text{H}_2\text{SiF}_6
\end{aligned}
\tag{3.1}
$$
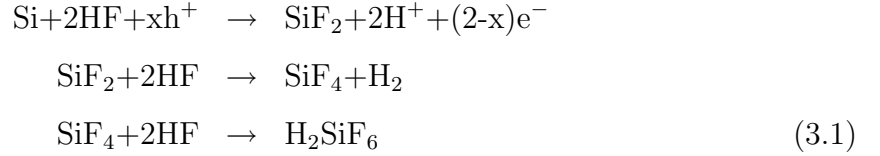
where h^+ and e^- stand for the free holes and electrons. Si atoms are dissolved into a form of the SiF_6^{2-} complexes, which requires the instantaneous presence of both the F^- ions and positive holes h^+ at the silicon surface (Fig. 3.1(c)). The presence of the h^+ in the p-type silicon wafer is assured due to the dopant (Boron). The dynamics of the holes h^+ and F^- ions can be governed by the current density control: at large current densities >10 mA/cm^{-2}, F^- ions reach the silicon surface later than holes, which will be already homogeneously dispersed all over the wafer surface, leading to a homogeneous surface electrochemical polishing. At smaller current densities F^- ions reach the surface before the holes. The holes will first reach the topography valleys, leading to an inhomogeneous surface etching, forming the porous structure sketched in Fig. 3.1(d). What is substantial from our point of view is the remaining silicon between the pores. It is formed by interconnected "islands" of crystalline silicon with mean size of several nanometers, i.e. Si-ncs (Fig. 3.1(d)). To improve the homogeneity of the etching process over a large surface, the electrodes should cover the whole etched surface to ensure a homogeneous electrical field. The top electrode, however, should not block the H$_2$ bubbles leaking from the wafer surface to ensure the functionality of the process described by Eq. 3.1. This can be ensured using a perforated top electrode and/or by stirring the etching solution.

One of the most important parameters defining the resulting porous structure is the porosity: the ratio of the pore volume to the total volume, which determines also the Si-ncs size, i.e. the pillars diameter in Fig. 3.1(d). The high porosity (70-80%) por-Si layer exhibits a bright luminescence and consists of long thin SiO$_2$ "wires" comprising Si-ncs of various sizes, diameter of which is limited from below to $\sim$3 nm by the limited hole diffusion into the pillars. To increase further the porosity (desirable effect in our case), the etching bath can be modified e.g. by adding an H$_2$O$_2$ (hydrogen peroxide) or using an additional post-etching in H$_2$O$_2$ solution. This approach represents our principal modification of the etching procedure, mentioned above. H$_2$O$_2$ catalyzes (enhances) the etching process, producing ultra-small Si-nc with surface passivated to some extent by -OH groups. The oxidative effect of H$_2$O$_2$, further reducing the Si-nc size, is given by the following equation:

$$\text{Si}+2\text{H}_2\text{O}_2 \quad \rightarrow \quad \text{Si(OH)}_4$$
$$2\text{Si(OH)}_4 \quad \leftrightarrow \quad \text{Si(OH)}_3\text{-O-Si(OH)}_3+\text{H}_2\text{O} \qquad (3.2)$$
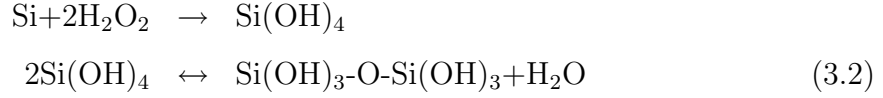
The direction of the equation, i.e. the Si(OH)_4 dissolution and condensation, depends on the the amount of water H_2O in the reaction and the air-humidity conditions. Dissolution prevails if the system is humid, condensation prevails under dry conditions.

According to our experimental experiences, the most important parameters governing the HF and H_2O_2 dissolution reaction type and velocity are the etch current density, silicon wafer doping and surface modification, etching duration, HF and H_2O_2 concentration, temperature and humidity. All these parameters have to be carefully adjusted to obtain reproducible results. During this thesis we tried many different etching parameters and sample treatment techniques, from which only a part will be described here, leading to samples with sufficiently good optical quality, suitable for the optical gain investigation and optical feedback application.

Etching parameters

For the por-Si preparation we used a p-type (Boron doped) crystalline Si wafer with $\langle 100 \rangle$ crystalline orientation and of 0.1 Ωcm resistivity. The current density of 1.6-2.5 mA/cm^{-2} was applied for $\sim$2 hours. As an electrolyte we used the HF acid (50% in H_2O) diluted in pure EtOH (100%) and H_2O_2 of different concentrations, as indicated in table 3.1. Diverse types of por-Si (i.e. interconnected Si-ncs attached to the Si wafer), used subsequently for the sample preparation, were classified according to the HF/EtOH/H_2O_2 solution concentration and H_2O_2 post-etching treatment. In table 3.1 we show the etching solution concentrations for the three different types of resulting nanocrystalline powder "standard" (no H_2O_2 treatment), "yellow" and "white" (H_2O_2 treated, called after their appearance under day light, not after their luminescence color). The ratio and volumes of the HF:EtOH:H_2O_2 in the etching solution together with the H_2O_2 concentration are presented in the middle column of Tab. 3.1. The post-etching treatment consists of a few minutes bath of freshly prepared por-Si layers in a H_2O_2-water solution of certain concentration as shown in the third column of Tab. 3.1.

type of Si-ncs (por-Si)	HF:EtOH:H$_2$O$_2$ (concentration)	post-etching bath
"standard"	1: 2.5 (15 ml: 37.5 ml)	
"yellow"	1: 2.46: 0.54 (3 % in water) (13 ml: 32 ml: 7 ml)	3 % H$_2$O$_2$ for 5 min
"white"	1: 2.8: 0.15 (30 % in water) (13 ml: 37 ml: 2 ml)	30 % H$_2$O$_2$ for 15 min

Table 3.1: *Table of etching parameters used for preparation of different types of Si-nc - "standard", "yellow" and "white" por-Si.*

3.2 Si-ncs/SiO$_2$ samples preparation

3.2.1 Si-ncs powder treatment

Optical properties of the por-Si layer exposed to air are not stable in time [27] [28] [29], because the porous structure tends to absorbs the air humidity due to its large active surface area. Besides, the silicon substrate absorbs strongly the UV laser pulses applied to pump optically the Si-ncs and a thin por-Si layer (several micrometers) on the surface can thus be damaged due to excessive heating of the substrate. Passivation of Si-ncs using an optically transparent matrix is therefore needed. To this goal, we used first to scrape off the por-Si film from the silicon substrate and melt it by mechanical pulverization to an Si-ncs powder. The "standard", "yellow" and "white" Si-ncs powders are composed of up to ∼1 μm large clumps of interconnected Si-ncs, which can be partially separated using ∼1 hour ultrasonic treatment of the Si-ncs powder dissolved in pure EtOH. Such powder can be dried and embedded into a solid SiO$_2$ based matrix by a sol-gel procedure, which maintains a good surface passivation at a high Si-nc filling factor and low-cost. The quality of such prepared "yellow" and "white" Si-ncs/SiO$_2$ samples is good enough, requiring no further treatment. However, the quality of a such prepared "standard" Si-ncs/SiO$_2$ sample is relatively poor due to the relatively larger Si-ncs clumps originating probably from the different etching and post-etching procedure, compared to "yellow" and "white" Si-ncs (no involvement of the H$_2$O$_2$). Therefore a solution of the "standard" Si-nc powder in pure EtOH was let to sediment in two steps: the "1st sediment" powder is the sediment found after ∼5 minutes on the cuvette bottom (the largest Si-ncs agglomerates) and the "2nd sediment" is the dried rest (finer Si-ncs) of the Si-ncs/EtOH solution. The dried 2nd sediment powder can be embedded into a solid SiO$_2$ based matrix by a sol-gel procedure to form so-called 2nd sediment "standard" Si-ncs/SiO$_2$ samples, whose optical quality is much higher than that of the non-sedimented or the 1st

sediment "standard" Si-ncs/SiO$_2$ samples. If we separate the "2nd sediment" in liquid solution instead of drying it, we can continue in the sedimentation process: after one hour sedimentation - the "3rd sediment" is the sediment found on the bottom of the cuvette and "4th sediment" is the rest, containing the finest Si-ncs clusters, which do not further sediment due to the Brown motion. The smallest Si-ncs clusters of the 3rd and 4th sediment were kept in pure EtOH solution and were not completely dried (contrary to the 1st and 2nd sediments) due to the strong reaggregation of the finest Si-ncs powder during the drying process. Only a partial drying of the solution was allowed, to lower the amount of the EtOH liquid to minimum.

3.2.2   Embedding of the Si-ncs powder into an SiO$_2$ sol-gel

Let us now describe the sol-gel procedure. The standard SiO$_2$ based sol-gel procedure uses tetrametoxysilane (TMOS) solution with reactants (HF acid), solidification process of which is shown in Fig. 3.2. The main parameters governing the solidification process of the TMOS solution are the pH factor given by the amount of the reactant in the solution (the more HF we add the faster the solidification process is) and the molar ratio of H$_2$O/Si, which can be changed by instantaneous annealing.
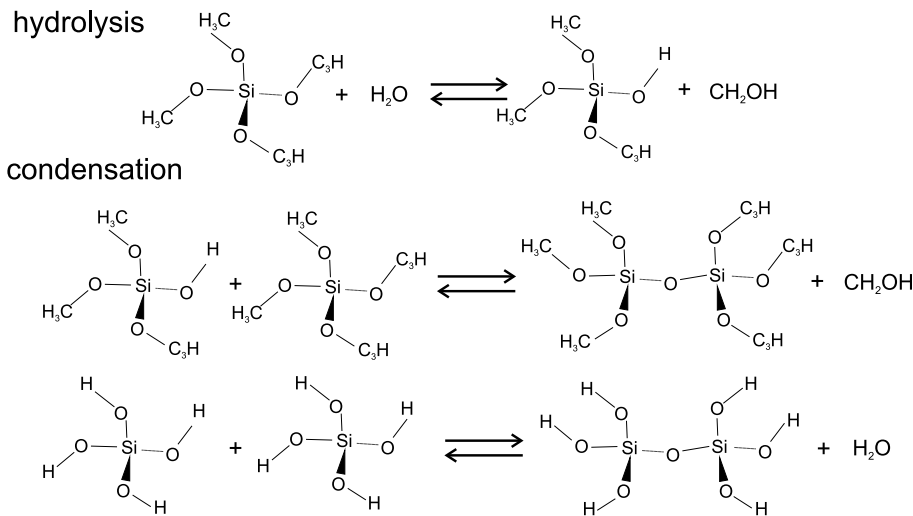
Figure 3.2: *Tetrametoxysilane (TMOS) hydrolysis and condensation.*

In our method we used an SiO$_2$ based sol-gel doped by Phosphorus (P concentration of 5.1021 at.%), commercially available as P509 Spin-On-Diffusant (SOD P509) of patented composition (Filmtronics Inc. corporation, see http://www.filmtronics.com/). Such a spin-on-diffusant, as may be actually clear from its name, is used currently in the standard silicon wafer processing for the crystalline silicon wafer doping by phosphorus. Compared to the standard TMOS sol-gels which has to be annealed at high temperatures, SOD P509 solution solidifies efficiently in air at ambient temperature

and pressure within few days (2-7 days), forming a stable solid state P-doped SiO$_2$ based matrix [30]. Such an SiO$_2$ based solid matrix is transparent in the visible spectral region with the refractive index close to an ordinary glass one (n_{P509}=1.42). The presence of phosphorus, even if not necessary in principle, enhances the surface passivation of Si-ncs, contributes slightly to the blue shifting and enhancement of their PL emission [74] [75] [76]. Moreover, we assume that it exhibits also a favorable impact on the mechanical strength of the resulting samples, since the samples prepared by the same setup using a similar SOD SiO$_2$ doped by Boron (B155, Filmtronics Inc.) has completely disintegrated.

In the early stages of the solidification process, the liquid P509 sol-gel solution can be filled with any amount of dried Si-ncs powder ("standard" 1st and 2nd sediment, "yellow", "white" or partially dried Si-ncs/EtOH solutions of "standard" 3rd and 4th sediments). The still liquid Si-ncs/SOD P509 solution undergoes a further ultrasonic treatment for ∼30-60 min to avoid larger agglomeration of the Si-nc. Longer ultrasonic treatment already intervene into the solidification process and could cause cracks in the matrix. The mixture of Si-ncs and SOD P509 is kept in spectroscopic quartz cuvettes of a volume of 3.5 ml (3.5 cm x 1.0 cm x 1.0 cm) with optically polished faces and bottom. After the ultrasonic treatment, the SOD P509 is already partially solidified into a gel-like structure and the gravitational sedimentation of the Si-ncs is limited. Finally a layer of densely packed Si-ncs in the SiO$_2$ based matrix is formed close to the cuvette bottom. Thickness of such a layer in a sample with the standard content of ∼2 mg of Si-ncs in ∼0.4 ml of SOD P509 amounts about ∼50 μm (after complete solidification), as measured by the μ-PL (micro-photoluminescence) spectroscopy (Fig. 3.3). In order to further increase the Si-ncs density, a centrifuge force has to be applied during the early stage of the solidification process for few minutes at 3000 revs per minute. The volume fraction of Si-ncs in the SiO$_2$ based matrix is driven by the total amount of the Si-ncs mixed with the liquid sol-gel SiO$_2$ and by the applied centrifuge force. The upper limit of the volume fraction of Si-ncs in the SiO$_2$ matrix is virtually limited by the material cohesiveness but need not to be achieved for our purpose, since the PL intensity is a function of the Si-ncs volume fraction and exhibits maximum around 10-20 vol.% (Fig. 3.4).

The number and the density of Si-ncs in the sample can be estimated from the volume of the Si-ncs rich layer and the total amount of Si-ncs. Solidified samples are of typical dimensions of 10x10x1 mm^3 with an Si-ncs rich layer on the cuvette bottom of the thickness below ∼50 μm. The standardly used amount of Si-ncs per sample is about M_{Si-nc}∼2 mg. The volume of an average Si-ncs (with diameter
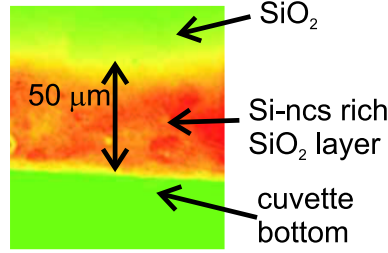
Figure 3.3: *μ-PL cross-section image of the Si-ncs rich layer on the cuvette bottom. The red color symbolize the emitting Si-ncs rich area. Sample consists of 2 mg of "standard" nonsedimented Si-ncs powder in 0.4 ml of SOD P509 solution (volume fraction ∼20 vol.%). No centrifuge treatment was used.*
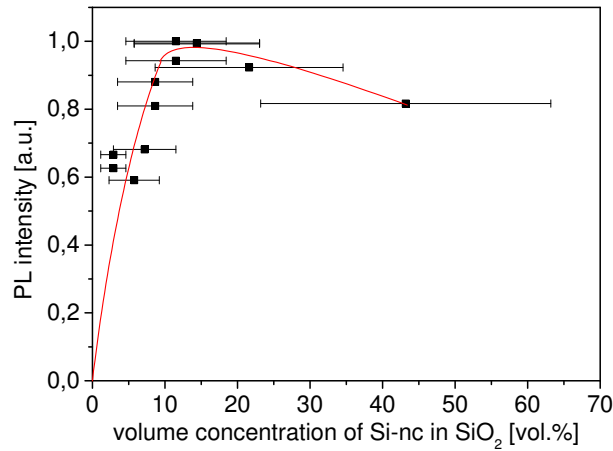
Figure 3.4: *PL intensity as a function of the Si-ncs/SiO₂ volume fraction. The maximal PL intensity was observed in samples with Si-ncs/SiO₂ volume fraction between 10 and 20 vol.%.*

R_{Si-nc}∼3 nm) is $V_{Si-nc} = \frac{4}{3}\pi(\frac{R_{Si-nc}}{2})^3 \approx 14.10^{-27}$ m³. The number of such Si-ncs in an average sample is thus $N_{Si-nc} = \frac{M_{Si-nc}}{\rho_{Si}V_{Si-nc}} \approx 6.10^{16}$, where ρ_{Si}=2330 kg/m³ is the density of crystalline silicon. The volume fraction of samples is thus at minimum $\xi_{Si-nc/SiO_2} = \frac{V_{Si-nc}N_{Si-nc}}{V_{layer}} \approx 17$ vol.%. or 10^{19} Si-nc/cm³. This value is close to the "ideal" concentration value for positive optical gain as estimated by Pavesi et al. in their Si-ncs/SiO₂ based samples prepared by Si⁺ ion implantation and PECVD [64].

Real color photo of the original por-Si layer, scrapped Si-ncs powder and final Si-ncs/SiO₂ samples in quartz cuvettes emitting under the UV lamp excitation is shown in Fig. 3.5.
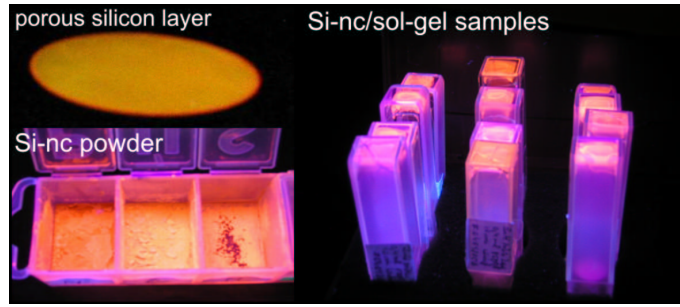
Figure 3.5: *Photo of light emission of a por-Si layer, Si-nc powder and resulting Si-ncs/SiO$_2$ samples in quartz cuvettes under UV lamp illumination. Photo is in the real colors. The blueish light is related to the excitation light reflection and diffusion and to the emission of the plastic box in which the Si-ncs powder has been kept.*

3.3 Conclusions

The above described original preparation technique is based on a combination of the modified electrochemical etching of silicon wafers (porous silicon) and SiO$_2$ based sol-gel processing. Such a preparation method affords many advantages as a relative simplicity, good reproducibility, low price and a high variability. It enables us to prepare samples with virtually arbitrary content of small Si-ncs in and SiO$_2$ matrix. The highest PL intensity was obtained for the Si-ncs volume fractions between 10-20 vol.%. The advantageously high density of Si-ncs in the SiO$_2$ based matrix, however, leads to the Si-ncs aggregation, lowering the optical quality of the samples. This represents the main drawback of the method. Optical quality can be partially increased using an ultrasonic treatment and a sedimentation of Si-ncs powders. Further improvement, necessary for the successful Si-ncs/SiO$_2$ based laser preparation, represents our continuous interest and is intensively studied.

Chapter 4

STRUCTURAL CHARACTERIZATION OF THE SAMPLES

The prepared samples were characterized using the High-Resolution Transmission Electron Microscopy (HRTEM), Raman spectroscopy and Fourier-Transform Infra-Red (FTIR) spectroscopy. These measurements yielded both the Si-ncs size distribution and information on the surface passivation.

4.1 Size distribution estimation from HRTEM and Raman spectra

Porous silicon is known to have relatively large distribution of Si-ncs sizes [77]. Estimation of the Si-ncs size from HRTEM scan is a direct method, since the Si-ncs crystalline cores can be "seen" in the HRTEM image. The average Si-ncs size, however, can be also determined from an indirect method as e.g. Raman spectroscopy, as will be shown afterwards.

4.1.1 HRTEM

To determine the size distribution of the "standard" and the "yellow" Si-ncs powders we have applied the HRTEM technique. Results are shown in Fig. 4.1(a-d). The "yellow" Si-ncs powder HRTEM image in Fig. 4.1(b) was used for the size distribution estimation, because it includes sufficiently large amount of various single Si-ncs. Taking into consideration the obtained Gaussian profile of the size distribution, we found the average Si-ncs size to be approximately ~2.7 nm with FWHM of ~0.86 nm (Fig. 4.1(d)). The average size of the "standard" Si-ncs was hardly possible to deter-

mine from the measured HRTEM images, since no such complex picture as the one in Fig. 4.1(b) has been obtained. However, the "standard" Si-ncs size is expected to be slightly larger, compared to the "yellow" one, as we confirm in the following using the Raman spectroscopy.
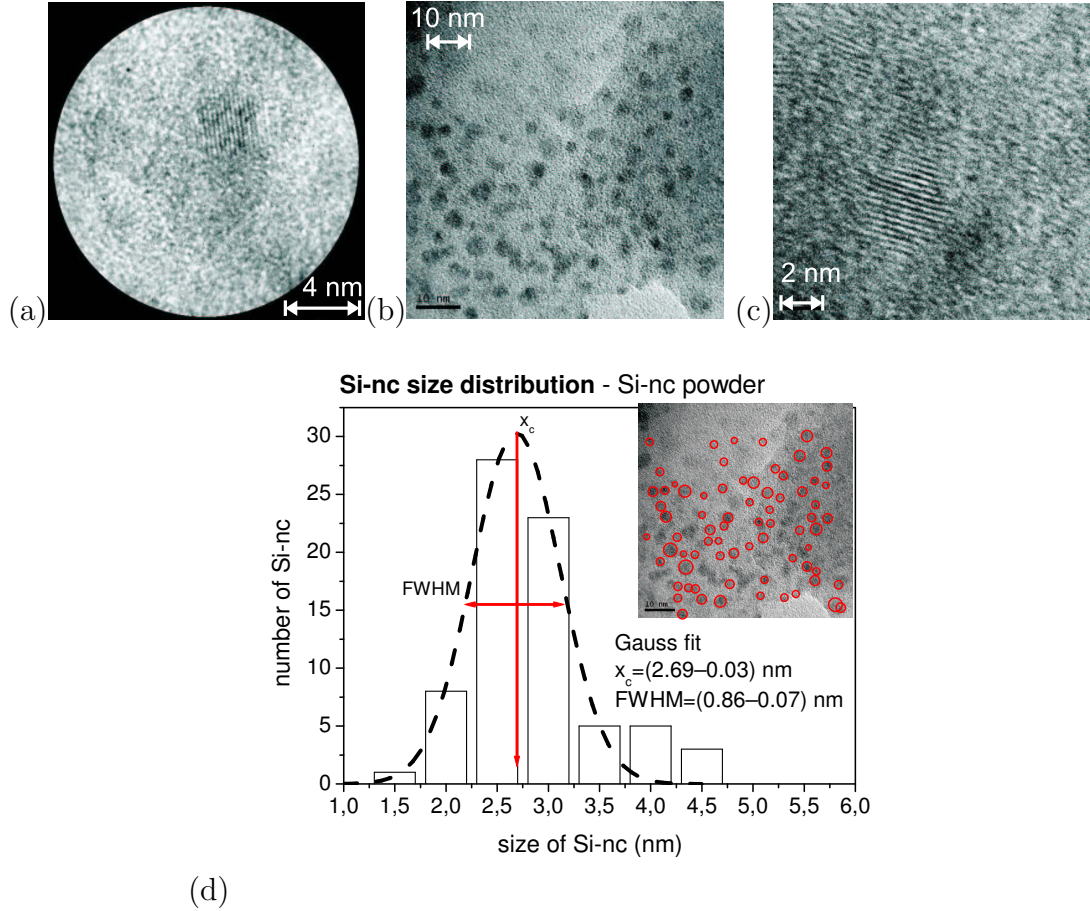
Figure 4.1: *HRTEM image of (a) a "standard" Si-ncs powder and (b-c) a "yellow" Si-ncs powder (thanks are due to Dr. S. Joulie from IPCMS Strasbourg, France and Dr. S. Bakardjieva PhD. from ÚACH in Řež, Czech Republic). (d) Size distribution estimation of the "yellow" Si-ncs powder from image in (b).*

4.1.2 Raman spectroscopy

Raman spectroscopy is another method, suitable for the Si-ncs average size estimation. The Raman spectra were measured in "standard" and "yellow" Si-ncs/SiO_2 samples (Fig. 4.3). Samples were excited using an UV excitation to enable us to study exclusively the thin Si-ncs rich layer on the Si-ncs/SiO_2 sample surface (due to a high absorption of UV light within the thin Si-ncs rich layer). The size was estimated from the shift of the sharp crystalline Si peak. Raman spectra of the silicon contain commonly two characteristic LO-TO phonon peaks: (i) a broad band at $\sim$480 cm^{-1} which corresponds to the amorphous phase and (ii) a sharp peak at $\sim$520 cm^{-1} from

the crystalline phase. In Si-ncs, the crystalline peak is shifted and broadened due to the phonon confinement effect, from which the Si-ncs size can be estimated. The "bond polarizibility model" [78] for Si-ncs smaller than 4 nm gives a simple relation between the Si-ncs average diameter R_{Si-ncs} and the peak shift $\Delta\omega(R_{Si-ncs})$ from the bulk Si peak position as

$$\Delta\omega(R_{Si-ncs}) = -A(\frac{a}{R_{Si-ncs}})^{\gamma} \tag{4.1}$$

where a=0.543 nm is the lattice constant of crystalline silicon, A=97.462 and γ=1.39 are the fit parameters describing the phonon confinement. The theoretical simulation of this dependence is plotted in Fig. 4.2.
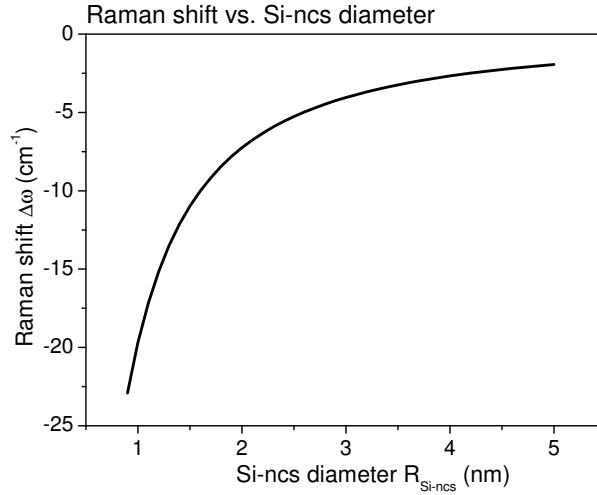
Figure 4.2: *Theoretical simulation of the Raman shift of the crystalline silicon peak according to the phonon confinement theory ("bond polarizibility model" [78]) as calculated using Eq. 4.1.*

However, some caution is needed here: Similar Raman peak shift can be caused, apart from the confinement effect, also by the thermal effects, which affect the interatomic potential and thus the Raman peak position and width during the laser irradiation. The thermal effects have been minimized here by testing the peak position stability against longer sample irradiation. We measured the Raman spectra in a "standard" and a "yellow" Si-nc/SiO_2 sample on a fresh place and after a few minutes irradiation and averaged them (see Fig. 4.3(a,b)). The measured peak positions and FWHM, the peak shift $\Delta\omega$ with respect to the crystalline peak at 520 cm^{-1} and Si-ncs mean diameter R_{Si-ncs} estimated using Eq. 4.1 are summarized in table in Fig. 4.3(a,b). The broader peak at a lower energy around 500 cm^{-1} corresponds to the disordered phase and will not be discussed here. The average diameter of

"standard" Si-ncs was estimated to be ∼3.8 nm and of "yellow" Si-ncs was found to be ∼2.6 nm, in excellent agreement with the result obtained from HRTEM scan in Fig. 4.1(d). Moreover, the HRTEM and Raman data demonstrate that the presence of H_2O_2 in the etching procedure leads to a Si-ncs size shrinkage, since the estimated mean size of the "standard" Si-ncs, where no additional H_2O_2 etching procedure has been used, is larger.
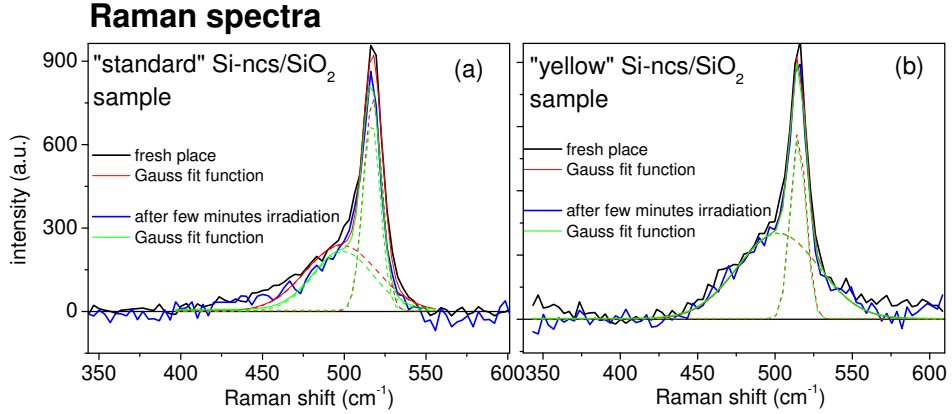
Si-ncs/SiO$_2$ sample	amorphous peak position (FWHM)	crystalline peak position ω (FWHM)	shift $\Delta\omega$	Si-ncs size R_{Si-ncs}
"standard"	498.4 cm^{-1} (43.9 cm^{-1})	517.5 cm^{-1} (11.4 cm^{-1})	2.5 cm^{-1}	4.1 nm
	499.5 cm^{-1} (36.4 cm^{-1})	516.7 cm^{-1} (10.7 cm^{-1})	3.3 cm^{-1}	3.5 nm
"yellow"	502.2 cm^{-1} (52.3 cm^{-1})	515.1 cm^{-1} (10.2 cm^{-1})	4.9 cm^{-1}	2.6 nm
	502.0 cm^{-1} (52.5 cm^{-1})	514.9 cm^{-1} (9.9 cm^{-1})	5.1 cm^{-1}	2.5 nm

Figure 4.3: *Raman spectra of (a) a "standard" and (b) a "yellow" Si-nc/SiO$_2$ sample. Signal was excited using InVia Renishaw Raman micro-spectrometer with continuous UV laser excitation (HeCd, 325 nm) of intensity ∼100 kW/cm^2. The measured peak positions and FWHM, the peak shift $\Delta\omega$ with respect to the crystalline peak at 520 cm^{-1} and Si-ncs mean diameter R_{Si-ncs} estimated using Eq. 4.1 are summarized in the table, together with the broad disordered phase peak position.*

4.2 Surface investigation - FTIR spectroscopy

The optical analysis of the chemical species on the Si-ncs surface can be done using FTIR spectroscopy. The "molecular" vibration and rotation absorption spectra, characteristic for each chemical bond, represent rather weak effects in the infrared spectral region. Corresponding signal is often beyond the sensitivity of a standard transmission spectrometer. Instead, much more sensitive FTIR spectrometer has to be used, where the detection wavelength is identified via the Fourier transform of an IR source interferogram supplied by a Michelson interferometer. Such method gives the information about the molecular chemical bonds from the whole sample volume.

Because the Si-ncs rich layer represents only a small sample fraction, in order to determine the influence of the H_2O_2 etching treatment, we have to measure and compare the FTIR spectra of both a "standard" (H_2O_2 non-treated) and a "yellow" (H_2O_2 treated) Si-ncs powder (Fig. 4.4). Compared to the "standard" Si-ncs powder, in the "yellow" Si-ncs powder we observed a higher signal of the -OH related bonds at frequencies $\sim$874 and 945 cm^{-1}, likely due to the additional H_2O_2 treatment. Strong signal at $\sim$3310 cm^{-1} is possibly related to the rest of water H_2O, resulting in the H_2O_2 oxidation reaction with Si as follows from Eq. 3.2. Other peaks can be identified with the oxygen related surface bonds vibrational modes: the oxygen bridges Si-O-Si bending mode at 792 cm^{-1}, stretching mode at $\sim$1055 cm^{-1} and a mode at $\sim$1160 cm^{-1} corresponding to the bond angle of $\sim$150 deg (cage-like structure). The frequencies of absorption peaks of the oxygen and hydrogen related surface bonds vibrations were taken from [79] [80] [81] [82]. As follows from the theoretical discussion in Chapter 2, this slightly different Si-ncs surface passivation and different Si-ncs mean size, caused by an additional H_2O_2 treatment, can change the emission properties of Si-ncs/SiO$_2$ samples. Such differences we will investigate throughout this thesis.
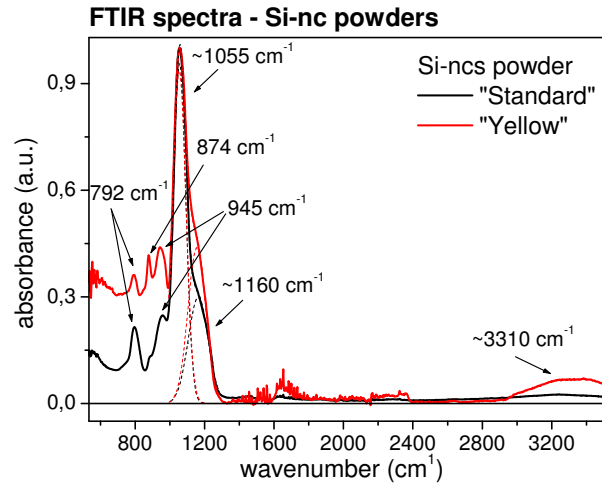
Figure 4.4: *FTIR absorption spectra of a "standard" and a "yellow" Si-nc powder measured using the FTIR spectrometer Excalibur (series DIGILAB).*

Chapter 5

LIGHT EMISSION AND OPTICAL LOSSES IN SI-NCS/SiO$_2$ SAMPLES

Study of the light emission and attenuation (optical losses) represent the first step in the essential optical characterization of the material, studied with respect to the possible future laser diode development. In this chapter we would like to present the most representative results on transmission, PL excitation, time-integrated and time-resolved PL emission spectra measured in our Si-ncs/SiO$_2$ samples.

5.1 Attenuation and emission spectra of Si-ncs/SiO$_2$ samples and pure SiO$_2$ matrix

As we discussed above, the emission and absorption spectra of an ensemble of Si-ncs will be inhomogeneously broadened even at low temperatures due to the sensitivity of the optical matrix element on the Si-ncs size (Eq. 2.4). Moreover, the spectral width can be further broadened due to the disordered surface potential and phonon assisted transitions in larger Si-ncs. One fundamental approach to better understanding of the optical transitions in Si-ncs has been represented by advanced experiments as e.g. a single Si-ncs time-resolved spectroscopy [51]. To perform a single Si-nc study, a very low concentration of nanocrystals in a given volume is required to avoid interaction of surrounding nanocrystals with the optical probe. On the other hand, to get StE and lasing, a dense system of Si-ncs is needed. Thus, at the present stage we concentrate fully on the optical properties, StE onset and light amplification conditions in an ensemble of Si-ncs embedded at high concentrations in SiO$_2$ based matrices investigated at room temperatures. However, a small step towards the single Si-nc spectroscopy was done, when studying the filtered colloidal suspensions of small Si-ncs in EtOH to understand the influence of the Si-ncs agglomeration and size distribution on the PL emission spectra development (see Fig. 5.8, Ref. [33]). This

very interesting subject deserves for sure our attention, however, since the obtainable Si-ncs density in the colloids under study was not sufficient for the optical gain measurements as performed by the VSL and SES methods in chapter 6, we did not perform a more detail study in the scope of this thesis. Let us now present the most interesting results obtained from the transmission/attenuation, PL excitation and PL emission spectra measured in our Si-ncs/SiO₂ samples.

Transmission/attenuation (absorbance) spectra

Attenuation of light of initial intensity $I_{exc}(0, \lambda_{exc})$ at wavelength λ_{exc}, passing through the passive material of thickness d can be described by the Beer-Lambert law:

$$I_{exc}(d, \lambda_{exc}) \;\cong\; I_{exc}(0, \lambda_{exc})e^{-\alpha_{tot}(\lambda_{exc})d} \tag{5.1}$$

where $\alpha_{tot}(\lambda_{exc})$ represents the total optical losses at wavelength λ_{exc}, including the material absorption $\alpha(\lambda_{exc})$ and optical losses $K(\lambda_{exc})$ due to the light scattering on inhomogeneities: $\alpha_{tot}(\lambda_{exc}) = \alpha(\lambda_{exc}) + K(\lambda_{exc})$. For the sake of simplicity, we neglect the reflection on the sample boundaries due to its low contribution. The absorption coefficient $\alpha(\lambda_{exc})$ can be estimated from the absorbance $A(\lambda_{exc})$, defined as the logarithm of the ratio of the detected energy $I_{exc}(d, \lambda_{exc})$ to the initial excitation energy $I_{exc}(0, \lambda_{exc})$, if the optical losses $K(\lambda_{exc})$ are negligible and the sample thickness d is known

$$A(\lambda_{exc}) \;\equiv\; ln(\frac{I_{exc}(d, \lambda_{exc})}{I_{exc}(0, \lambda_{exc})}) \cong -\alpha(\lambda_{exc})d \,. \tag{5.2}$$

Contrary to that, in the sample with high optical losses $K(\lambda_{exc})$, only the attenuation $\alpha_{tot}(\lambda)d$ (optical losses) can be measured. The optical losses can be determined from the transmittance coefficient $T(\lambda_{exc})$, defined as the ratio of the detected energy $I_{exc}(d, \lambda_{exc})$ to the initial excitation energy $I_{exc}(0, \lambda_{exc})$ as

$$T(\lambda_{exc}) \;\equiv\; \frac{I_{exc}(d, \lambda_{exc})}{I_{exc}(0, \lambda_{exc})} \cong e^{-\alpha_{tot}(\lambda_{exc})d} \,. \tag{5.3}$$

The transmittance T, from which the attenuation $\alpha_{tot}d$ (absorbance A) can be determined, can be measured in the standard transmission setup sketched in Fig. 5.1, provided the sample is partially transparent for the excitation wavelengths λ_{exc}.
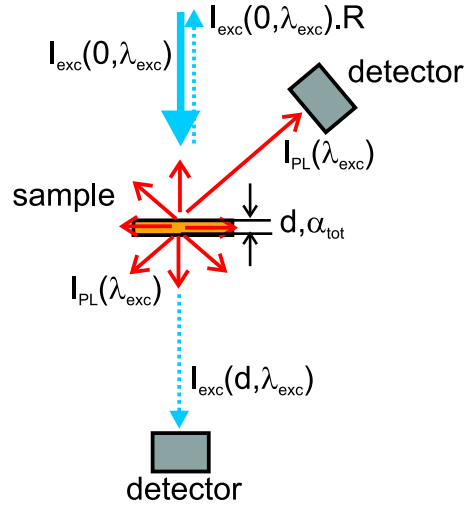
Figure 5.1: *Principal arrangement of the transmission and reflection experimental setup for measuring of the transmittance, attenuation/absorbance, PL emission and PL excitation spectra.*

PL excitation and emission spectra

If the sample is opaque and exhibits a strong emission response for the excitation wavelength, the attenuation (absorbance) spectrum $\alpha_{tot}(\lambda_{exc})$ can be, under certain conditions, estimated from the PL excitation spectra $I_{PL}(\lambda_{exc})$ in the "reflection" setup as sketched in Fig. 5.1. The excitation spectra show the PL emission response to the different excitation wavelengths λ_{exc} which is proportional with the luminescence efficiency η (complex function of λ_{exc} and other parameters) to the energy absorbed (and scattered) in the material:

$$I_{PL}(\lambda_{exc}) \;\cong\; \eta I_{exc}(0, \lambda_{exc})(1 - \exp^{-\alpha_{tot}(\lambda_{exc})d}) \,. \tag{5.4}$$

If the sample is optically thin, i.e. total optical losses are low $\alpha_{tot}d \ll 1$, the equation 5.4 can be simplified to $\frac{I_{PL}(\lambda_{exc})}{I_{exc}(0,\lambda_{exc})} \sim \alpha_{tot}(\lambda_{exc})d$, from which the spectral dependence of optical losses $\alpha_{tot}(\lambda_{exc})$ can be estimated. If the optical losses of the sample are high $\alpha_{tot}(\lambda_{exc})d \gg 1$, the PL excitation spectra will be similar to the emission spectrum of the excitation source, i.e. $I_{PL}(\lambda_{exc}) \sim I_{exc}(0, \lambda_{exc})$.

The PL emission spectrum $I_{PL}(\lambda_{exc})$ itself gives an essential information about the emission response to a certain excitation source, which can be represented by a single excitation wavelength λ_{exc} source (e.g. ultra-narrow spectral line of lasers) or by a more complex excitation spectrum as e.g. a Xe halogen lamp.

5.1.1   SiO$_2$ matrix optical properties

To be able to separate PL emission contributions of Si-ncs from that originating in pure SiO$_2$ matrix, we have measured first the optical properties of the pure SiO$_2$ matrix. The attenuation was measured across the visible spectral region $\lambda_{exc} \in$(400-800) nm (Fig. 5.2), where the SiO$_2$ matrix is optically transparent, i.e. do not absorb significantly the excitation light. We observed rather a flat spectral dependence of the losses (black line) - through the whole visible spectral region the optical losses value do not differ more than by 10 %. The transmittance around 600 nm is relatively high about 52 % (air as the reference, blue line). Losses are caused probably by the Mie scattering of the light on the air voids and inhomogeneities inside of the matrix. It can be described by the Lorenz-Mie theory, which represents an analytical solution of Maxwell's equations for the light scattering by spherical particles of all possible ratios of diameter to wavelength, uniformly distributed in the homogeneous medium. The limit case of the spectral dependence of the losses caused by the light scattering α_{scatt} on tiny particles, much smaller then the excitation wavelength λ_{exc}, is known as the Rayleigh scattering and gives $\alpha_{scatt} \propto \frac{1}{\lambda^4}$. This law describes well the spectral behavior of the total losses in the SiO$_2$ matrix, as shown in Fig. 5.2 (fit function - red line).
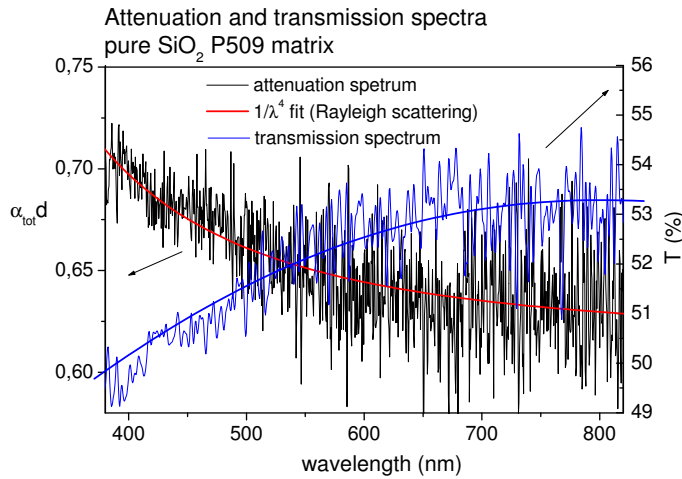
Figure 5.2: *Transmission/attenuation spectra of the pure SiO$_2$ P509 matrix measured in the transmission setup arrangement as sketched in Fig. 5.1 in the visible spectral region. Samples were irradiated at λ_{exc} using a spectrally broad Xe lamp, from which single excitation wavelengths were selected using a monochromator. The signal was detected at room temperature using a spectrometer with the Si-photodiode linear detector (Oriel Instaspec II). The red line represents a fit curve $\propto \frac{1}{\lambda^4}$ and corresponds to the Rayleigh scattering spectral dependence.*

When excited in the UV spectral region $\lambda_{exc} \in$(200-400) nm, the emission response

of SiO_2 matrix becomes important and the PL excitation spectra $I_{PL}(\lambda_{exc})$ in the reflection experimental setup has to be measured instead. The PL emission and PL excitation spectra of the SiO_2 matrix are shown in Fig.5.3. The pure SiO_2 sample is optically thin, thus the attenuation/absorption spectrum can be estimated from the PL excitation spectrum. Samples were excited using a Xe lamp, whose emission spectrum in the UV spectral range is shown in inset of Fig. 5.3. The important observation is that no SiO_2 matrix related PL emission has been observed under excitation at $\lambda_{exc} \geq 355$ nm, in particular at $\lambda_{exc}=355$ nm (see Figs. 5.10, 5.11).
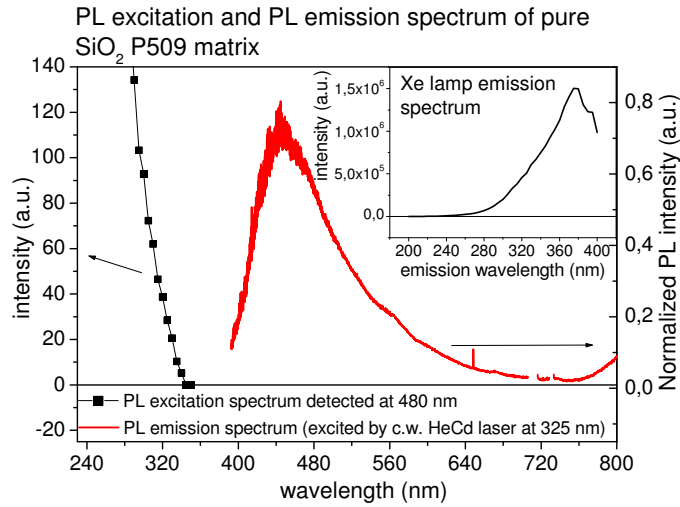
Figure 5.3: *PL excitation and emission spectra of the pure SiO_2 P509 matrix measured in the reflection experimental setup sketched in Fig. 5.1. PL excitation spectrum was excited in the UV spectral region using a spectrally broad Xe lamp, from which the single excitation wavelengths were separated using a monochromator. The signal at 480 nm was detected at room temperature using an air-cooled CCD camera. PL emission spectrum was excited using a continuous HeCd laser beam at 325 nm and detected at room temperature by a CCD camera (cooled by Peltier system to -40° C). The PL emission spectra were corrected for the spectral response of the detection system using a calibrated black body radiation source (ORIEL quartz tungsten halogen lamp 45 W). Inset: Xe lamp emission spectrum.*

5.1.2   Si-ncs/SiO₂ samples optical properties

(a) Attenuation and (b) PL emission spectra of "standard", "yellow", "white" and "Borsella" Si-nc/SiO_2 samples are presented in Fig. 5.4(a,b). The excitation and detection experimental conditions remain the same as in the previous measurements of the pure SiO_2 matrix (Figs. 5.2 and 5.3). The overall shape of the attenuation spectra is similar for all the measured samples, however, the spectra are shifted with respect to each other both in spectral position and in magnitude. The spectra shift towards

shorter wavelengths with decreasing Si-ncs size in a similar way as the emission spectra do, due to the quantum confinement effects. The reference "Borsella" Si-ncs/SiO$_2$ sample, which contains the largest Si-ncs of an average size of $\sim$5 nm [83], has the onset of absorption considerably red-shifted compared to our samples of the diameter of $\sim$2-3 nm (see Fig. 4.1).

PL emission spectra are shown in Fig. 5.4. The broad spectrum of the nonsedimented "standard" Si-ncs/SiO$_2$ sample is peaked at $\sim$675 nm with FWHM of 190 nm. The spectra of sedimented "standard" Si-ncs/SiO$_2$ samples are very similar, only the peak maxima slightly shift with the sedimentation degree to longer wavelength. This goes against intuitive expectations and can be explained in terms of different surface passivation, which is one of the main parameters governing the optical properties of the oxidized Si-ncs. The slightly different surface passivation of the different Si-ncs sediments can be caused by the fact, that they were kept for different time in the pure EtOH solution during the sedimentation process. The spectra of the H$_2$O$_2$ treated "yellow" and "white" Si-ncs/SiO$_2$ samples are noticeably blue shifted to $\sim$629 nm and $\sim$596 nm, respectively, and get considerably narrower - FWHM of 140 nm and 116 nm, respectively. This spectral narrowing indicates that, owing to H$_2$O$_2$ treatment, also the Si-ncs size distribution gets narrower, which can be considered, apart from the blue-shift, as an additional favorable factor for a gain medium with Si-ncs. The most red-shifted PL spectrum at $\sim$877 nm belongs to the reference "Borsella" sample with the largest Si-ncs of average size of $\sim$5 nm [83]. The emission peak around $\sim$450 nm of low intensity originates probably from some SiO$_2$ related defects or the SiO$_2$ matrix, where a similar blue emission band at $\sim$446 nm was observed (see also Fig. 5.3). The large Stokes-shift of the main emission band in our samples ($\sim$590-670 nm) with respect to the "absorption" edge (see Fig. 5.4(a)) at $\sim$400-450 nm is generally explained by carrier relaxation and self-trapping of the confined exciton on surface/interface related states [47] [56] [55] [84].

The decreasing amplitude of the optical losses in higher sediments of the "standard" Si-ncs (Fig. 5.4(a)) reflects an increasing optical quality of the samples. The optical quality of the "yellow" sample seems to be better than that of the 2nd sediment "standard" one, however, lower than the one of the 3rd sediment. The 3rd and 4th sediments optical losses are, however, not comparable in the absolute value with the other samples, because they contain much lower amount of the Si-ncs due to a few differences in the preparation technique - the powder was kept and transmitted in EtOH solution (see Sec. 3.2). All other presented samples, however, contain the same amount of Si-ncs of $\sim$2 mg per sample, and their optical losses are comparable in absolute values.
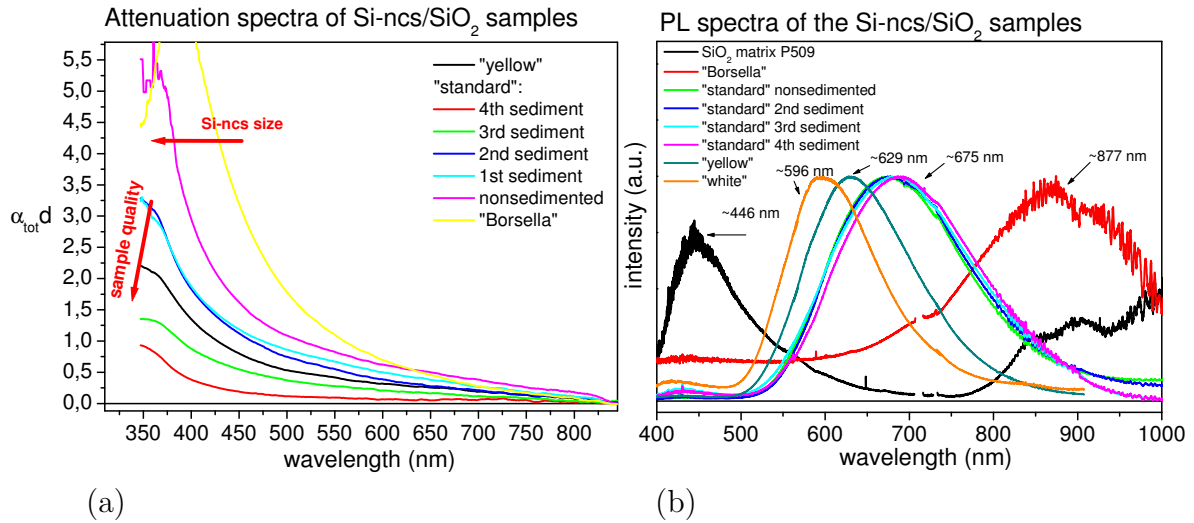
Figure 5.4: *(a) Attenuation and (b) PL emission spectra of typical "standard" Si-nc/SiO₂ samples (nonsedimented, 1st, 2nd, 3rd and 4th sediment), a "yellow", a "white" and a reference "Borsella" Si-nc/SiO₂ sample. The experimental conditions are similar to that in Figs. 5.2 and 5.3. The emission and attenuation spectra shift to shorter wavelength with decreasing Si-ncs size and the optical losses amplitude decreases with increasing samples optical quality. PL emission spectra are corrected for the spectral response of the detection system.*

Fig. 5.5 shows the transmission spectra, extracted from the data in Fig. 5.4(a). We can find here again a nice dependence of the total losses on the optical quality of the samples. Let us compare the transmittance of different samples at e.g. 600 nm (pure SiO₂ matrix as a reference). As expected, the nonsedimented "standard" sample exhibits the highest optical losses T <20 %, while the sedimented "standard" samples show decreasing losses with the increasing sedimentation level: the 1st sediment exhibits the transmittance of about T ~30 %, the 2nd sediment T ~70 % and the 3rd and 4th sediments have T ~80 % and T ~85 %, respectively; the "yellow" sample exhibits the transmittance of about T ~55 %.

5.1.3 Effect of an additional H₂O₂ treatment on the PL emission spectra of por-Si

Most of the PL spectra shown in Fig. 5.4(b) originate in the "standard" samples with sedimented Si-ncs, which were prepared in the HF/H₂O/EtOH electrochemical bath, without any intervention of H₂O₂. The effect of the H₂O₂ etching and post-etching treatment intensity, i.e. etching duration and H₂O₂ concentration, was studied on the PL emission spectra of the por-Si layer. Fig. 5.6 shows how the normalized PL spectra develop starting from dark-red emitting Si-ncs (as represented by the lowermost curve in Fig. 5.6, measured on the reference Si-ncs/SiO₂ sample fabricated
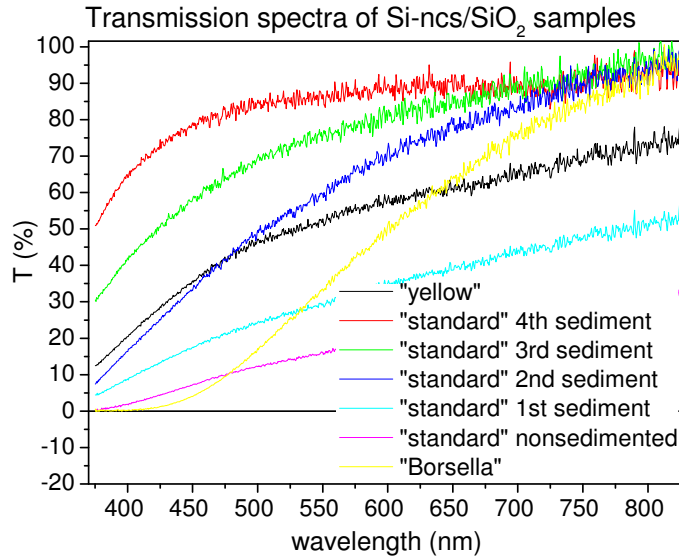
Figure 5.5: *Transmission spectra of typical "standard", "yellow" and reference "Borsella" Si-nc/SiO₂ samples. The main difference in optical properties seems to be a different magnitude of scattering losses due to a different samples homogeneity. 100% transmittance would belong to the pure SiO₂ matrix.*

by Si$^+$-ion implantation into Infrasil plate) over the "standard" and "yellow" por-Si films up to the "white" ones (uppermost curves in Fig. 5.6). A continuous blue shifting with the increasing strength of HF/H₂O₂ treatment is obvious.

This blue-shift correlates qualitatively with the Si-ncs size shrinkage as revealed by HRTEM and Raman investigations. What we observe in addition to that is the gradual appearance of a new band at ∼450 nm (Fig. 5.6) which becomes evergrowing with increasing intensity of the HF/H₂O₂ treatment. This radiation can either be due to the core emission of "free" confined exciton in tiny (single) Si-ncs that are developing after an intense and prolonged etching or due to the defects in oxidized Si-ncs surface shell (SiO₂ related material) emission. The interpretation in terms of SiO₂ based shell defects seems to be supported by the presence of a very similar emission band occurring also in the pure SiO₂ sol-gel based matrix (Fig.5.3). We would like to stress here, that no SiO₂ based matrix is present in the samples investigated here in Fig. 5.6. The spectral development with the decreasing Si-ncs size is not continuous and exhibit a clear short-wavelength cut-off. Using our technological process, PL emission spectra peaked below ∼585 nm in oxidized por-Si can be obtained by no means - neither by increasing H₂O₂ concentration in the etch bath nor by prolongation of the H₂O₂ post-etch treatment. Similar cut-off behavior has been observed for por-Si with different porosities exposed to air by Wolkin et al. in [47] (see Fig. 2.7(b)) and can be prescribed to the surface oxidation effects.
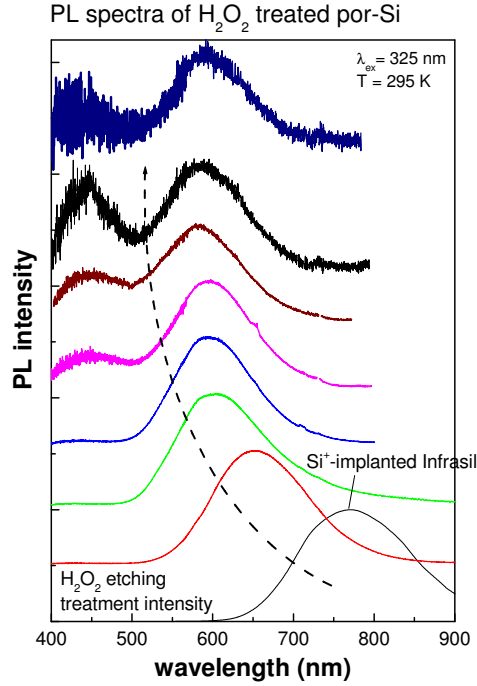
Figure 5.6: *PL spectra of H_2O_2 etched porous silicon and a reference sample fabricated by Si^+-ion implantation into Infrasil plate (lowermost curve). The emission spectra are continuously blue-shifting with the etching duration and H_2O_2 concentration till a certain limit, interpreted in terms of surface oxidation as in [47] (compare with Fig. 2.7(b)). Spectra, corrected for the spectral response of the detection system, were excited using a continuous HeCd laser at 325 nm. Signal was detected at room temperature using a CCD camera (cooled by Peltier system to -40° C).*
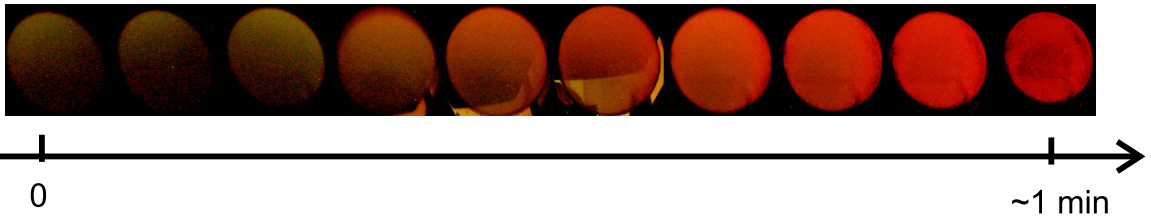
Figure 5.7: *Time sequence real-color photo of the fresh "standard" por-Si exposed to air within few seconds after preparation (before the sample was fully oxidized) under UV excitation lamp illumination. The emission color continuously red-shifts with progressing oxidation.*

This is supported by our own experimental results, when we observed a green-like PL emission by naked eye under the UV lamp excitation from a "standard" fresh por-Si layer within a few seconds after preparation, before the sample (exposed to the air) was fully oxidized; the color had changed rapidly to an orange one. The evolution of the spectrum is too fast to be correctly measured using the standard PL measurement setup, thus we present here only a real-color time-sequence photos of

the freshly prepared por-Si layer emission under the UV lamp excitation as shown in Fig. 5.7.

It is probably useless to say that we would had been happy if we could find a way to "conserve" this short wavelength intense green PL emission from a big ensemble of Si-ncs for our experiments searching for optical gain and StE (blue-shifted PL emission requirement). Unfortunately, we have not succeeded. We have observed stable very weak greenish PL emission in diluted colloidal suspensions of Si-ncs only, as will be presented in the following.

5.1.4   Green PL emission band observed in colloidal suspensions of Si-ncs in EtOH

The broad PL emission spectra of the Si-ncs/SiO$_2$ samples under the c.w. excitation by HeCd laser at 325 nm are observable in the visible region between 550-950 nm. The PL spectrum of an ensemble of Si-ncs is generally a composition of narrower spectra of single Si-ncs of different sizes, thus the greenish emission around 550 nm should be theoretically observable from the smallest Si-ncs within the prepared Si-ncs ensemble. In order to understand the influence of the size distribution on the PL emission spectra, we studied the sedimented colloidal "standard" Si-ncs powder suspensions in pure EtOH (Fig. 5.8, Ref. [33]).
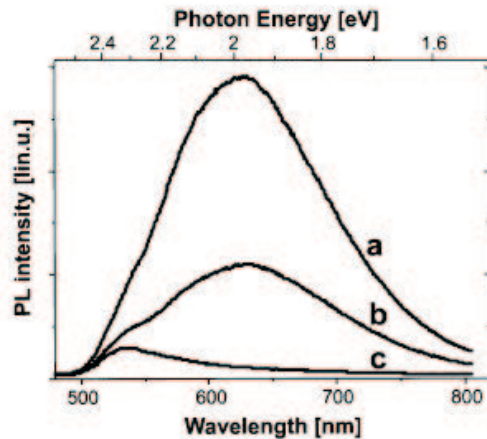
Figure 5.8: *PL spectra of a "standard" Si-ncs suspension in EtOH: (a) freshly shaked colloid of "standard" nonsedimented Si-ncs, (b) 1 hour sedimented colloid (corresponding to the 4th sediment "standard" Si-ncs powder) and (c) a filtered colloid. Filtration separates the smallest Si-ncs from the Si-ncs ensemble and their emission appears at the short-wavelength tail of the original Si-ncs ensemble emission spectrum in (a). Emission was excited using a c.w. Ar-ion laser (emission lines from 457 nm to 514 nm) and detected using Pentamax iCCD camera connected to an imaging spectrometer (Jobin-Yvon Triax 320). Spectra are corrected for the spectral response of the detection system. Taken from J. Valenta, K. Dohnalová et al. [33].*

Small amount of our "standard" Si-ncs powder was "dissolved" in ∼1 cm³ of pure ethanol. Its PL spectrum is peaked at ∼620 nm, as shown in Fig. 5.8(a). The 1 hour sedimented Si-ncs powder, corresponding to the 4th sediment "standard" Si-ncs powder, still consist of larger clusters and its PL emission spectrum is very similar to that of the nonsedimented "standard" Si-ncs/EtOH solution (see Fig. 5.8(b), compare with Fig. 5.4(b)). To remove larger Si-ncs and their clusters from the suspension, we filtered the 4th sediment "standard" Si-ncs/EtOH suspension through a teflon filter with pores of 200 nm. The filtered Si-ncs/EtOH suspensions became colourless and transparent and exhibits greenish PL peaked at ∼530 nm (Fig. 5.8(c)), which is not related to the EtOH solvent itself. The origin of the green-like emission is not very clear, because according to the generally accepted model the surface states related emission band in the orange-red spectral region should dominate in sufficiently small oxidized Si-ncs. The green emission band can be thus related to PL emission from surface states in extremely small (∼1 nm) Si-ncs, modified perhaps by the EtOH treatment or can be probably defect/impurity related. Similar greenish emission has been observed by other groups in different Si-ncs based samples [85] [86] [87] [88] [89] and a similar peak at 563 nm with PL decay time of ∼60-80 ns was observed by Stathis et al. in Suprasil SiO₂ [90] and by us in Figs. 5.13, 5.14 and 5.15.

The existence of a stable green emission of faster decay time in our Si-ncs is very interesting for the Si laser development and deserves more detailed study in the future, unfortunately the present obtainable amount of such filtered Si-ncs is not sufficient for the preparation of a high Si-ncs volume fraction sample as required for the StE onset.

5.2   Time resolved PL emission spectra of Si-ncs/SiO₂ samples

The steady-state emission properties of the Si-ncs/SiO₂ samples was discussed in the previous sections. In this section we will concentrate more on the dynamics of the processes, which - following the discussion in section 2.2.4 - represents an important step towards the further StE onset investigation. The decay time of the Si-ncs ensemble emission differs significantly from that of bulk silicon due to the quantum confinement, relaxation effects as excited carriers diffusion between the different Si-ncs ("hopping" effect [91] [92]), reabsorption of the short-wavelength emission by the larger Si-ncs, inhomogeneous distribution of radiative centers, disordered surface potential and size distribution [93]. It is known for long time that por-Si emission decay time is formed by two components - a "fast" one on the nanosecond time scale

and the "slow" one on the microsecond time scale, both at room temperature [94]. Since our samples contain por-Si grains embedded in the SiO$_2$ matrix, the emission dynamics is expected to be in general similar to the por-Si one with possible minor modifications. In this section we will present the time resolved PL emission spectra of our Si-ncs/SiO$_2$ samples, measured under various experimental conditions at room temperature. All spectra were corrected for the spectral response of the detection system by a calibrated black body radiation source (Oriel tungsten halogen lamp 45 W).

Stretched exponential decay of the PL emission of Si-ncs ensemble

The recombination of the carriers in localized states can be described by the single-exponential decay $I(t) \sim e^{-(\frac{t}{\tau})}$ and the free e-h pair recombination decays at longer times as the inverse quadratic function of time $I(t) \sim \frac{1}{t^2}$. The emission decay of the Si-ncs ensemble in SiO$_2$ matrix, however, differs from that two cases and follows the stretched exponential function (Fig. 5.9)

$$I_{PL} = I_0 e^{-(\frac{t}{\tau})^\beta} \tag{5.5}$$

$$0 \leq \beta \leq 1.$$
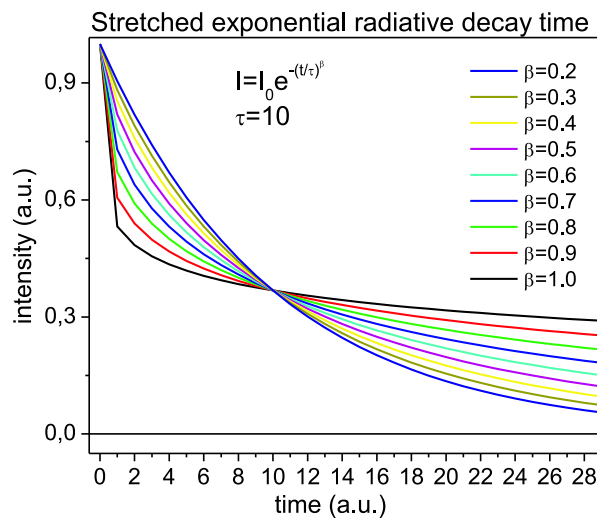
Figure 5.9: *Stretched exponential PL decay as a function of β. Coefficient $\beta=1$ leads to the single-exponential decay law.*

Stretched exponential decay limit for $\beta = 1$ leads to the single-exponential decay law of the e-h recombination in the localized state, as discussed above, while the smaller values of $\beta < 1$ correspond to a broad distribution of lifetimes of the relaxation processes, caused by the exciton "hopping" and/or cascade reabsorption of the emitted light by larger Si-ncs. Since the rate of hopping is higher for lower interdot potential barrier, identical Si-nc with different surrounding will have a different dynamics. Only an ensemble of fully isolated Si-nc or an ensemble of single-sized Si-ncs in a high potential barrier will have β close to 1. In general, the kinetic equation governing the relaxation processes in Si-nc consists of three terms: radiative recombination, nonradiative recombination and carrier diffusion ("hopping"), which all affect the resulting PL dynamics.

5.2.1 "Slow" PL emission component in Si-ncs/SiO$_2$ samples

Let us now discuss the "slow" PL emission component in our Si-ncs/SiO$_2$ samples separately. The signal was excited using a pulsed UV excitation at 355 nm (3rd harmonic of a Nd:YAG system, repetition rate 10 Hz, 8 ns pulse duration) and detected at room temperature using an intensified iCCD (cooled by Peltier system to -20°C). The spectra were corrected for the spectral response of the detection system.

First, we will present the time-resolved PL emission spectra of the "standard" 2nd sediment Si-ncs/SiO$_2$ sample #04050606 (Fig. 5.10(a,b)), detected using the gate width of 500 ns, shifted from the zero delay (with respect to the excitation pulse) to 15 μs by steps of 500 ns. The emission peak maximum shifts with time towards longer wavelengths (see inset in Fig. 5.10(a)) and its amplitude decays mono-exponentially with a decay time of τ=6 μs. Contrary to that, the PL intensity at a fixed emission wavelength follows the stretched exponential law (Fig. 5.10(b)). The PL lifetime τ grows roughly exponentially with the emission wavelength (inset in Fig. 5.10(b)) from $\sim$1.2 μs at 500 nm up to $\sim$20.7 μs at 680 nm. This is in agreement with the expected faster and blue-shifted emission of smaller Si-ncs predicted by a quantum confinement model, however, it can be explained also in terms of the above mentioned exciton "hopping". The coefficient β increases approximately linearly with increasing emission wavelength with the slope $\sim$0.002 nm^{-1} (inset in Fig. 5.10(b)). This can correspond e.g. to the reabsorption of the radiation emitted in smaller Si-ncs by the larger ones or by easier diffusion of the excitons from the smaller Si-ncs, where the confined excitons are localized more on the Si-ncs surface.

Very similar time resolved PL spectra were measured in the same experimental setup in the different type of Si-ncs/SiO$_2$ sample - a "yellow" one #04092003, as shown in Fig. 5.11. The emission decay time and β coefficient are of very similar

(a)

(b)
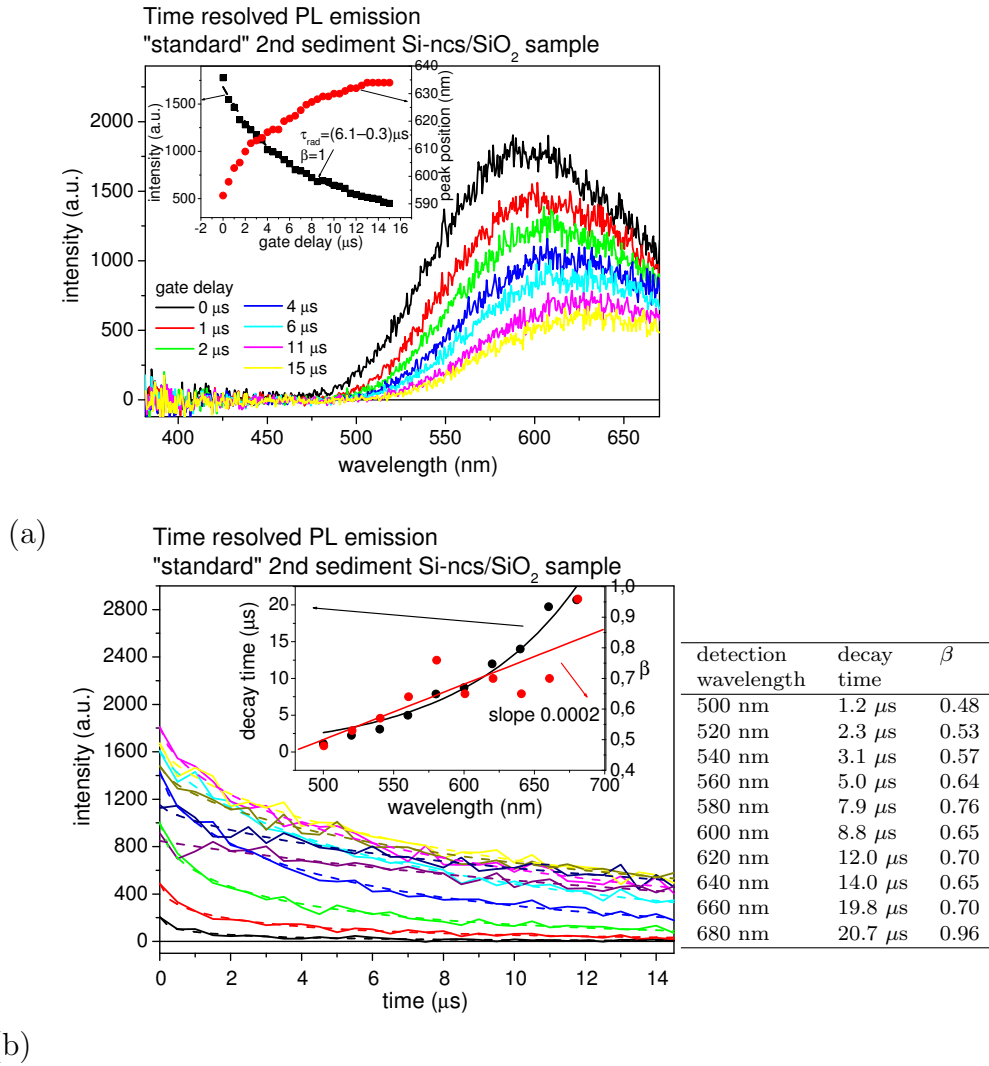
Figure 5.10: *(a) Time resolved PL spectra in a "standard" 2nd sediment Si-ncs/SiO₂ sample #04050606. Inset (a): spectral shift of the peak maxima in time and a single-exponential PL decay measured at the peak maxima spectral position. (b) Contrary to (a), at a fixed detection wavelength we get stretched-exponential PL decay and β <1. Inset (b): spectral behavior of the estimated PL decay time and coefficient β. Table: decay time and β at different emission wavelengths. PL decay time increases with the emission wavelength, i.e. blue-shifted emission of smaller Si-ncs is faster.*

values as observed in the previous "standard" Si-ncs/SiO₂ sample and exhibit very similar behavior as a function of the emission wavelength. This result indicates, that there is probably no significant difference in PL emission dynamics between these two types of samples.

These results were verified using an independent experimental setup with a pulsed excitation at 532 nm (Nd:YAG, 45 ps pulse duration, 1 Hz repetition rate, 25 mJ in pulse) and detection by a PMT with an oscilloscope (Fig. 5.12). Moreover, these observations are in line with established general features of PL dynamics in a variety

(a)

(b)

detection wavelength	decay time	β
460 nm	0.13 μs	0.23
480 nm	0.81 μs	0.48
500 nm	1.18 μs	0.49
520 nm	2.30 μs	0.57
540 nm	3.68 μs	0.59
560 nm	5.34 μs	0.62
580 nm	7.49 μs	0.64
600 nm	9.93 μs	0.66
620 nm	12.71 μs	0.67
640 nm	16.61 μs	0.68
660 nm	20.46 μs	0.70
680 nm	25.46 μs	0.73
700 nm	29.75 μs	0.66
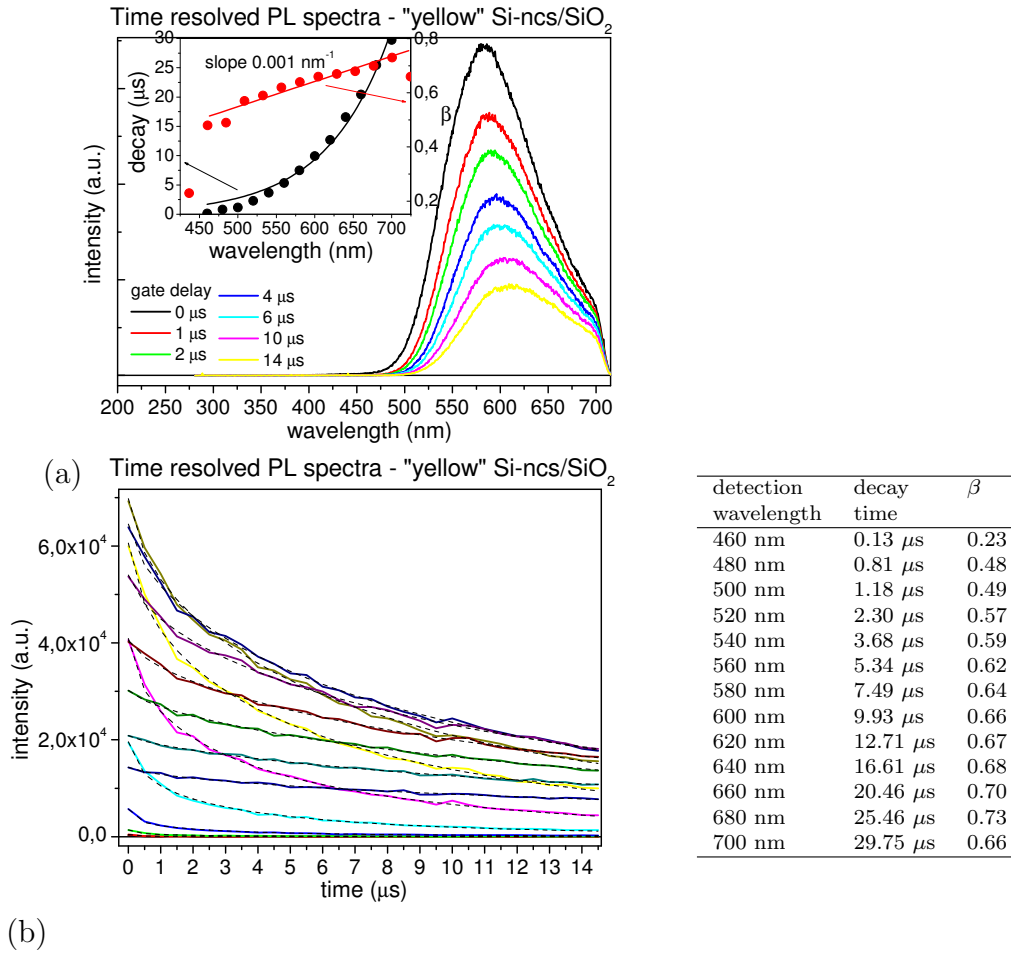
Figure 5.11: *(a) Time resolved PL spectra in a "yellow" Si-ncs/SiO₂ sample #04092003. Inset (a): PL decay and β as a function of the detection wavelength. (b) Stretched-exponential PL decay at fixed detection wavelengths. Table: decay time and β at different emission wavelengths. PL decay time again increases with the emission wavelength, i.e. blue-shifted emission of smaller Si-ncs is faster, as observed also in a 2nd sediment "standard" Si-ncs/SiO₂ sample in Fig. 5.10.*

of luminescent Si-ncs as reported e.g. in [95].

As a conclusion we assume that the "slow" PL emission component dynamics is probably independent of the excitation pulse parameters. Moreover, it is very similar in both "standard" and "yellow" Si-ncs/SiO₂ samples. Let us now explore the "fast" PL emission component properties.

5.2.2 "Fast" PL emission component in Si-ncs/SiO₂ samples

Up to now, the "fast" PL component of Si-ncs has been given much less attention in the literature compared to the "slow" one. Nevertheless, the "fast" PL emission component strongly differs from the "slow" one, as we demonstrate in Fig. 5.13, where the PL emission spectra of the "fast" and "slow" components of the pure SiO₂ matrix
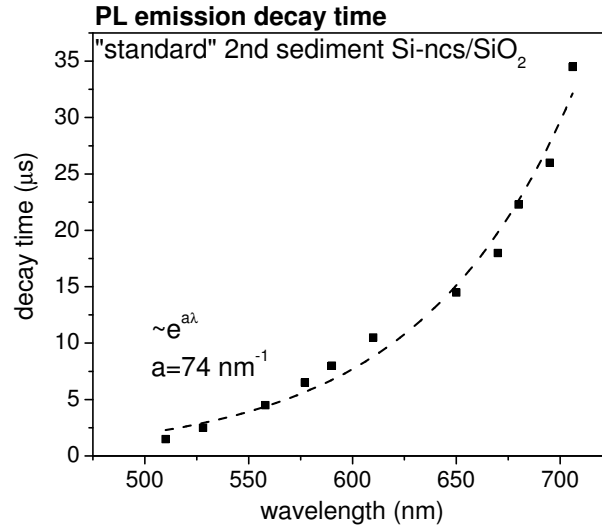
Figure 5.12: *PL decay time of the "standard" 2nd sediment Si-ncs/SiO₂ sample #04050605, measured under pulsed excitation at 532 nm (Nd:YAG, 45 ps pulse duration, 1 Hz repetition rate, 25 mJ in pulse) and detection by a PMT with an oscilloscope. Thanks are due to Mgr. K. Žídek.*

and a Si-ncs/SiO₂ "yellow" sample #04100502 are shown. The PL emission spectra of the pure SiO₂ matrix are under given excitation conditions peaked at ∼380 nm and are similar for both the "fast" and "slow" emission components. On the other hand, the PL emission spectra of the "yellow" Si-ncs/SiO₂ sample are very different and evolute in time. The "fast" component exhibits, besides the SiO₂ matrix related band at ∼380 nm, also an additional blue-band around 450 nm and a low intensity green-band at ∼550 nm. The "slow" component exhibits a high intensity orange-band at ∼600 nm, similar to that measured under the continuous excitation and as described in the previous section.

Let us now present the experimental study of the "fast" PL emission component only. The PL spectra of the pure SiO₂ matrix and a "white" Si-ncs/SiO₂ sample #05122101 are presented in Fig. 5.14(a,b). The time resolution of the setup is given by the excitation pulse duration ∼20 ns, which, however, do not affect the spectral position of the PL emission spectra. The spectra were detected by an oscilloscope at different delay times with respect to the excitation pulse, from -20 ns to 50 ns. The PL emission spectra of the pure SiO₂ matrix and a "white" Si-ncs/SiO₂ sample, in temporal coincidence with the excitation pulse, were extracted from Fig. 5.14(a,b) and plotted in Fig. 5.14(c). There is a clear difference between these two spectra, which appears to have a Lorentzian shape peaked at ∼472 nm with FWHM of ∼92 nm. The difference spectrum seems to be very similar to the "fast" PL emission component as
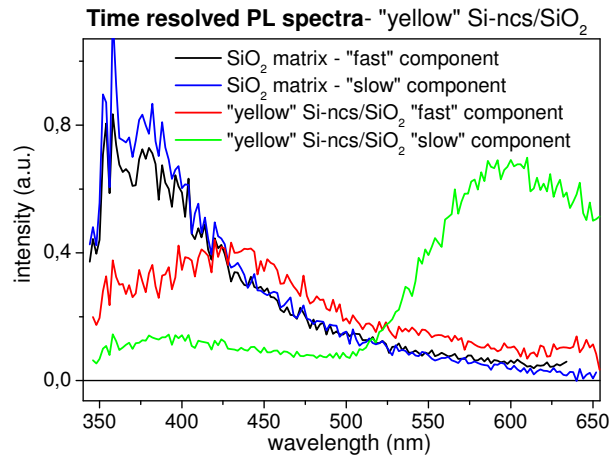
Figure 5.13: *Time resolved PL emission spectra of a "yellow" Si-ncs/SiO$_2$ sample #04100502 and of the pure SiO$_2$ matrix. Signal was excited using a XeCl excimer laser (308 nm, 20 ns pulse duration, 10 Hz repetition rate, excitation intensity of 1.2 MW/cm^2) and detected at room temperature using a PMT in conjunction with a boxcar integrator. The gate width of 50 ns at zero delay was adjusted for the "fast" component detection, gate width of 4 μs at delay of 10 μs for the "slow" one. The "fast" and "slow" PL component of pure SiO$_2$ matrix is similar, while in the "yellow" Si-ncs/SiO$_2$ sample are strongly different.*

measured in Fig. 5.13. The blue spectral component at ∼472 nm originates probably from the fast "free" confined exciton recombination within the crystalline Si-ncs core, because its peak position corresponds according to Kim et al. [50] to the average Si-ncs diameter of ∼2.8 nm. This is in excellent coincidence with the experimentally estimated average Si-ncs size by the HRTEM and Raman spectroscopy (compare Fig. 4.1 and 4.3). This spectrum is strongly blue-shifted with respect to the c.w. excited orange band at 600-650 nm, connected probably with the self-trapped exciton present in the longer times after excitation.

Till now we presented "fast" emission component, excited using the XeCl excimer laser at 308 nm. Let us now present "fast" PL emission spectra obtained under another excitation with an UV ∼ns pulsed excitation at 355 nm (3rd harmonic of a Nd:YAG system, 10 Hz, 8 ns pulse duration). The main difference (and advantage) of such excitation wavelength, compared to the previous one at 308 nm, is the negligible emission response of the SiO$_2$ matrix in this spectral range. This enables us to study separately the "fast" PL emission component of the Si-ncs themselves, while in the previous results in Figs. 5.13 and 5.14 we had to measure a pure SiO$_2$ matrix emission spectra as a reference.

The full set of the PL emission spectra development in a "standard" 2nd sediment Si-ncs/SiO$_2$ sample #04092002 is shown in Fig. 5.15(a). The signal was detected using an intensified iCCD camera, electronically pre-triggered in order to measure the whole

(a)   (b)

(c)
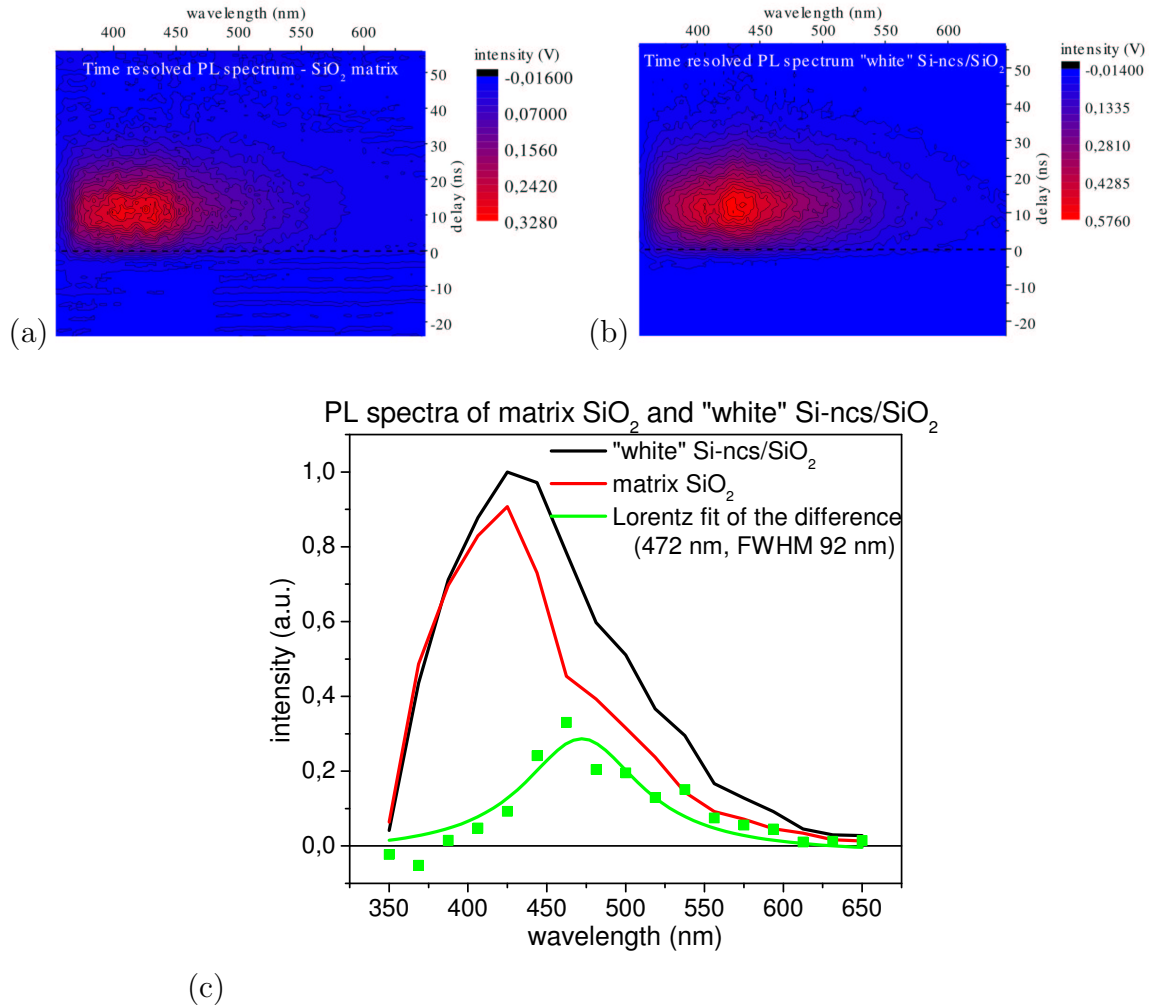
Figure 5.14: *Time resolved PL spectra of (a) the pure SiO₂ matrix and (b) a "white" Si-ncs/SiO₂ sample #05122101 excited using the XeCl excimer laser at 308 nm and detected using a PMT with an oscilloscope (50 Ω input). The red/blue color belong to a higher/lower signal. (c) Detail of the "fast" PL emission component spectra in (a,b), extracted from the emission concurring with the excitation pulse. The difference of the "white" Si-ncs/SiO₂ sample emission spectrum and pure SiO₂ matrix one form a Lorentz-like spectrum peaked at ∼472 nm with a low intensity band at ∼550 nm.*

PL emission peak development in time, including the period before and during the excitation. The detailed study of the PL spectra development within the ∼40 ns "before" the excitation (the zero delay has been assigned to the peak signal) and first ∼20 ns after excitation is plotted in Fig. 5.15(b-left). Likewise in Fig. 5.14(a) blue emission band at ∼450 nm together with a green-band around ∼550 nm have been observed, in excellent agreement with the above presented data measured under the different experimental conditions (compare e.g. Fig. 5.13). In particular, the low intensity green band at ∼550 nm is more pronounced here. It can be related to emission of small Si-ncs, as well as to some surface/interface related recombination, as discussed in section 5.1.4. The signal development after the first 20 ns is shown

(a) (b)
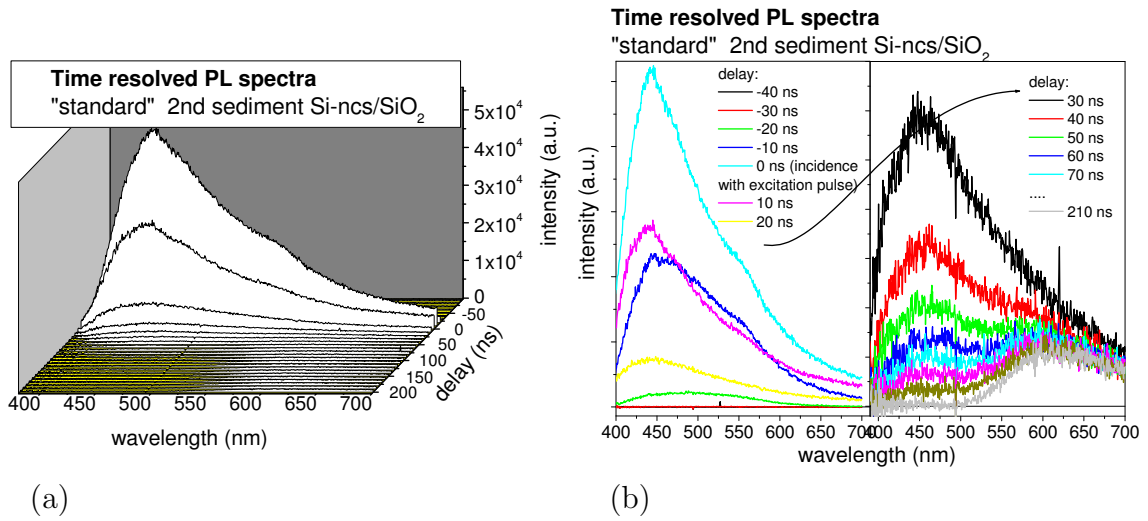
Figure 5.15: *Time resolved PL spectra of a "standard" 2nd sediment Si-ncs/SiO₂ sample #04092002. Signal was excited at 355 nm (3rd harmonic of a Nd:YAG system, 10 Hz, 8 ns pulse duration) and detected using an intensified iCCD camera (cooled by a Peltier system to -20° C) with the gate width of 10 ns and the gate delay (with respect to the excitation pulse) shifted from -40 ns to ∼210 ns by steps of 10 ns. (a) displays the whole detected signal resolved in time, while in (b) details of the signal are shown. The "fast" emission component contains two main contributions - one at ∼450 nm and second at ∼550 nm, the "slow" component appears at ∼620 nm.*

in Fig. 5.15(b-right) where the formation of the slower orange component at 600-650 nm can be clearly observed in good agreement with all presented figures in this section 5.2.

A similar study of the "fast" PL emission component measured under the same experimental conditions in an other place of the same "standard" 2nd sediment Si-ncs/SiO₂ sample #04092002 is shown in Fig. 5.16(a-b). Since the signal detection was not pre-triggered here, the "zero" gate delay is not exactly in temporal coincidence with the excitation pulse and is probably slightly delayed. The full time resolved spectra are shown in Fig. 5.16(a). The decay curves at fixed emission wavelengths, extracted from data in Fig. 5.16(a), are shown in Fig. 5.16(b) and follow the stretched exponential law (as defined by Eq. 5.5) with the decay times and β coefficient indicated in the Fig. 5.16(b) and plotted in the inset of Fig. 5.16(a). The decay time of the short wavelength emission appears to be very fast of the order of tens of ns - the blue-band emission at 440-460 nm decays with $\tau \sim 27$ ns and the green-band emission with $\tau \sim 34$ ns. The emission orange-band, on the other hand, decays in the μs scale - e.g. $\tau \sim 1.8$ μs at 600 nm. These values appear to be slightly different from those shown in Fig. 5.15 which, however, can be caused by a different sample consistence and surface passivation.

(a)

(b)
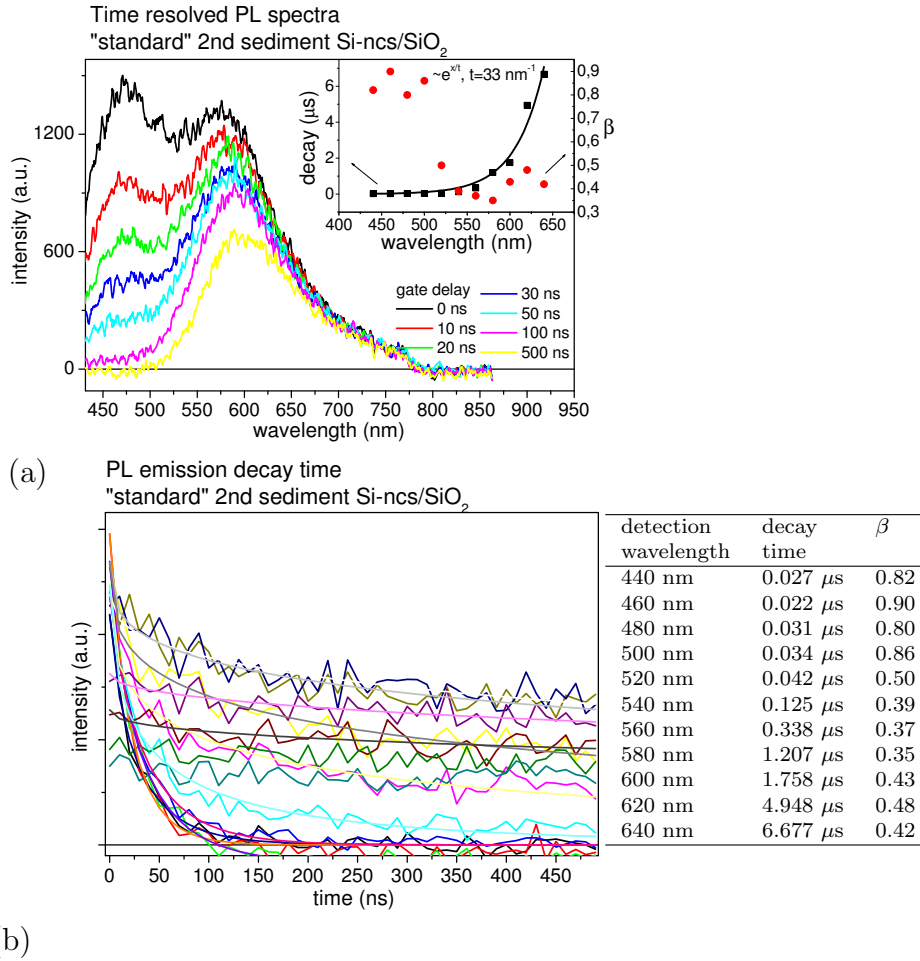
Figure 5.16: *Time resolved PL spectra of a "standard" 2nd sediment Si-ncs/SiO$_2$ sample #04092002. Signal was excited and detected in the same experimental setup as Fig. 5.15 with the gate width of 10 ns and the gate delay shifted from "zero" to ~500 ns by a step of 10 ns. (a) Time resolved PL spectra, inset: PL decay time and β coefficient spectral dependence, (b) stretched exponential decay curves (fit curves - smooth lines) at different fixed emission wavelengths. Table: decay time and β at different emission wavelengths.*

5.2.3 Time resolved PL emission intensity as a function of the the pump intensity in Si-ncs/SiO$_2$ samples

The time resolved PL emission intensity as a function of the the pump intensity for both the "fast" and "slow" emission components measured in a "standard" 2nd sediment Si-ncs/SiO$_2$ sample #04092002 is shown in Fig. 5.17(a,b). Signal was measured in similar experimental conditions as in Fig. 5.15 under variable excitation intensity. In insets of Fig. 5.17(a) and (b) there are plotted the output intensities as a function of the excitation intensity in log-log scale. The "fast" component input-output dependence was detected at the spectral peak maxima at ~490 nm and 580 nm, while the "slow" one at ~600 nm. The slope close to one at 490 nm and initial part of the curves at 580 nm and 600 nm is related to saturated or completely missing Auger

mechanism at this excitation regime. The curves at 580 nm and 600 nm exhibit saturation (sub-linear slope), which can be due to the Auger mechanism onset at a higher excitation fluency.

(a)   (b)
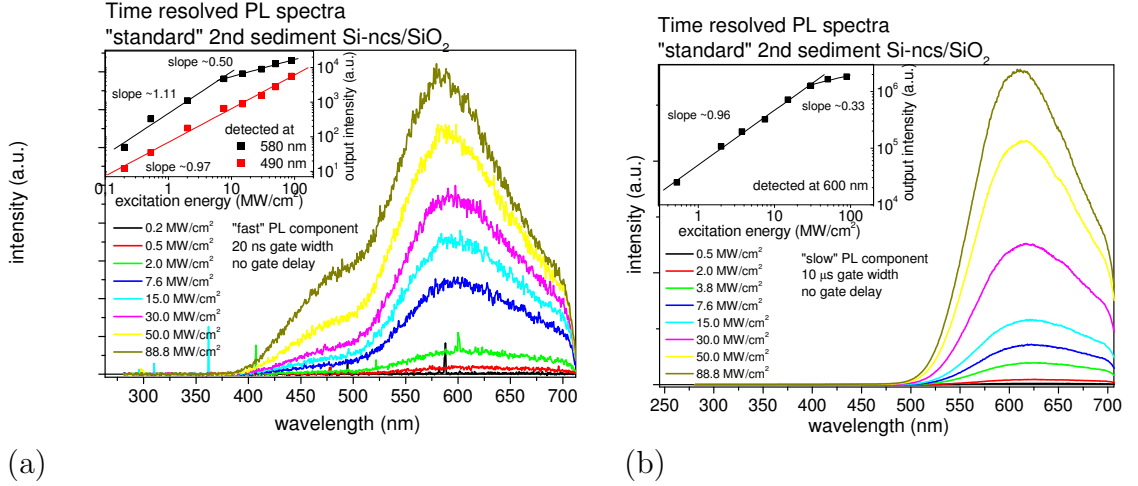
Figure 5.17: *Time resolved (a) "fast" and (b) "slow" PL emission components as a function of the excitation intensity, measured in "standard" 2nd sediment Si-ncs/SiO$_2$ sample #04092002. Signal was excited and detected in the same experimental setup as Fig. 5.15 with the gate width of 20 ns for (a) the "fast" emission component and of 10 μs for (b) the "slow" one (no gate delay). The excitation intensity varied from ∼0.25 MW/cm^2 up to 88 MW/cm^2. Insets: (a) "Fast" and (b) "slow" output intensity as a function of the excitation intensity at (a) 580 nm, 490 nm and (b) 600 nm in a log-log scale.*

5.2.4   "Ultrafast" PL dynamics in Si-ncs/SiO$_2$ samples

"Ultrafast" PL emission in "standard" 2nd sediment and "yellow" Si-ncs/SiO$_2$ samples has been discovered quite recently via femtosecond up-conversion technique with a time resolution of 300 fs [35]. An "ultrafast" PL emission decay of ∼400 fs and a high energy loss rate ≥3.8 eV/ps have been observed in the two studied Si-ncs/SiO$_2$ samples: "standard" 2nd sediment #04050605 and "yellow" #04102101 (Fig. 5.18). The energy loss rate is comparable with previously published data for electrons in CdSe and CdSSe NCs [96] [97]. The subpicosecond PL component originates probably in radiative recombination of core "free" excitons, which is rapidly quenched due to a very fast carrier trapping on the Si-ncs surface/interface energy levels. Auger quenching can be excluded here, since the ordinary Auger recombination cannot result in a subpicosecond PL decay [64]. Carriers forming the trapped e-h pair are spatially separated, which probably can suppress the nonradiative Auger mechanism in "free" confined excitons, being characterized by τ_{nr} ∼1 ns. As has been very recently suggested by Klimov et al. in [65], such ultrafast carriers trapping and their subsequent

spatial separation can lead to a "single-exciton optical gain" and enable us to reach the optical amplification at a pump fluency below the Auger mechanism threshold (see discussion in section 2.2.3). At a higher pump fluency, the Auger mechanism could appear, however, with low efficiency only, because of the spatial separation of the excited carriers in form of the self-trapped exciton. It is thus possible that the subpicosecond pumping opens a potential for "Auger-free" StE in Si-ncs. We plan to investigate this phenomenon in the near future.
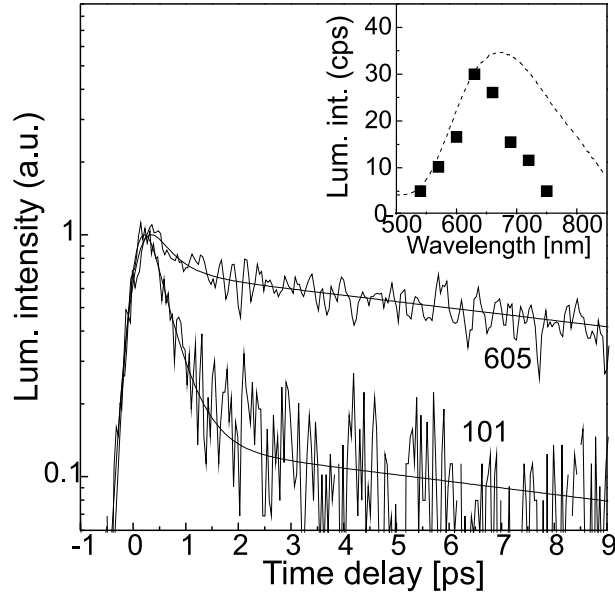
Figure 5.18: *(as taken from F. Trojánek, K. Dohnalová et al. [35]) "Ultrafast PL dynamics of "yellow" #04102101 (101) and "standard" 2nd sediment #04050605 (605) Si-ncs/SiO$_2$ samples. Signal was excited using a frequency-doubled Ti:sapphire laser (400 nm, pulse duration of 80 fs, energy ∼1 nJ, repetition rate 82 MHz) and detected at 630 nm. Smooth curves are two-exponential fits. Inset: comparison of ultrafast (zero-time) and time-integrated PL spectra (dashed curve) for "yellow" #04102101 Si-ncs/SiO$_2$ sample."*

5.3   Conclusions

In section 5.1 we investigated the basic optical properties of our Si-ncs/SiO$_2$ samples. The PL emission and absorption/attenuation spectra shape and spectral position do not differ significantly among all our Si-ncs/SiO$_2$ samples and the only significant difference arises from the different samples optical quality, i.e. optical losses caused by the scattering of light on inhomogeneities within the Si-ncs rich SiO$_2$ layer. The scattering losses are lower in samples with higher sediments of a "standard" Si-ncs (3rd and 4th sediment) and are usually lower in the "yellow" Si-ncs type. The reference "Borsella" Si-ncs/SiO$_2$ sample emission and attenuation spectra differ significantly from the Si-ncs/SiO$_2$ ones, since they contain larger Si-ncs (diameter of

$\sim$5 nm) prepared by different preparation technique. Moreover, we observed some further interesting features arising from an additional Si-ncs treatment: (i) an additional H$_2$O$_2$ treatment of porous silicon, further diminishing the Si-ncs core size in the porous layer, leads to a further blue-shift of the PL emission spectra. The spectral blue-shift is limited at $\sim$600 nm, as observed also by other groups; (ii) further filtering of the sedimented ensemble of Si-ncs in the colloidal EtOH suspension leads to a separation of the smallest Si-ncs, emitting around $\sim$550 nm. Amount of such filtered Si-ncs, however, is insufficient for the optical gain measurements.

In section 5.2 we presented the most interesting time-resolved PL emission spectra, excited in UV with the nanosecond and femtosecond pulses. Si-nc/SiO$_2$ samples exhibit a spectrally blue-shifted fast $\sim$ns component around $\sim$470 nm and 550 nm and a slow $\sim\mu$s component at $\sim$600 nm. The slow component emission spectra are very similar to the steady-state emission, presented in section 5.1. Quite recently, an ultrafast subpicosecond component has been discovered and interpreted in terms of quenching the interior exciton radiative recombination by carrier trapping on the nanocrystal surface. Such effect can lead to a possibility of an "Auger-free" StE onset in such type of nanocrystals.

Chapter 6

OPTICAL GAIN IN SI-NC/SiO$_2$ SAMPLES

In this chapter we will present the basic principle of the Variable Stripe Length (VSL) method for measuring the optical gain coefficient as proposed and realized in 1971 by K. L. Shaklee et al. [98]. Its applicability is, however, limited in case of lower gain coefficient magnitude, where a several artifacts can dominate over the gain effects and prevent unambiguous interpretation of the experimental results. To this end, we proposed to use VSL method in a combination with a Shifting Excitation Spot (SES) technique [40] [99], enabling us to distinguish between the real gain effects and observed gain-like artifacts. Finally we will present the experimental results obtained from our Si-ncs/SiO$_2$ samples and in a reference material - organic dyes in MeOH solution.

6.1   Variable Stripe Length (VSL) and Shifting Excitation Spot (SES) techniques

Positive net gain coefficient is the necessary condition for realization of any laser amplifier and oscillator. Because the gain coefficient is defined as the negative absorption coefficient, it can be measured by "Pump and Probe" techniques, where the optical absorption changes are induced by a strong photo-excitation and tested by a weaker test beam. The standard transmission "Pump and Probe" setup requires a sample optically thin at the pump wavelength, to allow penetration of the excitation beam through the whole sample thickness. Moreover, the absorption changes, i.e. optical gain coefficient, has to be strong enough to exceed the detection and excitation signal noise [40]. Therefore, this method is rather unsuitable for opaque thick samples with low optical gain, in particular for our samples. The VSL method is in principle a kind of "pump and probe" method where the spontaneous emission itself

plays the role of the testing beam. Therefore it is applicable for those excitation wavelengths only, where the spontaneous emission is strong enough. This method is experimentally easier and can be used also for samples with smaller optical gain. It is suitable also for samples in the form of an active luminescent thin layer prepared on a non-transparent or optically nonuniform substrate. In the following sections we will describe the VSL method principle, discuss its limits and applicability for low-gain materials, explain the necessity of the SES technique in low gain and inhomogeneous materials and show the results measured by this methods in our samples.

6.1.1 VSL technique

The sample for the VSL method should be homogeneous with well defined planar geometry. Light emission of the sample is excited by an intense laser beam focused into a narrow line (excitation stripe) of a homogeneous intensity profile, as can be seen from Fig. 6.1. Thus, a laser beam with a rectangular beam cross-section is ideal for the excitation (N$_2$ laser; XeCl, KrF excimer lasers), however, a (modified) Gaussian beam profile can be also used if the constant excitation profile along the whole excitation stripe length is guaranteed. The excitation stripe can be created by a cylindrical lens directly on the sample active surface, or preferably through a double projection system using an additional spherical lens between the cylindrical one and the sample.
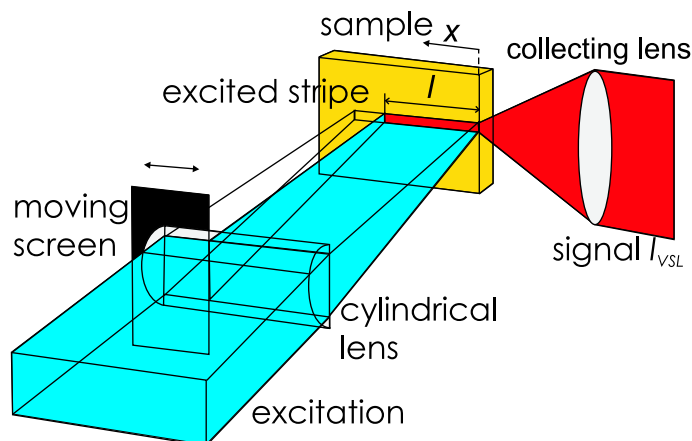
Figure 6.1: *VSL experimental setup principal sketch as suggested by Shaklee in [98].*

The double projection system with magnification smaller than one has some advantages as minimizing the diffraction effects occurring on the adjustable screen and making it possible to place the adjustable screen nearby the focal plane of the cylindrical lens to perform a clean cut of the excitation stripe. The VSL method basic

idea is to measure the emission output I_{VSL} at a certain emission wavelength λ from the sample edge as a function of the excitation stripe length l being changed by the adjustable (moving) screen, i.e. $I_{VSL}(l, \lambda)$. The spontaneous emission originating in the excitation stripe is emitted randomly into all directions and can induce stimulated emission when passing through the already excited region in the sample where the population inversion has been established. This is possible only within the excited stripe-like area, thus the common arrangement of the detection system consist in the projection of the emitting point on the sample edge towards the entrance detector spectrometer slit in the direction of the excited stripe, where the stimulated emission is expected. High numerical aperture (NA) and short focus of a collecting lens are preferred to have high efficiency of the light collection. The second lens, imaging the emission from the sample onto the spectrometer slit, has to cover well the spectrometer grating area (to fit the spectrometer NA), so its focal length is usually longer.

6.1.2 One-dimensional (1D) VSL model

The net gain coefficient $G(\lambda)$ is in fact a negative attenuation coefficient and thus can be defined in the same way as a relative change of the light intensity at wavelength λ passing an infinitesimal distance dx (compare with Eq. 2.1): $G(\lambda) = \frac{dI(x,\lambda)}{dx}\frac{1}{I(x,\lambda)} = g(\lambda) - K$, where $g(\lambda)$ is the material gain coefficient, equal usually to the negative band-to-band absorption coefficient $\alpha(\lambda)$ (see Eq. 2.3)) and $K(\lambda) = K$ describes the optical losses caused by light scattering (taken as spectrally independent). The total increment of the detected light along a path dx is given as a sum of spontaneous emission $I_{SpE}(\lambda)$ and the emission enhanced by StE (ASE - Amplified Spontaneous Emission)

$$dI_{VSL}(x, \lambda) = G(\lambda)I_{VSL}(x, \lambda)dx + I_{SpE}(\lambda)dx, \tag{6.1}$$

where $I_{SpE}(\lambda)$, $G(\lambda)$ and the emission light coupling efficiency to the detection system are taken (ideally) to be independent of x. By integration the previous equation for the stripe length from 0 to l we get the basic "VSL equation"

$$I_{VSL}(l, \lambda) = I_{SpE}(\lambda)\frac{e^{G(\lambda)l} - 1}{G(\lambda)}, \tag{6.2}$$

describing the signal intensity evolution with increasing stripe length l. From Eq. 6.2 the net gain coefficient $G(\lambda)$ for a single detected wavelength λ can be evaluated as a fit parameter. The occurrence of light amplification due to the StE is achieved when $G(\lambda) > 0$.

The spectral dependence of the coefficient $G(\lambda)$, i.e. the net gain spectrum, can be estimated from comparing VSL spectra $I_{VSL}(l, \lambda)$ and $I_{VSL}(2l, \lambda)$ for stripe lengths l and $2l$ according to

$$G(\lambda) = \frac{ln(\frac{I_{VSL}(2l,\lambda)}{I_{VSL}(l,\lambda)} - 1)}{l}, \qquad (6.3)$$

which follows from Eq. 6.2 after a simple algebra. When dealing with low-gain materials, special care has to be taken here to subtract carefully the noise level.

6.1.3   Limits of the VSL method

VSL method is excellent for determination of higher net gain coefficients as we shall demonstrate in section 6.2 for organic dye solutions, or as can be seen from original data reported by Shaklee et al. [98] (Fig. 6.2). Its applicability is, however, limited in cases of both the very high and low net gain coefficients as follows:
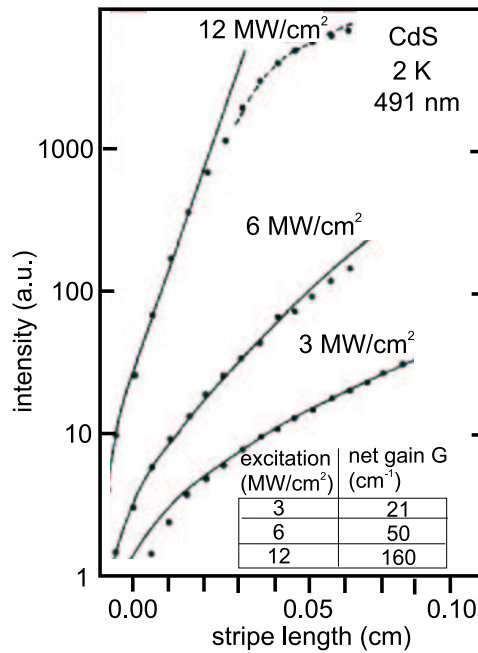
Figure 6.2: *VSL measurements in CdS at 2 K. Variation of light output (ASE) intensity with length of the excited region for indicated pump intensities. The points are experimental and the solid lines are fit curves using Eq. 6.2. Resulting values of G at λ=491 nm are shown in the inset table. Taken from [98].*

High gain limitation

The upper limit of the VSL method is given by the saturation of gain at high photon fluency, when the population inversion is depopulated by incoming photons

via StE process. According to the four-level model [100] the critical value of the stripe length l_c ("critical length"), from which the experimental data starts to deviate from the 1D model, is inversely proportional to the pump intensity $l_c \sim \frac{1}{I_{pump}}$ and is shorter for higher gain values. If l_c falls below $\sim$10 μm, which is approximately the shortest reachable VSL stripe length due to the inevitable diffraction effects on the adjustable screen, the net gain coefficient evaluation falls below the setup resolution. The gain value producing such strong saturation of the VSL signal below the stripe length of 10 μm is approximately G=5000 cm^{-1}, giving the upper gain limit condition of the VSL method to be $\sim Gl_c < 5$.

Low gain limitations

More interesting for our purpose is the low gain limit of the VSL method. It is given by the approximate condition $Gl \ll 1$, leading to approximate equation $e^{Gl} \approx 1 + Gl$, when Eq. 6.2 becomes a linear function of the stripe length, independent of the gain value: $I_{VSL}^{lowgain}(l, \lambda) \approx I_{SpE}(\lambda)l$. In such a case it is hardly possible to distinguish between the negative and positive values of the net gain coefficient. Moreover, multiple parasitic effects can dominate over the low StE effect and cause a gain-like distortion of the VSL signal (gain-like artifact) or just distort the VSL curve so much that no simple interpretation is possible. To ensure the validity of the 1D theoretical model described in section 6.1.2, several conditions have to be fulfilled [40] [99]:

- *A constant excitation intensity over the whole excited stripe length.* Even in this case, however, inevitable diffraction on the adjustable screen distorts the excitation stripe for shorter stripe lengths (as will be discussed later) and has to be examined carefully.

- *VSL stripe of negligible width*, because the internal reflections within the excited area are not included within the 1D VSL model and can further distort the VSL curve. The stripe width can be minimized down to the diffraction limit using the double projection system with magnification smaller than one and by careful adjustment of the sample position.

- *A constant coupling efficiency of the emission from any part of the excited stripe to the detector.* The problem can arise in the low gain materials case, where a longer excitation stripe has to be used. If the focal point of the detection lens is placed inside of the sample, confocal effects can cause gain-like artifacts (as will be discussed later).

- *Homogeneity and planarity of the sample, as well as the rectangular well shaped sample edge.*

- One should also *avoid the waveguiding effects*, which also are not included in the 1D VSL model [99].

6.1.4 SES technique

Many of the artifacts coming from the effects described above can act as a gain-like effect and can be minimalized or completely removed by a careful setup arrangement and using samples of sufficient quality. An additional experimental method, however, is necessary to prove unambiguously the StE onset. To this end we propose a simple extension of the VSL method called "Shifting Excitation Spot" (SES) method (Fig. 6.3; [40]), introduced independently in a simple modification in Refs. [101] and [102] to measure the optical losses in laser waveguide structures.
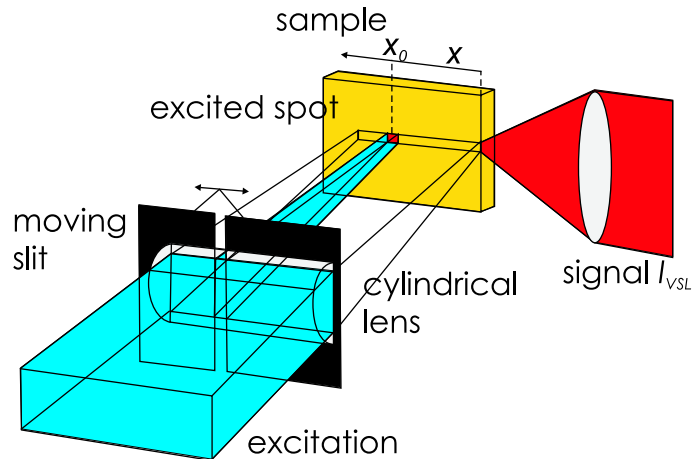
Figure 6.3: *Sketch of the SES experimental setup principle [40] [99].*

The whole experimental setup is in fact identical with the VSL one, except the excited area shape, which in the SES method forms only a small rectangular segment on the samples surface instead of the long stripe. Therefore SES experimental arrangement differs from the VSL setup only in replacing the adjustable screen by an adjustable slit (Fig. 6.3). The excited segment has to be short enough to prevent the StE onset. The excited segment is moved within the virtual VSL "stripe area" by steps of a comparable length with the spot size ($\sim$ tens of μm). The SES detected signal includes the same artifacts and parasitic effects - if any - as the VSL signal, except the StE effect. Ideal SES signal (without the gain-like and parasitic effects) follows the Lambert-Beer law

$$I_{SES}(x,\lambda) = I_{SpE}(\lambda)e^{-\alpha_{tot}(\lambda)x}, \tag{6.4}$$

where $x \in (0,l)$ is the spot position measured from the sample edge, l is the virtual VSL stripe length and $\alpha_{tot} = \alpha_{BB}(\lambda) + K$ denotes the total optical losses (positive band-to-band absorption coefficient $\alpha_{BB}(\lambda)$ and constant optical losses K). The SES signal in the ideal example yields thus the magnitude of the total losses α_{tot}. In a real example the parasitic effects and gain-like artifact has to be included as a general function $\beta(x)$ [40] of the SES spot position in the sample x:

$$
\begin{aligned}
dI_{SES}(x,\lambda) &= \beta(x)(-\alpha_{BB}(\lambda) - K)I_{SES}(x,\lambda)dx + \beta(x)I_{SpE}(\lambda)dx \tag{6.5} \\
dI_{VSL}(x,\lambda) &= \beta(x)(g(\lambda) - K)I_{VSL}(x,\lambda)dx + \beta(x)I_{SpE}(\lambda)dx.
\end{aligned}
$$

Unfortunately a simple extraction of the $\beta(x)$ function from experimental data is hardly possible. Nevertheless, the most common effects as non-constant emission coupling to the detection system (as confocal effect), sample inhomogeneity, sample non-planarity and excitation inhomogeneous profile can be revealed and excluded by comparing of VSL and SES experimental data: if no StE in the sample is present, the SES signal integrated with respect to the segment positions x over the VSL stripe length l should give exactly the same result as the VSL method, i.e. $\int_0^l I_{SES}(x,\lambda)dx \equiv I_{SES}(l,\lambda) = I_{VSL}(l,\lambda)$. On the other hand, if the StE is present, VSL and SES curves differs:

$$\text{stimulated emission} \leftrightarrow I_{VSL}(l,\lambda) > \int_0^l I_{SES}(x,\lambda)dx.$$

This condition can be rewritten using Eq. 6.2 and Eq. 6.4 as

$$I_{SpE}\frac{e^{G(\lambda)l} - 1}{G(\lambda)} > I_{SpE}\frac{1 - e^{-\alpha_{tot}(\lambda)l}}{\alpha_{tot}(\lambda)} \tag{6.6}$$

6.1.5   VSL & SES methods for low gain measurements

To the best of our knowledge, the comparison of the VSL and integrated SES results as we proposed in [99] and [40] and expressed above by Eq. 6.6, represents the only reported method, which enables us to separate the gain-like artifacts from genuine optical gain coefficient, giving the clear evidence of the StE presence. All possible artifacts are present in both SES and VSL result, while the StE contribution occurs only within the VSL results. The simple rule which can help us to distinguish between the gain-like artifacts and the real gain effects is therefore the sign of the difference curve, which follows from Eq. 6.6:

$$I_{VSL}(\lambda, l) - I_{SES}(\lambda, l) = I_{SpE}\left(\frac{e^{G(\lambda)l} - 1}{G(\lambda)} - \frac{1 - e^{-\alpha_{tot}(\lambda)l}}{\alpha_{tot}(\lambda)}\right). \qquad (6.7)$$

If sign of this difference is positive and its value is increasing with increasing excitation intensity, then the real gain is present. The difference spectra can be fitted using Eq. 6.7, if the attenuation coefficient α_{tot} is estimated from attenuation measurements, or from the SES curve. For illustration in Fig. 6.4 we present the comparison of the VSL and integrated SES curves measured in one of our Si-ncs/SiO$_2$ samples. Black line and circles in (a) represent a typical example when no light amplification has been observed (VSL and integrated SES curves are similar) although the curves are exponentially shaped in their initial parts. Contrary to that, (b) (red solid line and circles) represents one of the examples when the StE onset has been observed because of the positive difference between the VSL and integrated SES curves. Relevant experimental set-up will be discussed in section 6.1.7.
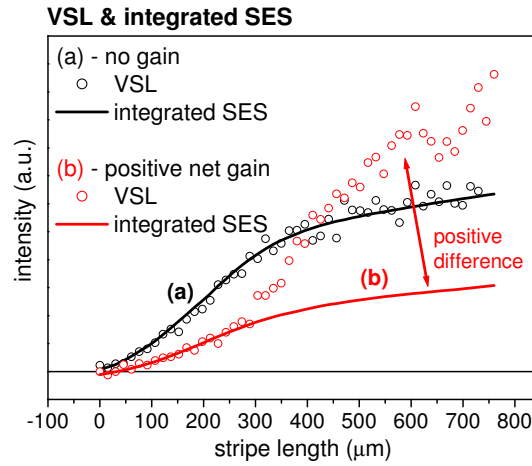
Figure 6.4: *VSL and integrated SES comparison as measured under low (black circles and line) and high (red circles and line) excitation intensity in a typical Si-nc/SiO$_2$ sample. At lower excitation intensity the VSL and integrated SES curves are similar, i.e. no StE is present. At higher excitation intensity, however, the difference between the VSL and integrated SES curves becomes positive, being a sign of the StE onset.*

6.1.6 Gain-like artifacts

Let us now discuss in more details some of the frequently observed artifacts, which can lead to a gain-like distortion of the VSL curves.

6.1.6.1   Pump beam diffraction effects

As discussed above, the homogeneous intensity profile of the beam along the whole excitation stripe length has to be guaranteed using e.g. the excimer type laser excitation with the homogeneous rectangular beam profile. In the VSL setup, however, inevitable diffraction effects on the adjustable screen cause the distortion of the excitation beam, which becomes important especially for short stripe lengths as sketched in Fig. 6.5.
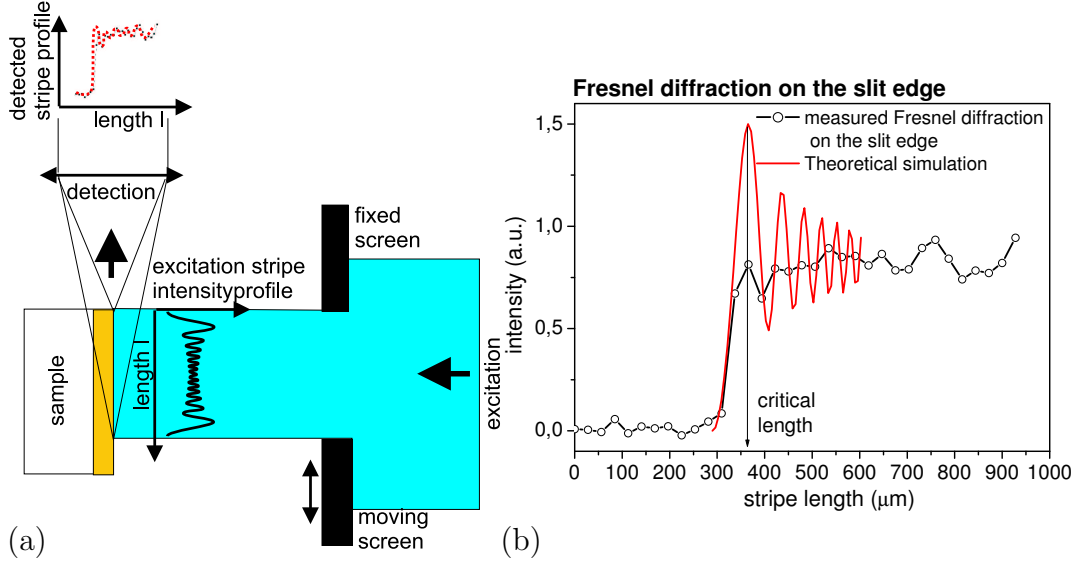
Figure 6.5: *Fresnel diffraction on the screen edge - (a) schematic view and (b) the experimental result.*

The diffraction effect causes a spatially shifted increase of the excitation intensity compared with the one adjusted by the slit position and this can lead to a high artificial gain value below a certain "critical length" $l_{critical}$ (Fig. 6.5). Contrary to the real optical gain coefficient $G(\lambda, I_{exc})$ such artificial gain value is given purely by the diffraction shape intensity profile and does not vary neither with excitation intensity nor with detection wavelength. This effect may be lowered using a double projection of the stripe image. Fresnel diffraction image of the excitation stripe reflection can be measured e.g. in the VSL experimental setup as an excitation intensity scattering (Fig. 6.5(a)) as has been suggested by Dal Negro et al. [64] [103]. Such a pump beam diffraction test includes information about the excitation beam homogeneity. Complex information about the excitation stripe homogeneity, however, is also fully included in the SES signal as we would like to demonstrate in the following pair of measurements in our "standard" Si-ncs/SiO₂ samples (Fig. 6.6(a,b)), where both the pump scattering test and an SES curve were measured to determine the StE onset. The image of the excitation stripe, distorted by diffraction, exhibits a sharp increase in intensity below a certain "critical length" $l_{critical}$. The same effect is revealed also

by the SES measurement. Moreover, the SES data include more complex information about all other present signal distortions. The VSL and integrated SES curves in Fig. 6.6(a) are similar, thus no StE onset is present, even if the VSL curve exhibits an exponential shape for lengths larger than $l_{critical}$, where the modulation due to Fresnel diffraction is already negligible. According to Eq. 6.4 we estimated from the SES curve a high total optical losses of α_{tot}=111 cm^{-1}. Results measured in the second similar sample are shown in Fig. 6.6(b). The sample exhibits much lower optical losses of α_{tot}=10 cm^{-1} an the VSL curves clearly differ for higher excitation intensities from that of integrated SES. Moreover, the difference curves have a positive sign and increase with the excitation intensity, as shown in inset of Fig. 6.6(b). Both the positive sign of the difference curves and their dependence on the excitation intensity are a clear evidence of the StE onset.

6.1.6.2 Confocal effect

The confocal effect occurs in the measurements with longer excitation stripes, necessary for investigation of low-gain materials. The point is that the emitting segments distant from the collecting lens focal point are imaged in a plane in front of the spectrometer input slit, which increases the losses of the signal as seen by the monochromator and detector. This can be optimized using a collecting lens with smaller NA to increase the focus depth into the sample which is, however, hardly compatible with the high NA requirement for efficient signal collection. Another possibility is to use a larger spectrometer slit. The confocal effect can be properly tested using again the SES method, as we demonstrate in Fig. 6.7(a), where the SES signal as a function of the focal point displacement from the sample edge is shown. The focal point of the detection system placed inside the sample leads to an artificial increase of the SES signal with the spot position x next to the focal point, where the collecting efficiency is the highest. In Fig. 6.7(b), the comparison of the VSL and integrated SES curves, together with the measured SES curve are shown. The gain-like distortion of the VSL curve below the $l_{critical}$, where the VSL and integrated SES curve match each other, is caused mainly by the confocal effect, and has been fitted according to Eq. 6.2 by an artificial gain value of nearly 54 cm^{-1}.

6.1.7 VSL & SES experimental setup

The VSL stripe and SES spot were formed via focusing the XeCl excimer laser beam (308 nm, pulse duration ∼20 ns, repetition rate 10 Hz) and using the adjustable screen (slit) as sketched in Figs. 6.1, 6.3 and 6.8. This type of excitation source has been chosen due to several important reasons - due to its homogeneous rectangular

(a)

(b)
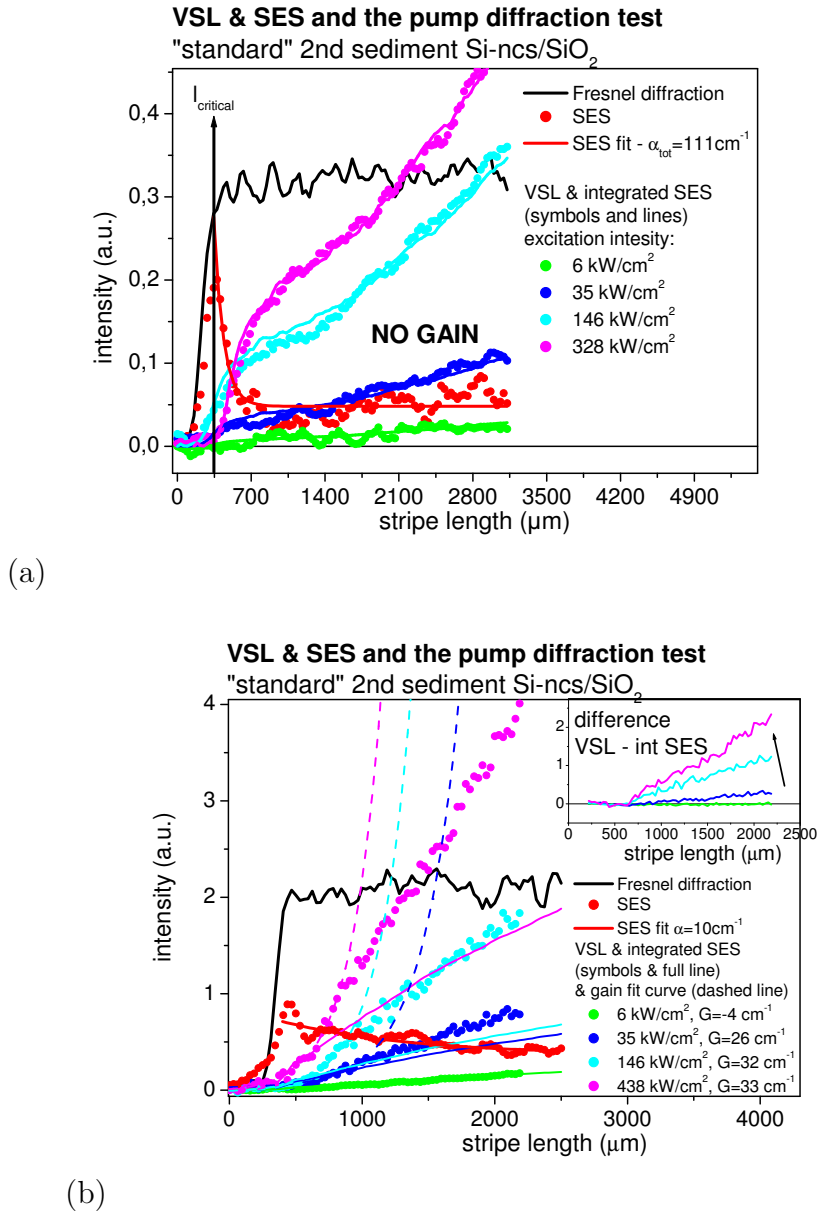
Figure 6.6: *VSL, SES and pump beam diffraction test measured in two different "standard" 2nd sediment Si-nc/SiO₂ samples (a) #04050605 and (b) #04050603. No gain is present in (a), because VSL and integrated SES curves are similar, although an exponential shape of VSL was observed. In (b) VSL and integrated SES differ significantly and this difference (inset in (b)) increases with excitation intensity, i.e. positive net gain is present. Signal was detected at the emission peak maxima 600 nm using a PMT and a box car integrator with the gate width of ∼150 μs, coincident with the excitation pulse. The pump scattered signal towards the detection system was detected at the excitation wavelength of 308 nm.*

beam profile and pulsed character and because of the strong response of our investigated material in this spectral region (high absorption, strong PL emission). The beam was focused by a cylindrical lens of focal length f=50 mm, whose focal point was located nearby the movable screen (slit) position to perform a clean cut of the

(a)

(b)
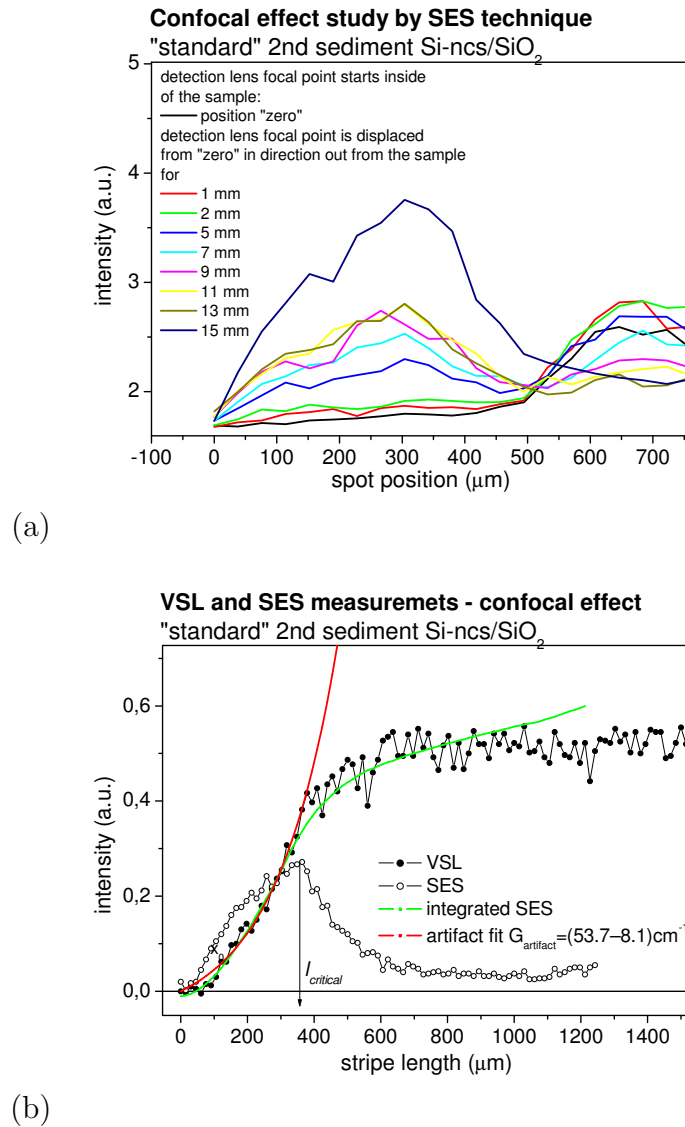
Figure 6.7: *(a) Confocal effect as measured by the SES method (sample's position is fixed with respect to the excitation, detection lens is shifted to displace the focal point of the collecting lens from the sample edge), (b) SES and integrated SES in comparison with the VSL curve, the artifact gain estimation.*

excitation stripe.

The projection of the stripe image from the focal point of the cylindrical lens onto the sample surface was done using the double projection system with magnitude M=0.3 (two spherical quartz lenses with focal lengths f=300 mm and 100 mm, Fig. 6.8) in order to minimize the diffraction effects on the movable screen (slit) as discussed above. The VSL/SES signal was detected in the direction perpendicular to the excitation beam using another double projection system imaging the emission point from the sample edge to the spectrometer slit. The collection lens of a focal length f=55 mm and a numerical aperture $NA \approx 0.34$ has been chosen to be a good
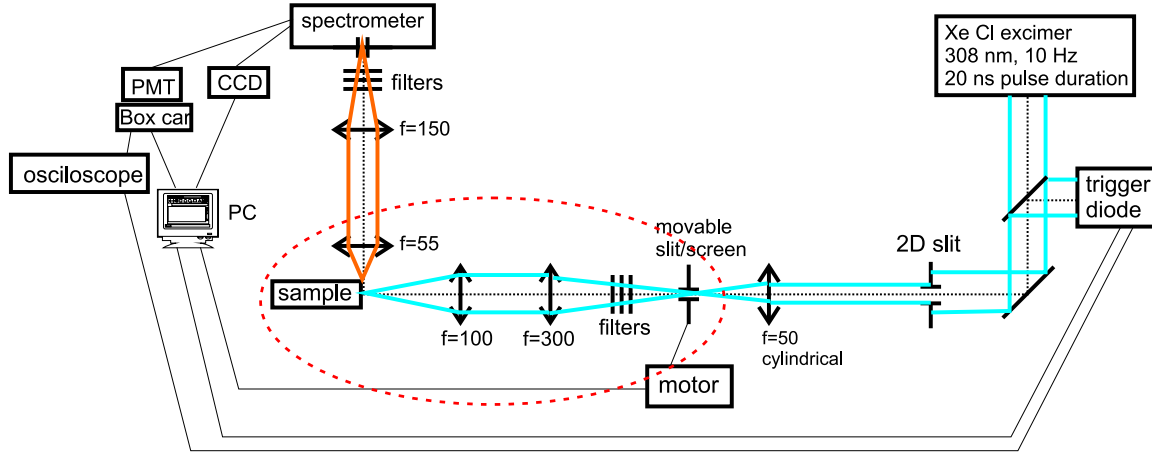
Figure 6.8: *VSL and SES experimental setup. The movable screen/slit is shifted using a servo-motor connected to PC.*

compromise between the efficient light collection requiring a high NA on one side and relatively low NA required to reduce the confocal effect on the other side. The relay lens of f=150 mm and $NA \approx 0.13$ has been chosen to fit the spectrometer aperture ($NA \approx 0.12$). The signal was detected using a PMT with a boxcar integrator system or using the nitrogen cooled CCD camera. All measurements were done at room temperature and presented spectra have been corrected for the spectral response of the detection system using a calibrated black body radiation source (Oriel tungsten halogen lamp 45 W).

6.1.7.1   VSL stripe and SES spot size, excitation intensity

The VSL stripe and SES spot size were measured using the linear Reticon camera placed in the sample position. To reduce the high excitation beam intensity in the focal point, many attenuating filters had to be used, which, however, distorts the stripe and spot shape. These measurements therefore could not be performed with a high accuracy (the estimated error can be as high as ∼20 μm). Average SES spot and VSL stripe width was estimated from a set of measurements shown in Fig. 6.9(b) to be around 90±20 μm. The measured stripe/spot length image on sample position was found to be ∼2.63-3.2 times smaller than the stripe/spot image nearby the movable screen/slit. This number is in good agreement with the theoretically calculated magnification of the double projection system of $M = 0.3$ between the screen and the sample (see Fig. 6.8).

Concerning the excitation intensity, the maximal pump fluency used in our VSL and SES measurements was estimated by a calibrated Joule-meter to be ∼1.6 mJ per pulse per stripe area of ∼0.02 cm^2 (100 μm x 2 cm). The pulse duration was nearly 20 ns, which gives the maximum excitation power density value of 4.0 MW/cm^2.
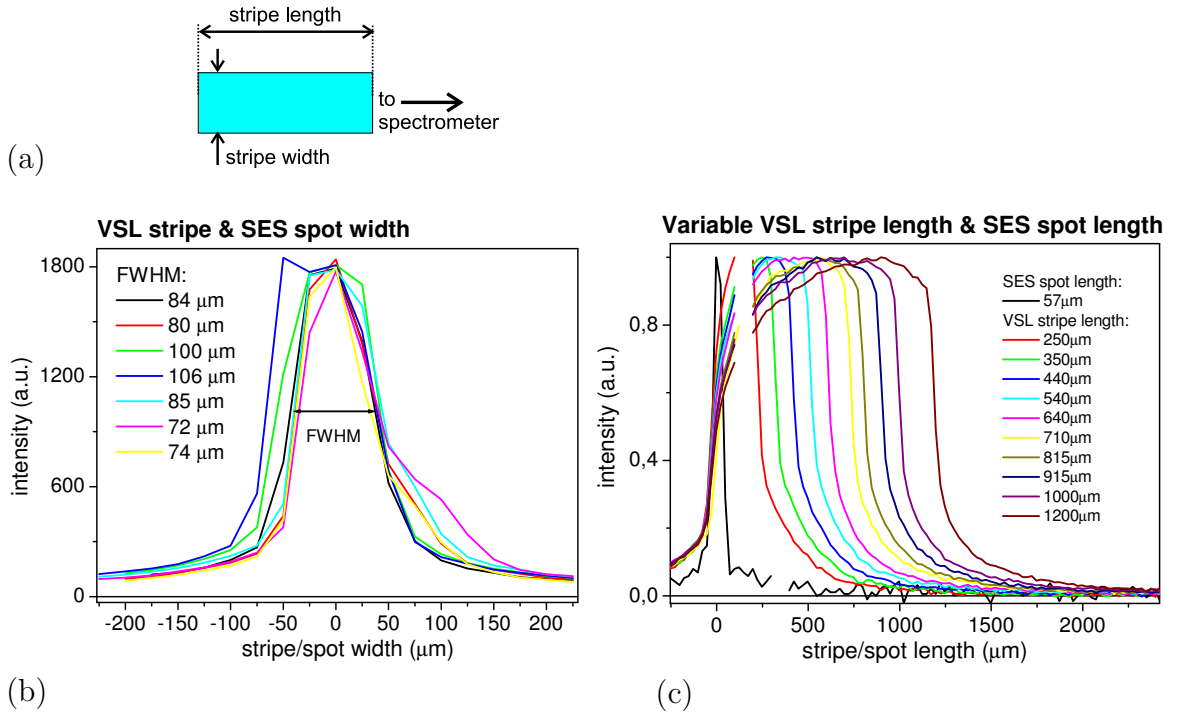
Figure 6.9: *(a) The excitation stripe/spot size estimation sketch. (b) Set of measurements of the VSL stripe and SES spot width. (c) SES spot and variable VSL stripe length. The stripe/spot image was measured at the sample position using linear Reticon camera.*

Let us now estimate the average number of excited e-h pairs per Si-ncs $\langle N \rangle$ in our typical Si-ncs/SiO$_2$ sample, which is an important parameter for the Auger mechanism onset and StE onset competition. The number of excitation photons of energy 4.1 eV (308 nm) within the pulse duration and impinging on the above area amounts $\sim$2x10^{15}. The number of Si-ncs of diameter of 3 nm and a volume fraction (in the 50 μm thick layer) of 17 vol.% ($\sim$10^{19} Si-ncs/cm^3) in such excitation stripe area would be similarly around 10^{15}. If we assume that each single photon is absorbed by a single Si-ncs, the average number of excited e-h pairs per Si-ncs $\langle N \rangle$ would be equal or below 2. Following the discussion about the Auger mechanism and four-level system formation in oxidized Si-nc in sections 2.2.2 and 2.2.3, such excitation fluency appears to be ideal for StE onset in our Si-ncs/SiO$_2$ samples. Moreover, only a part of the total amount of the excitation photons will be absorbed by the Si-ncs rich layer of finite width $\sim$50 μm (e.g. if α_{tot}=50 cm^{-1}, just $(1 - e^{-\alpha_{tot}d}) \sim 0.22$, i.e. 22% of excitation photons will be absorbed). Then, the average number of the excited e-h pairs per single Si-nc $\langle N \rangle$ can fall below 1, which is still sufficient for achieving population inversion and at the same time sufficiently low to prevent from excessive Auger quenching.

6.2　Experimental results in solutions of organic dyes in methanol

The experimental VSL and SES setup was first tested using solutions of organic dyes in methanol (MeOH) in which StE and lasing has already been well known for a long time. They are easily achievable which makes them excellent reference material for optical gain measurement. The StE onset critically depends on the dye concentration, sample homogeneity and type of solvent which has to be precisely adjusted. We have measured optical gain coefficient of Rhodamine 6G, Coumarin 460 and Coumarin 450 dissolved in MeOH. Solutions were placed into spectroscopic quartz cuvettes and measured by the standard VSL/SES methods.

First, we measured optical gain in solution of Rhodamine 6G/MeOH. PL spectrum (i.e. emission spectrum excited using a small spot) and VSL spectra (i.e. emission spectrum excited using the VSL stripe of variable length and/or intensity) as a function of the excitation intensity are shown in Fig. 6.10. The PL spectrum is peaked at ∼580 nm with a FWHM of ∼40 nm. The VSL spectra peak maximum shifts with increasing excitation intensity from ∼580 nm down to ∼570 nm and their FWHM narrows from ∼40 nm down to ∼20 nm (inset in Fig. 6.10). The peak maximum shift can be assigned to the absorption tail saturation and to the onset of positive net gain, which is placed on the short-wavelength spectral side of the emission spectrum. The peak narrowing is a general feature of ASE. Moreover, the output intensity as a function of the excitation intensity (output-input intensity dependence) exhibits in a log-log scale a threshold behavior characteristic for the StE onset (inset in Fig. 6.10).

The VSL and SES results, measured at the peak maximum at 580 nm are shown in Fig. 6.11. The SES signal is nearly constant, i.e. the sample is optically transparent and exhibits negligible optical losses. VSL curves were compared with the integrated SES curve and fitted using Eq. 6.2 (net gain coefficient G as a fit parameter). At the lowest excitation intensity (2 kW/cm²) both the VSL curve and the integrated SES curve are similar and the net gain coefficient is negative G = -4 cm^{-1}, i.e. no StE is present at such low excitation regime. With increasing excitation intensity the difference between the VSL and integrated SES curves increases and the value of the net gain increases from G=167 cm^{-1} at 54 kW/cm² up to G=203 cm^{-1} at the highest excitation intensity of 335 kW/cm². The saturation length, i.e. the length at which the VSL curve starts to saturate with respect to the exponential law Eq. 6.2, shortens for higher net gain values, which is another clear proof of the light amplification origin of the observed features. Moreover, a clear emission directionality was observed by a naked eye. All these results are transparent evidence of the StE onset and light
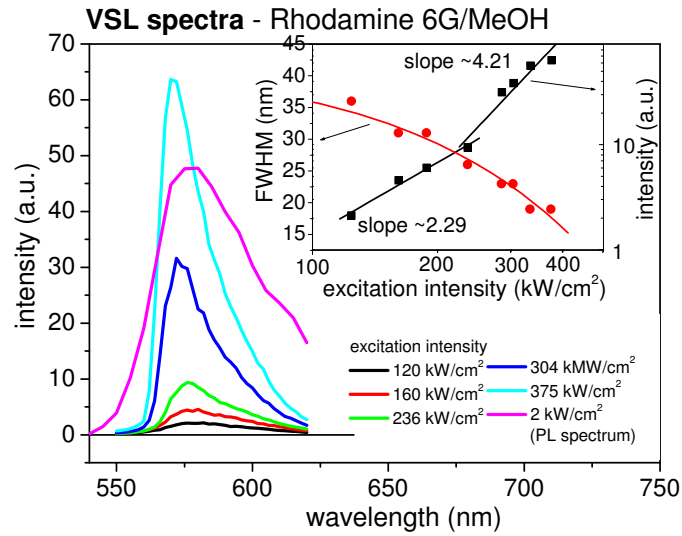
Figure 6.10: *Normalized PL spectrum and VSL spectra measured in Rhodamine 6G/MeOH with a fixed stripe length of 1 cm and a variable excitation intensity. The PL spectrum (orange curve) was excited using the excitation spot of intensity $\sim$2 kW/cm^2, the VSL spectra were excited using a stripe of a fixed length of 1 cm and pump intensity varying from $\sim$100 kW/cm^2 up to 400 kW/cm^2. Signal was detected using a PMT with boxcar integrator with a gate delay of 100 ns and a width of 120 ns. Inset: spectral narrowing and the output intensity as a function of the excitation intensity. Output-input intensity dependence in the log-log scale exhibit a threshold and a super-linear slope, which together with the spectral narrowing with increasing excitation intensity is a clear evidence of the StE onset.*

amplification in the reference Rhodamine 6G/MeOH sample.

Similar results were measured in another organic dye solution - Coumarin 460/MeOH, as shown in Fig. 6.12. VSL spectra were excited using the stripe of a fixed length and a variable intensity. Spectra are peaked at $\sim$461 nm and their FWHM significantly narrows from $\sim$40 nm down to $\sim$5 nm with increasing excitation intensity. Moreover, the peak intensity dependence on the excitation intensity in a log-log scale (inset in Fig. 6.12) exhibits again the threshold behavior and a super-linear slope above the threshold intensity, both properties are characteristic for the onset of StE.

In the case of such high optical quality samples with high net gain coefficient, a special care has to be taken of the sample geometry, since the cuvette containing the organic dye solution can form a simple resonator (rectangular cuvette with polished sides). The multiple reflections in such a resonator are not consistent with the single-pass amplification as described by the 1D VSL model. In all above presented
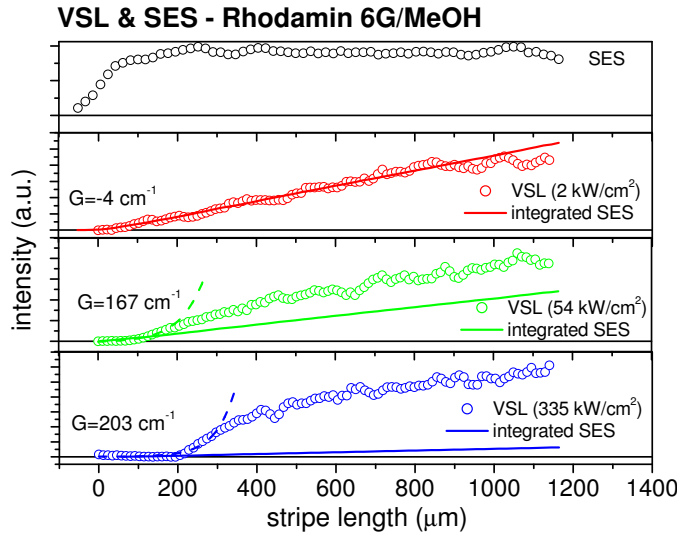
Figure 6.11: *VSL and SES measurements in a Rhodamine 6G/MeOH sample detected at the emission peak maxima at 580 nm. Signal was detected using a PMT with a boxcar integrator using a gate delay of 100 ns and a width of 120 ns. The VSL and integrated SES curves are similar for the lowest excitation and their difference significantly increases with increasing excitation intensity. The net gain coefficient, fitted using Eq. 6.2, increases from -4 cm⁻¹ for the lowest excitation intensity up to ∼203 cm⁻¹ for the highest one.*

measurements, the cuvettes were tilted with respect to the excitation stripe axis to prevent the lasing onset between the polished cuvette faces. In Fig. 6.13, on the other hand, we present the VSL spectra measured in a Coumarin 450/MeOH sample with the cuvette faces perpendicular to the excited stripe direction, forming a resonator of length ∼1 cm. The perpendicular cuvette faces, representing the resonator mirrors, were made from optically polished quartz glass with reflectivity around ∼4 % in the visible spectral region. The VSL spectra, excited with a stripe of a fixed length and a variable intensity, exhibit a random lasing mode structure. The output-input intensity dependence at one of the mode peaks maxima (at 449 nm) is plotted in a log-log scale in inset of Fig. 6.13(a) and exhibit a super-linear slope of ∼2.51, characteristic for the StE onset. Fig. 6.13(b) shows the VSL spectra measured in the same sample with a fixed excitation intensity and a variable stripe length. The output intensity as a function of the excitation stripe length (VSL curve), extracted from Fig. 6.13(b) at the emission wavelength of 449 nm, is shown in the inset. The net gain value of ∼26±2 cm⁻¹ was estimated using Eq. 6.2, however, we would like to stress here, that it cannot be simply identified with the net gain coefficient G, because the multiple passage of the emission within the cuvette is not consistent with the 1D model validity requirements.

As a conclusion: we clearly observed a single-passage positive net gain of G=203 cm⁻¹
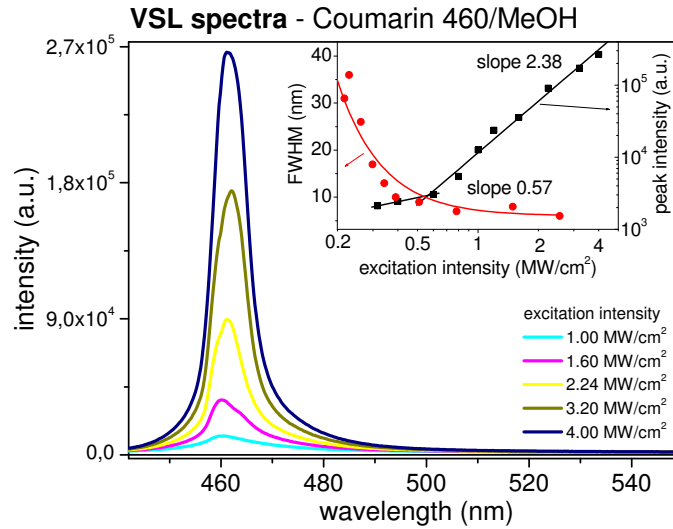
Figure 6.12: *VSL spectra of Coumarin 460/MeOH excited by a stripe of a fixed length of 380 µm and a variable intensity of 0.32-4.00 MW/cm^2. The spectra were detected at room temperature using a nitrogen cooled CCD camera (-100°C) and were integrated over 300 ms. Inset: spectral narrowing and output intensity as a function of the excitation intensity. Output-input dependence exhibit a threshold behavior and super-linear slope in a log-log scale, which together with the spectral narrowing is a clear evidence of the StE onset.*

in the reference organic dye solution in methanol. The attenuation of emitted spontaneous and stimulated emission, passing through the active material, was so low, that its magnitude was under resolution of the SES method. The lasing and a random lasing mode structure in the emission spectra were observed, when the active reference sample was placed into a simple resonator, formed by the optically polished faces of the cuvette. This type of low quality resonator (low reflectivity of the quartz cuvette faces), placed around such a high volume of an active material (cavity length of 1 cm), is possible to use only in such samples with high optical quality.

6.3 Experimental results in Si-nc/SiO$_2$ samples

All the samples were carefully prepared and tested with respect to the optical gain measurements and were chosen according to their emission properties, optical quality and optimum Si-ncs content in the SiO$_2$ matrix (10-20 vol.%). Optical quality of the samples was the highest achievable one in the framework of our recent preparative techniques, as described in Chapter 3. The PL emission spectra of the investigated Si-ncs samples were significantly blue-shifted to 580-670 nm (see Fig. 5.4) as compared with Si-ncs standardly prepared by other preparation methods as PECVD or Si$^+$ ion implantation [16] [21] [63]. Both sufficiently high Si-ncs content in SiO$_2$ matrix at suf-
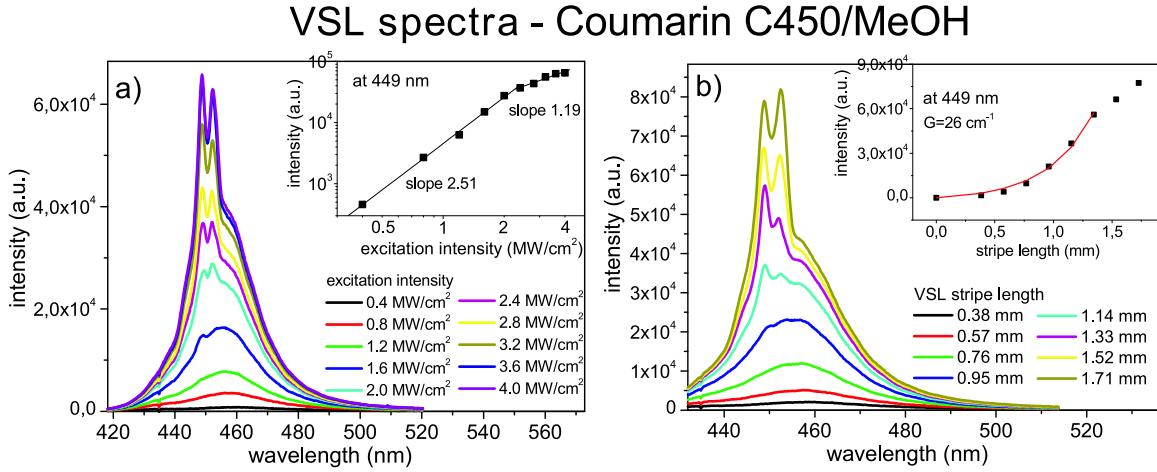
Figure 6.13: *VSL spectra of a Coumarin 450/MeOH sample as a function of (a) the excitation intensity (with a fixed stripe length of 1.5 mm) and (b) the stripe length (with a fixed excitation intensity of 4.0 MW/cm^2). The signal was excited and measured under the same experimental conditions as the previous sample in Fig. 6.12. The random lasing modes appears due to the external cavity formed by the cuvette polished faces. Insets: (a) the output-input intensity dependence in a log-log scale at 449 nm; (b) VSL curve detected at 449 nm.*

ficiently high optical quality and the blue-shifted emission make our samples unique and suitable for the StE onset observation. As we have already seen in chapter 5.2, the time-resolved PL emission spectra exhibit very complex time behavior. Observed "ultrafast" subpicosecond PL component was interpreted in terms of the ultrafast trapping of the free confined carriers on the surface states, quenching the emission from confined "free" exciton recombination and avoiding core Auger recombination, which both decay in ns scale. Surface trapping leads to a spatial separation of the carriers, which recombine subsequently in µs time scale, independently of the excitation pulse duration. The peak wavelength of the "fast" ∼ns PL emission component is blue-shifted to 450-580 nm with respect to the "slow" one, which is peaked around 580-630 nm. Due to that, we can expect two main, significantly different regions for the optical gain measurements - the "fast" blue-shifted emission within first few tens of ns after excitation and the "slow" orange emission band in the µs range. In the following we will investigate both the "fast" and the "slow" gain components applying the time-resolved VSL and SES measurements, together with the steady-state optical gain using the time-integrated VSL spectra. Most of the interesting results were measured on the first generation of the samples - the sedimented "standard" Si-ncs/SiO$_2$. "Yellow" and "white" Si-ncs/SiO$_2$ samples represent the second samples generation, which has been optimized later - along with building the Distributed Feedback Laser (DFL) setup, described in the following chapter 7. This is the main reason why the "yellow" and "white" samples were less investigated during this part of the thesis.

In section 6.3.1 we will present the typical results, achieved from a "standard" 2nd sediment sample and in section 6.3.2 we show some results on a "standard" 4th sediment. Other types of samples - "yellow" and "white" - will be shortly discussed in the appendix sections 9.2.1 and 9.2.2.

6.3.1   "Standard" 2nd sediment Si-ncs/SiO$_2$

Let us now present the most representative VSL and SES measurement results in the "slow" emission component of "standard" 2nd sediment Si-ncs/SiO$_2$ samples, where a strong signal has been achieved even at relatively low excitation pump fluency.

6.3.1.1   "Slow" emission component

In Fig. 6.14 we show a VSL spectrum of a "standard" 2nd sediment Si-ncs/SiO$_2$ sample #021018. The VSL spectrum has a broad FWHM of ∼100 nm and is peaked around 600-610 nm.
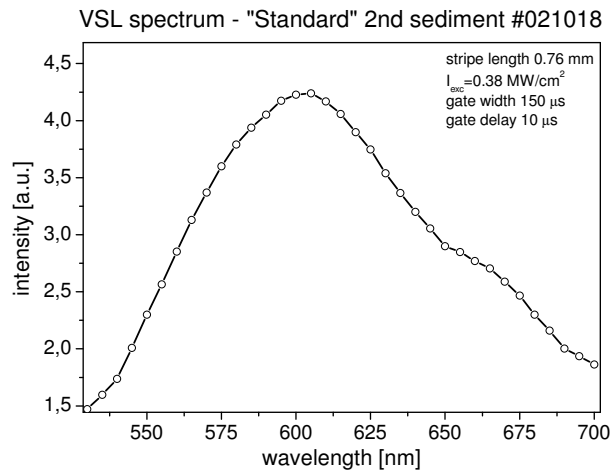
Figure 6.14: *VSL spectrum of the "slow" emission component of a "standard" 2nd sediment Si-nc/SiO$_2$ sample #021018, excited with a stripe of length of 0.76 mm and intensity 0.38 MW/cm^2. The signal was detected using a boxcar integrator and a PMT with the gate width of 150 μs and gate delay of 10 μs.*

The VSL and SES measurements, measured in the same sample #021018, are presented in Figs. 6.15, 6.16 and 6.17. The signal was detected at the peak maximum of ∼610 nm. Comparison of the VSL (circles, Fig. 6.15) and integrated SES results (lines, Fig. 6.15) shows increasing gap between the both curves with increasing excitation intensity and the stripe length, while for the lowest excitation intensity the both curves are identical. As we have discussed before (Eq. 6.6), the increasing gap

between the VSL and integrated SES curves is a clear evidence for the StE occurrence. Below a critical length, estimated here to be $\sim$200 μm, we have fitted for illustration an artificial gain value of $G_{art}\sim$46 cm^{-1}, which originates possibly in interplay between the output angle of StE and the numerical aperture of the detection optics. The artifact origin can be discovered directly from comparison of the VSL and integrated SES curves, which are in this region identical, i.e. no StE present. Moreover, the value of the artificial gain G_{art} is insensitive of the excitation intensity, which is an additional proof of its artifact origin. The output intensity as a function of the excitation intensity is plotted in a log-log scale in inset of Fig. 6.15. It shows a sub-linear behavior for a short excitation stripe length of l=200 μm (slope of $\sim$0.95), related probably to the saturated or completely missing Auger recombination and a super-linear behavior (slope of $\sim$1.6 - ASE) for the stripe length of l=400 μm. This is another evidence for the StE observation.
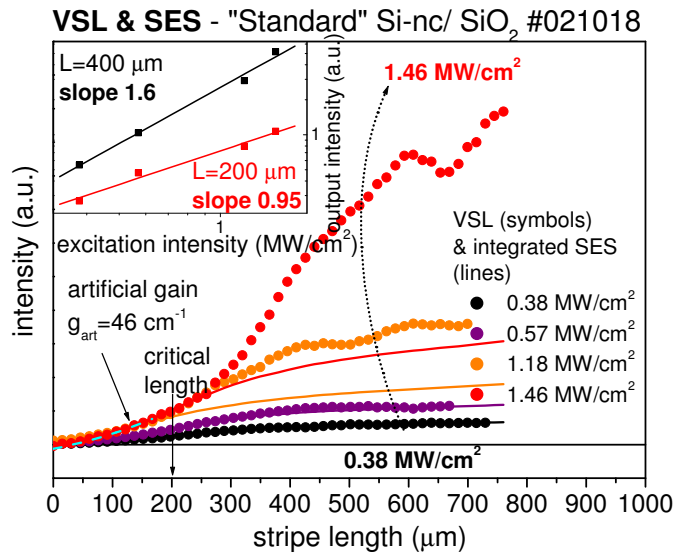
Figure 6.15: *"Slow" component VSL and SES curves comparison in a "standard" 2nd sediment Si-nc/SiO$_2$ sample for different excitation intensities. Signal was detected at the peak maxima of $\sim$610 nm with the gate width of 150 μs and gate delay of 10 μs. Inset: output intensity as a function of the excitation intensity for two stripe lengths of 200 μm and 400 μm. The difference between VSL and integrated SES curves increases with excitation intensity, which is a clear evidence of the StE onset. Moreover, a super-linear slope of the output-input intensity dependence in a log-log scale - sign of StE onset - was observed for the stripe length of 400 μm.*

To enhance the visibility of the switch of the VSL curve shape from the concave to the convex one with increase of the excitation intensity, we plotted a detail of Fig. 6.15 in Fig. 6.16. The switch of the shape is caused by the change of the net gain coefficient from negative to positive value, very much like in Ref. [22]. The shape switch can be

taken as another proof of the StE onset, while the excitation insensitive artificial gain value G_{art} does not exhibit such behavior. Yet another proof of the StE onset: the net gain spectrum $G(\lambda)$ (inset in Fig. 6.16), determined using Eq. 6.3 for l=300 μm, is negative for the lowest excitation intensity and positive for the highest excitation intensity. The gain spectrum is peaked at ∼600 nm with FWHM of ∼100 nm, likewise the VSL spectrum plotted in Fig. 6.14.
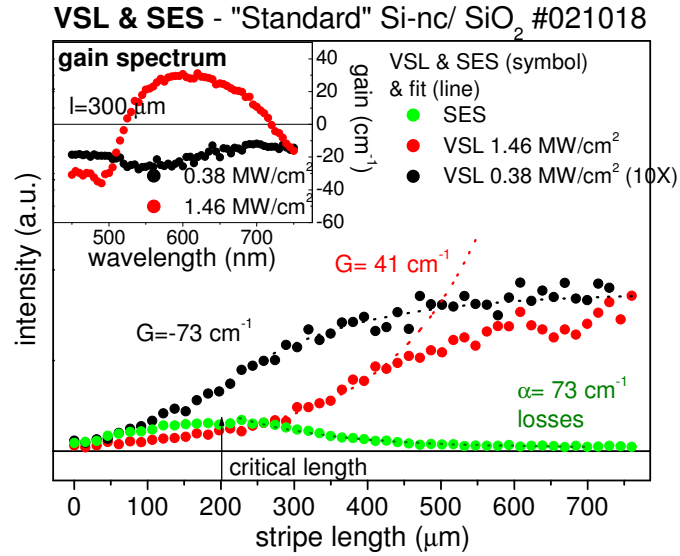
Figure 6.16: *Detail from Fig. 6.15: "Slow" VSL and SES curves in a "standard" 2nd sediment Si-nc/SiO$_2$ sample for the lowest and highest excitation intensity. Inset: gain spectra at the lowest and at the highest excitation intensity. Clear switch of the VSL curves shape is caused by change of the net gain sign from negative to positive, which is a clear evidence of the StE onset. Moreover, a positive net gain spectrum was evaluated using Eq. 6.3 at higher excitation intensity.*

To complete this detailed optical gain investigation, we plotted the difference between the VSL and integrated SES curves in Fig. 6.17. The difference curve is zero below the critical length, where only the above artificial gain has been observed, and increases with increasing excitation intensity above this length (StE onset). The net gain coefficient was fitted from the difference curves according to Eq. 6.7, taking into account the value of losses α =73 cm^{-1}, fitted from the SES curve in Fig. 6.15. All the presented results represent a consistent evidence for the presence of single-pass light amplification.

We note that there exists an uppermost excitation intensity limit (sample and place dependent, 1-3 MW/cm^2) above which the sample starts to burn. (Data distorted by the sample permanent damage under very high excitation are not shown.) As an example we can take the following results in Fig. 6.18, measured in the same
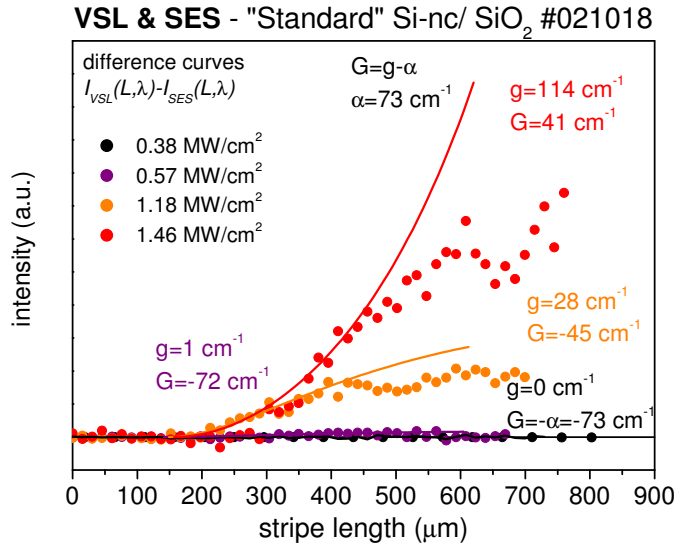
Figure 6.17: *Difference between the VSL and integrated SES curves (data taken from Fig. 6.15) in a "standard" 2nd sediment Si-nc/SiO$_2$ sample, fitted using Eq. 6.7. The difference curve increases with excitation intensity as a clear evidence of StE presence.*

sample #021018 on another place. The difference of VSL and integrated SES curves is positive and increases with the excitation intensity. Above a certain excitation intensity level of ~1 MW/cm^2, however, the VSL curves significantly drops down and the difference curves become zero, probably due to the permanent sample damage.

Spectral narrowing with increasing excitation intensity is one of important features of the ASE spectra. This effect is, however, very low in such a wide size distribution ensemble of Si-ncs, where the inhomogeneous broadening dominates over the spectral shape. Here we would like to show the most interesting result, observed in another place of the "standard" 2nd sediment Si-ncs/SiO$_2$ sample #021018 (Fig. 6.19). VSL spectra were measured with a fixed stripe length and under a variable excitation intensity. The spectral width (FWHM) as a function of the excitation intensity is shown in inset of Fig. 6.19. FWHM decreases from ~200 nm for the lowest excitation intensity down to ~120 nm for the highest one, which is very close to the width of the gain spectrum itself, as obesrved in Fig. 6.16. As we discussed above, the gain, emission and absorption spectra are inhomogeneously broadened due to the finite Si-ncs size distribution width. The spectral narrowing of the inhomogeneously broadened spectrum can be calculated according to [104] from the Lindford formula

$$\frac{\Delta\nu_{ASE}}{\Delta\nu_0} = \left(\frac{e^{G(\lambda)l}-1}{e^{G(\lambda)l}G(\lambda)l}\right)^{\frac{1}{2}}, \tag{6.8}$$
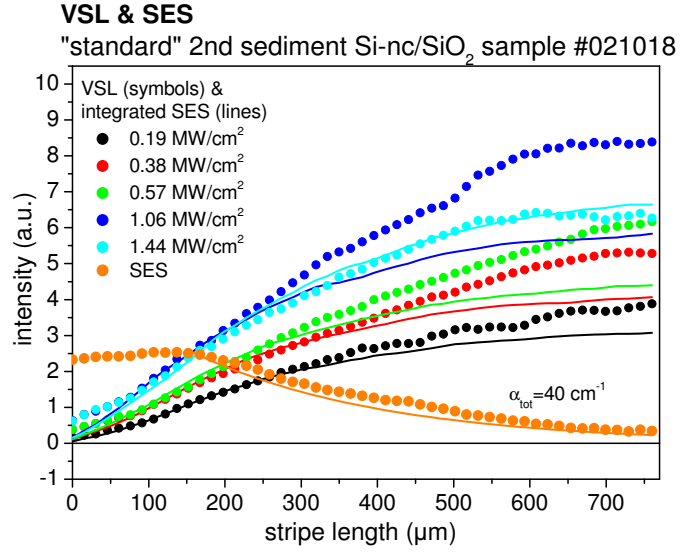
(a)
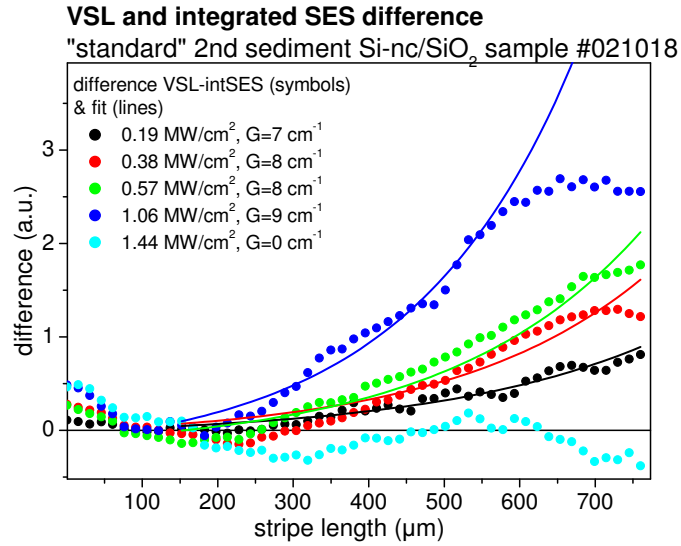
(b)

Figure 6.18: *(a) "Slow" component VSL and SES curves measured in a "standard" Si-nc/sol-gel sample #021018. The signal was detected with the gate width of 150 μs and the gate delay of 10 μs. (b) VSL and integrated SES curves difference for different excitation intensities, fitted according to Eq. 6.7. The increasing difference between VSL and integrated SES curves is a clear evidence of the StE presence.*

where $\Delta\nu_{ASE}$ is the Gaussian profile FWHM of the ASE spectrum and $\Delta\nu_0$ that of the spontaneous emission profile, $G(\lambda)$ is the net gain coefficient and l is the excitation stripe length. If we consider the linewidth narrowing from 200 nm down to 120 nm at the peak gain, we get the narrowing of ∼0.6, giving for the stripe length of ∼1.3 mm the net gain value of $G \doteq 20$ cm^{-1}, consistent with that displayed in Fig. 6.16.
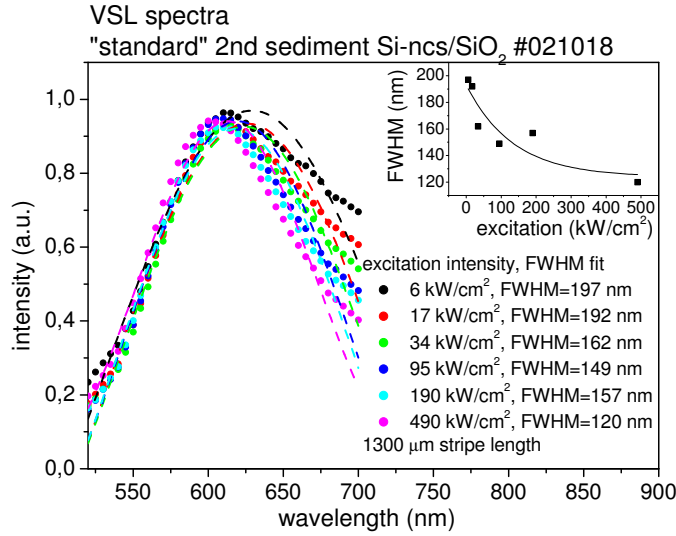
Figure 6.19: *"Slow" component VSL spectra as a function of the excitation intensity ($\sim$6 kW/cm^2 up to $\sim$490 kW/cm^2) measured in a "standard" 2nd sediment Si-ncs/SiO$_2$ sample #021018 with fixed excitation stripe length of 1.3 mm. Detection conditions remain the same as in Fig. 6.15. The spectral width (FWHM) decreases with increasing excitation intensity as shown in the inset, which is a sign of StE onset. The spectral narrowing corresponds according to Eq. 6.8 to the net gain coefficient of $\sim$20 cm^{-1}.*

A similar gain spectrum can be also determined from the VSL curves, measured in the same "standard" 2nd sediment sample #021018 at different emission wavelengths, as displayed in Fig. 6.20. The VSL curves were fitted according to the Eq. 6.2 above the critical length, estimated here to be $\sim$500 μm. The estimated net gain values are plotted in inset of Fig. 6.20 and form a gain spectrum. It is important to note here that the net gain coefficient $G(\lambda)$ spectral dependence is one of the important features, helping us to distinguish between the optical gain effects and artifacts, which are supposed to be spectrally insensitive. Moreover, the gain spectrum estimated from the VSL curves in Fig. 6.20 is quite similar to those presented in Fig. 6.16, where the gain spectra were found using the standard comparative method based on Eq. 6.3.

6.3.1.2 "Fast" emission component

The results concerning the "slow" component may seem to be surprising, since the fast Auger mechanism can be supposed to prevent StE onset in the μs time scale. In our samples, however, the reported ultrafast subpicosecond formation of the self-trapped excitons can significantly lower or completely remove this nonradiative recombination channel and facilitate the StE even for longer times in μs scale. To
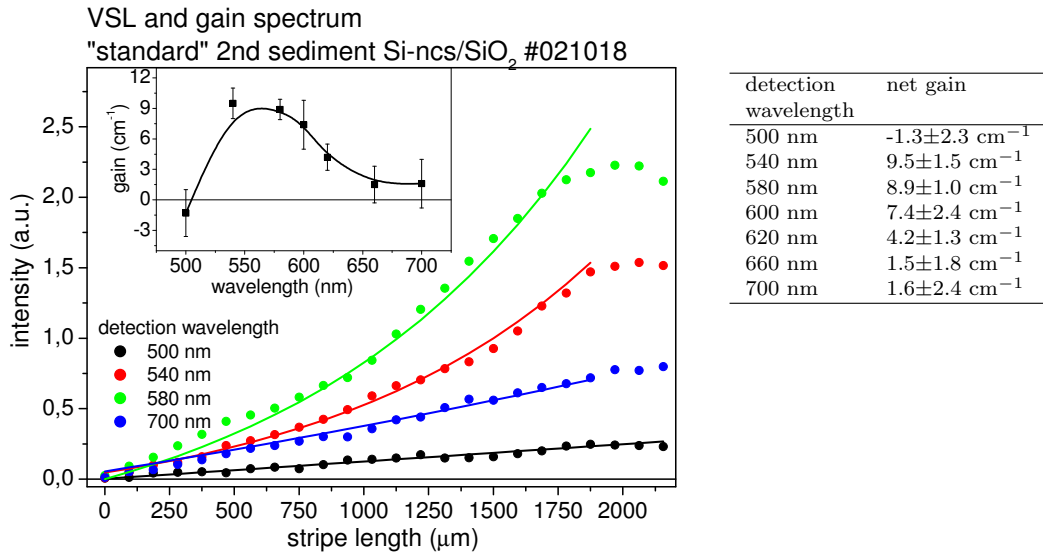
Figure 6.20: *"Slow" component VSL measurement in a "standard" 2nd sediment Si-ncs/SiO₂ sample #021018, detected at different emission wavelengths (a gate delay of 10 μs, a gate width of 150 μs). Excitation intensity was adjusted to ∼500 kW/cm². Extracted net gain values form a gain spectrum plotted in inset.*

understand better the time behavior of the optical gain, we present the comparison of the "fast" and "slow" components of the VSL spectra of a "standard" 2nd sediment Si-ncs/SiO₂ sample #04092001 in Fig. 6.21.

This sample (is prepared in the similar way as the previously studied sample #021018 and contain the same amount of "standard" 2nd sediment Si-ncs. The VSL and SES "slow" and "fast" component curves (symbols), measured under a fixed pump intensity at different emission wavelengths are shown in Figs. 6.22(a) and 6.23(a). The SES curves for the "fast" and "slow" components were carefully measured at the signal peak maxima - i.e. at 380 nm for the "fast" decay component and at 610 nm for the "slow" decay component. VSL curves are compared with integrated SES curves (solid lines) and fitted above $l_{critical}$ according to Eq. 6.2 (dotted lines). The estimated net gain values are indicated in tables and form gain spectra, shown in Figs. 6.22(b) and 6.23(b). The "fast" gain spectrum is slightly blue-shifted with respect to the "slow" one and exhibits higher gain values.

Therefore, relatively small positive net gain has been discovered in a "fast" emission component of our Si-ncs/SiO₂ samples at short wavelengths around 570 nm. To the best of our knowledge, this is the first observation of this kind but ought to be considered with caution, since origin of the discovered gain is not clear (SiO₂ impurity or SiO₂ defects or tiny Si-ncs ?). Since the following optical DFL experiments will
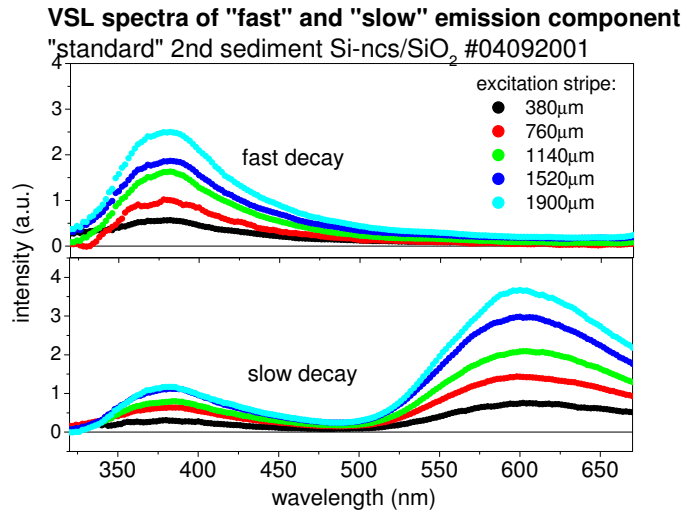
Figure 6.21: *VSL spectra of "fast" and "slow" emission components in a "standard" 2nd sediment Si-ncs/SiO$_2$ sample #04092001. Signal was excited using the stripe of a variable length from ~0.4 mm up to ~2 mm and a fixed pump intensity of ~1.2 MW/cm^2. The signal was detected at room temperature using a PMT and a boxcar integrator ("fast" component: no gate delay, gate width of ~50 ns; "slow" component: gate delay of ~10 μs, gate width of ~4 μs).*

be realized in time-integrated regime (chapter 7), our main interest will be focused now mainly on the "slow" emission component and on the time-integrated spectra. The "fast" component optical gain is planned to be investigated in more details in the future.

6.3.1.3   Time-integrated measurements

Up to now we discussed the time-resolved VSL and SES measurements. Let us now present some VSL spectra integrated in time, as measured in another "standard" 2nd sediment sample #04050607. This sample was prepared in the same way as the previous two samples #021018 and #04092001 but contain a half amount of the "standard" 2nd sediment Si-ncs powder, compared to #021018 and #04092001. Lower Si-ncs content leads to better optical quality, because the amount of the light scattering Si-ncs clumps is lower. Longer stripe lengths have to be used, on the other hand, to get significant gain effects. Fig. 6.24(a-c) displays the VSL spectra, measured with three different fixed stripe lengths and under a variable excitation intensity. For each stripe length we estimated the output-input intensity dependence at the emission peak maxima at 630 nm, plotted in insets of Figs. 6.24(a-c). The linear slope in the log-log scale, indicating spontaneous emission with missing Auger mechanism to a large extent, was measured for the two shortest excitation stripe lengths of 380 μm

"fast" decay component VSL
"standard" 2nd sediment Si-ncs/SiO$_2$ #04092001

(a)

(b)

detection wavelength	net gain G
380 nm	-0.4 ± 1.2 cm^{-1}
400 nm	-1.7 ± 1.2 cm^{-1}
450 nm	2.2 ± 0.7 cm^{-1}
500 nm	9.8 ± 3.1 cm^{-1}
550 nm	11.5 ± 5.1 cm^{-1}
580 nm	14.6 ± 2.5 cm^{-1}
600 nm	18.7 ± 3.1 cm^{-1}
620 nm	24.2 ± 0.9 cm^{-1}
650 nm	23.3 ± 3.3 cm^{-1}
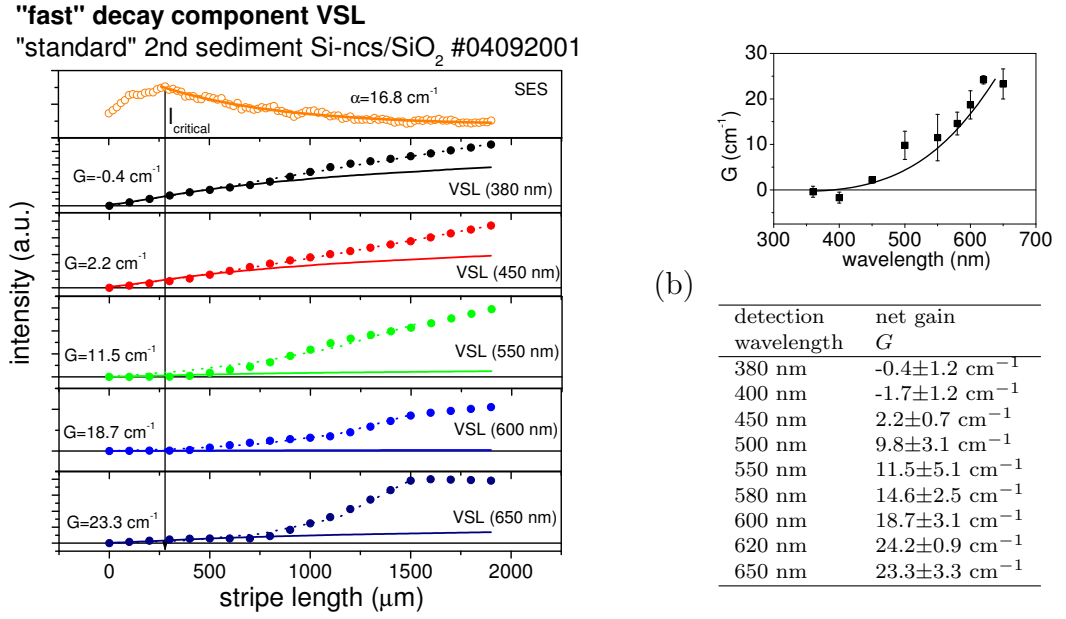
Figure 6.22: *(a) VSL, SES curves (symbols) and integrated SES curves (solid lines) measured under a fixed pump intensity of ~ 1.2 MW/cm^2 for the "fast" emission component at different emission wavelengths in a "standard" 2nd sediment Si-ncs/SiO$_2$ sample #04092001. Optical gain coefficient was fitted (dotted lines) above the $l_{critical}$ according to Eq. 6.2. (b) Fitted net gain coefficient $G(\lambda)$ forms a positive net gain spectrum. Excitation and detection conditions remain the same as in Fig. 6.21.*

and 950 μm. For the longest stripe of the length of ~ 3660 μm we observed a threshold behavior with the initial part of a sub-linear slope (~ 0.76) and a super-linear slope (~ 1.33) above the threshold excitation intensity of ~ 2 MW/cm^2, which can be a sign of the StE onset.

The observation of the threshold in the output-input intensity dependence seems to be very interesting and may signalize the necessity of the higher optical quality of the samples. In this sample we reached probably higher optical quality by the half Si-ncs content in the sample, however, this is generally not a good strategy, since the shorter StE build-up time τ_{StE} is connected with the higher Si-ncs volume fraction (see section 2.2.4). The search of an ideal sample with highest possible optical quality at highest possible volume fraction of Si-ncs (keeping in mind the concentration PL quenching as in Fig. 3.4) is our primary goal for the future investigation.

As the most successful result of this section we would like to present an optical feedback effect on the VSL spectra of a "standard" 2nd sediment Si-ncs/SiO$_2$ sample #04092002. VSL spectra measured from two different places in the sample are shown in Figs. 6.25(a-b). This sample contains again the smaller amount of Si-ncs like the

"slow" decay component VSL and SES
"standard" 2nd sediment Si-ncs/SiO$_2$ #04092001

detection wavelength	net gain G
380 nm	-5.4±2.7 cm^{-1}
400 nm	-4.9±2.9 cm^{-1}
450 nm	-5.4±1.7 cm^{-1}
500 nm	-6.8±1.8 cm^{-1}
550 nm	0.5±0.7 cm^{-1}
580 nm	0.7±0.9 cm^{-1}
600 nm	0.5±0.7 cm^{-1}
620 nm	-0.2±0.9 cm^{-1}
650 nm	-0.9±0.5 cm^{-1}
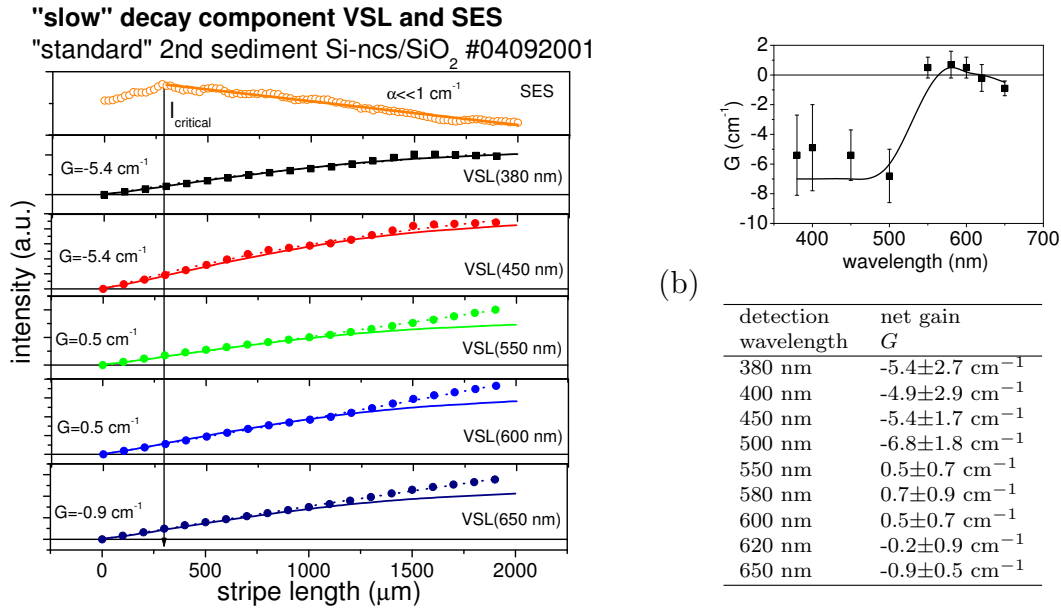
(a)

Figure 6.23: *(a) VSL, SES curves (symbols) and integrated SES curves (solid lines) measured under a fixed pump intensity of $\sim$1.2 MW/cm^2 for the "slow" emission component at different emission wavelengths in a "standard" 2nd sediment Si-ncs/SiO$_2$ sample #04092001. Optical gain coefficient was again fitted above the $l_{critical}$ (dotted lines) according to Eq. 6.2. (b) Fitted net gain coefficient $G(\lambda)$, forming the gain spectrum, is mostly negative - no light amplification was observed. Excitation and detection conditions remain the same as in Fig. 6.21.*

above sample #04050607 in Figs. 6.24(a-c). In order to enhance the possible StE effect we added an external mirror of high reflectivity (more than 90 %) on one side of the sample (cuvette) and precisely adjusted the cuvette to be perpendicular to the excitation stripe axis, i.e. we build a simple laser cavity likewise in Fig. 6.13. The excitation stripe length was adjusted to cover the whole sample volume between the cuvette faces (1 cm). We found an enhanced threshold behavior of the output-input intensity dependence with a sub-linear slope in the log-log scale of $\sim$0.60 together with a super-linear slope of $\sim$1.77-1.90 above the threshold intensity of $\sim$2.0 MW/cm^2. This result is a continuous extension of the observations discussed above and deserves to be stressed because it demonstrates beyond doubts - and independently of the VSL fitting and without applying the SES method - that positive net gain occurs in our (best) samples.

In conclusion we would like to stress that we clearly observed a positive net gain coefficient in "standard" 2nd sediment samples and we can prove it unambiguously. The samples were often burned, since a high pump fluency is necessary to overcome
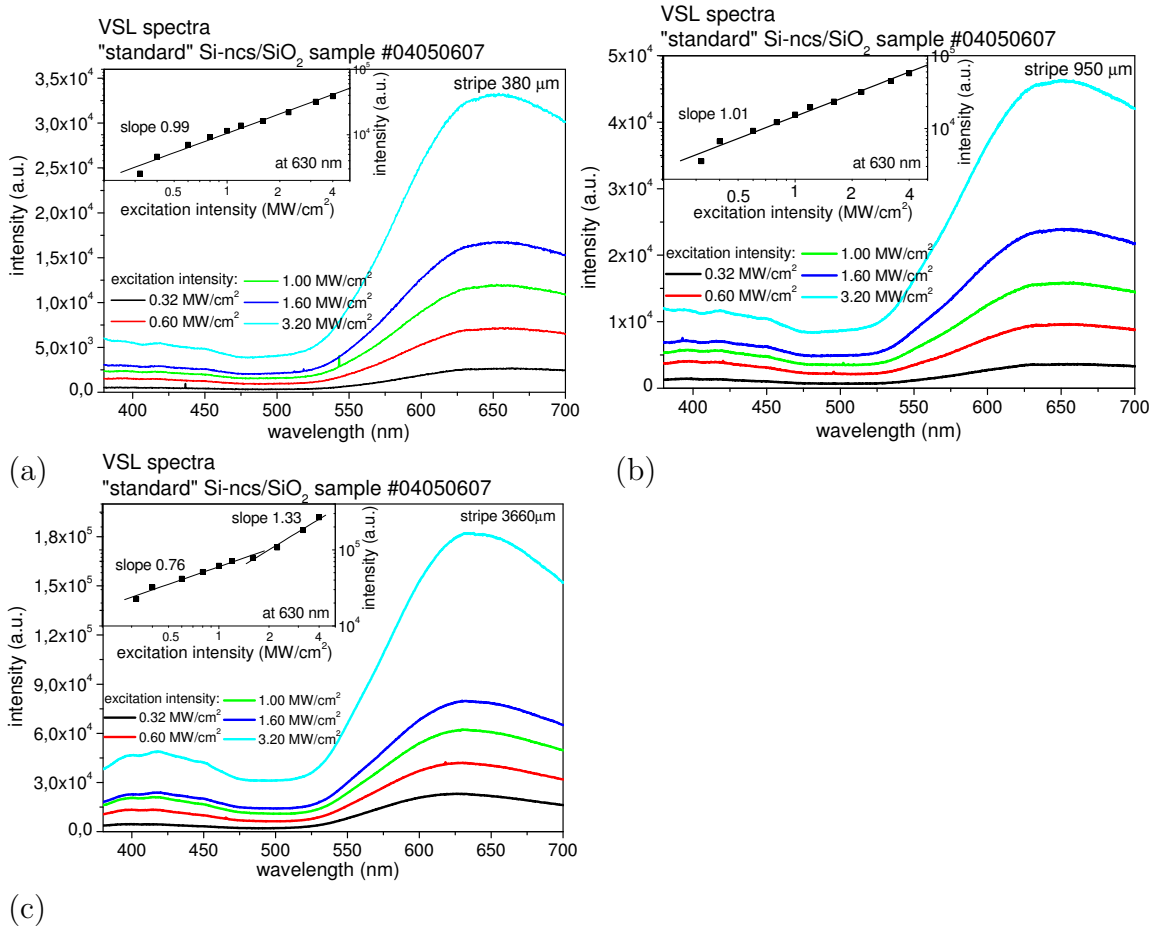
Figure 6.24: *Time integrated VSL spectra of a "standard" 2nd sediment Si-ncs/SiO₂ sample #04050607. Signal was excited using a stripe of three different fixed lengths (a) 380 μm, (b) 950 μm and (c) 3660 μm and a variable intensity (0.32-4.00 MW/cm²). Signal was detected using a nitrogen cooled (-100° C) CCD camera. Inset: the output-input intensity dependence in the log-log scale, detected at the peak maxima at 630 nm.*

the high optical losses. Despite this disadvantage, the gain was observed in all studied time regimes. The critical limit for the StE onset in our samples seems to arise from the sample structural inhomogeneity and scattering losses, since the results vary from sample to sample, from place to place. In the following we will present the most representative time-integrated VSL spectra measured in a "standard" 4th sediment Si-ncs/SiO₂ sample.

6.3.2 "Standard" 4th sediment Si-ncs/SiO₂

The higher sediments of the "standard" Si-ncs powder - the 3rd and 4th ones - were produced to increase the optical quality of the samples. However, the content of Si-ncs in a "standard" 3rd and 4th sediment Si-ncs/SiO₂ sample is much lower than that in the 2nd sediment. Lower density of Si-ncs can assure a high optical quality,

(a)   (b)
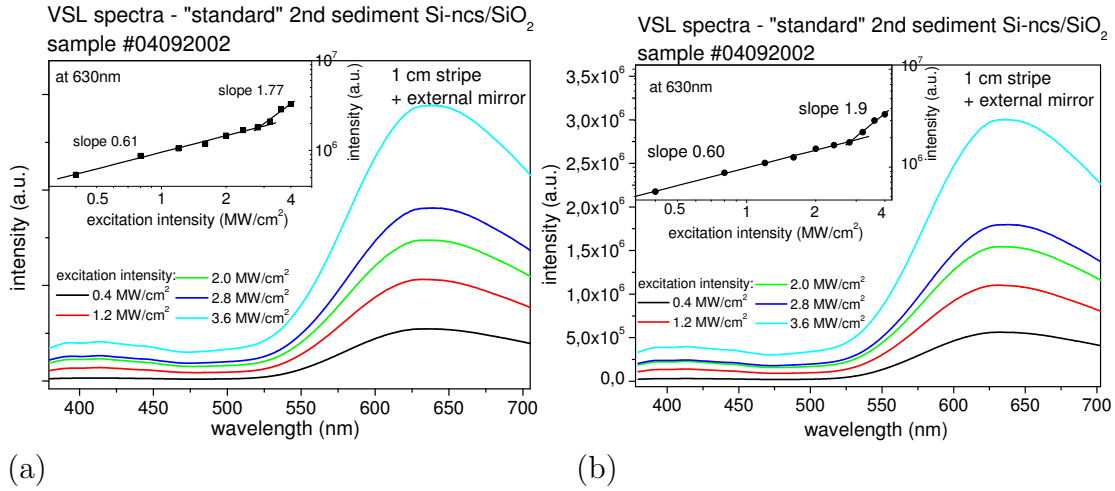
Figure 6.25: *Time integrated VSL spectra of a "standard" 2nd sediment Si-ncs/SiO$_2$ sample #04092002, enhanced by an external cavity, measured in two different places (a,b) of the sample. The pump intensity was varied from 0.4 MW/cm^2 up to 4.0 MW/cm^2, the stripe length was adjusted to its maximum value - 1 cm. A clear threshold was observed in the output-input dependence in the log-log scale (insets) above ~3 MW/cm^2 as a sign of the StE onset.*

i.e. lower scattering loss, however, at the cost of a lower optical gain (see discussion in section 2.2.4).

Fig. 6.26(a-b) shows the time integrated VSL curves measured in a "standard" 4th sediment Si-ncs/SiO$_2$ sample at different emission wavelengths. Signal was excited using a fixed excitation intensity and a variable stripe length. VSL curves were fitted according to Eq. 6.2. Estimated net gain values form a gain spectrum (Fig. 6.26(b)) and are indicated in the table in Fig. 6.26. The net gain coefficient magnitude continuously increases from negative values at short emission wavelengths to the positive values around the VSL spectra peak maximum at 620-630 nm. The sign of the net gain coefficient switches from the negative to the positive values at around 570 nm. The overall spectral dependence of the optical gain is very similar to that, measured in the "standard" 2nd sediment sample in Fig. 6.23.

6.3.3   Pure SiO$_2$ matrix

As a reference we measured the time-resolved VSL spectra of the "slow" and "fast" emission component in the pure SiO$_2$ matrix, to enable us to separate the contribution related purely to Si-ncs. Signal was excited using a stripe of a fixed excitation intensity and a variable length (Fig. 6.27). Both VSL spectra of the "fast" and "slow" components are nearly insensitive to the excitation stripe length, i.e. no StE onset was observed.

VSL spectra - "standard" 4th sediment
Si-ncs/SiO$_2$ sample

G=-15.3 cm^{-1}

VSL (380 nm)

G=-10.6 cm^{-1}

VSL (460 nm)

G=-3.7 cm^{-1}

VSL (540 nm)

G=2.9 cm^{-1}

VSL (620 nm)

G=2.6 cm^{-1}

VSL (660 nm)

intensity (a.u.)

stripe length (mm)

(a)

net gain G (cm^{-1})

wavelength (nm)

(b)

Emission wavelength	net gain
380 nm	-15.3±3.5 cm^{-1}
420 nm	-11.6±2.9 cm^{-1}
460 nm	-10.6±2.0 cm^{-1}
500 nm	-8.3±1.5 cm^{-1}
540 nm	-3.7±0.8 cm^{-1}
580 nm	2.0±0.4 cm^{-1}
600 nm	2.9±0.5 cm^{-1}
660 nm	2.6±0.5 cm^{-1}
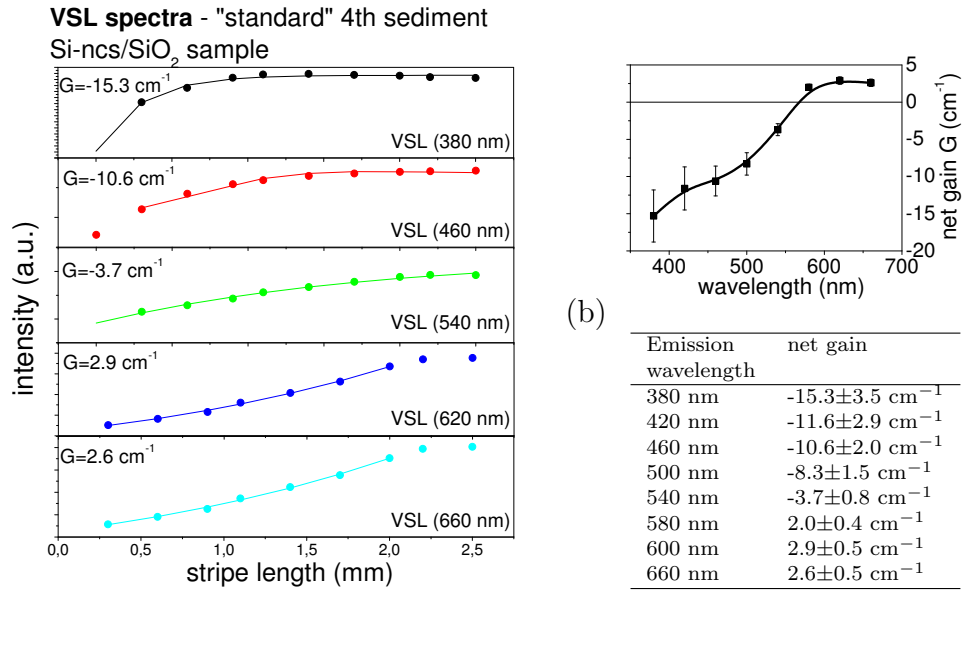
Figure 6.26: *(a) Time integrated VSL curves (symbols) of a "standard" 4th sediment Si-ncs/SiO$_2$ sample for different emission wavelengths. Signal was excited with a fixed excitation intensity of 0.32 MW/cm^2 and a variable stripe length (0.3-2.5 mm). Signal was detected at room temperature using a nitrogen cooled (-100°C) CCD camera. (b) The net gain values extracted from (a) form a gain spectrum. The net gain coefficient values were fitted using Eq. 6.2 (lines) and are indicated in the table.*

VSL curves measured at different emission wavelengths in the pure SiO$_2$ matrix are plotted in Fig. 6.28(a,b) for "fast" and "slow" emission components, respectively. The net gain coefficient fitted according to Eq. 6.2 has only negative values from ∼-10 cm^{-1} to -20 cm^{-1} and seems to be nearly spectrally independent. This result appears to be in excellent agreement with the standard attenuation and transmission measurements presented in Fig. 5.2. As we discussed above in section 5.1.1, the optical losses are probably caused by the light scattering on the air voids in the SiO$_2$ sol-gel matrix.

6.4   Conclusions

In this chapter we presented the VSL method used standardly for the characterization of the light amplification. This method fails under too high, or low net optical gain regimes. We have proposed a novel approach - a combination of the SES and VSL techniques, which enable us to extend the VSL applicability to comparatively low net gain values. Using these methods, we have revealed a positive optical gain in
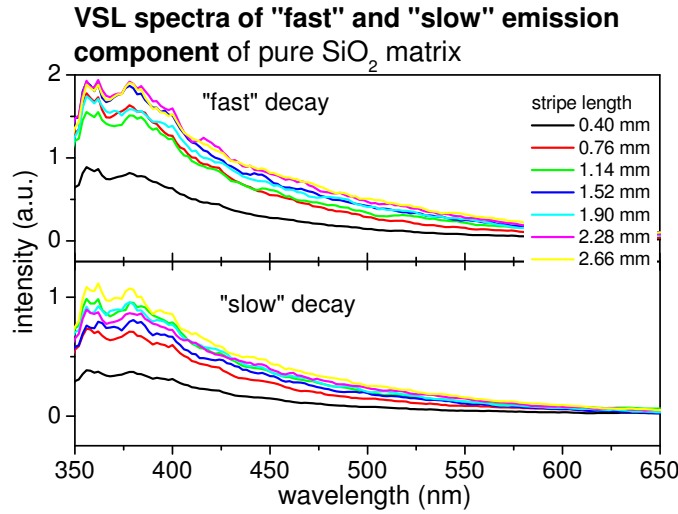
Figure 6.27: *Time resolved VSL spectra of the "slow" and "fast" emission components of the pure SiO$_2$ matrix (top: "fast" component, bottom: "slow" component). Signal was excited using a fixed excitation intensity of 1.2 MW/cm^2 and a variable stripe length from ∼0.8 mm up to ∼3 mm. The signal was detected at room temperature using a PMT and a boxcar integrator ("fast" component: no gate delay, gate width of ∼50 ns; "slow" component: gate delay of ∼10 μs, gate width of ∼4 μs).*

(a)   (b)
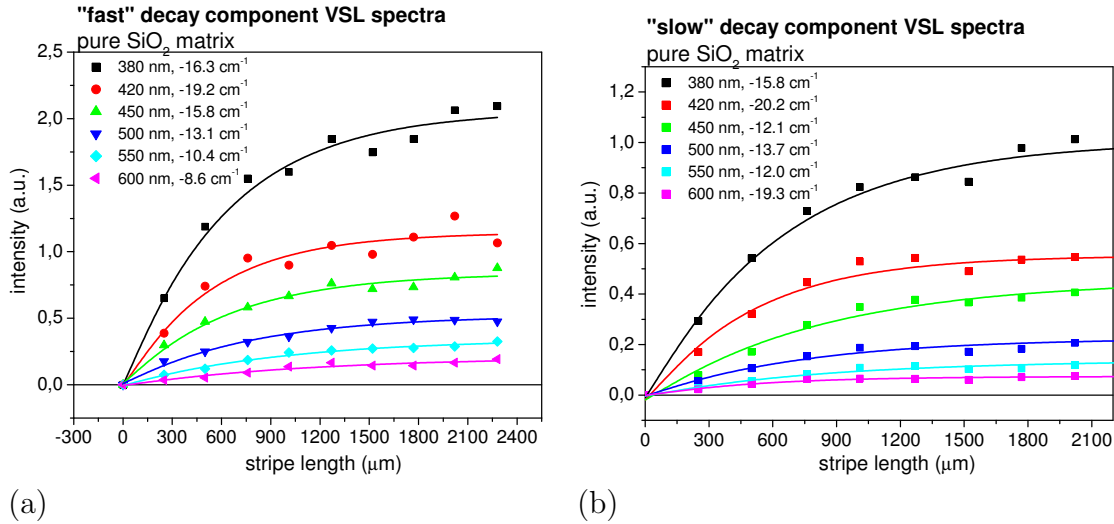
Figure 6.28: *Time-resolved VSL curves of (a) "fast" and (b) "slow" emission components measured at different emission wavelengths in the pure SiO$_2$ matrix. VSL curves (symbols) are fitted using Eq. 6.2 (fits - solid lines). Detection and excitation conditions remain the same as in Fig. 6.27. No net gain has been observed.*

a majority of experiments (albeit not in all of them) performed on various samples in the "slow" emission component, originating safely in the ensemble of Si-ncs (not in the SiO$_2$ matrix). The values of the net gain coefficient at the "slow" emission component

peak maxima around λ=600 nm have ranged between 2-70 cm^{-1}. This observation confirms principle features of recent results obtained by different authors in differently prepared Si-ncs samples [16] [21] [22] [63]. Moreover, these results indicate that the "orange" emission band, originating from the self-trapped exciton recombination, is not strongly affected by Auger quenching, in agreement with the recent suggestion by e.g. Kamenev et Nassiopoulou [71]. We observed also a relatively small positive "fast" net gain in our Si-ncs/SiO$_2$ samples at short wavelengths around 570 nm. To the best of our knowledge, this is the first observation of this kind but ought to be considered with caution, since origin of the discovered gain is not clear. The results obtained in the other types of samples, "yellow" and "white" Si-ncs/SiO$_2$ ones, are shown in appendix sections 9.2.2 and 9.2.1.

The suitable samples for the subsequent DFL application, described in the following chapter 7, were chosen according to their optical quality rather then according their type, since we have found no significant difference between the "standard", "white" and "yellow" Si-ncs/SiO$_2$ samples optical gain properties.

Chapter 7

DISTRIBUTED FEEDBACK LASER

Necessary conditions for lasing are (i) single-passage positive net optical gain and (ii) positive optical feedback. In the previous chapter we have evidenced positive optical net gain in various Si-ncs/SiO$_2$ samples. In this chapter we attempt to realize an optically pumped Distributed Feedback Laser (DFL) structure. The optical feedback increases the overall light path in the pumped active material and selects an emission mode, where the energy will be preferably stored. This can be provided by an external cavity in which a large volume of the active material is placed between the two end reflectors, however, long-scale high optical quality is required. The end reflectors can be a single pair of a high reflective mirrors or Bragg distributed mirrors. However, laser oscillation can occur without the benefit of the end reflectors if a spatially periodic active medium, i.e. having periodic modulation of index of refraction and absorption/gain coefficient, is used. The periodic modulation can be induced optically via nonlinear optical interaction with the matter.

An optically induced DFL grating has some advantages as the cavity tuneability and relatively easy alignment, provided that sufficiently strong optical nonlinear effects as a complex refractive index change induced by strong light illumination are present. The positive optical feedback in such a system is provided by a coherent backscattering from periodic perturbations in the amplifying medium. The coherence of this process depends on the average material homogeneity length l_{hom}. In the case of a short-scale homogeneity material, coherent backscattering is only partial, resulting in broad selected modes. In our samples, on one hand we have advantageous high volume fraction of Si-ncs, leading to efficient strong emission and positive optical net gain, which, on the other hand, leads to aggregation of Si-ncs into micrometer-scale clusters that scatter light emitted by Si-nc. This increases the overall optical losses and causes loss of the propagation directivity and coherence of emitted light on a micrometer scale. For this reason, application of such a material as an active medium in

an external laser cavity is questionable and we proposed to use for the mode selection
a distributed internal DFL cavity. This will be described in the following.

7.1 DFL principle - Bor's configuration

The DFL grating has been optically induced using a XeCl excimer laser excitation
having a homogeneous rectangular beam profile. Because of generally lower temporal
and spatial coherence of this type of laser, we have built the setup in Bor's configura-
tion ([105]; see Fig. 7.1), introduced originally for organic-dye lasers excited by such
type of lasers. The intense stripe-like laser beam of wavelength λ_{exc} (after focusing
by a cylindrical lens) is divided by a holographic grating (with the grating constant
d) into two first diffraction orders of almost equal intensities I_0 under the angle

$$\alpha = \arcsin(\frac{\lambda_{exc}}{d}). \tag{7.1}$$
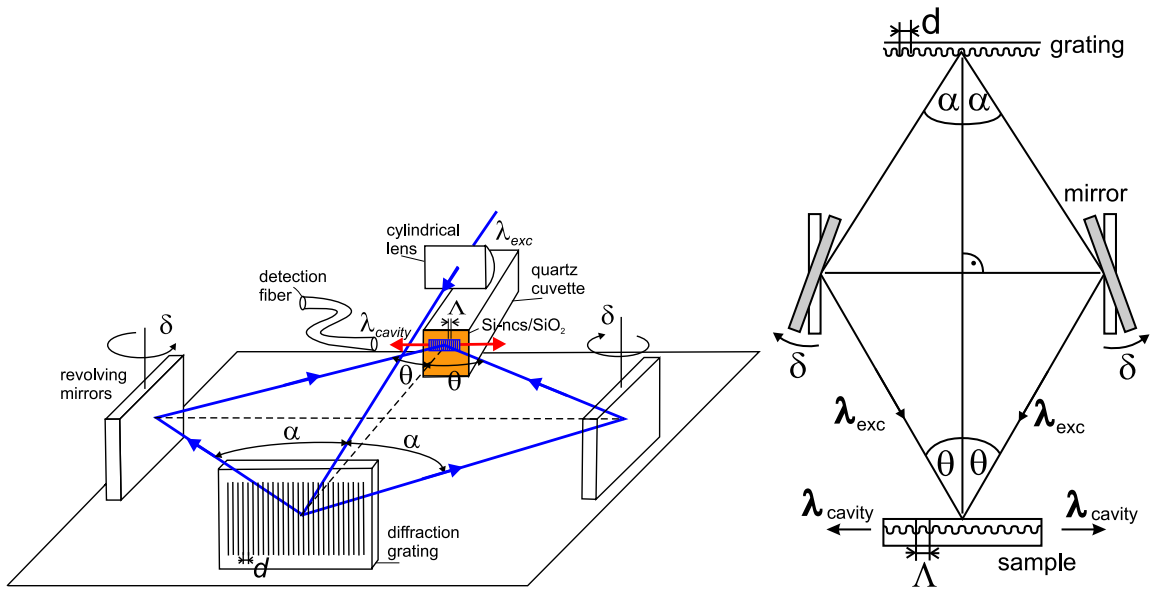
Figure 7.1: *Principal arrangement of the optically induced DFL cavity in Bor's configu-
ration [105].*

Subsequently both beams are reflected by two mirrors revolving over the angle δ
and directed under the tunable incident angle $2\theta = 2(\alpha - 2\delta)$ onto the active layer
where they interfere. The stripe-like spatial profile of the excitation beams leads
to a grating-like linear interference pattern of spatial profile $I(x) \propto cos(\frac{2\pi x}{\Lambda})$, where
$\Lambda = \frac{\lambda_{exc}}{2\sin\theta}$ is the grating period. The direction of propagation x of amplified light is
parallel with the interference pattern long axis and lies within the sample surface plane
(within the Si-ncs rich SiO_2 layer). We would like to stress here, that the active Si-ncs
rich layer is not a waveguiding structure, as follows from the preparation technique
procedure and can be clearly seen from the μ-PL emission image in Fig. 3.3. The

DFL cavity induced by the interference pattern (i.e. the periodic modulation of the complex refractive index) selects cavity modes at the wavelengths

$$\lambda_{cavity} \approx \frac{\Lambda 2 n_0}{K_g} = \frac{n_0 \lambda_{exc}}{K_g \sin\theta},$$ (7.2)

tunable via the angle δ (or θ); K_g is the grating order (in our setup K_g=1) and n_0 is the linear part of the refractive index of the sample. The constructive interference occurs for beams with the phase shift of $\varphi = 2\pi M$ (M are natural numbers). For illustration we plotted in Fig.7.2 the tunable range of the cavity mode wavelength for two different materials - organic dye solutions in methanol with refractive index n_0=1.33 and our Si-ncs/SiO$_2$ samples, whose refractive indices vary between 1.6 and 1.8. The grating constant of the used holographic grating was d=333 nm (3000 tr./mm).
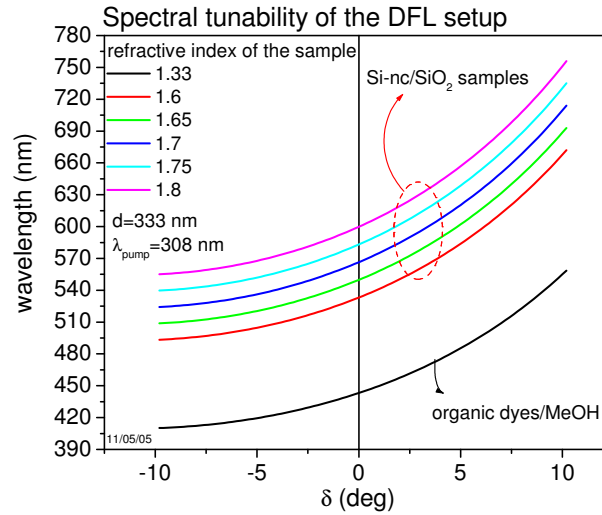
Figure 7.2: *Cavity mode wavelength λ_{cavity} dependence on refractive index n_0 of the active medium and the revolving angle δ.*

The intense periodic illumination modulates both the absorption/gain coefficient and the refractive index of the active layer. Tuneability is provided via synchronous revolving mirrors by the same angle δ, directly varying the DFL cavity grating constant Λ. Light emission, influenced by the DFL cavity, is detected in the direction of the distributed cavity (x-axis) from the edge of the sample, similarly to the VSL method setup.

7.2 Theoretical model

The mode selection performed with the aid of the Bragg type grating is usually applied in materials with high positive net gain and long-scale optical homogeneity as organic dyes solutions. Our samples, on the other hand, have lower optical gain and are homogeneous only over a shorter length. In this case, current theoretical approach to the DFL description [106] is not immediately applicable any more. In the following we present our simple theoretical model describing the mode selection in such materials.

7.2.1 Quality of the DFL cavity

The quality of the optically induced DFL cavity is given by (i) the quality of the interference pattern and (ii) strength of the nonlinear response of the excited material - i.e. the modulation depth of the complex refractive index.

7.2.1.1 Interference pattern quality

The interference pattern quality is given by its length and modulation depth, both driven by the temporal and spatial coherence of the two incident excitation beams, interfering on the surface of the sample. The temporal coherence describes the ability of the radiation to interfere in dependence upon the difference in path lengths between the two beams. The maximum allowed path difference is called the coherence length $l_{coherence} = \frac{\lambda_{pump}^2}{\Delta\lambda_{pump}}$, where $\Delta\lambda$ is the width of the excitation spectrum. Due to the fact that the XeCl excimer laser, used in our setup, has an open laser cavity, its coherence length is relatively short, somewhere between $l_{coherence}^{XeCl} \sim 100~\mu$m [107] and $\sim 500~\mu$m [108]. According to our experimental experiences, we expect $l_{coherence}^{XeCl}$ to be between $\sim 200-300~\mu$m. As mentioned above, the necessary condition for the interference observation therefore reads

$$|L - L'| \leq l_{coherence}, \tag{7.3}$$

where $|L - L'|$ is the path difference (see Figs. 7.3 and 7.4). This condition is always fulfilled for $\delta=0$ (Figs. 7.3(a-b)) and for all the points on the axis of symmetry (Fig. 7.3(c)) where $|L-L'|=0$. On the other hand, for $\delta \neq 0$, the optical path difference depends on the distance Δx from the axis of symmetry (Figs. 7.3(d) and 7.4), as we are going to discuss.

Due to the relatively short $l_{coherence}$, even for small δ a small part only of the total excited area (which is of maximal length of $\sim$1 cm) will be modulated by the
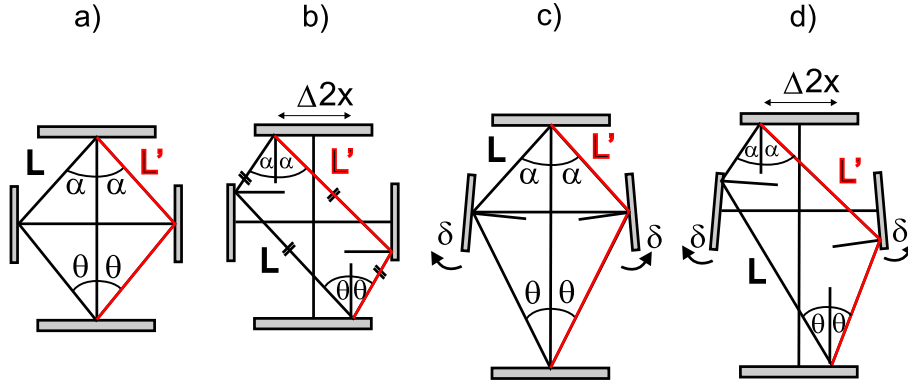
Figure 7.3: *Schematic view of different geometrical situations - (a) $\delta=0$ and $\Delta x=0$; (b) $\delta=0$ and $\Delta x \neq 0$; (c) $\delta \neq 0$ and $\Delta x=0$; (d) $\delta \neq 0$ and $\Delta x \neq 0$.*

interference. The length of the interference pattern $2\Delta x$ can be calculated from a simple geometrical analysis, as sketched in Fig.7.4 and discussed hereafter. The known parameters are the angles α, δ and $\theta = \alpha - 2\delta$ and a fixed distance between the revolving mirrors $2c$=8 cm. The optical paths L and L' as a function of the displacement Δx are given by equations

$$
\begin{aligned}
L &= l_0 + l_1 = \frac{a - \Delta y}{\cos \alpha} + \frac{b + \Delta y}{\cos \theta} \\
L' &= l'_0 + l'_1 = \frac{a + \Delta y}{\cos \alpha} + \frac{b - \Delta y}{\cos \theta} \\
\Delta y &= \frac{\Delta x}{\tan \alpha - \tan \delta} \\
a &= \frac{c}{\tan \alpha} \\
b &= \frac{c}{\tan \theta}.
\end{aligned}
\tag{7.4}
$$

The condition Eq. 7.3 can be then rewritten as

$$
|L - L'| = 2|\Delta y \frac{\cos \theta - \cos \alpha}{\cos \theta \cos \alpha}| \leq l_{coherence},
\tag{7.5}
$$

The maximal interference pattern length $2\Delta x \equiv L_{cavity}$ follows from Eqs. 7.4 and 7.5 to be

$$
2\Delta x \equiv L_{cavity} \leq |l_{coherence} \frac{(\tan \alpha - \tan \delta) \cos \alpha \cos \theta}{\cos \theta - \cos \alpha}|
\tag{7.6}
$$

and is plotted in Fig. 7.5 for different angles δ. For the cavity mode formation, we need to have the cavity length L_{cavity} as long as possible, which can be in our setup assured only in a relatively narrow range of the tuning angle $\delta \in$ (-3°,3°), where $L_{cavity} \geq 1$ mm (Fig. 7.5). This limits the spectral tuneability range of the cavity to
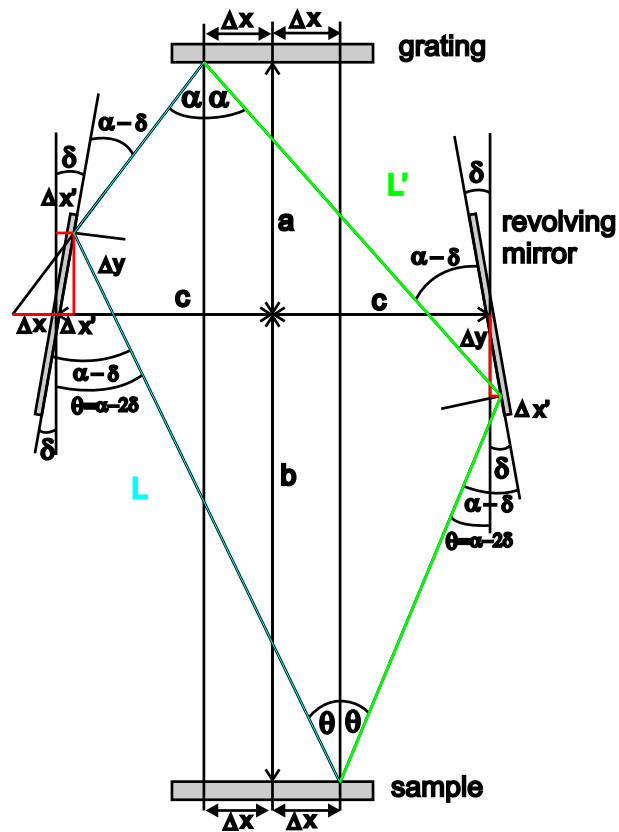
Figure 7.4: *Detailed sketch of the DFL system geometry for calculation of the interference pattern length.*

$\lambda_{cavity}(\delta{=}0)\pm16$ nm, i.e. $\sim$427-466 nm for organic dye solutions with $n_0{=}1.33$ and $\sim$546-595 nm for Si-ncs/SiO$_2$ samples with $n_0 \doteq 1.7$.
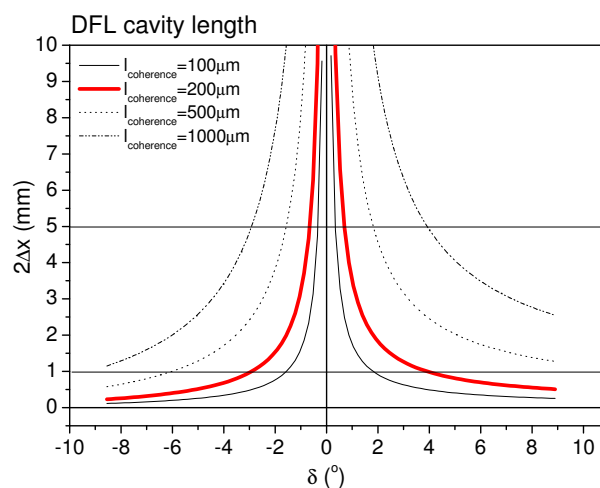
Figure 7.5: *DFL cavity length, i.e. the length of the interference pattern, as a function of the excitation source coherence length $l_{coherence}$ and revolving angle δ, as calculated on the basis of Eq. 7.6.*

7.2.1.2   Nonlinear complex refractive index

According to the model above, one can optimize the length of the interference image, however, the DFL cavity quality depends also on the strength of the optically induced changes of the complex refractive index $\tilde{n} = n + in'$, where n is the real part and n' is the imaginary part of the refractive index, both depending on the wavelength and excitation intensity I_{exc}. One can write

$$
\begin{aligned}
n(\lambda, I_{exc}) &= n_0(\lambda) + \Delta n(\lambda, I_{exc}) \\
n'(\lambda, I_{exc}) &= \frac{\lambda}{4\pi}(\alpha_0(\lambda) + \Delta\alpha(\lambda, I_{exc})),
\end{aligned}
\tag{7.7}
$$

where $\Delta n(\lambda, I_{exc})$ and $\Delta\alpha(\lambda, I_{exc})$ are the refractive index and absorption coefficient changes induced by strong intensity light illumination. In case of the positive optical gain $G(\lambda, I_{exc})$ we can write $\Delta\alpha(\lambda, I_{exc}) \approx G(\lambda, I_{exc})$.

Real part of the linear refractive index n_0

The linear part of the refractive index n_0 of Si-ncs/SiO$_2$ samples in the studied visible range can be measured using e.g. the Abbe-hemisphere method. Using this experimental technique, we measured refractive index of the pure SiO$_2$ sol-gel matrix to be $n_{0(SiO_2)}$=1.42, which is close to the refractive index of the standard glass $n_{0(glass)}$=1.45. This small difference in refractive indices can be due to the air voids formed during the solidification process in the sol-gel SiO$_2$ based matrix. The refractive index of the "standard" 4th sediment sample (sample with the lowest content of Si-ncs) was measured to be $n_{0(4sed)} \approx$1.64, which represents the lowest refractive index of our samples. Since the Abbe-hemisphere method is applicable to the samples with refractive index smaller than the refractive index of the hemisphere itself only, which is $\sim$1.7, the refractive indices of other samples with higher volume fraction of Si-ncs could not be measured by this method and were calculated using the Bruggeman's effective medium theory [73] expressed by the equation

$$
f\frac{\varepsilon - \varepsilon_{eff}}{\varepsilon + 2\varepsilon_{eff}} + (1 - f)\frac{\varepsilon_M - \varepsilon_{eff}}{\varepsilon_M + 2\varepsilon_{eff}} = 0,
\tag{7.8}
$$

where f is the filling factor (f=1 for pure Si, f=0 for pure SiO$_2$), $\sqrt{\varepsilon} = n_{0(Si)}$ is the refractive index of silicon, $\sqrt{\varepsilon_M} = n_{0(SiO_2)}$ is the refractive index of the SiO$_2$ sol-gel matrix, $\sqrt{\varepsilon_{eff}} = n_{0(Si-ncs/SiO_2)}$ is the refractive index of the Si-ncs/SiO$_2$ sample with the filling factor f. We calculated refractive indices for the two limit volume fractions of 20 vol.% (f=0.2) and 10 vol.% (f=0.1), as $n_{0(Si-nc/SiO_2)} \approx$1.78 and $\approx$1.59 respectively (see Fig. 7.6). It is interesting to note that the Brugemann's equation

Eq. 7.8 leads to a quadratic equation for refractive index, giving more exact solution than we could get from an intuitive simple interpolation $n_{0(Si-ncs/SiO_2)} = fn_{0(Si)} + (1-f)n_{0(SiO_2)}$. The difference is significant up to $f = 0.6$, as demonstrated in Fig. 7.6.
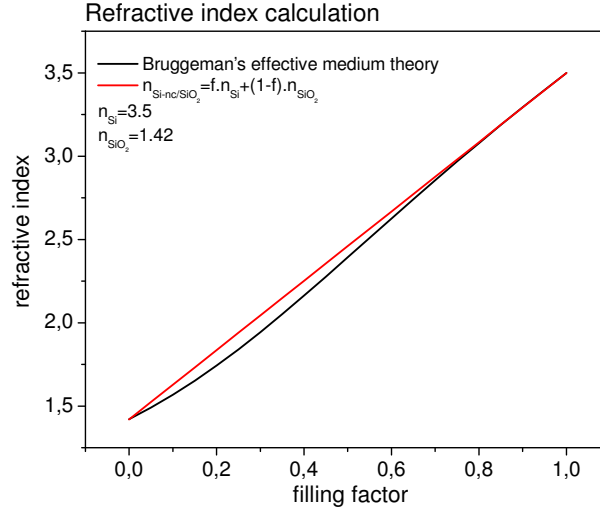
Figure 7.6: *Refractive index calculation.*

Real part of the nonlinear refractive index $\Delta n(\lambda, I_{exc})$

Interaction of light (represented by its electrical field amplitude E) with matter (characterized by its susceptibility tensor $\chi(E)$ and permittivity tensor $\varepsilon_{tot}(E)$) can be described by the polarization P as follows

$$P \;=\; \varepsilon_0 \chi(E) E, \tag{7.9}$$

where ε_0 is the permittivity of the vacuum. The susceptibility and permittivity as a function of the amplitude E of incident light can be expressed in terms of series

$$\chi(E) \;=\; \chi^{(1)} + \chi^{(2)} E + \chi^{(3)} EE^* + ... \tag{7.10}$$
$$\varepsilon_{tot} \;=\; (1 + \chi(E))\varepsilon_0$$

where $\chi^{(i)}$ is the susceptibility of i-th order. The first nonlinear term in Eq. 7.10, depending linearly on the electric field, leads to a relatively strong electro-optical effects as e.g. the Pockels effect and the second harmonic generation. These effects, as well as other nonlinear effects of higher even orders in Eq. 7.10, are absent in silicon due to its crystalline point group symmetry. Only much weaker effects of the second

nonlinear order (plus all odd orders) depending on the excitation intensity $I_{exc} = EE^*$ are allowed. The real part of the nonlinear refractive index in silicon is given by the real part of the complex permittivity as $n = \sqrt{\varepsilon_{tot}} = \sqrt{\varepsilon + \varepsilon_2 I_{exc}} = \sqrt{\varepsilon + \varepsilon_0 \chi^{(3)} I_{exc}} = \sqrt{\varepsilon}(\sqrt{1 + \frac{\varepsilon_0 \chi^{(3)} I_{exc}}{\varepsilon}}) \approx \sqrt{\varepsilon}(1 + \frac{1}{2}\frac{\varepsilon_0 \chi^{(3)} I_{exc}}{\varepsilon}) = n_0 + \frac{1}{2}\frac{\varepsilon_0 \chi^{(3)} I_{exc}}{n_0} = n_0 + n_2 I_{exc} = n_0 + \Delta n$. Coefficient $n_2 \approx \frac{1}{2}\frac{\varepsilon_0 \chi^{(3)}}{n_0}$ gives the magnitude of the material response on the intense light illumination, unique for each material and linearly proportional to $\chi^{(3)}$.

The main microscopic effects which can lead to a significant refractive index change in silicon materials are the free carrier effects (change of the refractive index due to the high density of free carriers), the optical Kerr effect (the change of the refractive index with excitation intensity) and slow thermal effects. The weight of these processes differs for different excitation regimes - for shorter excitation pulses (fs, ps) only the weak optical Kerr effect takes place, while using longer excitation pulses (ns) or continuous excitation, much stronger and slower free carriers effects and thermal effects can be observed. Thus the excitation conditions, under which the value of $\chi^{(3)}$ was measured, has to be specified. In our calculations we take $n_2 \sim 10^{-8} \frac{cm^2}{W}$ value, reported by Vijaylakshmi et al. [109], measured under excitation conditions similar to ours (8 ns pulses, 355 nm) on similar type of Si-ncs/SiO$_2$ based samples. A rough estimate gives us the maximal refractive index change Δn to be ~ 0.006. Because of the negligible photo carrier diffusion in Si-ncs/SiO$_2$ samples, the refractive index change, which is predominantly due to the free carrier effect, persist over the whole luminescence decay time, i.e. the induced optical grating is in temporal coincidence with the Si-ncs emission.

The modulated refractive index leads to increased reflectivity within the modulated area, which can be described by a reflectivity coefficient R. This can be simply calculated as

$$R = (\frac{n - n_0}{n + n_0})^2 = (\frac{\Delta n}{2n_0 + \Delta n})^2 \tag{7.11}$$

Considering the refractive index $n_0 \approx 1,7$ and $\Delta n \approx 0,006$ as estimated above, the reflectivity of the single element of the distributed mirror is of the order of $R \approx 10^{-6}$. The value of reflectivity is low, nevertheless the number of elements within the whole interference pattern being high, for total cavity length of 1 mm we get approximately 10^4 of elemental mirrors and the total reflectivity becomes $\sim 10^{-2}$.

7.2.2   Mode selection - theoretical model

In Fig. 7.7 we show a schematic model of the DFL mode selection in low homogeneity samples. The uppermost case "DFLoff" describes the situation when only a single excitation beam is incident on the sample surface, i.e. no interference pattern

can be observed. The lowermost case "DFLon" describes the situation when two excitation beams interfere on the sample surface and form a DFL cavity of maximal length $L_{cavity} = N\Lambda$ (part "B"), where N is the natural number and denotes the total number of the interference maxima within the interference pattern. L_{cavity} depends on the angle δ and excitation source coherence (as discussed above) and can be calculated using Eq. 7.6. The rest of the excitation stripe (parts "A" and "C") is not modulated and contributes by a phase insensitive light amplification only like in the VSL experiments.

The interference maxima are placed at positions x_i separated by Λ. Ideally, only the Si-ncs placed in the interference maxima x_i are excited and emit light, while the other Si-ncs do not. In the frame of our simple model, an ensemble of Si-ncs at the position x_i is replaced by a single emitter. Such emitter emits light randomly to all directions, however, we can detect only the light emitted forward in a direction to the detector and the light scattered backward on the distributed DFL grating as sketched in Fig. 7.7 (red arrows). The DFL cavity can be described with a sufficient accuracy as a set of semitransparent mirrors with reflectivity $r(x) \propto R\delta(x_i)$ (black arrows in $r(x)$ scheme in Fig. 7.7), where R comes from Eq. 7.11, placed at interference maxima, where the most significant refractive index changes are located. Because the reflectivity R is relatively very low and R^n is negligible for $n > 1$, multiple reflections will be neglected.

The contribution of the modulated imaginary part of the complex permittivity is for the measured optical gain (of the order of few tens of cm^{-1}) much smaller than the contribution of the real part, i.e. $\Delta n(\lambda, I_{exc}) \gg \frac{\lambda}{4\pi}G(\lambda, I_{exc})$ ($\Delta n \approx 0.006$ and $\frac{\lambda}{4\pi}G$ is of order of 10^{-5}). Therefore, the imaginary part of the refractive index does not significantly contribute to the cavity mode shape formation and can be taken as an invariable average net optical gain coefficient $\bar{G}$ (Fig. 7.7).

Among the most important parameters, affecting the mode spectra, belongs the sample homogeneity. This can be described in terms of an average distance l_{hom} on which the light emitted by each single Si-nc preserves its directionality and coherence before it is scattered on inhomogeneities. The mode selection is then provided only by a part of the distributed cavity ("cavity segment") of length $\sim l_{hom} = K_{hom}\Lambda$ around the emitter (K_{hom} is the natural number and denotes the number of the unit mirrors in the cavity segment; see Figs. 7.7 and 7.8(a-c)).

The effect of such a cavity segment can be easily included in our model. Moreover, the character of the segment directly corresponds with the character of the inhomogeneity of the sample, which thus can be determined. In our calculations we concentrate basically on the two main cavity segment types - a "blurred" one
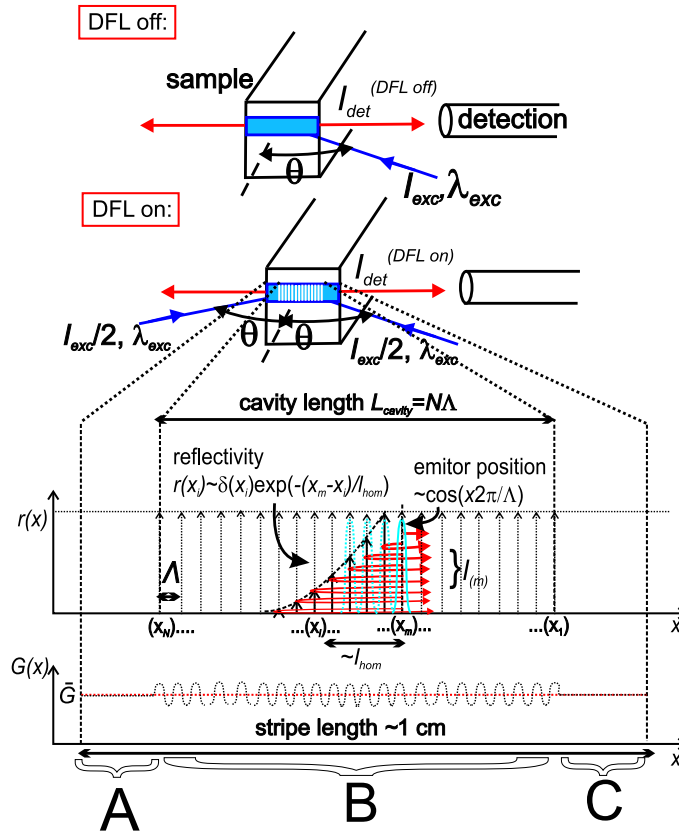
Figure 7.7: *Schematic model of the DFL mode selection calculation. The uppermost case "DFLoff" describes the situation when only a single excitation beam is incident on the sample surface, i.e. no interference pattern can be observed. The lowermost case "DFLon" describes the situation when two excitation beams interfere on the sample surface and form a DFL cavity of maximal length $L_{cavity} = N\Lambda$ calculated using Eq. 7.6 (part "B"). The rest of the excitation stripe (parts "A" and "C") are not modulated and contribute by a phase insensitive light amplification only like in the VSL experiments.*

(Fig. 7.8(a)), described using an exponential reflectivity decay $\sim e^{-\frac{x_m}{l_{hom}}}$ weight function ($x_m \geq 0$ is the distance from the emitter; $x_m = 0, \Lambda, 2\Lambda, ..., K_{hom}\Lambda, ...$). The feedback calculation is then made ideally for $x_m \in (0, \infty)$ or for x_m from zero till a length $K\Lambda \gg l_{hom}$, i.e. $x_m = 0, \Lambda, 2\Lambda, ..., K_{hom}\Lambda, ..., K\Lambda$. This type of segment can correspond to a material with homogeneously distributed small scattering centers as in organic dyes solutions. The second type of segment, which corresponds better with our situation in Si-ncs/SiO$_2$ samples, can be called "sharply" defined segment (Fig. 7.8(b)), related to a "sharp-boundary" type of inhomogeneities in the material (this can be prescribed e.g. to the the high refractive index contrast of crystalline Si and SiO$_2$, where $n_{0(Si)} = 3.5$ and $n_{0(SiO_2)} = 1.5$). This can be included in the feedback calculation as a likewise exponential reflectivity decay $\sim e^{-\frac{x_m}{l_{hom}}}$ but taking x_m from zero till the length equal to l_{hom} only, i.e. $x_m = 0, \Lambda, 2\Lambda, ..., K_{hom}\Lambda$ (red arrows in Fig. 7.8(b)). Another, even simpler possibility is to describe such type of segments using a defined number of distributed mirror units K_{hom} in the segment,

each of full reflectivity R, instead of the exponential decay weight function (red arrows in Fig. 7.8(c)). However, for small l_{hom} (as in our samples), both approaches of the "sharply" defined cavity segment lead to similar results.
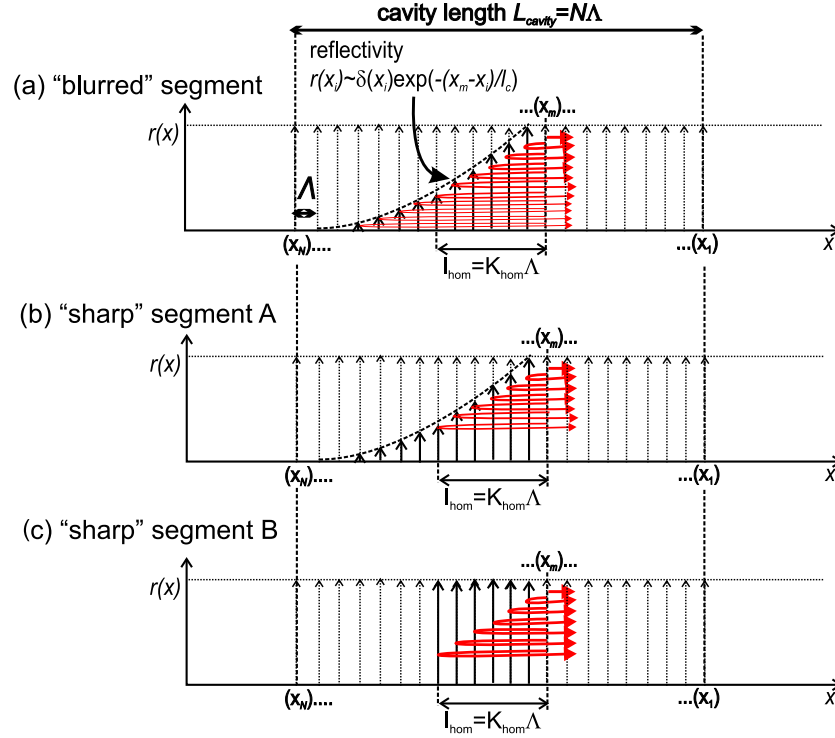
Figure 7.8: *Schematic sketch of a different types of cavity "segment", used in our model. (a) "Blurred" cavity calculation scheme, used for high homogeneity samples, where the calculation includes all possible first order reflection; (b) "sharp" cavity calculation scheme for low homogeneity samples, where the reflection is limited by a sharp edge (inhomogeneity); (c) the most simplified "sharp" cavity calculation scheme. In the following calculation we use the scheme (b), which describes better the real situation.*

To make a step closer to a real situation, we introduced a cosine-profile weight function $F(x) = \frac{1}{A+B}(B + A\cos\frac{2\pi}{\Lambda}(x - \frac{\Lambda}{2}))$ to express the fact that the Si-ncs emission is excited by a cosine-like interference pattern profile forming the DFL cavity (the emitter position x is peaked at each interference maxima and copying also the interference minima - see the blue cosine-like curve in scheme Fig. 7.7; coefficients A and B define the interference pattern quality). Due to many different effects (as size distribution, different radiative decays, hopping and blinking effects, relaxation processes caused by the non-resonant excitation, etc.), emissions of different single Si-ncs are not correlated in phase, time and wavelength and we consider the interference occurs within the light emitted by each single emitter only. The mode selection is thus calculated separately for each emitter, the rest of the cavity and the non-modulated rest of the excitation stripe contributing only by a phase insensitive average gain/absorption coefficient $\bar{G}$ and by losses caused by the induced reflectivity

of the rest of the modulated part.

Light emitted by a single emitter, reflected backwards from the distributed grating segment ("cavity segment" of length l_{hom}) of total reflectivity r_{total}, can be expressed as $E_r = E_0 r_{total}$. The total reflectivity coefficient r_{total} can be estimated by many different approximative methods. In our model we have chosen the relatively simple intuitive method as known from the standard Fabry-Perot resonator, where the total reflectivity can be expressed as a sum of the partially reflected beams from distributed mirror units, each of reflectivity R, as

$$r_{total}(\lambda) = r \frac{1 - e^{-\frac{K}{K_{hom}}} T^K e^{2iK\Phi(\lambda)}}{1 - e^{-\frac{1}{K_{hom}}} T e^{2i\Phi(\lambda)}} \int_{x=0}^{\Lambda} F(x) e^{2i(\frac{\Phi_{deph}(\lambda,x)}{2} + \frac{2\pi x n_0}{\lambda})} dx, \qquad (7.12)$$

where $\Phi(\lambda) = \frac{2\pi}{\lambda} \Lambda n_0 - i\bar{G}\Lambda$ is the phase shift between two mirrors and $\Phi_{deph}(\lambda, x) \approx \frac{\Phi(\lambda)}{2} + \frac{2\pi}{\lambda} x n_0$ is the phase shift between the first mirror and the emitter position. K is an eligible integer, defining the segment character - for $K \gg K_{hom}$ we get the "blurred" type of segment, for $K \approx K_{hom}$ we get the "sharp" type, which we shall use in the following. $T = 1 - R$ is the transmittivity coefficient. Total normalized emitted intensity from one emitter fixed in a position x_m is given by the sum of light emitted forward and light reflected backward in the direction of the detection system, which can be for $l_{hom} \ll L_{cavity}$ written as

$$I_m(\lambda) = I_0(\lambda)(1 + r_{total})^2, \qquad (7.13)$$

where $I_0(\lambda)$ is the normalized spectrum of the PL emission of the ensemble of Si-ncs excited within each interference maxima area. The phase mismatch between the light emitted forward and backward is taken to be in average zero due to the chaotic and disordered nature of the system, which is in good agreement with the experimental observations.

As discussed above, due to the lower excitation source coherence, only a small central part of the excitation stripe is modulated by the interference, as sketched in Fig. 7.7. Signal detected from all emitters (for m from 1 to N) excited within the central modulated part "B" of length $L_{cavity} = N\Lambda$ in Fig. 7.7 is given by the expression (being a sum of a geometric progression)

$$I_{tot}(\lambda) = \frac{I_m(\lambda)}{N} T e^{\Lambda\bar{G}} \left(\frac{1 - T^N e^{N\Lambda\bar{G}}}{1 - T e^{\Lambda\bar{G}}} \right). \qquad (7.14)$$

The normalization by N comes from the fact that we sum together N emitter contributions, each ideally equal to 1, i.e. $I_0(\lambda)$ normalized to 1. Signal detected

from the whole excitation stripe of length L (including the modulated part "B", surrounded by the two unmodulated parts "A" and "C", each of length $\frac{L-L_{cavity}}{2}$) is then given as

$$I_{det}^{DFLon}(\lambda) \approx I_0(\lambda)T^N e^{\bar{G}\frac{L-L_{cavity}}{2}} e^{\bar{G}L_{cavity}} \frac{e^{\bar{G}\frac{L-L_{cavity}}{2}} - 1}{\bar{G}} + I_{tot}(\lambda)e^{\bar{G}\frac{L-L_{cavity}}{2}} + \quad (7.15)$$

$$+ I_0(\lambda)\frac{e^{\bar{G}\frac{L-L_{cavity}}{2}} - 1}{\bar{G}},$$

where the first term describes the emission of the part "A", passing to the detector through the areas "B" and "C", the second term is the emission from the modulated part "B" and the third term represents the emission from part "C". The mode structure comes only from the central part "B", whose length is driven mainly by the excitation laser coherence length and by the value of the angle δ as discussed above. The rest of the excited area contributes only by an amplified spontaneous emission very much like in the previously described VSL method.

7.3 Cavity modes simulations in a low homogeneity material

To check the performance of our model, we have numerically simulated the shape of the mode $I_{tot}(\lambda)$ (Eq. 7.14) for different sample homogeneities l_{hom} at fixed cavity quality and fixed mode position λ_{cavity} (Fig. 7.9). The parameters for simulation were chosen to fit the best the observed results, presented throughout the following section 7.6. To eliminate the effect of gain/losses at the beginning, we consider the average net gain coefficient $\bar{G}$ equal to zero. The simulation was done for $\delta=0$, when the interference pattern quality is the highest and the cavity length is the longest one $L_{cavity} =1$ cm ($N \approx 60\ 000$), limited virtually by the sample size only. The refractive index under illumination in the interference maxima was taken to be $n=1.776$, in the interference minima $n_0=1.77$ ($\Delta n=0.006$). The segment of the cavity, contributing to the coherent backscattering of the emitted light, has been considered to be the "sharp" one, described using the exponentially decreasing reflectivity with sharply cut borders (Fig. 7.8(b)). The simulation was done for different homogeneities $l_{hom} = K_{hom}\Lambda$ for $K_{hom}=1$; 2; 3; 4 and 5 (i.e. l_{hom} of 0.17 μm; 0.33 μm; 0.50 μm; 0.66 μm and 0.83 μm). Mode peak positions and FWHM estimated from the simulated curves in Fig. 7.9 are indicated in table in Fig. 7.9.

The mode spectra FWHM in Fig. 7.9 obviously get narrower and the mode contrast (i.e. the ratio of the mode minima to the maxima) increases with increasing

Figure 7.9: *The DFL mode selection simulation for different homogeneities $K_{hom}=1, 2, ...$ 5. The mode spectra width is broadening and mode contrast is lowering with the decreasing sample homogeneity length l_{hom}. Moreover, a blue-shift of the mode peak maxima towards the limit value given by Eq. 7.2 was observed with increasing sample homogeneity. The average net gain coefficient $\bar{G}$ was considered here to be equal to zero. Table: mode peak positions and FWHM estimated from simulated curves.*

homogeneity l_{hom}. Moreover, the mode position slightly shifts to shorter wavelengths with increasing l_{hom}, as can be seen from the table in Fig. 7.9. The mode position shifts with increasing homogeneity length towards the limit theoretical value λ_{cavity} given by Eq. 7.2 for the infinitely high homogeneity length $l_{hom} \rightarrow \infty$. For the above parameters, the simulated cavity mode position in low homogeneity sample (at $\sim$600 nm) is shifted for nearly 10 nm from the theoretical λ_{cavity}, which is 590 nm. This shift we will take into account, when discussing experimental results from our samples in section 7.6.

Due to the "sharp" type of the cavity segment we can observe additional side modes appearing around 430-490 nm. Some of them are indicated in the table in Fig. 7.9, the rest of them, which is not included in the table is of too low intensity to be visible under our experimental conditions and will be neglected. Side modes occurrence in the cavity influenced spectra is characteristic for the "sharp" segment boundaries, being not involved in the spectra of samples with "blurred" inhomogeneity character and high optical quality.

The mode contrast in Fig. 7.9 is very low (note the scale on the ordinate axis), mainly due to the low homogeneity and zero net optical gain. Notice that the overall

mode intensity is lower than 1 (Fig. 7.9) even for the zero net gain coefficient (total optical losses are also equal to zero), i.e. the intensity is lowered by the cavity effect itself because of the losses caused by the induced grating reflectivity. To overcome these inevitable losses, i.e. to have $I_{tot} \approx 1$, minimal positive net gain value of $\bar{G}_{min} \approx 0.17$ cm^{-1} has to be reached at least (for above parameters $N \approx 60\ 000$, n_0=1.77, Δn=0.006, K_{hom}=4).

In Fig. 7.9 we studied the influence of the various sample homogeneity length l_{hom} on the cavity mode shape. Let us now fix the sample homogeneity and study the effect of varying angle δ, i.e. the cavity tuneability. In Figs. 7.10(a,b) we plotted the cavity mode spectral shape simulated for different angles δ, a fixed homogeneity of l_{hom}=660 nm (K_{hom}=4) and two different net gain coefficients of (a) $\bar{G}$=1 cm^{-1} and (b) $\bar{G}$=20 cm^{-1}. The mode spectra are normalized and a constant background has been subtracted. In this case, the quality of the cavity differs for each angle δ, as follows from discussion in section 7.2.1.1. This means, that the cavity length L_{cavity} has been re-calculated for each δ using Eq. 7.6 - e.g. for δ=-3° we get $L_{cavity} \sim 1$ mm ($N \sim 7000$), while for δ=0 we have the full cavity length of ~ 1 cm (N=60 000). It is clearly visible from the cavity mode shape in Figs. 7.10(a,b) that the varying total cavity length L_{cavity} and the net gain value $\bar{G}$ do not affect significantly the mode width and overall shape, predominantly given by the sample homogeneity $l_{hom} \ll L_{cavity}$. However, the mode position shifts with varying angle δ, which is in the analysis of the experimental results the most important evidence of the DFL cavity functionality, as we will demonstrate in the following sections 7.5 and 7.6. Surprising to a large extent is a very large FWHM of the modes shown in Fig. 7.10, which is much broader than expected for a lasing system. This can be related in our model to (i) a low optical quality of the sample (small l_{hom}) and/or (ii) a low DFL cavity quality (small Δn and L_{cavity}) and/or (iii) an inhomogeneously broadened ASE background, FWHM of which has been found in the previous optical gain measurements to be at least as high as 100 nm (see e.g. Fig. 6.16). The mode contrast $\frac{I_{min}}{I_{max}}$, depending on l_{hom} rather than on other parameters (for fixed Δn), is for $\bar{G}$=20 cm^{-1} and a full cavity length L_{cavity}=1 cm less than 0.4%. Due to that, it is difficult to "see" the mode structure directly. To enhance the mode visibility, we shall be comparing the "DFLon" and "DFLoff" spectra, as discussed in the next section.

7.3.1 DFL difference spectra

In order to enhance the low contrasting mode visibility, we frequently compare through sections 7.5-7.6 the spectra with the DFL cavity switched "on" $I_{det}^{DFLon}(\lambda)$ ("DFLon") and "off" $I_{det}^{DFLoff}(\lambda)$ ("DFLoff"), measured under nominally the same av-
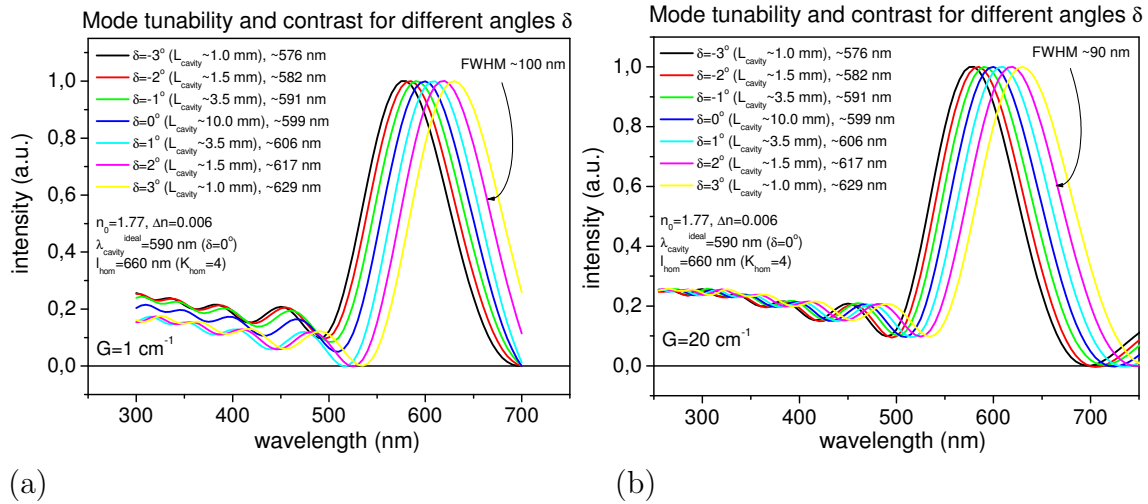
Figure 7.10: *Simulation of the cavity mode tuneability for different δ at fixed $K_{hom}=4$ ($l_{hom} \approx 660$ nm) and (a) $\bar{G}=1$ cm^{-1}; (b) $\bar{G}=20$ cm^{-1}.*

erage excitation intensity. This concept of comparison of the "DFLon" and "DFLoff" spectra is very close to that used in optical gain measurements, where the "visibility" of the low gain effects is being enhanced using the comparison of the "gain on" (VSL) and "gain off" (integrated SES) curves.

The "DFLoff" spectra were measured with a single excitation beam of intensity $2I_0$, which is in fact identical with the VSL method, so the signal is given by the same formula describing also the VSL signal: $I_{det}^{DFLoff}(\lambda, l) = I_0(\lambda)\frac{e^{\bar{G}(\lambda)l}-1}{\bar{G}(\lambda)}$.

The "DFLon" spectra were measured using two pump beams (each of intensity I_0), interfering on the sample surface. As we mentioned above, the average excitation intensity is in both "DFLoff" and "DFLon" cases similar and equal to $2I_0$, however, in the "DFLon" case is inhomogeneously distributed due to the interference occurrence - in the interference maxima reaches $4I_0$ and in the interference minima is equal to zero. Since the light amplification is a nonlinear effect with the excitation intensity, the amplified spontaneous emission (ASE) contribution will differ in "DFLon" spectra from that in "DFLoff" ones.

In the low net gain regime, where the ASE output intensity depends approximately linearly on the excitation intensity, the ASE contribution would be in both "DFLon" and "DFLoff" cases similar, while the feedback effect will be present only in the "DFLon" signal. In such a case, "DFLon" and "DFLoff" difference spectra will be fully related to the cavity mode described by our simulations.

Different will be the situation, when the present optical gain is higher. Then the difference spectra probably include both the cavity mode (tunable with δ) and the rest of the spectrally broad ASE background (insensitive to δ). In such a case,

the shift of the difference spectra with the varying angle δ can be lower then expected from our model simulations. Moreover, the contrast of the observed spectral changes (the ratio of the spectral changes amplitude minimum to its maximum) can be higher, compared to the expected one for the purely cavity mode contribution only (we observed the spectral changes contrast at the peak maxima λ_{cavity} as high as $\sim$10%, when the purely cavity mode contribution will lead to $\sim$0.3-0.4% only - see Fig. 7.10). However, in all cases, the mode tuneability remains the direct proof of the cavity functionality and its active influence on the sample emission. Equally important is that the positive sign of the difference spectrum of "DFLon" and "DFLoff" is related to a positive net optical gain ($\bar{G} > 0$), since the difference in case of the passive cavity ($\bar{G} < 0$) will be negative, because of increased light path in a lossy material. This is what we are going to study in the following experimental section - the influence of the varying angle δ and excitation intensity I_{exc} on the difference spectra $I_{det}^{diff}(\lambda)$. The theoretical discussion and a practical example of the difference spectra analysis is in more details presented in appendix section 9.3.

7.4 DFL experimental setup realization

The principal scheme of the optically induced DFL cavity is shown in Fig. 7.1. Our particular DFL experimental realization is presented in Fig. 7.11 as a top view (a) and a side view (b). The axis of the excitation beams has been vertically tilted with respect to the horizontal plane, to pass the excitation beam under the sample to the diffraction grating and then on the sample surface. Such "tilted" configuration has been chosen as a consequence of the excitation using a low coherence XeCl laser, where the asymmetrical configuration (excitation beam passing beside the sample) would lead to a much lower interference pattern quality. The excitation beam is splitted to its two first diffraction orders of almost equal intensities I_0 via diffraction on a holographic grating with 3000 gr/mm (grating period of d=333 nm) under the angle α=67.5° (according to Eq. 7.1). The zero diffraction order was cut by an absorbing screen. The revolving mirrors were first carefully adjusted using an additional HeNe laser to be perfectly perpendicular to the diffraction holographic grating and to be parallel to each other, which defines the position of revolving mirrors for angle δ=0. The maximal intensity of each diffracted beam was about $I_0^{max}\sim$144 kW/cm^2, limited by the damage threshold of the holographic grating. The interference pattern, formed on the sample active layer, was of width of $\sim$100 μm and of maximal length of $\sim$1 cm, limited by the length of the sample. The emission was detected

from the edge of the sample (cuvette) using a plastic optical fiber with small NA, connected to a spectrometer and a liquid nitrogen cooled CCD camera ($\sim$100 K). DFL experimental setup was each time, when changing angle δ, first tested using an organic dye solution in MeOH in which the tunable laser action had to be achieved. The cuvette with the dye was slightly tilted with respect to the cavity axis to prevent lasing between the polished cuvette faces. The adjusted cuvette with a lasing dye solution was then carefully replaced (using an additional HeNe laser) by a tilted cuvette containing the Si-ncs/SiO$_2$ sample to match precisely the reference sample position. All measurements were done at room temperature and the spectra were corrected for the spectral response of the detection system using a calibrated black body radiation source ORIEL (tungsten halogen lamp). The spectra were integrated in time, i.e. without time resolution (time resolved DFL measurements are planned for the future).
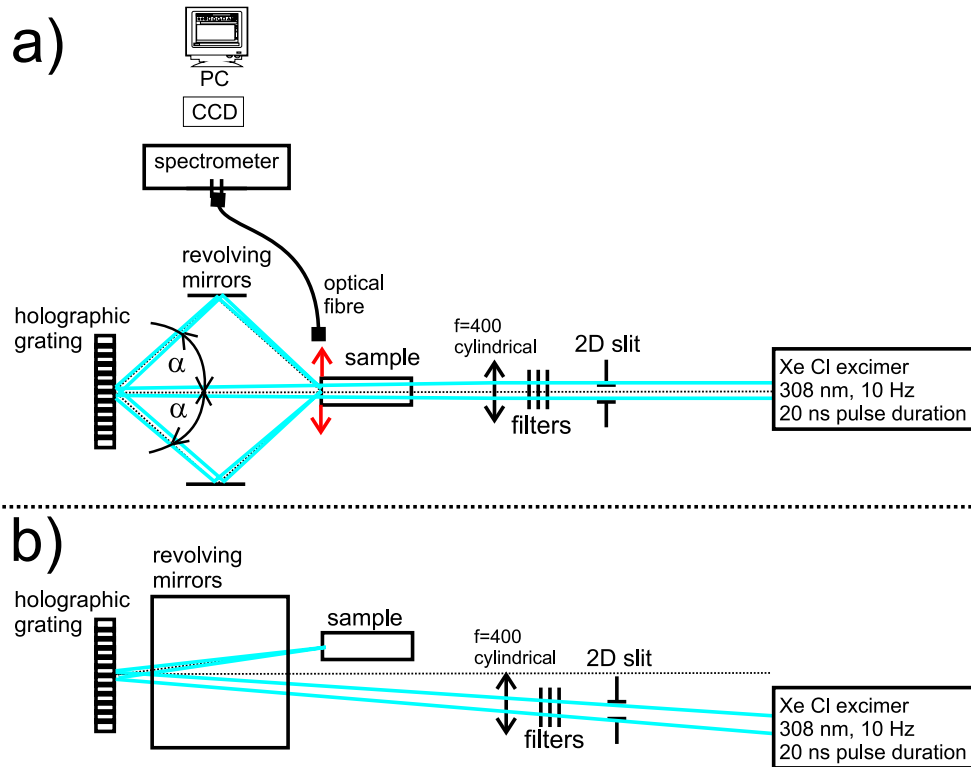
Figure 7.11: *DFL experimental setup. (a) Top view and (b) side view. Excitation beam is tilted with respect to the horizontal plane.*

7.5   DFL results in reference samples - organic dyes in methanol

The solutions of the organic dyes in methanol were used as reference samples to test the functionality of the DFL setup. The laser action in organic dyes is very sensitive to the type of the solvent, dye concentration, excitation intensity and solution homogeneity. Under our excitation conditions (XeCl excimer laser at 308 nm, 20 ns pulse duration) and our type of organic dyes, the recommended solvent is methanol (MeOH). The organic dyes concentration in MeOH is individual for each type and, besides the solution homogeneity, represents the most critical parameter for the achievement of lasing.

In Fig. 7.12(a-b) we present the "DFLon" spectra obtained in Coumarin 440/MeOH sample at a fixed cavity mode position and under a variable excitation intensity. The mode formation at $\sim$439 nm at higher excitation intensities is clearly observable. The output-input intensity dependence in the log-log scale is shown in inset of Fig. 7.12(a) and exhibits a laser threshold: the slope of the curve is super-linear (of 1.5) below the threshold and corresponds to an amplified spontaneous emission (ASE). The slope above the threshold reaches 2.7. The mode formation and narrowing of the emission spectra, as measured in a similar sample under similar experimental conditions, can be clearly seen in Fig. 7.12(b). The observed mode position at λ=438-439 nm is in good agreement with the calculated λ_{cavity}=440 nm using Eq. 7.2 for angle $\delta = 0.5°$ and refractive index n_0=1.33.

In Fig. 7.13 we present the emission spectra of solutions of Coumarin 440, 450 and 460 in MeOH, measured this time at a fixed excitation intensity and under various angles δ. The tuneability of the DFL cavity was successfully tested over the full range of possible angles $\delta \in$(-3;3)°. Outside this range, the modes appear to be unstable and of low contrast. The observed mode positions agree well with the calculated λ_{cavity} using Eq. 7.2 for the adjusted angles δ and refractive index n_0=1.33 - see table in Fig. 7.13. Observed spectra represent also a very nice evidence of the cavity length dependence on the angle δ, directly affecting the mode contrast. The further the angle δ from 0° is, the shorter the cavity is and - the lower the mode contrast become and the ASE background increases. This is demonstrated via the ratio of the mode intensity to the ASE background intensity which is highest for the angles around δ=0 and decreases for larger $|\delta| >$0.

To understand better the mode formation and spectral changes induced by the DFL cavity, we plotted in Figs. 7.14(a-c) the difference spectra I_{det}^{diff} measured in three different samples - solutions of Coumarin 440, 450 and 460 in MeOH. Three typical

(a)   (b)
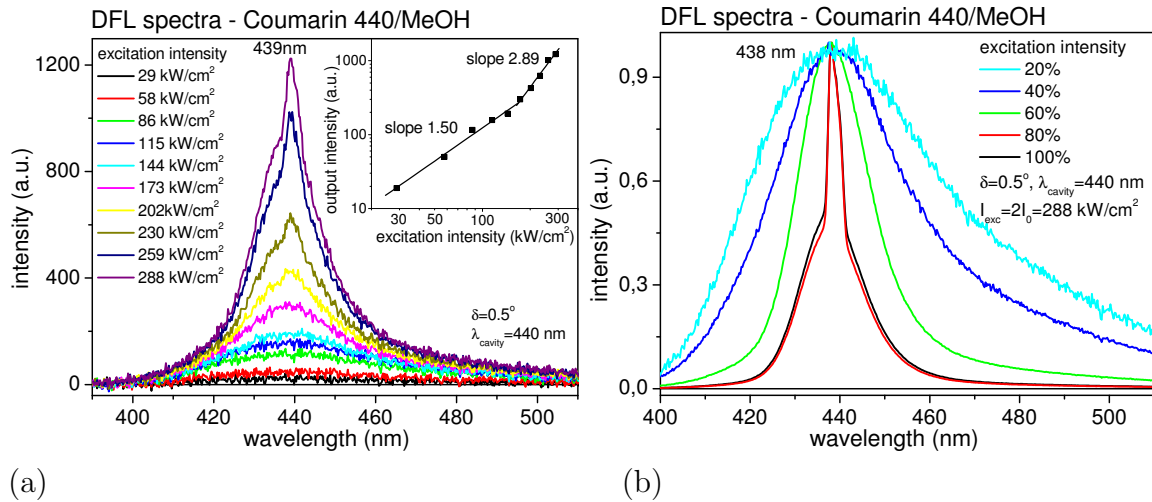
Figure 7.12: *(a) "DFLon" spectra of Coumarin 440/MeOH sample at a fixed cavity mode $\lambda_{cavity} = 440$ nm ($\delta = 0.5°$) and a variable excitation intensity (from $I_0 = 15$ kW/cm^2 to 144 kW/cm^2). Inset: output-input intensity dependence in a log-log scale. (b) Normalized emission spectra of Coumarin 440/MeOH sample in the DFL cavity - mode formation and peak narrowing.*

color dye	δ	calculated λ_{cavity}	measured peak position
C440	1°	437.3 nm	437.9 nm
	0.5°	440.2 nm	440.8 nm
C450	0.3°	442.0 nm	442.6 nm
	0.2°	442.0 nm	442.6 nm
	-0.3°	445.0 nm	446.0 nm
	-0.9°	449.0 nm	449.9 nm
	-1.5°	453.8 nm	453.7 nm
C460	1°	457.7 nm	457.1 nm
	-2.0°	461.7 nm	461.0 nm
	-3.0°	466.0 nm	464.6 nm
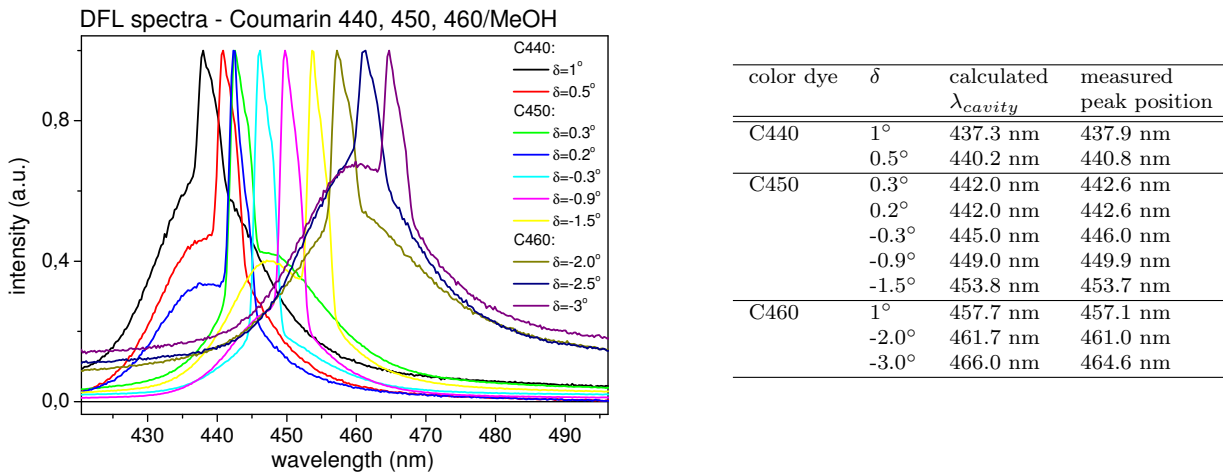
Figure 7.13: *"DFLon" spectra of solutions of Coumarin 440,450 and 460 in MeOH for different angles δ and a fixed excitation intensity of $I_0 = 144$ kW/cm^2. Calculated and measured laser wavelength are noted in the table.*

situations are displayed. Fig. 7.14(a) presents the ideal case - the "DFLoff" spectrum (red solid line) is broader and does not exhibit any mode structure, while the "DFLon" spectrum (black solid line) is narrower with a well shaped cavity mode at 447 nm given by the adjusted angle value of $\delta = -0.5°$. The difference spectrum is plotted in green line and shows a positive well shaped narrow cavity mode, surrounded with a negative parts, caused by the "DFLon" spectral narrowing. Because of the lower stability of

the lasing system at high excitation fluency, the spectral mode width can fluctuate, as can be seen from Fig. 7.14(b), where the "DFLoff" spectrum is surprisingly narrower than the "DFLon" one. Another situation can be observed from the result plotted in Fig. 7.14(c), where the ASE background intensity in "DFLon" spectra increased, compared to the "DFLoff" one and its contribution appears aside the mode structure also in the difference spectra. The last situation is probably the most interesting for us, because the very similar effect we observed in most of our Si-ncs/SiO$_2$ sample.
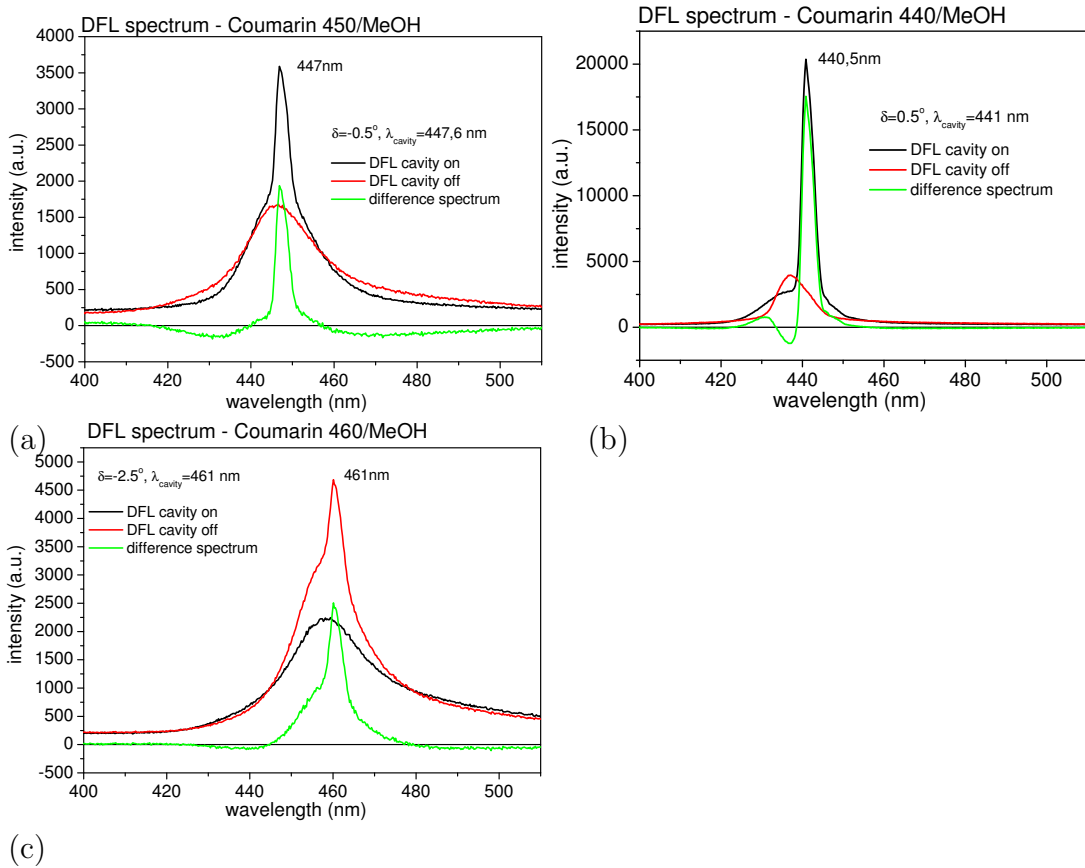
Figure 7.14: *"DFLon" (black lines) and "DFLoff" (red lines) spectra of Coumarin 440, 450 and 460 solutions in MeOH: Bragg mode formation and emission spectrum narrowing. The difference spectra are plotted in green lines. Both "DFLon" and "DFLoff" spectra were measured under the nominally same average excitation intensity I_0=144 kW/cm^2.*

To conclude this section: a successful laser action induced by the DFL cavity application was observed in all studied reference organic dye samples. These samples were each time used in the course of measurements of Si-ncs/SiO$_2$ samples (when tuning the cavity by varying the angle δ) to test the functionality of the feedback.

7.6   DFL results in Si-ncs/SiO$_2$ samples

This section represents the description of our attempt to realize a DFL in a system of densely packed Si-ncs. The occurrence of a single passage optical gain in our cuvettes containing the active Si-ncs/SiO$_2$ medium has been carefully verified, as described in chapter 6. To be sure of the DFL cavity functionality, the DFL system was during each measurement and for each different angle δ tested using a cuvette with organic dye solution. The adjusted cuvette with the lasing dye solution was then carefully replaced (with help of the HeNe laser) by a tilted cuvette containing the Si-nc luminescent layer. The cuvettes, containing the samples were always slightly tilted, with respect to the horizontal plane axis, to avoid the formation of an external resonator between the polished cuvette faces.

Our attention is focused on the emission originating firmly in Si-ncs, i.e. on the "orange" band peaked at about 600 nm. To assure a strong emission response in this spectral range, all experimental parameters of the DFL setup as holographic grating constant, revolving mirror distance, setup geometry, excitation wavelength, etc. were thus chosen to obtain the central cavity mode $\lambda_{cavity}(\delta = 0)$ near the "orange" band emission peak maxima. The mode structure is discussed in terms of the homogeneity degree of the samples and compared with the simulated modes presented in section 7.2. Let us now present the most representable results, measured in "yellow" Si-ncs/SiO$_2$ samples and various sediments of "standard" samples.

7.6.1   "Yellow" Si-ncs/SiO$_2$

Fig. 7.15(a) shows the "DFLoff" spectra, excited using a single beam of intensity $2I_0$. In such case, all spectral changes are predominantly caused by the ASE contribution, since no optical feedback is applied. The blue emission band at λ_1, originating from the SiO$_2$ matrix emission, was fitted using a single Lorentz shape curve peaked at 380-400 nm. Our main interest, however, is focused on the orange emission band spectral changes at λ_2 in the "DFLoff" spectra, originating purely from the Si-ncs emission. This orange band was fitted using a single Lorentz shape curve. The peak maximum is continuously blue-shifting with increasing excitation intensity: from 646 nm (FWHM of 142 nm) at the lowest excitation intensity to 624 nm (FWHM of 134 nm) at the highest excitation intensity. The difference $I_{det}^{DFLoff}(144\,\mathrm{kW/cm^2}) - I_{det}^{DFLoff}(4\,\mathrm{kW/cm^2})$, plotted in inset in Fig. 7.15(a), is peaked at 597 nm (FWHM of 147 nm). This spectral change can be fully ascribed to the ASE background, because no DFL cavity was present at this time.

The "DFLon" spectra in Fig. 7.15(b), on the other hand, were excited using

(a)

(b)
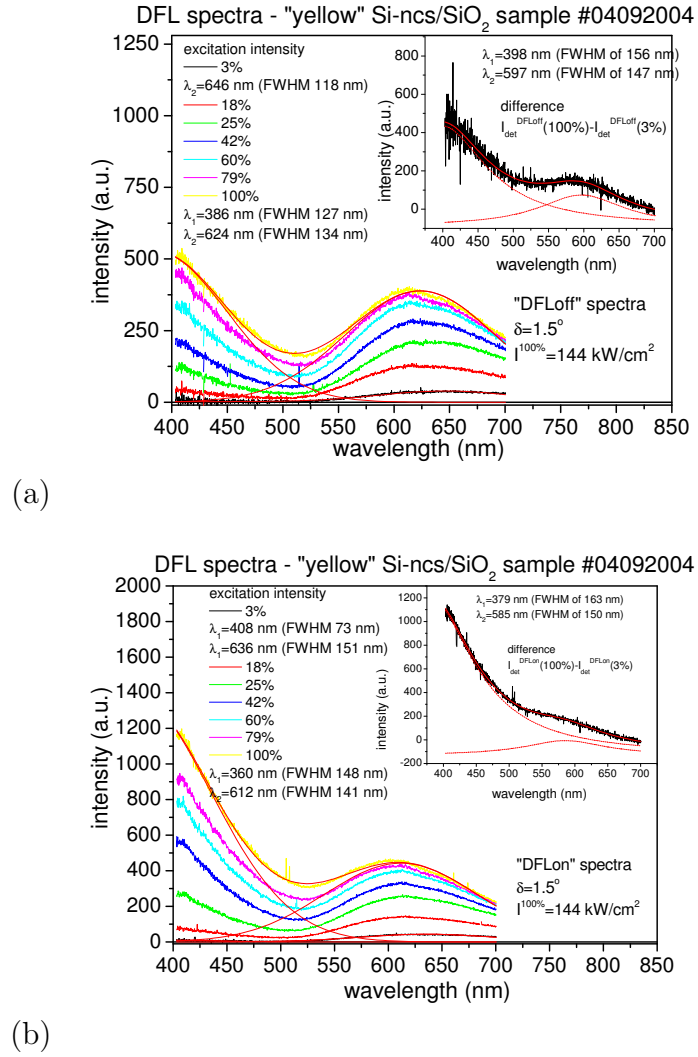
Figure 7.15: *(a) "DFLoff" and (b) "DFLon" spectra of a "yellow" Si-ncs/SiO₂ sample #04092004, measured with a fixed angle δ=1.5° and under variable excitation intensity (4-144 kW/cm²). Insets: Difference between the spectra measured at the highest and the lowest excitation intensity, fitted using two Lorentz shape curves.*

both beams (each of intensity I_0) and are thus influenced by the DFL cavity. The peak maxima of the orange emission band of "DFLon" are slightly blue-shifted with respect to that of "DFLoff" spectra shown in Fig. 7.15(a) to 636 nm (FWHM of 151 nm) at the lowest excitation intensity of 4 kW/cm² and 612 nm (FWHM of 141 nm) at the highest excitation intensity of 144 kW/cm². The corresponding difference spectrum $I_{det}^{DFLon}(144 \text{ kW/cm}^2) - I_{det}^{DFLon}(4 \text{ kW/cm}^2)$, plotted in inset of Fig. 7.15(b), is peaked at 585 nm (FWHM of 150 nm). In this case, the difference spectrum contains both the ASE background and the cavity mode contribution. Since the differences $I_{det}^{DFLoff}(144 \text{ kW/cm}^2) - I_{det}^{DFLoff}(4 \text{ kW/cm}^2)$ and $I_{det}^{DFLon}(144 \text{ kW/cm}^2) - I_{det}^{DFLon}(4 \text{ kW/cm}^2)$ lead to different results, these results confirm the strong influence of the cavity mode on the difference spectra. At the same

time, however, the presence of the ASE background can lead to a slightly different mode positions, FWHM, and mode contrast than expected from our simple model.

In Fig. 7.16 we present the difference spectra $I_{det}^{diff}(\lambda) = I_{det}^{DFLon}(\lambda) - I_{det}^{DFLoff}(\lambda)$ extracted from the "DFLon" and "DFLoff" spectra, presented above in Fig. 7.15(a,b). The FWHM of the difference spectra "orange" band gets narrower and the peak maximum shifts with increasing excitation intensity, as indicated in the table and inset in Fig. 7.16. The narrowing of the difference spectra can be a sign of the StE onset. The mode position and FWHM at the highest excitation intensities clearly converges to ∼570 nm with FWHM of ∼70 nm, which we interpret as a sign of a "laser threshold". It means that the DFL cavity performance is "switching on" at higher excitation intensities only, while at the lowest pumping intensity no DFL cavity influence appears due to either the gain absence or too low net gain value. The relatively narrow FWHM of ∼70 nm, observed at highest excitation intensities, can be related (according to our model) to a high optical quality of the sample with $l_{hom} \gtrsim 1~\mu$m. This is very interesting result, since this sample contains a half amount of Si-ncs (1 mg of "yellow" Si-ncs, instead of usual 2 mg), which is consistent with higher optical quality and thus the narrower mode width. Moreover, the refractive index, corresponding to the mode limit peak position at ∼570 nm, amounts n_0=1.64 only. This is very low value, compared to other samples, and can be again related to a lower content of Si-ncs in this sample. The mode shifting to shorter wavelengths with increasing excitation intensity in Fig. 7.16 can be related to the fact that a part of the difference spectra belongs to ASE background, which is blue shifting due to the absorption bleaching at higher excitation fluency.

These results confirm that the observed spectral mode position, FWHM and contrast can be influenced not only by the cavity effect but also by the presence of the ASE background, which cannot be neglected here. The cavity mode tuneability via varying the angle δ, however, represents a direct proof of the cavity performance and the feedback influence on the sample emission, even if obviously no lasing has been observed due to high scattering losses and/or low quality of the DFL cavity.

The cavity mode tuneability (via varying the angle δ) at a fixed excitation intensity has been studied in similar "yellow" Si-ncs/SiO$_2$ samples (a) #050506 and (b) #05122105 in Figs. 7.17(a,b). The difference spectra $I_{det}^{diff}(\lambda)$ were fitted using Lorentz shaped curves, the blue emission band related to the SiO$_2$ matrix was subtracted. The measured peak position shifts with varying angle δ, as indicated in tables in Fig. 7.17(a,b). The refractive index values n_0 were calculated to match best

DFL spectra - "yellow" Si-ncs/SiO$_2$ sample #04092004

excitation intensity	peak position (FWHM)
4 kW/cm^2	606 nm (358 nm)
26 kW/cm^2	588 nm (121 nm)
36 kW/cm^2	584 nm (90 nm)
60 kW/cm^2	577 nm (70 nm)
86 kW/cm^2	572 nm (64 nm)
114 kW/cm^2	568 nm (70 nm)
144 kW/cm^2	$\sim$556 nm (73 nm)
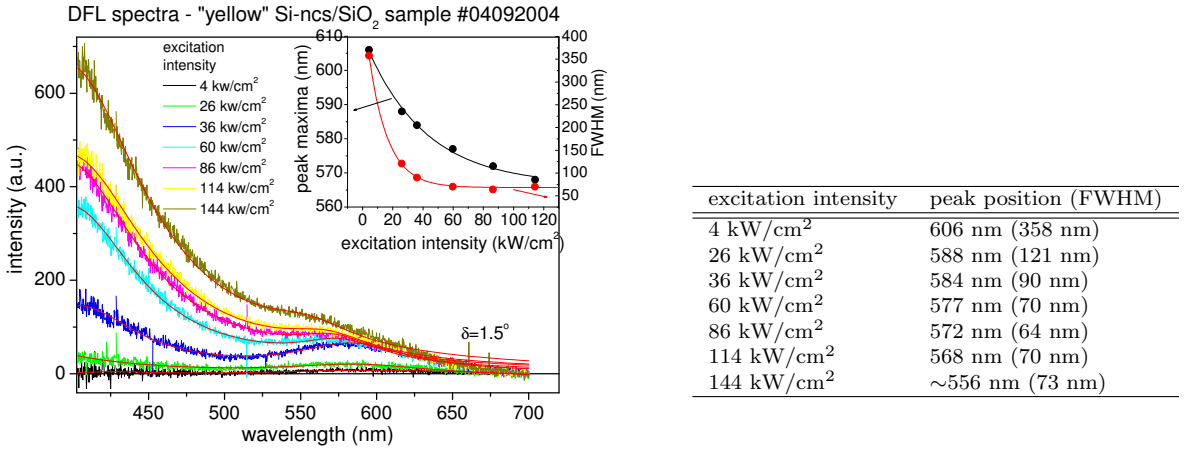
Figure 7.16: *Difference spectra $I_{det}^{diff}(\lambda)$ between the "DFLon" and "DFLoff" spectra from Fig. 7.15(a,b), measured with a fixed angle δ=1.5°. Inset: Difference spectra FWHM narrowing and the mode spectral position shifting with increasing excitation intensity. Table: Difference spectra "orange" band peak position and FWHM, fitted using Lorentz shape curve.*

the measured peak positions and then used to estimate the theoretical mode positions λ_{cavity}, indicated as arrows in Figs. 7.17(a,b). This was done making use of Eq. 7.2 and taking into account a constant red-shift of the cavity mode of about 10 nm in a low homogeneity samples, according to Fig. 7.9. The theoretically calculated mode positions using refractive indices of (a) n_0=1.754 and (b) n_0=1.694 respectively, agree reasonably with the measured peak positions indicated in tables in Figs. 7.17(a,b). According to our simulations in section 7.3, the FWHM of 130 nm can correspond to the l_{hom} smaller than 500 nm (if we assume that the mode contribution is dominant, compared to the ASE background). The refractive index value n_0=1.754, estimated in sample #050506 from the measured peak positions in Fig. 7.17(a), is somewhat higher than usual in our samples, caused obviously by higher amount of Si-ncs grains in the measured place. This can lead to lower optical quality of the sample, as supported independently by the relatively wide FWHM of the difference spectra.

The second investigated sample #05122105 (Fig. 7.17(b)), on the other hand, exhibits much higher optical quality, reflected in the narrower FWHM $\sim$80 nm of the difference spectra and lower estimated average refractive index of n_0 =1.694 (both can be related to a lower amount of Si-ncs grains in the measured place). According to our simulations, the difference spectrum FWHM of 80 nm, if related predominantly to the cavity mode, implies a higher homogeneity of the sample about l_{hom} $\approx$800 nm. The difference spectra peak position is shifting again with varying angle δ as a sign that the Si-ncs emission "feels" the DFL cavity influence. The observed mode shift, however, is slightly lower than expected when compared with the theoretically cal-

culated λ_{cavity} - see tables in Figs. 7.17(a,b). This small mismatch can be due to a higher ASE background contribution, which cannot be here simply subtracted/fitted. All these effects together with the positive sign of the difference spectra, however, indicate the positive feedback effect on the emission of the sample.

δ	calculated λ_{cavity}	measured peak position (FWHM)
-1.4°	583.8 nm	580.6 nm (137 nm)
-0.8°	588.4 nm	588.4 nm (130 nm)
0.0°	594.7 nm	591.7 nm (132 nm)

(a)

δ	calculated λ_{cavity}	measured peak position (FWHM)
-1.5°	563 nm	570 nm (82 nm)
-1.0°	567 nm	575 nm (78 nm)
-0.5°	571 nm	574 nm (75 nm)
0.5°	579 nm	579 nm (79 nm)
1.0°	584 nm	580 nm (77 nm)
1.5°	588 nm	584 nm (89 nm)

(b)
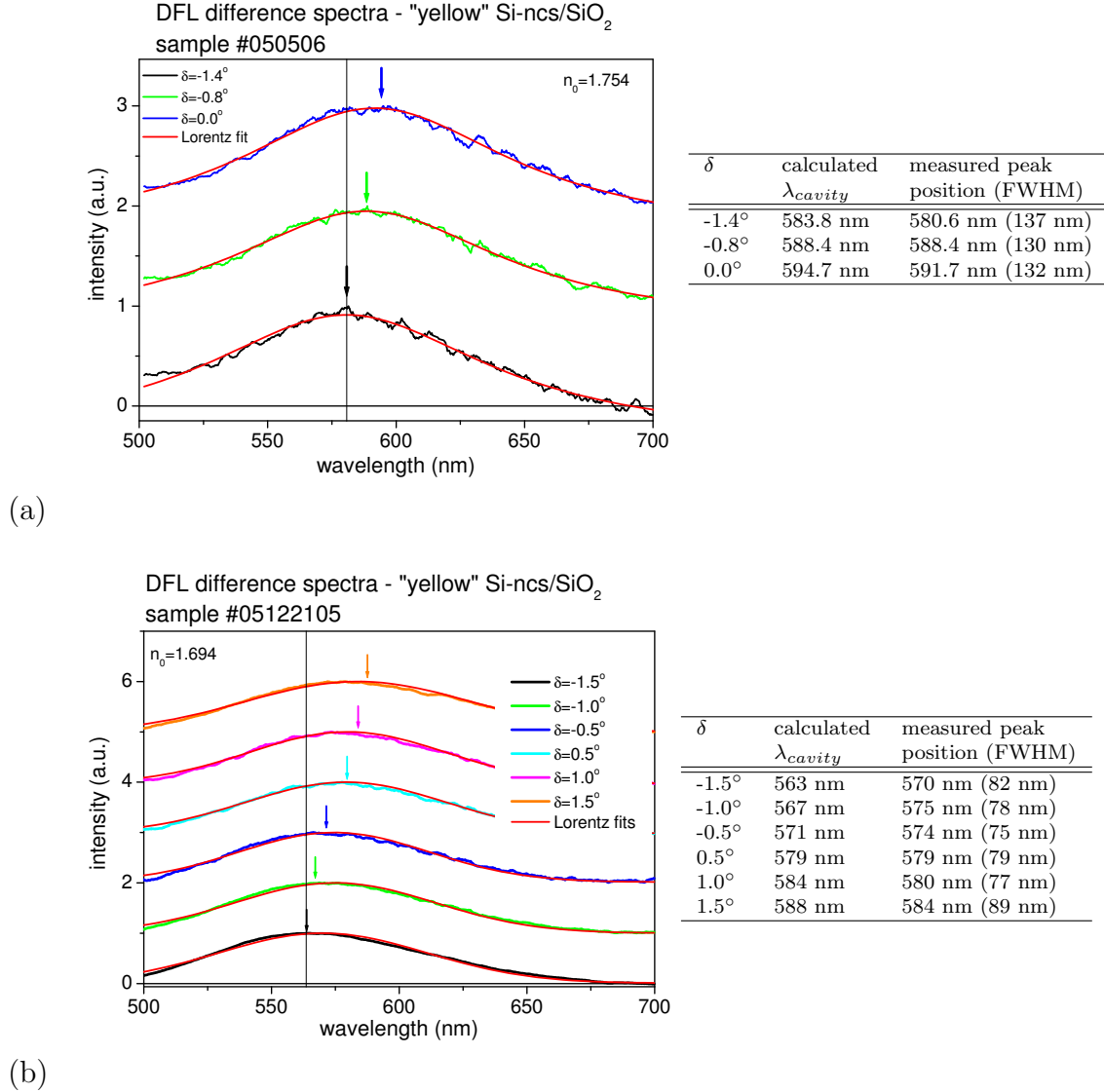
Figure 7.17: *Difference $I_{det}^{diff}(\lambda)$ spectra measured for various angles δ and a fixed excitation intensity of $I_0 = 144$ kW/cm² in "yellow" Si-nc/SiO₂ samples (a) #050506 and (b) #05122105. The blue emission band at ∼380-400 nm, related purely to the SiO₂ matrix, was fitted using a Lorentz shape curve and subtracted. The theoretically calculated cavity mode positions were calculated according to Eq. 7.2, using the estimated refractive indices. Both theoretically calculated and measured mode positions are in good agreement and are indicated as arrows. Their values are shown in tables.*

Another interesting results were observed in the "yellow" Si-ncs/SiO₂ sample #04092004, studied already in the previous Figs. 7.15 and 7.16. The difference spectra

including the blue emission band, measured this time at a fixed excitation intensity varying the angle δ are shown in Fig. 7.18(a). To enhance the visibility of the cavity mode we again plotted in Fig. 7.18(b) the difference spectra got rid of the blue emission band (fitted using a single Lorentz shape curve). The resulting difference spectra had to be fitted using two Lorentz shape curves, because an additional side modes around 490-500 nm with FWHM of ~40 nm appeared. This effect can be related to a "sharply" defined cavity segment (compare with Fig. 7.10), which corresponds to the sharply defined scattering centers in Si-ncs/SiO$_2$ sample. These scattering centers can originate from some larger clumps of Si-ncs. Fitted peak positions of the main cavity mode and of the additional side modes are indicated in table in Fig. 7.18. The refractive index, adjusted to fit the best the measured mode positions, was found to be ~n_0=1.731. Corresponding theoretically calculated mode positions (arrows in Fig. 7.18) are again indicated in the table in Fig. 7.18 and are in good agreement with the observed peak shift, proving the DFL cavity functionality and mode dominant contribution in this sample. The main mode FWHM amounts 100-145 nm, which can be related, according to our model, to the sample homogeneity average length l_{hom} of about 400-660 nm. The side modes position around 490-500 nm correspond to sample homogeneity close to $l_{hom} \approx 800$ nm. However, since the main mode FWHM can be influenced by the ASE spectrally broad band, relevant estimation of the average homogeneity length should be considered as qualitative only.

7.6.2 "Standard" 2nd sediment Si-ncs/SiO$_2$

Results very similar to those observed in the previous section in "yellow" Si-ncs/SiO$_2$ samples we observed in the "standard" 2nd sediment Si-ncs/SiO$_2$ samples. In Fig. 7.19 we show the difference spectra $I_{det}^{diff}(\lambda)$, measured under similar experimental conditions as in Fig. 7.16. A similar mode position shifting and FWHM narrowing with increasing excitation intensity were observed, both similarly converging to the limit value at ~597 nm (FWHM of ~89 nm). The mode position corresponds to the refractive index value of n_0=1.72, which is a sign of higher content of Si-ncs in the SiO$_2$ matrix. This is in good agreement with the sample parameters, since this sample contains twice as high amount of Si-ncs than the comparative "yellow" sample in Fig. 7.16. The higher amount of Si-ncs leads to both the lower optical quality, reflected in broader FWHM of ~89 nm (compared to Fig. 7.16), and higher StE, reflected in a higher mode contrast (compared again to Fig. 7.16).

The tuneability of the selected modes (difference spectra $I_{det}^{diff}(\lambda)$) via varying angle δ, similar to results in Figs. 7.17 and 7.18, was also observed in a "standard" 2nd sediment Si-ncs/SiO$_2$ sample #04092001, as shown in Fig. 7.20. The blue emission

DFL spectra - "yellow" Si-nc/SiO$_2$ sample #04092004

δ	calculated λ_{cavity}	measured main peak position (FWHM)	side mode position (FWHM)
-1.1°	578 nm	580 nm (145 nm)	487 nm (44 nm)
-0.6°	582 nm		
0.0°	587 nm	587 nm (116 nm)	490 nm (45 nm)
0.5°	591 nm	590 nm (103 nm)	514 nm (69 nm)
1.4°	600 nm	594 nm (94 nm)	501 nm (38 nm)
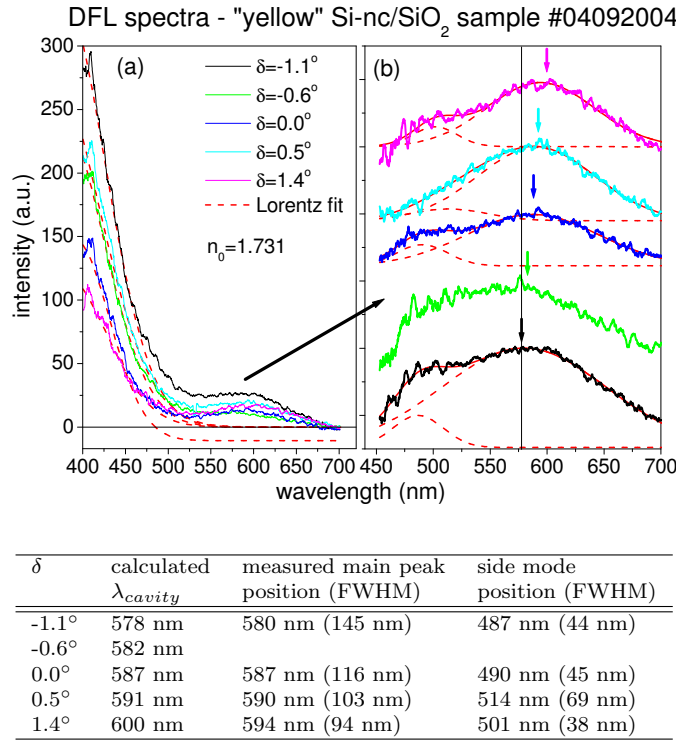
Figure 7.18: *(a) Difference spectra $I_{det}^{diff}(\lambda)$ measured at fixed excitation intensity of I_0=144 kW/cm^2 in a "yellow" Si-ncs/SiO$_2$ sample #04092004 for various angles δ from -1.1° to 1.4°. (b) Difference spectra after subtracting the blue emission band, fitted using two Lorentz shape curves - the main cavity mode and a side mode. The measured and calculated peak positions (arrows) are indicated in the table.*

DFL spectra - "standard" 2nd sediment Si-ncs/SiO$_2$ sample #04092001

excitation intensity	peak position (FWHM)
4 kW/cm^2	612 nm (226 nm)
26 kW/cm^2	589 nm (141 nm)
36 kW/cm^2	597 nm (93 nm)
60 kW/cm^2	595 nm (123 nm)
86 kW/cm^2	597 nm (105 nm)
114 kW/cm^2	598 nm (111 nm)
144 kW/cm^2	597 nm (89 nm)
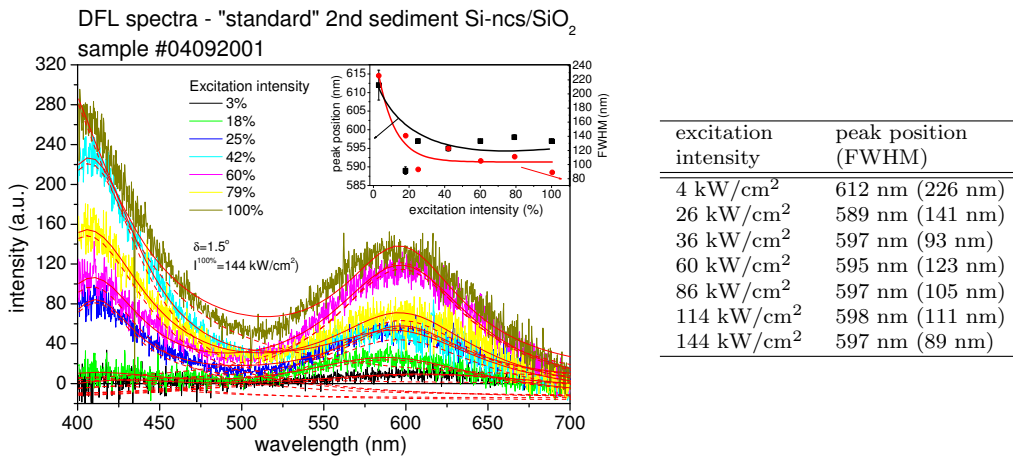
Figure 7.19: *Difference spectra $I_{det}^{diff}(\lambda)$ measured in a "standard" 2nd sediment Si-ncs/SiO$_2$ sample with a fixed angle δ=1.5° and a variable excitation intensity (4-144 kW/cm^2). Inset: FWHM narrowing and the mode spectral position shifting with increasing excitation intensity.*

band, related to SiO_2 matrix emission, was again subtracted. The difference spectra can be, as before, fitted using a Lorentz curve (red lines). The measured mode positions are indicated in the table in Fig. 7.20 and lead to an average refractive index value of approximately n_0=1.703. The theoretically calculated mode positions (arrows in Fig. 7.20), estimated according to Eq. 7.2 for refractive index n_0=1.703 (and taking into account the blue-shift of the mode position in low homogeneity samples as in Fig. 7.9) are in good agreement with the measured ones (see table in Fig. 7.20). The clear shift of the difference spectra proves the dominant role of the cavity mode contribution here.
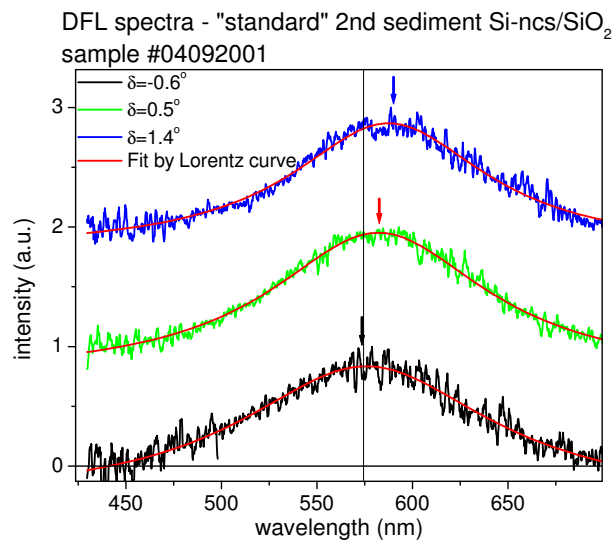
δ	calculated λ_{cavity} according to (Eq. 7.2)	fitted peak position (FWHM)
-0.6°	573 nm	575.8 nm (162 nm)
0.5°	582 nm	582.2 nm (139 nm)
1.4°	590 nm	587.6 nm (125 nm)

Figure 7.20: *Difference spectra $I_{det}^{diff}(\lambda)$ measured for three different angles δ and fixed excitation intensity of I_0=144 kW/cm^2 in a "standard" 2nd sediment Si-nc/SiO_2 sample #04092001. The blue emission band at $\sim$380-420 nm, related purely to the SiO_2 matrix was fitted using a Lorentz shape curve and subtracted. The measured and theoretically calculated mode positions (arrows) are in agreement with each other and are indicated in the table.*

7.6.3 "Standard" 4th sediment Si-ncs/SiO_2

We have already noted in several sections that the optical quality of the sample can be increased by lowering the amount of larger clumps by sedimentation. In this section we present the results obtained from the highest sediment - "standard" 4th sediment Si-nc/SiO_2 sample #04050303.

Fig. 7.21 represents the DFL spectra measured with a fixed excitation intensity

and a variable angle δ. For δ=-0.8° a low contrasting cavity mode appears at 560 nm (FWHM of 200 nm), corresponding with a relatively very low refractive index of n_0=1.668, which corresponds well with the measured refractive index of this particular sample using the Abbe hemisphere in section 7.2.1.2. For the other two angles δ, no modes originating from the Si-ncs emission (the orange-band) show up. The low mode contrast and missing modes can be due to a too low content of the Si-ncs in this type of sample (and in this particular place), which was prepared from the finest, one-hour sedimented Si-ncs powder. As we can see, such sample has a lower refractive index and preserves advantageously low scattering losses, however, at a cost of lower net gain coefficient, insufficient for a visible cavity mode building. The blue emission band around 380-400 nm, originating from the SiO_2 matrix emission, appears in all DFL spectra. Although the blue emission band may seem interesting, it is out of our primary interest here, because it is not related to the Si-ncs emission.
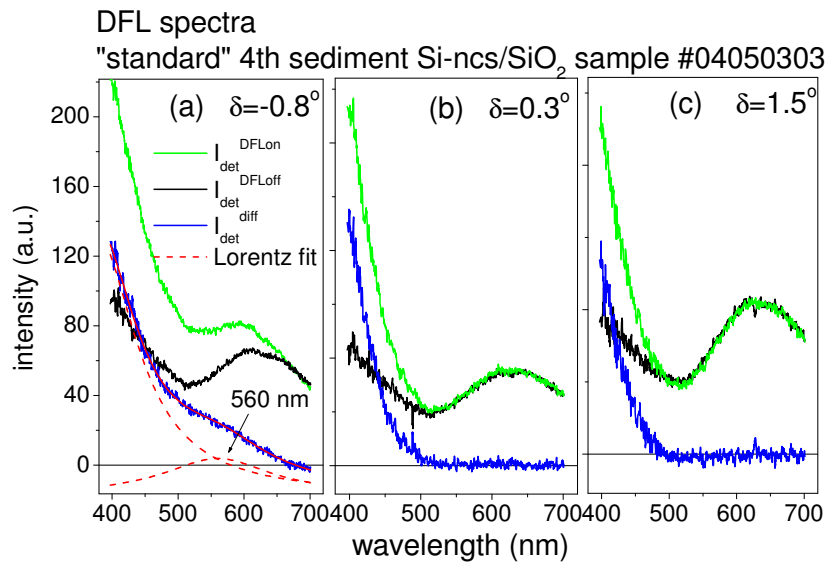
Figure 7.21: *DFL spectra of a "standard" 4th sediment Si-ncs/SiO$_2$ sample #04050303 for three different angles δ (adjusted to -0.8°, 0.3° and 1.5°).*

For completeness we show in Fig. 7.22 the difference spectra at fixed angle δ and variable excitation intensity, very much like in the Fig. 7.16. The orange emission band peak originating from the Si-ncs emission can be hardly recognized here, compared to the Fig. 7.16, probably due to a too low content of the Si-ncs in this type of sample as discussed above.

Therefore, the highest sediment of the "standard" Si-ncs/SiO$_2$ samples - the 4th sediment Si-ncs/SiO$_2$ sample - exhibits a high optical quality due to a low Si-ncs content, however, at the cost of a lower net gain coefficient, insufficient for a visible
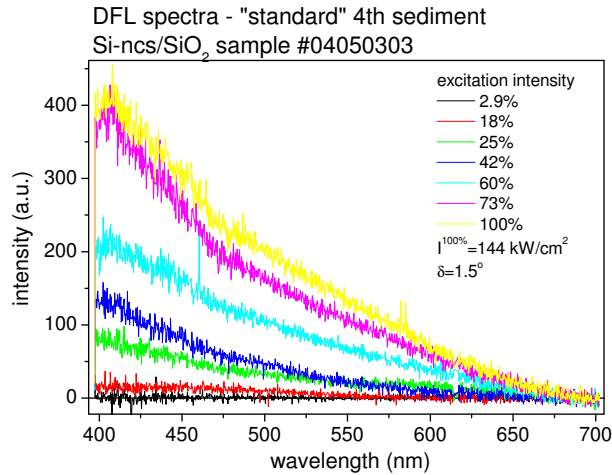
Figure 7.22: *Difference spectra $I_{det}^{diff}(\lambda)$ of a "standard" 4th sediment Si-ncs/SiO$_2$ sample #04050303, measured with a fixed angle $\delta=1.5°$ and a variable excitation intensity (4-144 kW/cm^2).*

cavity mode building. In the following section we will present results measured in a "standard" 3rd sediment Si-ncs/SiO$_2$ sample. Such sample exhibit still a higher optical quality at higher amount of Si-ncs, compared to the 4th sediment.

7.6.4   "Standard" 3rd sediment Si-ncs/SiO$_2$

In this section we present the most representative results measured in the "standard" 3rd sediment Si-ncs/SiO$_2$ sample #04050301. Fig. 7.23 shows the difference spectra $I_{det}^{diff}(\lambda)$ measured with a fixed excitation intensity and a variable angle δ [36]. The blue emission band, originating from the SiO$_2$ matrix emission, was subtracted. The resulting difference spectra seem to consist of two peaks, fitted here by two Lorentz shape curves. One at a fixed position around 550 nm, connected probably with the ASE background, since a similar band has been observed in the "fast" PL component (see section 5.2.2). The second one shifts with varying angle δ, being thus probably related to the cavity mode contribution. The fitted peak positions are indicated in the table in Fig. 7.23 and correspond to the refractive index of $n_0=1.71$. Such refractive index value is slightly lower than in a typical 2nd sediment samples and higher than measured in the 4th sediment ones. The theoretically calculated cavity mode positions (arrows in Fig. 7.23; according to Eq. 7.2) for $n_0=1.71$ are in excellent agreement with the measured ones, both indicated in the table in Fig. 7.23. This is clear evidence of the positive feedback effect.

In many cases we observed an interesting additional mode structure in the difference spectra, very much like that one simulated previously in our model with sharply

DFL spectra - "standard" 3rd sediment Si-nc/SiO$_2$
sample #04050301

δ	calculated λ_{cavity} according to (Eq. 7.2)	fitted peak position
-0.6°	576 nm	578 nm
0.0°	580 nm	582 nm
1.5°	598 nm	597 nm
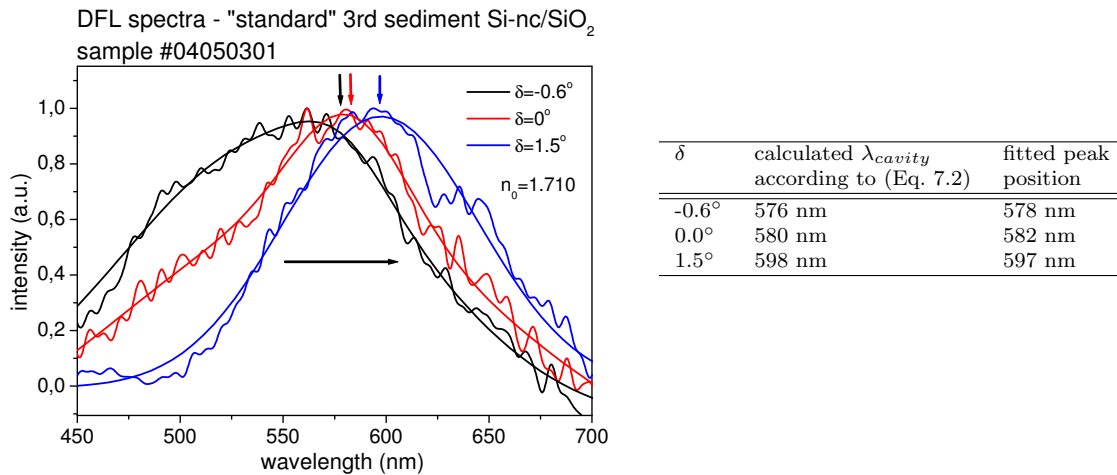
Figure 7.23: *Difference spectra $I_{det}^{diff}(\lambda)$ measured for three different angles δ=-0.6°, 0° and 1.5° and a fixed excitation intensity of I_0=144 kW/cm^2 in a "standard" 3rd sediment Si-nc/SiO$_2$ sample #04050301. The blue emission band at ~380-420 nm, related purely to the SiO$_2$ matrix, was fitted using a Lorentz shape curve and subtracted. The measured and calculated cavity mode positions (arrows) for n_0=1.71 are indicated in the table.*

defined inhomogeneities (see section 7.3). In Fig. 7.24 we show the difference spectra $I_{det}^{diff}(\lambda)$ measured on the same sample but in a different place. The main cavity mode shifts with varying the angle δ and agree with the calculated λ_{cavity} (see the table in Fig. 7.24). The side modes were observed for all angles δ around ~450 nm (FWHM of 20 nm) and correspond to a "sharply" defined inhomogeneities in the sample. Their spectral position can be related, according to our model, to $l_{hom} \approx$600 nm (compare Fig. 7.9). Possible interpretation of this observation can be put forward in terms of the occurrence of Si-ncs clumps with mean size of $\gtrsim$600 nm (in this sample and at this particular measurement place).

7.7   Conclusions

At higher volume fractions, Si-ncs tend to aggregate and form ~μm scale clusters, scattering light of comparable wavelength. This makes samples partially opaque and increases scattering losses. The optical feedback cannot be applied in a form of an external cavity. In such samples with a short homogeneity length we can apply only a distributed type of the cavity as DFL. We can summarize the main results presented in chapter 7 as follows.

- We have realized a first attempt towards the experimental manifestation of an optically pumped laser containing Si-ncs as an active medium.

DFL spectra - "standard" 3rd sediment Si-ncs/SiO$_2$
sample #04050301
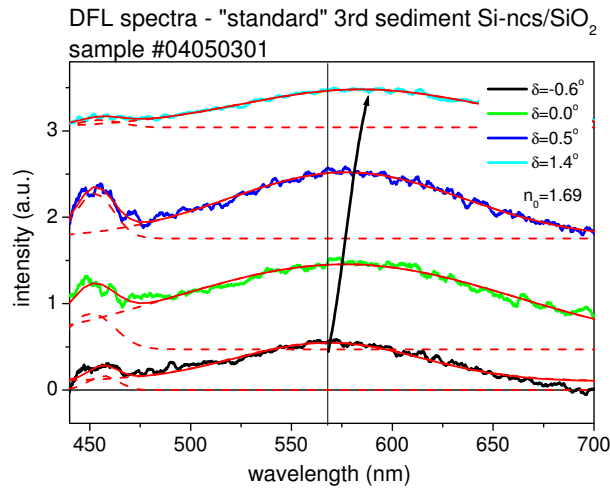
δ	calculated λ_{cavity} according to (Eq. 7.2)	fitted peak position (FWHM)	side mode
-0.6°	568.7 nm	568 nm (91 nm)	457 nm (15 nm)
0.0°	573.4 nm	576 nm (172 nm)	451 nm (22 nm)
0.5°	577.6 nm	577 nm (116 nm)	453 nm (18 nm)
1.4°	585.7 nm	584 nm (120 nm)	455 nm (22 nm)

Figure 7.24: *Difference spectra $I_{det}^{diff}(\lambda)$ of a "standard" 3rd sediment Si-ncs/SiO$_2$ sample #04050301. Spectra were measured at fixed excitation intensity of I_0=70 kW/cm^2 and variable angle δ from -0.6°, 0.0°, 0.5° to 1.4°. The blue emission band, fitted using a Lorentz shape curve, was subtracted. The measured cavity modes and side modes positions are indicated in the table together with the theoretically calculated mode positions.*

- We have shown the achievement of the optical feedback. However, output emission modes have continued to be considerably broad, which can be ascribed to several reasons: low optical gain, low pumping fluency, low quality and insufficient length of the DFL resonator and a mediocre homogeneity of the samples. Nevertheless,

  - The spectral tuneability of the output modes in the difference spectra has proved that the Si-ncs feel the resonator feedback and respond to it.

  - Occurrence of the additional modes, predicted by the model for a sample with "sharply" defined inhomogeneities, appears as another, independent proof of the DFL cavity effect on our samples.

  - The positive sign of the difference spectra has turned out to be an additional evidence for the occurrence of positive optical gain in our samples, independent of the VSL and SES measurements.

  - Comparison of the DFL theoretical model, created in the framework of the thesis, with the observed difference spectra has enabled us to quantify the inhomogeneity of the distribution of the active centers (Si-ncs) in the SiO$_2$

matrix (clusters with typical dimensions of 600-800 nm). This causes high optical losses due to the Mie scattering.

Chapter 8

CONCLUSIONS AND DISCUSSION

The results, obtained in the framework of this thesis can be summarized as follows:

- Samples preparation

  - We have developed an original method, based on a modified electrochemical etching of Si wafers with application of H_2O_2, combined with a sol-gel technique. It enables us to prepare samples with virtually arbitrary content of small Si-ncs ($\sim$2-3 nm) exhibiting blue-shifted emission spectra.

  - The doping by Phosphorus, which is dissolved in the SiO_2 sol-gel solution, probably enhances the surface passivation of Si-ncs and contributes to blue shifting and enhancement of their PL emission. Moreover, it seems to have a favorable impact on the mechanical strength of the resulting samples.

  - Both, the blue shifted emission and the high volume fraction of Si-ncs in SiO_2 matrix are believed to be advantageous for an easier stimulated emission onset.

  - The high density of Si-ncs in the SiO_2 based matrix, however, leads to Si-ncs aggregation, lowering the optical quality of the samples. Further improvement is necessary for the future Si-ncs/SiO_2 based laser development and is intensively studied at present.

  - The highest PL emission intensity has been obtained for the Si-ncs volume fractions between 10-20 vol.%.

- Photoluminescence emission properties

  - Steady-state PL spectra of our Si-ncs/SiO_2 samples are remarkably blue-shifted with respect to Si-ncs/SiO_2 samples prepared by other methods to $\sim$600-650 nm.

- The spectral blue-shift is limited down at ~600 nm, as observed also by other groups. Further filtering of the sedimented ensemble of Si-ncs in the colloidal EtOH suspension leads to a separation of the smallest Si-ncs, emitting around ~550 nm. Amount of such filtered Si-ncs is, however, insufficient for the optical gain measurements.

- Time resolved PL emission exhibits "fast" and "slow" emission components in nanosecond and microsecond scale. Moreover, we observed a sub-picosecond emission component, originating probably in quenching the fast emission component by an ultrafast trapping of carriers on Si-ncs/SiO_2 surface/interface states. Trapping of the e-h pair in the form of a self-trapped exciton leads to a spatial separation of the carriers, suppressing probably the fast Auger nonradiative process.

- The "fast" emission component contains two main components - peaks around ~480 nm and ~550 nm. The first one corresponds probably to a "free" confined exciton recombination. The band at ~550 nm is of unknown origin, probably related to defect/impurity states. The "slow" emission component is peaked around 600-650 nm and originates in self-trapped exciton recombination in surface/interface related states. It has represented our main interest pointing towards the realization of the DFL cavity.

- Optical gain

  - In measuring optical gain we have applied a novel approach - a combination of SES and VSL techniques. This has enabled us to extend the VSL applicability to relatively low net gain values.

  - In a majority of experiments (albeit not in all of them) performed on various types of our samples we have revealed a positive optical gain in the "slow" emission component, originating safely in the ensemble of Si-ncs. The values of gain at around λ=600 nm have ranged from zero to 70 cm^{-1}. This observation confirms principle features of recent results obtained by different authors in differently prepared Si-ncs samples.

  - We observed also a relatively small positive "fast" net gain in our Si-ncs/SiO_2 samples at short wavelengths around 570 nm. To the best of our knowledge, this is the first observation of this kind but ought to be considered with caution, since origin of the discovered gain is not clear.

- Optical feedback

- To best of our knowledge, we have realized a first attempt about the experimental manifestation of an optically pumped laser containing Si-ncs as an active medium, making use of optically induced DFL cavity.

- We created a simple model to describe the effect of a such distributed cavity on emission of low homogeneity samples.

- Comparison of this DFL theoretical model with the observed difference spectra has enabled us to quantify the inhomogeneity of the distribution of the active centers (Si-ncs) in the SiO_2 matrix (clusters with typical dimensions of 600-800 nm). This causes high optical losses due to the Mie scattering.

- The spectral tuneability of the output modes in the difference spectra has proved that the Si-ncs feel the resonator feedback and respond to it, even if output emission modes have continued to be considerably broad, mainly due to low quality and insufficient length of the DFL resonator and a mediocre homogeneity of the samples.

- The positive sign of the difference spectra has turned out to be an additional evidence for the occurrence of positive optical gain in our samples, independent of the VSL and SES measurements.

Let us attempt to summarize all factors which could have made lasing in our ensemble of Si-ncs in a DFL cavity difficult and let us indicate, how to proceed further:

- Aggregation of Si-ncs into clusters about the same size as the wavelength of the generated light. Possible remedy: Declusterization of Si-ncs powder during sample fabrication, possibly using ammonia.

- Low refractive index nonlinearity $\Delta n(I_{exc})$ of the matrix. Possible remedy: application of another transparent matrix with high $\Delta n(I_{exc})$. Possibly TiO_2.

- Short coherence length of the XeCl pump laser. Remedy is in principle easy - the use of another type of laser with higher degree of coherence. At the same time there are now strong indications that a fast quasi-resonant pumping (100 fs, 400 nm) is more favorable for the occurrence of optical gain than high-photon energy (308 nm) nanosecond pulses.

- Still relatively large Si-ncs size distribution, together with perhaps still too big mean Si-nc size. This seems to be an issue. More intense electrochemical etching leading to ultra-small silicon nanoparticles may contribute to resolving this problem.

- "Blinking" of Si-ncs along with rapid nonresonant carrier tunneling from smaller to larger nanoparticles are also likely to affect unfavorably light amplification in an ensemble of Si-ncs. However, their role is not fully understood at present.

Chapter 9

APPENDIX

9.1 List of samples

Tabular summary of some of the prepared samples with important preparation parameters is presented in table 9.1.

The "Borsella" comparative samples were prepared by embedding the Si-ncs powder (thanks are due to prof. E. Borsella et al. [83], who prepared the Si-ncs powder by laser pyrolysis and high temperature annealing) into our standard sol-gel SiO_2 P509 matrix, no sedimentation was applied. The powder consists of relatively large Si-ncs of the diameter around 5 nm [83].

9.2 Optical gain

9.2.1 "White" Si-ncs/SiO_2 sample

"White" sample represents the last sample generation, prepared using an intense H_2O_2 etching treatment, which results in slightly different Si-ncs surface passivation and smaller crystallite core size. The slight difference in the surface passivation can lead to a different StE dynamics. To investigate this, we performed time-integrated and time-resolved VSL and SES measurements, presented in the following.

The time-integrated VSL spectra measured in a "white" Si-ncs/SiO_2 sample #05122101 are shown in Fig. 9.1(a-b). The VSL curves in Fig. 9.1(a) were fitted using Eq. 6.2. Estimated net gain values $G(\lambda)$ form a gain spectrum, plotted in Fig. 9.1(b), the values are indicated in the table. No positive gain has been found in this case. We present the gain spectrum here, because the overall tendency is the same as observed in the samples with a positive net gain coefficient. This can be related to positive material gain $g(\lambda)$, however, overwhelmed by the high optical losses $\alpha(\lambda)$, which leads to a negative net gain value $G(\lambda) = g(\lambda) - \alpha(\lambda)$.

Sample No.	sediment	Si-ncs [mg]	P509 [ml]	centrifuge
	"standard"			
04102103	non-sedimented	2	0.5	10 min, 2500 revs/min
04050601	1st sediment	1.5	0.5	
021018	2nd sediment	2	0.4	
04050602	2nd sediment	1.5	0.5	
04050603	2nd sediment	1.5	0.5	10 min, 2500 revs/min
04050605	2nd sediment	2.5	0.5	10 min, 2500 revs/min
04050606	2nd sediment	1.5	0.5	10 min, 2500 revs/min
04050607	2nd sediment	1	0.5	10 min, 2500 revs/min
04092001	2nd sediment	2	0.4	10 min, 2500 revs/min
04092002	2nd sediment	1	0.4	10 min, 2500 revs/min
04050301	3rd sediment		0.5	
04050302	3rd sediment		0.5	10 min, 2500 revs/min
04050303	4th sediment		0.5	10 min, 2500 revs/min
04050604	4th sediment		0.5	10 min, 2500 revs/min
	"yellow"			
04092003		2	0.4	10 min, 2500 revs/min
04092004		1	0.4	10 min, 2500 revs/min
04100502		3	0.5	10 min, 2500 revs/min
04102101		2	0.5	5 min, 2500 revs/min
050506		2	0.4	10 min, 2500 revs/min
05122104		2	0.4	2 min, 3000 revs/min
05122105		2	0.4	2 min, 3000 revs/min
05122106		3	0.4	2 min, 3000 revs/min
	"white"			
05122101		2	0.4	2 min, 3000 revs/min
05122102		2	0.4	2 min, 3000 revs/min
05122103		2	0.4	2 min, 3000 revs/min
	"Borsella"			
04100501		1	0.5	10 min, 2500 revs/min
04102102		1	0.5	10 min, 2500 revs/min
	"pure SiO$_2$ matrix"			
05122112		0	0.5	

Table 9.1: *List of samples.*

The time-resolved VSL and SES measurements on the "slow" gain component measured in another place of the same "white" Si-ncs/SiO$_2$ sample #05122101 are shown in Figs. 9.2(a,b). The signal was detected at the signal maxima at 620 nm using a PMT and a boxcar integrator with the gate delay of 10 μs and gate width of 10 μs. The excitation conditions remain unchanged. The optical losses of $\sim$14 cm^{-1} were estimated from the SES curve in Fig. 9.2(a), which is a sign of a good optical quality at this particular place of the sample. The net gain coefficient was estimated using Eq. 6.7(fit in Fig. 9.2(b), solid lines) from the VSL (symbols) and integrated SES (lines) difference curves plotted in Fig. 9.2(b)(symbols). The net gain coefficient increases with the increasing excitation intensity from zero for the lowest excitation

intensity of 0.8 MW/cm^2 up to $\sim$11 cm^{-1} for the highest excitation intensity of 4.0 MW/cm^2. The positive difference of the integrated SES and VSL curves together with the values of net gain which are increasing with increasing excitation intensity are again good evidence of the StE onset.

Emission wavelength	net gain
450 nm	-7.9±0.4 cm^{-1}
500 nm	-6.5±0.4 cm^{-1}
550 nm	-4.2±0.5 cm^{-1}
580 nm	-3.7±0.5 cm^{-1}
600 nm	-3.6±0.5 cm^{-1}
650 nm	-3.5±0.5 cm^{-1}
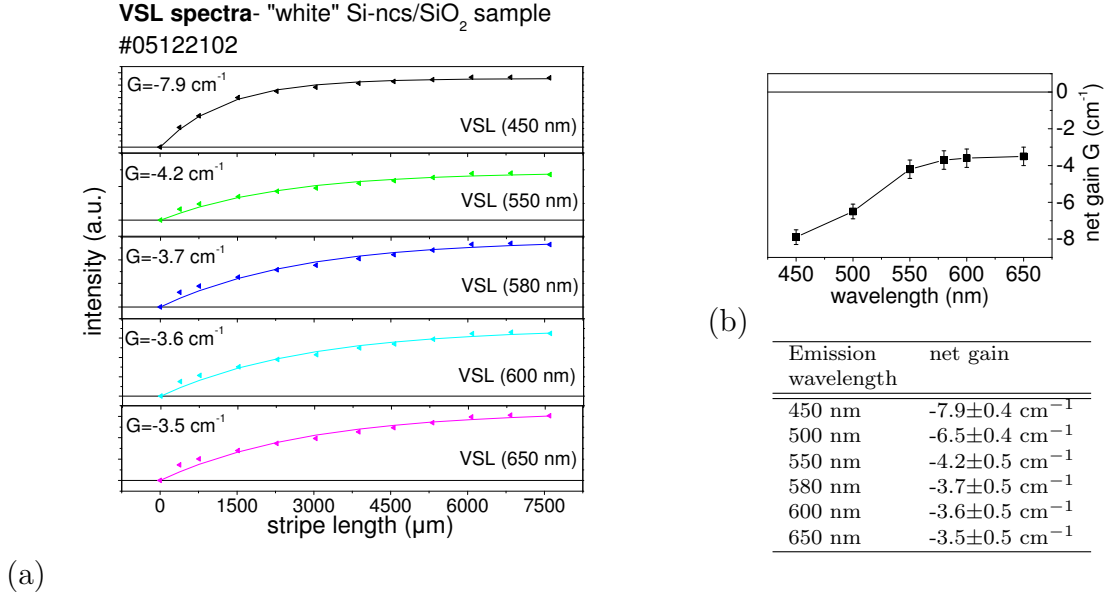
Figure 9.1: *(a) The time-integrated VSL curves (symbols) measured in a "white" Si-ncs/SiO$_2$ sample #05122101 at fixed emission wavelengths. The estimated net gain values (solid lines are the fit curves), indicated in the table, form a negative gain spectrum, presented in (b).*
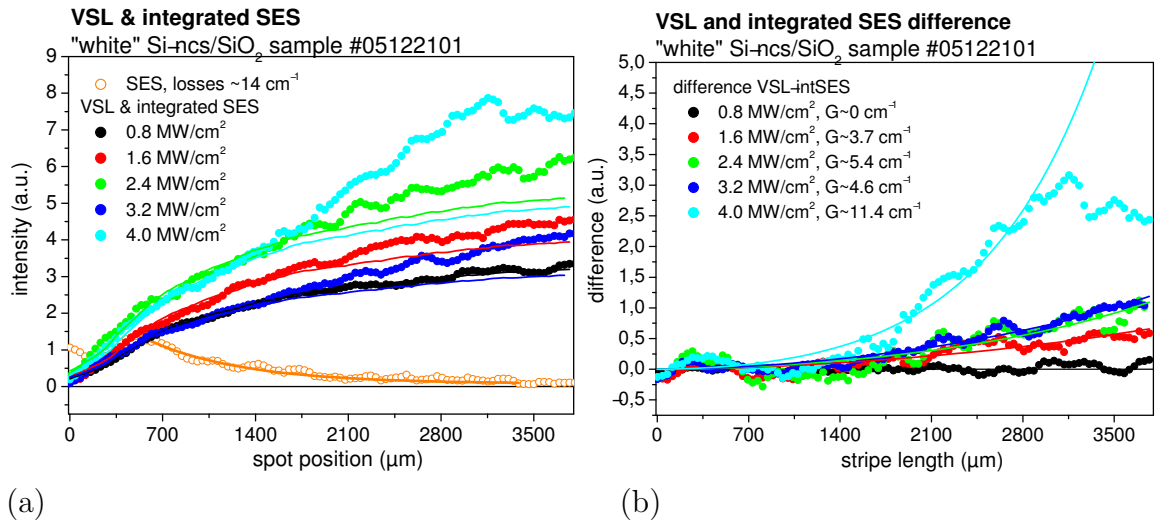
Figure 9.2: *(a) "Slow" VSL and SES (symbols) measured in a "white" Si-nc/SiO$_2$ sample #05122101 at 620 nm. VSL curves are compared with integrated SES (solid lines). (b) VSL and integrated SES differences (symbols), fitted according to Eq. 6.7 (solid lines). Increasing difference curve with higher excitation intensity is a clear evidence of the StE onset.*

Results of the "fast" VSL and SES measurement in a "white" Si-ncs/SiO_2 sample
are shown in Figs. 9.3(a,b). The signal was detected at 570 nm with the gate of width
of 150 ns, coincident with the excitation pulse. The VSL and SES curves are shown
in Fig. 9.3(a) (symbols), the difference of the VSL and integrated SES is plotted in
the (b, symbols). Optical losses estimated from the SES curve were evaluated to
be around 13 cm^{-1}, which is relatively low. The integrated SES curve (solid line in
Fig.9.3(a)) obviously differs from the VSL curve for longer stripe lengths and higher
excitation intensities, which can be a sign of the StE onset. In Fig. 9.3(b) we plotted
the VSL and integrated SES difference (symbols), from which the net gain value can
be estimated according to Eq. 6.7(solid line). The difference curve rise above the
"zero" curve above the threshold excitation intensity of $\sim$3 MW/cm^2. Estimated
gain values are shown in reasonable agreement with foregoing results measured in
another place of the same sample.

(a)   (b)
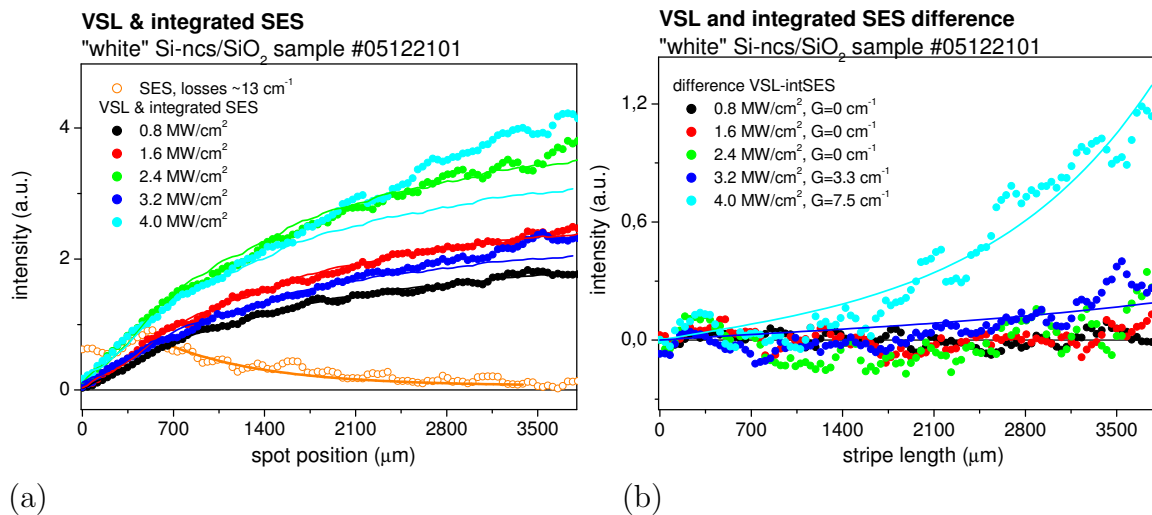
Figure 9.3: *"Fast" emission component detected at 570 nm. (a) VSL, SES (symbols)
and integrated SES (solid lines) in "white" Si-nc/SiO_2 sample #05122101. (b) Difference
between VSL and integrated SES (symbols), fitted according to Eq. 6.7(solid lines).*

Very similar results, measured in the same sample but on another place are shown
in Fig. 9.4. The signal was detected at the peak maximum at 570 nm using a PMT and
a boxcar integrator with the gate width of 1 μs (longer integration then previously),
coincident with the excitation pulse. Higher optical losses of $\sim$59 cm^{-1} were estimated
from the SES curve, which is a sign of lower optical quality at this particular place
of the sample. The VSL signal was excited using a stripe of a variable length under
a variable intensity from 0.4 MW/cm^2 up to 4 MW/cm^2. The VSL curves again
obviously differ from the integrated SES curves, as presented in Fig. 9.4(a). The
difference curves, plotted in Fig. 9.4(b), increase with the excitation intensity, which

can be sign of the StE onset. The net gain values were estimated from the difference curves using Eq. 6.7 and are very similar to that measured previously from another place in this sample.

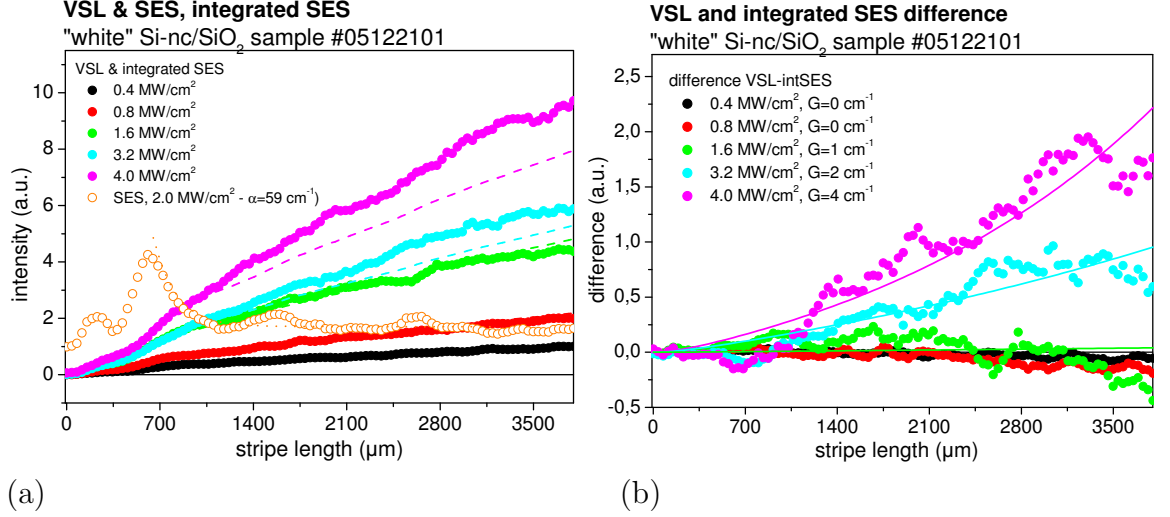**Figure 9.4:** *"Fast" emission component detected at 570 nm. (a) VSL and SES in a "white" Si-nc/SiO₂ sample #05122101. (b) VSL and integrated SES difference for different excitation intensities.*

For the sake of clearness we also present here the VSL and SES measurements in another "white" Si-ncs/SiO₂ sample, measured under similar excitation and detection conditions (at λ=570 nm), where no StE onset has been achieved (Fig. 9.5). The presented VSL and integrated SES curves match over the full range of the stripe lengths for all tested excitation intensities. The optical losses were relatively very low, which can be related to relatively high optical quality of the sample, however, at the expense of a lower Si-ncs density, which was probably not sufficient for StE onset.

9.2.2 "Yellow" Si-ncs/SiO₂ sample

The "yellow" Si-ncs/SiO₂ sample represent another type of samples, prepared using an additional H_2O_2 etching treatment. One of the most representative results of "fast" VSL and SES detected at 570 nm is shown in Fig. 9.6. The difference spectra are positive and increase from zero with increasing excitation intensity. The net gain values were estimated using Eq. 6.7 to increase from 0 cm^{-1} for the lowest excitation intensity, where the VSL and integrated SES curves are similar (no StE present), up to 15 cm^{-1} for the highest excitation intensity.
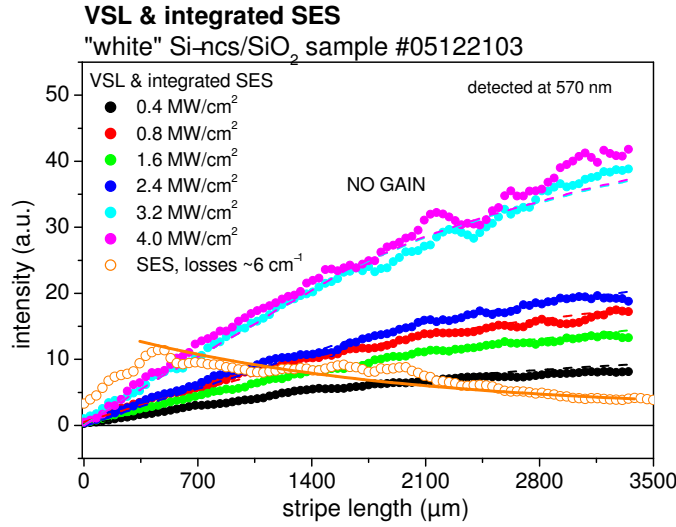
Figure 9.5: *"Fast" emission component detected at 570 nm. VSL and SES in a "white" Si-nc/SiO$_2$ sample #05122103. No net gain is observed, probably due to a lower Si-ncs density, insufficient for the StE onset.*

(a)   (b)
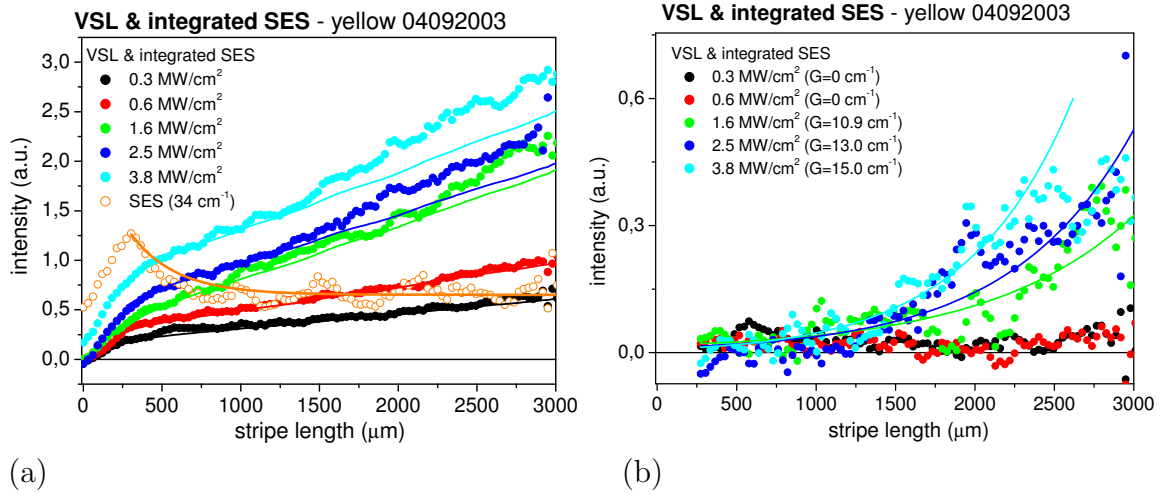
Figure 9.6: *"Fast" emission component at 570 nm. (a) VSL and SES in a "yellow" Si-nc/SiO$_2$ sample #04092003. (b) VSL and integrated SES difference for different excitation intensities. The presence of positive net gain confirms good sample quality and is coherent with the above results.*

9.3   DFL difference spectra

The influence of the DFL cavity on the emission is twofold: (i) due to the inhomogeneous excitation by interference pattern, the intensity of the emission will change (the excitation intensity at the interference maxima reaches $4I_0$, at the interference minima is equal to zero); (ii) due to the periodical modulation of refractive index, the

emission spectra shape will change, i.e. a cavity mode will be selected.

These effects can be expressed in a simple way by a linear increase of the whole spectra by the normalization coefficient a and as a small nonlinear change of the spectral shape expressed as a small increment $\Delta I(\lambda)$, i.e. $I_{det}^{DFLon}(\lambda) \approx aI_{det}^{DFLoff}(\lambda) + \Delta I(\lambda)$. This approximation is valid in our case, since the emission of different Si-ncs emitters is uncorrelated, the ASE background is inhomogeneously broadened and the studied mode structure is of low contrast due to lower homogeneity of the sample and shorter L_{cavity}. Slightly different situation will be in high gain and high optical quality samples, where it is not possible to include the spectral changes $\Delta I(\lambda)$ as a small increment, however, in such case no "DFLon" and "DFLoff" comparison is necessary. In our experimental setup we can define the coefficient a simply as a ratio of $I_{det}^{DFLon}(\lambda)$ and $I_{det}^{DFLoff}(\lambda)$ at λ=700 nm, where the feedback and gain effect can be neglected, i.e. $a = \frac{I_{det}^{DFLon}(700\ nm)}{I_{det}^{DFLoff}(700\ nm)}$.

Finally, the $I_{det}^{DFLon}(\lambda)$ and $I_{det}^{DFLoff}(\lambda)$ spectra comparison can be done as a difference or ratio of $I_{det}^{DFLon}(\lambda)$ and $I_{det}^{DFLoff}(\lambda)$ spectra. Because the cavity mode corresponds with the $\Delta I(\lambda)$, the difference spectrum $I_{det}^{diff}(\lambda) \equiv I_{det}^{DFLon}(\lambda) - aI_{det}^{DFLoff}(\lambda) \approx \Delta I(\lambda)$ will lead to better results (i.e. more visible spectral changes $\Delta I(\lambda)$) than the spectra ratio, where $I_{det}^{rel}(\lambda) \equiv \frac{I_{det}^{DFLon}(\lambda)}{I_{det}^{DFLoff}(\lambda)} \approx \frac{aI_{det}^{DFLoff}(\lambda) + \Delta I(\lambda)}{I_{det}^{DFLoff}(\lambda)} = a + \frac{\Delta I(\lambda)}{I_{det}^{DFLoff}(\lambda)}$. Measured difference spectrum $I_{det}^{diff}(\lambda)$ thus demonstrate mainly the feedback effect and of course, should be tunable with varying the angle δ.

An instructive example of the difference spectra $I_{det}^{diff}(\lambda)$ analysis is shown in Fig. 9.7, where the "DFLon" (green line) and "DFLoff" (black line) spectra, measured in a "standard" 2nd sediment Si-ncs/SiO$_2$ sample #04092001 are plotted. The as measured "DFLoff" spectrum was normalized to $aI_{det}^{DFLoff}(\lambda) \equiv \frac{I_{det}^{DFLon}(700\ nm)}{I_{det}^{DFLoff}(700\ nm)} I_{det}^{DFLoff}(\lambda)$ (red line) and subtracted from "DFLon" to get the enhanced spectral shape change $\Delta I(\lambda)$. The difference $I_{det}^{diff}(\lambda) = \Delta I(\lambda)$ (blue line) was fitted (red dashed lines)- for the clarity of the presentation - using two Lorentziens: a blue-band peak around 400 nm related to the SiO$_2$ matrix contribution and the orange emission band related to the Si-ncs emission. The latter, on which our attention is focused, is peaked at λ =586 nm with FWHM of 128 nm. As we discussed above in section 7.3.1, the broad FWHM of the difference spectra can be related to (i) a low optical quality of the sample, provided the cavity mode contribution dominantly affect the difference spectra shape; a low quality of the DFL cavity (too low nonlinear changes of refractive index or to short cavity length L_{cavity}); (iii) an inhomogeneously broadened ASE background contribution. The ASE presence in the difference spectra can hinder the clear interpretation of the spectral changes in terms of the cavity mode. The difference spectra tuneability with angle δ, however, remains the direct proof of the

dominant role of the cavity mode in the difference spectra and the cavity functionality
and its active influence on the sample emission. The positive sign of the difference
spectra is also an important feature, related to a positive net optical gain ($\bar{G} > 0$),
since the difference in case of the passive cavity ($\bar{G} < 0$) will be negative, because of
increased light path in a lossy material (see Fig. 7.9). The study of the influence of
the varying angle δ and excitation intensity I_{exc} on the difference spectra $I_{det}^{diff}(\lambda)$ is
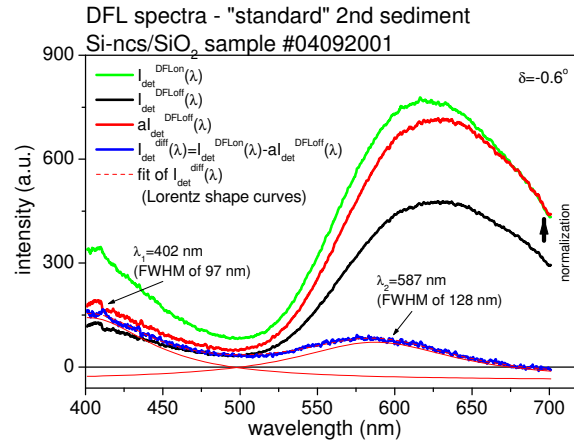the main subject of the DFL experimental section 7.6.

Figure 9.7: *DFL spectra of a "standard" 2nd sediment Si-ncs/SiO$_2$ sample #04092001.
Signal was detected using a nitrogen cooled CCD camera. The excitation intensity was
I_0=144 kW/cm^2, the cavity mode was adjusted by fixing the angle $\delta = -0.6°$.*

Bibliography

[1] *http://www.intel.com/research/platform/sp/hybridlaser.htm.*

[2] *http://www.intel.com/technology/mooreslaw/index.htm.*

[3] L. C. Kimerling. *Silicon microphotonics.* Appl. Surf. Sci., **159-160**, 8–13 (2000).

[4] L. C. Kimerling. *Photons to the rescue: Microelectronics becomes Microphotonics.* The Electrochemical Society Interface, page 28 (summer 2000).

[5] N. Mathur. *Beyond the silicon roadmap.* Nature, **419**, 573–574 (10th October, 2002).

[6] *http://www.itrs.net/reports.html.*

[7] D. J. Lockwood, editor. *Light Emission in Silicon - From Physics to Devices*, volume Semiconductors and Semimetals 49. Academic Press USA (1998).

[8] A. Masaaki, H. Shoji, M. Toshiaki and Y. Kazuo. *Performance and hot-carrier effects of small CRYO-CMOS devices.* IEEE Transactions on Electron Devices (ISSN 0018-9383), **ED-34**, 8–18 (1987).

[9] G. T. Reed. *Device physics: The optical age of silicon.* Nature, **427**, 595–596 (12th February, 2004).

[10] J. Faist. *Optoelectronics: Silicon shines on.* Nature, **433**, 691–692 (17th February, 2005).

[11] K. Wada, D.H. Ahn, D.R. Lim, J. Michel and L.C. Kimerling. *Si microphotonics for optical interconnection.* Thin Solid Films, **508**, 418–421 (2006).

[12] *http://www.intel.com/research/platform/sp/.*

[13] *http://hyperphysics.phy-astr.gsu.edu/hbase/tables/elabund.html.*

[14] A. Liu, R. Jones, L. Liao, D. Samara-Rubio, D. Rubin, O. Cohen, R. Nicolaescu and M. Paniccia. *A high-speed silicon optical modulator based on a metaloxidesemiconductor capacitor.* Nature, **427**, 615–618 (2004).

[15] L. T. Canham. *Silicon quantum wire array fabrication by electrochemical and chemical dissolution of wafers.* Appl. Phys. Lett., **57**(10), 1046 (1990).

[16] L. Pavesi, L. Dal Negro, C. Mazzoleni, G. Franzo and F. Priolo. *Optical gain in silicon nanocrystals.* Nature, **408**, 440 (2000).

[17] *http://optics.org/cws/article/research/11347.*

[18] S. G. Cloutier, P. A. Kossyrev and J. XU. *Optical gain and stimulated emission in periodic nanopatterned crystalline silicon.* Nature materials, **4**, 887 (2005).

[19] H. Rong, A. Liu, R. Jones, O. Cohen, D. Hak, R. Nicolaescu, A. Fang and M. Paniccia. *An all-silicon Raman laser.* Nature, **433**, 292–294 (2005).

[20] *http://www.intel.com/research/platform/sp/hybridlaser.htm.*

[21] K. Luterová, I. Pelant, I. Mikulskas, R. Tomasiunas, D. Muller, J.-J. Grob, J.-L. Rehspringer and B. Hönerlage. *Stimulated emission in blue-emitting Si^+-implanted SiO_2 films?* J. Appl. Phys., **91**, 2896 (2002).

[22] P. M. Fauchet, J. Ruan, H. Chen, L. Pavesi, L. Dal Negro, M. Cazzaleni, R. G. Elliman, N. Smith, M. Samoc and B. Luther-Davies. *Optical gain in different silicon nanocrystal systems.* Opt. Mater., **27**, 745 (2005).

[23] J. Ruan, P. M. Fauchet, L. Dal Negro, M. Cazzaleni and L. Pavesi. Appl. Phys. Lett., **83**, 5479 (2003).

[24] L. Dal Negro, M. Cazzaleni, L. Pavesi, S. Ossicini, D. Pacifici, G. Franzo, F. Priolo and F. Iacona. *Dynamics of stimulated emission in silicon nanocrystals.* Appl. Phys. Lett., **82**, 4636 (2003).

[25] M. Cazzaleni, D. Kovalev, L. Dal Negro, Z. Gaburro and L. Pavesi. *Polarized Optical Gain and Polarization-Narrowing of Heavily Oxidized Porous Silicon.* Phys. Rev. Lett., **93**, 207402 (2004).

[26] S. Ossicini, L. pavesi and F. Priolo. *Light Emitting Silicon for Microphotonics*, volume 194. Springer Berlin (2003).

[27] P. Knápek, K. Luterová, J. Kočka, A. Fejfar, I. Pelant, J. Linnros and N. Lalic. *Short-term degradation of porous silicon light-emitting diodes.* J. Luminescence, **72-4**, 992 (1997).

[28] J. Linnros, N. Lalic, P. Knápek, K. Luterová, J. Kočka, A. Fejfar and I. Pelant. *Instabilities in electroluminescent porous silicon diodes.* Appl. Phys. Lett., **69**, 833 (1996).

[29] J. Kočka, J. Oswald, A. Fejfar, R. Sedlacik, V. Železný, H. TheHa, K. Luterová and I. Pelant. *Charge transport in porous silicon: Considerations for achievement of efficient electroluminescence.* Thin Solid Films, **276**, 187 (1996).

[30] V. Švrček, I. Pelant, J. L. Rehspringer, P. Gilliot, D. Ohlmann, O. Crégut, B. Hönerlage, T. Chvojka, J. Valenta and J. Dian. *Photoluminescence properties of sol-gel derived SiO_2 layers doped with porous silicon.* Mater. Science & Engineering C: Biomimetic and Supramolecular Systems, **19**, 233 (2002).

[31] K. Dohnalová, K. Luterová, J. Valenta, J. Buršík, M. Procházka, V. Křesálek, B. Hönerlage and I. Pelant. *Grains of porous silicon embedded in SiO_2: Studies of optical gain and electroluminescence.* Solid State Phenomena, **99-100**, 31 (2004).

[32] K. Luterová, K. Dohnalová, V. Švrček, I. Pelant, J. P. Likforman, O. Crégut, P. Gilliot and B. Hönerlage. *Optical gain in porous silicon grains embedded in sol-gel derived SiO_2 matrix under femtosecond excitation.* Appl. Phys. Lett., **84**(17), 3280 (2004).

[33] J. Valenta, P. Janda, K. Dohnalová, D. Nižňanský, F. Vácha and J. Linnros. *Silicon nanocrystals in colloidal solutions: from single nanocrystals to photonic structures.* Optical Materials, **27**(5), 1046 (2005).

[34] K. Luterová, M. Cazzanelli, J. P. Likforman, D. Navarro, J. Valenta, T. Ostatnický, K. Dohnalová S. Cheylan, P. Gilliot, B. Hönerlage, L. Pavesi and I. Pelant. *Optical gain in nanocrystalline silicon: comparison of planar waveguide geometry with a non-waveguiding ensemble of nanocrystals.* Optical Materials, **27**(5), 750 (2005).

[35] F. Trojánek, K. Neudert, P. Malý, K. Dohnalová and I. Pelant. *Ultrafast photoluminescence in silicon nanocrystals measured by femtosecond up-conversion technique.* J. Appl. Phys., **99**, 116108 (2006).

[36] K. Dohnalová, I. Pelant, P. Gilliot, O. Crégut and B. Hönerlage. *Towards laser of silicon nanocrytals in a distributed feedback cavity.* Appl. Phys. Lett., **88**, 251105 (2006).

[37] K. Dohnalová, K. Kůsová, I. Pelant, J. Valenta, P. Gilliot, M.Gallart, O. Crégut, J. L. Rehspringer and B. Hönerlage. *Emission properties of a distributed feedback laser cavity containing silicon nanocrystals.* J. of Luminescence, **121**, 259 (2006).

[38] F. Trojánek, K. Neudert, K. Žídek, K. Dohnalová, I. Pelant and P. Malý. *Femtosecond photoluminescence spectroscopy of silicon nanocrystals.* Phys. Stat. Sol. (c), **3**, 3873–3876 (2006).

[39] K. Luterová, K. Dohnalová, F. Trojánek, K. Neudert, P. Gilliot, B. Hönerlage, P. Malý and I. Pelant. *Porous silicon grains in SiO_2 matrix: Ultrafast photoluminescence and optical gain.* J. Non-Cryst. Solids, **352**, 3041 (2006).

[40] J. Valenta, K. Luterová, R. Tomasiunas, K. Dohnalová, B. Hönerlage and I. Pelant. *Optical gain measurements with variable stripe length technique.* Towards the first silicon laser, Ed. by L. Pavesi, S. Gaponenko and L. Dal Negro, NATO Science Series II (2003).

[41] I. Pelant and K. Dohnalová. *Nanotechnologie ve službách informatiky.* Technický Týdeník, **1/2005**, 19.

[42] M. A. Green, J. Zhao, A. Wang, P. J. Reece and M. Gal. *Efficient silicon light-emitting diodes.* Nature, **412**, 805 (2001).

[43] W. L. Ng, M. A. Lourenco, R. M. Gwilliam, S. Ledain, G. Shao and K. P. Homewood. *An efficient room-temperature silicon-based light-emitting diode.* Nature, **410**, 192 (2001).

[44] M. J. Chen, J. L. Yen, J. Y. Li, J. F. Chang, S. C. Tsai and C. S. Tsai. *Stimulated emission in a nanostructured silicon pn junction diode using current injection.* Appl. Phys. Lett., **84**, 2163 (2004).

[45] T. Trupke, M. A. Green and P. Wurfel. *Optical gain in materials with indirect transitions.* J. Appl. Phys., **93**, 9058 (2003).

[46] W. P. Dumke. *Interband transitions and maser action.* Phys. Rev., **127**(5), 1559 (1962).

[47] M. V. Wolkin, J. Jorne, P. M. Fauchet, G. Allan and C. Delerue. *Electronic States and Luminescence in Porous Silicon Quantum Dots: The Role of Oxygen.* Phys. Rev. Lett, **82**, 197 (1999).

[48] B. Delley and E. F. Steigmeier. *Quantum confinement in Si nanocrystals.* Phys. Rev. B, **47**(3), 1397 (1993).

[49] D. K. Yu, R. Q. Zhang and S. T. Lee. *Structural transition in nanosized silicon clusters.* Phys. Rev. B, **65**, 245417 (2002).

[50] T.-Y. Kim, N.-M. Park, K.-H. Kim, G. Y. Sunga, Y.-W. Ok, T.-Y. Seong and C.-J. Choi. *Quantum confinement effect of silicon nanocrystals in situ grown in silicon nitride films.* Appl. Phys. Lett., **85**(22), 5355 (2004).

[51] j. Valenta, R. Juhasz and J. Linnros. *Photoluminescence spectroscopy of single silicon quantum dots.* Appl. Phys. Lett., **80**, 1070 (2002).

[52] Mark S. Hybertsen. *Absorption and emission of light in nanoscale silicon structures.* Phys. Rev. Lett., **72**(10), 1514 (1994).

[53] D. Kovalev, H. Heckler, M. Ben-Chorin, G. Polisski, M. Schwartzkopff and F. Koch. *Breakdown of the k-Conservation Rule in Si Nanocrystals.* Phys. Rev., **81**, 2803 (1998).

[54] J. Diener, D. Kovalev, H. Heckler, G. Polisski and F. Koch. *Exciton states of silicon nanocrystals studied by magneto-optical spectral hole burning.* Phys. Rev., **63**, 073302 (2001).

[55] J. De la Torre, G. Bremond, A. Souifi, G. Guillot, N. Buffet and P. Mur. *Simultaneous observation of Self Trapped Exciton and Q-confined exciton luminescence emission in silicon nanocrystals.* Opt. Mater., **27**, 1004 (2005).

[56] I.Vasiliev, J. R. Chelikowsky and R. M. Martin. *Surface oxidation effects on the optical properties of silicon nanocrystals.* Phys. Rev. B, **65**, 121302 (2002).

[57] G. Allan, C. Delerue and M. Lannoo. *Nature of Luminescent Surface States of Semiconductor Nanocrystallites.* Phys.Rev.Lett., **76**, 2961 (1996).

[58] A. Yu. Kobitski, K. S. Zhuravlev, H. P. Wagner and D. R. T. Zahn. *Self-trapped exciton recombination in silicon nanocrystals.* Phys.Rev.B, **63**, 115423 (2001).

[59] Toshihide Takagahara and Kyozaburo Takeda. *Theory of the quantum confinement effect on excitons in quantum dots of indirect-gap materials.* Phys. Rev. B, **46**(23), 15578 (1992).

[60] M. H. Nayfeh, N. Rigakis and Z. Yamani. *Photoexcitation of Si-Si surface states in nanocrystallites.* Phys. Rev. B, **56**, 2079 (1997).

[61] Nayfeh et al. Mater. Res. Soc. Symp. Proc., **486**, 243 (1998).

[62] M. H. Nayfeh, N. Barry, J. Therrien, O. Akcakir, E. Gratton and G. Belomoin. *Stimulated blue emission in reconstituted films of ultrasmall silicon nanoparticles.* Appl. Phys. Lett., **78**, 1131 (2001).

[63] L. Khriachtchev, M. Rasanen, S. Novikov and J. Sinkkonen. *Optical gain in Si/SiO$_2$ lattice: Experimental evidence with nanosecond pulses.* Appl. Phys. Lett., **79**, 1249 (2001).

[64] L. Dal Negro, M. Cazzanelli, N. Daldosso, Z. Gaburro, L. Pavesi, F. Priolo, D. Pacifci, G. Franzo and F. Iacona. *Stimulated emission in plasma-enhanced chemical vapour deposited silicon nanocrystals.* Physica E, **16**, 297 (2003).

[65] V. I. Klimov, S. A. Ivanov, J. Nanda, M. Achermann, I. Bezel, J. A. McGuire and A. Piryatinski. *Single-exciton optical gain in semiconductor nanocrystals.* Nature, **447**, 441–446 (2007).

[66] L. Pavesi and M. Ceschini. *Stretched-exponential decay of the luminescence in porous silicon.* Phys. Rev. B, **48**, 17625 (1993).

[67] A. A. Seraphin, S.-T. Ngiam and K. D. Kolenbrander. *Surface control of luminescence in silicon nanoparticles.* J. Appl. Phys., **80**(11), 6429 (1996).

[68] V. I. Klimov, A. A. Mikhailovsky, D. W. McBranch, C. A. Leatherdale and M. G. Bawendi. *Quantization of Multiparticle Auger Rates in Semiconductor Quantum Dots.* Science, **287**, 1011 (2000).

[69] C. Delerue, M. Lanoo, G. Allan, E. Martin, I. Mihalcecsu, J. C. Vial, R. Romestain, F. Muller and A. Bsiesy. *Auger and Coulomb charging effects in semiconductor nanocrystallites.* Phys. Rev. Lett., **75**, 2228 (1995).

[70] R. M'ghaïeth, H. Maâref, I. Mihalcescu and J. C. Vial. *Auger effect as the origin of the fast-luminescent band of freshly anodized porous silicon.* Phys. Rev. B, **60**, 4450 (1999).

[71] B. V. Kamenev and A. G. Nassiopoulou. *Self-trapped excitons in silicon nanocrystals with sizes below 1.5 nm in Si/SiO$_2$ multilayers.* J. Appl. Phys., **90**, 5735 (2001).

[72] A.A. Mikhailovsky, A. V. Malko, J. A. Hollingsworth, M. G. Bawendi and V. I. Klimov. *Multiparticle interactions and stimulated emission in chemically synthesized quantum dots.* Appl. Phys. Lett., **80**, 2380 (2002).

[73] W. Theiss. *Optical properties of porous silicon.* Surf. Sci. Rep., **29**, 91 (1997).

[74] M. Fujii, A. Mimura, S. Hayashi, K. Yamamoto, C. Urakawa and Hitoshi Ohta. *Improvement in photoluminescence efficiency of SiO$_2$ films containing Si nanocrystals by P doping: An electron spin resonance study.* J.Appl.Phys., **87**(4), 1855 (2000).

[75] A. Mimura, M. Fujii, S. Hayashi, D. Kovalev and Frederick Koch. *Photoluminescence and free-electron absorption in heavily phosphorus-doped Si nanocrystals.* Phys.Rev B, **62**(19), 1265 (2000).

[76] V. Švrček, I. Pelant, J.-L. Rehspringer, P. Gilliot, D. Ohlmann, O. Crégut, B. Hönerlage, T. Chvojka, J. Valenta and J. Dian. *Photoluminescence properties of solgel derived SiO$_2$ layers doped with porous silicon.* Mater. Sci. Eng C, **19**, 233 (2002).

[77] R. J. Martín-Palma, L. Pascual, P. Herrero and J. M. Martínez-Duart. *Monte Carlo determination of crystallite size of porous silicon from x-ray line broadening.* Appl. Phys. Lett., **87**, 211906 (2005).

[78] G. Viera, S. Huet and L. Boufendi. *Crystal size and temperature measurements in nanostructured silicon using Raman spectroscopy.* J. Appl. Phys., **90**, 4175 (2001).

[79] L. Tsybeskov, Ju. V. Vandyshev and P. M. Fauchet. *Blue emission in porous silicon: Oxygen-related photoluminescence.* Phys. Rev. B, **49**, 7821 (1994).

[80] P. G. Pai, S. S. Chao, Y. Takagi and G. Lucovsky. *Infrared spectroscopic study of SiO$_x$ films produced by Plasma Enhanced Chemical Vapor Deposition.* J. Vac Sci. Technol. A, **4**, 486 (1986).

[81] X. L. Wu, T. Gao, G. G. Siu, S. Tong and X. M. Bao. *Defect-related infrared photoluminescence in Ge$^+$-implanted SiO$_2$ films.* Appl. Phys. Lett., **74**, 2420 (1999).

[82] D. Krapf, A. Davidi, J. Shappir and A. Saar. *Infrared photo-induced absorption spectroscopy of porous silicon.* Phys. Stat. Sol.(a), **197**(2), 566 (2003).

[83] E. Trave, V. Bello, G. Mattei, M. Mattiazzi, E. Borsella, M. Carpanese, F. Fabbri, M. Falconieri, R. DAmato and N. Herlin-Boime. *Surface control of optical properties in silicon nanocrystals produced by laser pyrolysis.* Applied Surface Science, **252**, 4467 (2006).

[84] J. Diener, D. Kovalev, H. Heckler, G. Polisski and F. Koch. *Exciton states of silicon nanocrystals studied by magneto-optical spectral hole burning.* Phys. Rev. B, **63**, 073302 (2001).

[85] A. Kux and M. Ben Chorin. *Red, green and blue luminescence in porous silicona study of excitation spectra.* Thin Solid Films, **276**, 272 (1996).

[86] M. V. Wolkin, J. Jorne, P. M. Fauchet, G. Allan and C. Delerue. *Electronic States and Luminescence in Porous Silicon Quantum Dots: The Role of Oxygen.* Phys. Rev. Lett., **82**, 197 (1999).

[87] K. Kimura and S. Iwasaki. *Vibronic Fine Structure Found in the Blue Luminescence from Silicon Nanocolloids.* Jpn. J. Appl. Phys., **38**, 609 (1999).

[88] J. P. Wilcoxon, G. A. Samara and P. N. Provencio. *Optical and electronic properties of Si nanoclusters synthesized in inverse micelles.* Phys. Rev. B, **60**, 2704 (1999).

[89] J. D. Holmes, K. J. Ziegler, R. Ch. Doty, L. E. Pell, K. P. Johnston and B. A. Korgel. J. Am. Chem. Soc., **123**, 3743 (2001).

[90] J. H. Stathis and M. A. Kastner. *Time-resolved photoluminescence in amorphous silicon dioxide.* Phys. Rev. B, **35**(6), 2972 (1987).

[91] L. Pavesi and M. Ceschini. *Stretched-exponential decay of the luminescence in porous silicon.* Phys. Rev. B, **48**(6), 17625 (1993).

[92] L. Pavesi, M. Ceschini and H. Eduardo Roman. *Recombination dynamics in porous silicon.* Thin Solid Films, **255**(6), 67 (1995).

[93] D. Amans, O. Guillois, G. Ledoux, D. Porterat and C. Reynaud. *Influence of light intensity on the photoluminescence of silicon nanostructures.* J.Appl.Phys., **91**, 5334 (2002).

[94] A. Pifferi, P. Taroni, A. Torricelli, G. Valentini, P. Mutti, G. Ghislotti and L. Zanghieri. *Nanosecond time-resolved emission spectroscopy from silicon implanted and annealed SiO2 layers.* Appl. Phys. Lett., **70**, 348 (1997).

[95] C. Garcia, B. Garrido, P. Pellegrino, R. Ferre, J. A. Moreno, L. Pavesi, M. Cazzanelli and J. R. Morante. *Absorption cross-sections and lifetimes as a function of size in Si nanocrystals embedded in SiO2.* Physica E, **16**, 429–433 (2003).

[96] M. C. Nuss, W. Zinth and W. Kaiser. *Femtosecond carrier relaxation in semiconductor-doped glasses.* Appl. Phys. Lett., **49**, 1717 (1986).

[97] V. I. Klimov, D. W. McBranch, C. A. Leatherdale and M. G. Bawendi. *Electron and hole relaxation pathways in semiconductor quantum dots.* Phys. Rev. B, **60**, 13740 (1999).

[98] K. L. Shaklee and R. F. Leheny. *Direct determination of optical gain in semiconductor crystals.* Appl. Phys. Lett., **18**(11), 475 (1971).

[99] J. Valenta, I. Pelant and J. Linnros. *Waveguiding effects in the measurement of optical gain in a layer of Si nanocrystals.* Appl. Phys. Lett., **81**, 1396 (2002).

[100] K. L. Shaklee, R. E. Nahory and R. F. Leheny. *Stimulated recombination of highly excited semiconductors.* Proc. 11th Int. Conf. Phys. Semicond., Warszava 1972, Polish Scientific Publishers, **2**, 853–862 (1972).

[101] P.C. Mogensen, P.M. Smowton and P. Blood. *Measurement of optical mode loss in visible emitting lasers.* Appl. Phys. Lett., **71**, 1975 (1997).

[102] P.M. Smowton, E. Herrmann, Y. Ning, H. D. Summers, P. Blood and M. Hopkinson. *Optical mode loss and gain of multiple-layer quantum-dot lasers.* Appl. Phys. Lett., **78**, 2629 (2001).

[103] L. Dal Negro. *Stimulated Emission and Light Transport in Low Dimensional Silicon Structures.* PhD thesis, Universitá Degli Studi di Trento, Dipartimento di Fisica (2003).

[104] O. Svelto, S. Taccheo and C. Svelto. *Analysis of amplified spontaneous emission: some corrections to the Linford formula.* Opt. Communications, **149**, 277–282 (1998).

[105] Zs. Bor. *A novel pumping arrangement for tunable single picosecond pulse generation with a N_2 laser pumped distributed feedback dye laser.* Optics Communications, **29**(1), 103 (1979).

[106] J. Carrol, J. Whiteaway and D. Plumb. *Distributed feedback semiconductor lasers.* IEE Circuits, Devices and Systems series, **10** (1998).

[107] D. Mills and K. W. Kolasinski. *Non-lithographic method of forming ordered arrays of silicon pillars and macropores.* J. Phys. D: Appl. Phys., **38**, 632 (2005).

[108] K. A. Valiev, L. V. Velikov, G. S. Volkov and D. Yu. Zaroslov. Sov. J. Quantum Electron., **17**, 806 (1987).

[109] S. Vijayalakshmi, H. Grebel, G. Yaglioglu, R. Pino, R. Dorsinville and C. W. White. *Nonlinear optical response of Si nanostructures in a silica matrix.* J. Appl. Phys., **88**(11), 6418 (2000).

Curriculum Vitae

Personal data

Name:	RNDr. Kateřina Dohnalová
Date and place of birth:	28th August 1980, Prague, Czech Republic
Nationality:	Czech
Address:	Academy of Sciences, Institute of Physics
	Department of Thin Films
	Cukrovarnická 10, Praha 6 - 162 53, Czech Republic
	Email: dohnalov@fzu.cz,nanokatka@nipax.cz
	Phone: +420 220 318 414

Education

2003–2007   Post-graduate "doctorat cotutelle" studies at the Université Louis Pasteur in Strasbourg (Université Strasbourg 1), France and Faculty of Mathematics and Physics, Charles University in Prague, Czech Republic. (specialization: Quantum optics and optoelectronics)
PhD thesis on *Study of optical amplification in silicon based nanostructures*

2003–2007   Doctorate Programme at the Faculty of Mathematics and Physics, Charles University in Prague, Czech Republic, doctoral degree 'RNDr.'. (specialization: Optics and optoelectronics)

1998–2003   Graduate studies at the Faculty of Mathematics and Physics, Charles University in Prague, Czech Republic, master degree 'Mgr.'. (specialization: Optics and optoelectronics)
Master thesis on *Luminescence properties of silicon nanostructures prepared by novel methods*

Research interests

- optical properties of semiconductors, semiconductor nanostructures (optical properties and preparation methods), optical gain, light amplification, laser oscillators and generators, optical feedback, integrated optoelectronics, silicon photonics

- crystallization of amorphous silicon, transport properties of amorphous, microcrystalline silicon thin films, solar cells, photovoltaic structures

Work experience

since 2001   Part time research position in the Institute of Physics, Academy of Sciences of the Czech Republic, Prague.

Professional activities, publications, citations, coneferences, invited lectures

Author or co-author of 10 scientific publications that were published in impacted international scientific journals [1-10]. The publication [7] has been selected for publishing in July 4, 2006 issue of Virtual Journal of Nanoscale Science & Technology - www.vjnano.org. The publication [8] has been awarded by the "Young Scientist award" at international conference E-MRS Spring Meeting in Nice, 2006. Author of other non-impacted publications [11-21], 3 invited talks and lectures [30-32]. Conference contributions [22-29] were not published. Citations: Publication [1] -2x, [2]-1x, [3]-21x, [4]-2x, [5]-6x, [7]-2x - total number of citations: 34.

Scholarships and scientific awards

2006   "Young Scientist Award" at international conference E-MRS 2006 Spring Meeting, Nice, France
2003   French government scholarship "doctorat cotutelle"
2001   1st prize in the doctoral thesis competition at international conference JUNIORMAT 2001 in Brno, Czech Republic

Organization activities

January 2004   organization of the invited talk of Prof. Dr. Kevin Warwick - "Cyborg engineering" from the University of Reading in Great Britain, under the Academy of Sciences of Czech Republic auspices

Interests, other skills:

Language skills: Czech, English (advanced, active), French (basic, active), German (basic, passive), Russian (basic, passive)
Computer skills: MS Windows, MS Office, Origin, Mathcad 2000, Corel Draw, Corel PhotoPaint, Adobe Photoshop, LaTeX, programming in Pascal
Other skills and interests: driving license B, computer graphics, classical graphic and painting techniques, climbing, organ and piano-playing

List of publications

Publications in impacted scientific journals

1. P. Fojtík, K. Dohnalová, T. Mates, J. Stuchlík, I. Gregora, J. Chval, A. Fejfar, J. Kočka and I. Pelant, *Rapid crystallization of amorphous silicon at room temperature*, Philosophical Magazine B **82**, 1785 (2002).

2. K. Dohnalová, K. Luterová, J. Valenta, J. Buršík, M. Procházka, V. Křesálek, B. Hönerlage and I. Pelant, *Grains of porous silicon embedded in SiO₂ Studies of optical gain and electroluminescence*, E-MRS Fall Meeting, Warsaw 2003, Solid State Phenomena Vols. **99-100** (2004) pp. 31-34.

3. K. Luterová, K. Dohnalová, V. Švrček, I. Pelant, J. P. Likforman, O. Crégut, P. Gilliot and B. Hönerlage *Optical gain in porous silicon grains embedded in sol-gel derived SiO₂ matrix under femtosecond excitation*, Applied Physics Letters **84** (17), 3280-3282 (2004).

4. J. Valenta, P. Janda, K. Dohnalová, D. Nižňanský, F. Vácha and J. Linnros *Silicon nanocrystals in colloidal solutions: from single nanocrystals to photonic structures*, E-MRS Spring Meeting, Strasbourg 2004, Optical Materials **27** (5), 1046 (2005).

5. K. Luterová, M. Cazzanelli, J. P. Likforman, D. Navarro, J. Valenta, T. Ostatnický, K. Dohnalová, S. Cheylan, P. Gilliot, B. Hönerlage, L. Pavesi and I. Pelant *Optical gain in nanocrystalline silicon: comparison of planar waveguide geometry with a non-waveguiding ensemble of nanocrystals*, E-MRS Spring Meeting, Strasbourg 2004, Optical Materials **27** (5), 750 (2005).

6. F. Trojánek, K. Neudert, P. Malý, K. Dohnalová and I. Pelant *Ultrafast photoluminescence in silicon nanocrystals measured by femtosecond up-conversion technique*, Journal of Applied Physics **99** (11), 116108 (2006)

7. K. Dohnalová, I. Pelant, P. Gilliot, O. Crégut and B. Hönerlage *Towards laser of silicon nanocrytals in a distributed feedback cavity*, Applied Physics Letters **88**, 251105 (2006) (selected for publishing in July 4, 2006 issue of Virtual Journal of Nanoscale Science & Technology - www.vjnano.org)

8. K. Dohnalová, K. Kusová, I. Pelant, J. Valenta, P. Gilliot, M.Gallart, O. Crégut, J. L. Rehspringer and B. Hönerlage *Emission properties of a distributed feedback laser cavity containing silicon nanocrystals*, Journal of Luminescence **121**, 259-262 (2006) (awarded by the "Young scientist award" at the E-MRS Spring Meeting in Nice, France (June 2006)

9. K. Luterová, K. Dohnalová, F. Trojánek, K. Neudert, P. Gilliot, B. Hönerlage, P. Malý and I. Pelant *Porous silicon grains in SiO$_2$ matrix: Ultrafast photoluminescence and optical gain*, Journal of Non-Crystalline Solids **352**, 3041 (2006)

10. F. Trojánek, K. Neudert, K. Žídek, K. Dohnalová, I. Pelant and P. Malý *Femtosecond photoluminescence spectroscopy of silicon nanocrystals*, Phys. Stat. Sol. (c) **3** (2006), 3873

Publications in reviewed international conference proceeding

11. P. Fojtík, K. Dohnalová, T. Mates, J. Stuchlík, I. Gregora, J. Chval, K. Knížek, J. Kočka and I. Pelant.; *Electric field induced crystallization of Ni covered hydrogenated amorphous silicon at room temperature*, 19th ICAMS, Nice, France, 27.-31. 8. 2001

12. J. Valenta, K. Luterová, R. Tomasiunas, K. Dohnalová, B. Hönerlage and I. Pelant; *Optical gain measurements with variable stripe length technique*, Towards the first silicon laser, NATO conference, Trento, Italy, 21.-26. 9. 2002, published in NATO Science Series II, 2003

13. K. Dohnalová, K. Luterová, J. Valenta, J. Buršík, M. Procházka, V. Křesálek, B. Hnerlage and I. Pelant: *Grains of porous silicon embedded in SiO$_2$: studies of optical gain and electroluminescence*, E-MRS Fall Meeting 2003, Warszaw, Poland, 15.-19.9.2003

14. K. Luterová, M. Cazzanelli, J.-P. Likforman, D. Navarro, J. Valenta, T. Ostatnický, K. Dohnalová, S. Cheylan, P. Gilliot, B. Hönerlage, L. Pavesi and I. Pelant, *Optical gain in nanocrystalline silicon: comparison of planar waveguide geometry with a non-waveguiding ensemble of nanocrystals*, E-MRS Spring Meeting 2004, Strasbourg, France, 24.-27.5 2004 (invited talk)

15. J. Valenta, P. Janda, K. Dohnalová, D. Nižňanský, F. Vácha and J. Linnros, *Silicon nanocrystals in colloidal solutions: from single nanocrystals to photonic structures*, E-MRS Spring Meeting 2004, Strasbourg, France, 24.-27.5 2004

16. K. Luterová, K. Dohnalová, F. Trojánek, K. Neudert, P. Gilliot, B. Hönerlage, P. Malý and I. Pelant: *Optical gain in silicon nanocrystals*, 21. ICANS, Lisabon 2005 (invited talk)

17. F. Trojánek, K. Neudert, K. Žídek, K. Dohnalová, I. Pelant and P. Malý: *Femtosecond photoluminescence spectroscopy of silicon nanocrystals*, Quantum Dots 2006, Chamonix, France 1.-6.5.2006 (invited talk)

18. K. Dohnalová, K. Kůsová, I. Pelant, J. Valenta, P. Gilliot, M. Gallart, O. Crégut, J. L. Rehspringer and B. Hönerlage: *Emission properties of a distributed feedback laser*

cavity containing silicon nanocrystals, E-MRS Spring Meeting 2006, Nice, France, 28.5.-2.6.2006

Publications in non-review international conference proceedings

19. K. Dohnalová, P. Fojtík, T. Mates, J. Stuchlík, I. Gregora, J. Kočka and I. Pelant: *Nová levná metoda niklem indukované krystalisace a-Si:H za pokojové teploty*, JUNIORMAT'01, 19.-20.9. 2001, Ústav materiálového inženýrství F. Píška, Brno, p.154-155

20. T. Mates, A. Fejfar, P. Fojtík, K. Luterová, M. Ledinský, K. Dohnalová, M. Dienstbier, I. Pelant and J. Kočka; *Grains in thin microcrystalline silicon films studied by combined AFM microscope*, Nano02, Brno, 19.-21.10.2002

Publications in national scientific journals

21. I. Pelant and K. Dohnalová, *Nanotechnologie ve službách informatiky*, Technický Týdeník 1/2005, p.19

Presentations at conferences, not published

22. P. Fojtík, K. Dohnalová, T. Mates, J. Stuchlík, I. Gregora, J. Chval, K. Knížek, J. Kočka and I. Pelant, *Electric Field Induced Crystallization of Ni-covered Hydrogenated Amorphous Silicon at Room Temperature*, 19th International Conference on Amorphous and Microcrystalline Semiconductors, 27.-31. 8. 2001, Nice, France

23. T. Mates, A. Fejfar, P. Fojtík, K. Luterová, M. Ledinský, K. Dohnalová, M. Dienstbier, I. Pelant and J. Kočka, *Zrna v tenkých vrstvách mikrokrystalického křemíku studovaná kombinovanou AFM mikroskopií*, prezentováno na Národní konferenci NANO'02, 19-21. 11. 2002, FSI VUT, Brno

24. I. Pelant, K. Luterová, K. Dohnalová and J. Valenta: *Od křemíkových nanokrystalů ke křemíkovému laseru*, NANO/SME/IST (Slovenská akadémia vied), Smolenice, Slovakia, 17.-18.3. 2003 (invited talk)

25. P. Fojtík, K. Dohnalová, T. Mates, J. Stuchlík, A. Fejfar, J. Kočka and I. Pelant, *Room Temperature Electric Field Induced Crystallization of Hydrogenated Amorphous Silicon*, presented at 2nd aSiNet Workshop on Thin Silicon held jointly with 9th Euroregional Workshop on Thin Silicon Devices, 19.-21. 2. 2003, Lisbon, Portugal

26. K. Dohnalová, I. Pelant, K. Luterová and J. Valenta: *Laser with silicon nanocrystals?*, 2nd aSiNet workshop, Lisbon, Portugal, 19.-21.2. 2003

27. K. Dohnalová, K. Luterová, I. Pelant, T. Ostatnický, J. Valenta, B. Hönerlage and S. Cheylan, *Silicon nanocrystals - way to silicon laser?*, A*Star workshop, Singapore, 15.-20.11 2004

28. T. Mates, B. Rezek, P. Fojtík, I. Drbohlav, M. Ledinský, K. Luterová, K. Dohnalová, H. Stuchliková, J. Stuchlík, S. Honda, L. Fekete, A. Fejfar and J.Kočka, *Structure and Properties of Thin Silicon Films Deposited at Low Substrate Temperatures*, presented at 3rd aSiNet Workshop on Thin Silicon, 25.-27. 2. 2004, Bratislava, Slovak Republic

29. K. Dohnalová, P. Gilliot, M. Gallart, O. Crégut, J. L. Rehspringer, F. Trojánek, A. Fojtík, K. Kůsová, K. Luterová, I. Pelant and B. Hönerlage, *Optical gain measurements on ensemble of silicon nanocrystals embedded in SiO_2*, Congrés Societé Francaise de Physique, Lille, France, 29.8.-2.9 2005

Invited talks

30. K. Dohnalová, K. Luterová, I. Pelant, J. Valenta, J. Buršik, V. Křesálek and B. Hönerlage, *Si nanocrystals in SiO_2 matrix: Silicon laser?*, IPCMS Strasbourg, France, 13/02/04 (B. Hönerlage)

31. K. Dohnalová, K. Luterová, I. Pelant, J. Valenta, J. Buršik, V. Křesálek and B. Hönerlage, *Si nanocrystals in SiO_2 matrix: Silicon laser?*, University of Stuttgart, Germany, 16/02/04 (Dr. Ing. Markus Schubert)

32. K. Dohnalová, I. Pelant and B. Hönerlage, *Towards the first silicon laser*, Institute of Physics, Department of Theoretical Physics, Strasbourg, France, 27/05/05 (03/06/05)(Dr. Dietmar Weinmann)